

**ORIGIN AND GENESIS OF THE GOLDENVILLE IRON FORMATIONS AND  
IMPLICATIONS FOR MINERALIZATION, BAIE VERTE, NEWFOUNDLAND,  
CANADA**

By Carly Mueller

A Thesis submitted to the  
School of Graduate Studies  
in partial fulfillment of the requirements for the degree of

**Master of Science**

**Department of Earth Sciences**

Memorial University of Newfoundland

**December 2022**

St. John's, Newfoundland and Labrador

## ABSTRACT

The Goldenville iron formation (IF) and associated sedimentary rocks, within the Point Rousse complex of the Baie Verte Peninsula, hosts the Goldenville Au deposit and produced 23 tonnes of ore between 1904-1906 (158 oz gold recovered). The Goldenville IF marks the end of Cambrian-Ordovician (~489-485 Ma) Au-rich VMS activity (i.e., VMS Rambler-Ming district), is considered to be correlative with the Nugget Pond IF with both iron formations believed to form a marker unit between the Mount Misery Formation and the overlying Snooks Arm Group cover sequence (~470 Ma), and captures paleo-oceanic redox conditions during the transition from the Cambrian to Ordovician. Despite economic, stratigraphic, and geological importance of the Goldenville IF, it has received very little textural-mineralogical-geochemical study.

The Goldenville horizon is a laterally discontinuous, fine-grained, and laminated unit within argillites, volcaniclastic rocks, and basalt flows. Chemostratigraphy provides evidence of multiple iron formation horizons between the Mount Misery Formation and the overlying Snooks Arm Group cover sequence. In particular, the position of the Goldenville iron formation is lower in stratigraphy and contained within the Mount Misery Formation. In the IF, the lithogeochemical data reflect varying contributions from detrital material, hydrothermal discharge, and hydrogenous elements scavenged from seawater. Samples with the highest hydrothermally sourced Fe and Mn abundance preserve evidence in their REE+Y chemistry for two distinct oxide particle scavenging shuttles that operated in a volcanically active basin with oxygenated bottom waters. Textural evidence of gold in and proximal to the IF suggests that hydrothermal fluids

interacted with Fe<sup>3+</sup>-bearing minerals within the IF, resulting in wall rock sulfidation and the co-precipitation of gold and pyrite.

## **GENERAL SUMMARY**

Iron formations, including the Goldenville and Nugget Pond horizons, on the Baie Verte Peninsula, Newfoundland, are host to a number of Au deposits. The Goldenville IF formed at the end of Cambrian into the Ordovician (~489-485 Ma), hosts gold mineralization, captures ocean oxygenation conditions at its time of formation, and is a distinct unit between the Mount Misery Formation and the Snooks Arm Group cover sequence in some locations. This work showed that there are multiple IFs at this boundary and the Goldenville horizon is below the contact to the Snooks Arm Group.

The Goldenville IF is a laterally discontinuous, fine-grained, and laminated iron-rich unit within argillites, volcaniclastic rocks, and basalt flows. In the IF, the data reflect varying contributions from multiple sources of the ocean basin it was formed within. Goldenville IF samples with the highest iron composition have distinct rare earth element and Yttrium signatures akin to modern oxygenated seawater.

Gold in and proximal to the IF is along edges of magnetite and quartz veins, indicating fluid interaction with iron-rich wall rock depositing gold and pyrite. The research within demonstrates that the Goldenville IF provides important data for understanding stratigraphy, Cambrian-Ordovician Ocean oxygen conditions, and reevaluates the unit as a target for gold mineralization.

## **ACKNOWLEDGMENTS**

I would like to thank the Piercey research group: Matt Manor, Nikola Denisová, Maciej Pawlukiewicz, Robert King, Marko Szmihelsky, Regan Jacobson, Rosie Cobbett, and Kei Quinn for their regular research discussions, camaraderie, advice, and group dinners. I would like to acknowledge Matt and Nikola for their time to discuss and edit early drafts of this work; without their immense help and support, this thesis would not be complete. I am particularly grateful for the members of the 5016 office (Maciej, Robert, and Marko) and Amy Parkinson, whose daily jokes, discussions, and coffee walks made my time at Memorial University most memorable. I would also like to thank Dr. Stephen Piercey and Dr. Michael Babechuk for guidance and critiques throughout the changing timeline of this project. Finally, I would like to thank the group espresso machine (endearingly named Phil) whose caffeine supply and regular coffee breaks were vital to finishing this research.

This research was completed with the support of the exploration team at Anaconda Mining Inc., namely David Copeland, Paul McNeill, Steve Barrett, Dean Courage, Linsey Gale, Mike Kelly, Alison Cox, and Michelle English. Their support in and out of the field was greatly appreciated. David Copeland helped in co-designing this research project, and his contributions have not gone unnoticed. I would also like to thank Georgian Manuc, who I spent time within Baie Verte mapping and discussing the idiosyncrasies of the Baie Verte Peninsula.

I would like to thank those outside of academia at MUN whose support was most appreciated. In particular, Dr. J. Brian Mahoney, who provided advice when I needed it

most and the endless support in my geology career from the very beginning. I would like to thank Amanda Storey for her unwavering honest opinions and realizing that my infrequency to visit and making it to life events is a reality of having a friend fond of rocks a minerals hundreds of miles, and a country, away. For those not explicitly named here, your support now and throughout my career has not gone unappreciated. Thank you.

Multiple sources provided financial support for this project: 1) Natural Resources Canada Targeted Geosciences Initiative-5 (TGI-5) grant to Dr. Stephen Piercy; 2) in-kind support from Anaconda Mining Ltd.; 3) a Natural Sciences and Engineering Research Council of Canada (NSERC) Discovery Grant and an NSERC Collaborative Research and Development Grant to Dr. Stephen Piercy; 4) a Memorial University School of Graduate Studies Fellowship and teaching assistantship to the author; and 5) Society of Economic Geologists' Graduate Student Fellowship awarded to the author.

## TABLE OF CONTENTS

<b>ABSTRACT.....</b>	<b>ii</b>
<b>GENERAL SUMMARY .....</b>	<b>iv</b>
<b>ACKNOWLEDGMENTS .....</b>	<b>v</b>
<b>TABLE OF CONTENTS .....</b>	<b>vii</b>
<b>LIST OF TABLES .....</b>	<b>xii</b>
<b>LIST OF FIGURES .....</b>	<b>xiii</b>
<b>LIST OF APPENDICES .....</b>	<b>xiv</b>
<b>CHAPTER 1: Introduction and Overview.....</b>	<b>15</b>
<b>1.1 Introduction.....</b>	<b>15</b>
<b>1.2 Site History .....</b>	<b>18</b>
<b>1.3 Regional Geology .....</b>	<b>20</b>
<b>1.4 Local Geology .....</b>	<b>21</b>
<b>1.5 Stratigraphy.....</b>	<b>24</b>
<b>1.6 Orogenic Au.....</b>	<b>26</b>
<b>1.7 Overview of Exhalative Iron Formations .....</b>	<b>29</b>
<b>1.7.1 REE Proxies for Ancient Seawater Composition, Redox, and Hydrothermal Vent Fluid-Seawater Dynamics.....</b>	<b>32</b>
<b>1.7.2 Iron Formation and their Utility in VMS and Orogenic Au Exploration .</b>	<b>37</b>

<b>1.8 Thesis Objectives.....</b>	<b>39</b>
<b>1.9 Co-authorship Statement .....</b>	<b>40</b>
<b>1.10 Presentation .....</b>	<b>40</b>
<b>References .....</b>	<b>41</b>
<b>Chapter 2: Origin and Genesis of the Goldenville Iron Formations Associated with Base Metals and Orogenic Au, Baie Verte, Newfoundland, Canada .....</b>	<b>60</b>
<b>2.1 Abstract.....</b>	<b>60</b>
<b>2.2 Introduction.....</b>	<b>62</b>
<b>2.3 Tectonic and Regional Setting .....</b>	<b>64</b>
<b>2.4 Regional Geologic and Stratigraphic Setting of the Goldenville Horizon .....</b>	<b>65</b>
<b>2.5 Lithofacies.....</b>	<b>68</b>
<b>2.5.1 Igneous and Clastic Sedimentary Lithofacies .....</b>	<b>68</b>
<b>2.5.2 Iron Formation Lithofacies .....</b>	<b>71</b>
<b>2.6 Lithogeochemistry.....</b>	<b>74</b>
<b>2.6.1 Sampling, Analytical Methods, and QA/QC .....</b>	<b>74</b>
<b>2.6.2 Results .....</b>	<b>77</b>
<b>2.7 Discussion.....</b>	<b>89</b>
<b>2.7.1 Stratigraphic Relationships Relative to the Goldenville Iron Formation..</b>	<b>89</b>

<b>2.7.2 Evaluating Detrital, Hydrothermal, and Hydrogenous Components in the Goldenville horizon .....</b>	<b>91</b>
<b>2.7.3 Evaluating Cerium for Paleoredox; Inferring Conditions in the Humber Seaway throughout the Cambrian-Ordovician.....</b>	<b>94</b>
<b>2.7.4 Implications for Exploration; Au and Base Metal Mineralization .....</b>	<b>100</b>
<b>2.8 Conclusion .....</b>	<b>102</b>
<b>References .....</b>	<b>103</b>
<b>Chapter 3: Summary and Future Research .....</b>	<b>149</b>
<b>3.1 Summary.....</b>	<b>149</b>
<b>Appendices.....</b>	<b>154</b>
<b>Appendix A. Graphic Logs.....</b>	<b>154</b>
<b>Appendix B: List of samples and methods used for rocks from the Goldenville Horizon and related stratigraphy.....</b>	<b>204</b>
<b>Appendix C: Petrography of rocks from the Goldenville Horizon and related stratigraphy .....</b>	<b>211</b>
<b>Appendix D: Precision and accuracy data for in house reference materials SLV-MC and IOC-1.....</b>	<b>221</b>
<b>Appendix E: Whole-rock geochemistry for rocks from the Goldenville Horizon and related stratigraphy.....</b>	<b>231</b>

**Appendix F: Additional whole-rock geochemistry collected for rocks from the  
Goldenville Horizon and related stratigraphy .....267**

## **LIST OF TABLES**

### **Chapter 2**

- Table 2.1** Summary of geochemical characteristics of simplified lithologies from rocks proximal to the Goldenville Iron Formation
- Table 2.2** Summary of geochemical characteristics of IF rocks of the Goldenville horizon

## LIST OF FIGURES

### Chapter 1

- Figure 1.1** a) Simplified map of the tectonostratigraphic terranes of Newfoundland, and b) simplified geologic map of the Baie Verte Peninsula.
- Figure 1.2** Simplified geology map of the Point Rousse project on the Baie Verte Peninsula.
- Figure 1.3** Simplified geologic map of the Goldenville mine area with logged drill holes and surface samples.
- Figure 1.4** Representative regional stratigraphy of the Baie Verte Peninsula.
- Figure 1.5** Representative cross-section of the tectonic settings in which gold deposits are formed.
- Figure 1.6** Schematic of fluid flow into accreted ocean arc.
- Figure 1.7** Schematic of the buoyant and non-buoyant plume associated with a hydrothermal vent.

### Chapter 2

- Figure 2.1** a) Simplified map of the tectonostratigraphic terranes of Newfoundland, and b) simplified geologic map of the Baie Verte Peninsula.
- Figure 2.2** Simplified geology map of the Point Rousse project on the Baie Verte Peninsula.
- Figure 2.3** Representative regional stratigraphy of the Baie Verte Peninsula.
- Figure 2.4** Simplified geology of the Goldenville mine area with logged drill hole locations.
- Figure 2.5** Representative cross-sections across the Goldenville area.
- Figure 2.6** Graphic logs of the Goldenville area with a focus on the Goldenville iron formation.
- Figure 2.7** Photographs of the main lithology variations proximal to the Goldenville iron formation; a-d) basalt variation, e) volcaniclastic unit, f) intrusive unit, and g-h) argillite variation.
- Figure 2.8** Photographs of the Goldenville iron formation and associated mineralization.
- Figure 2.9** Photographs and photomicrographs of mineralization within the Goldenville iron formation.
- Figure 2.10** Alteration plot for the coherent basalt flows – Hasimoto alteration index vs. chlorite-carbonate-pyrite index.
- Figure 2.11** Key element ratios for the differing basalt suites against  $\text{Al}_2\text{O}_3/\text{Na}_2\text{O}$ ,  $\text{Nb}/\text{Y}$ , and  $\text{Zr}/\text{Y}$ .
- Figure 2.12** Discrimination diagrams for the differing basalt suites of the Goldenville deposit.

- Figure 2.13** Primitive mantle-normalized trace element plots for the two geochemical volcanic suites of the rocks proximal to the Goldenville horizon.
- Figure 2.14** Th/Yb vs Nb/Yb diagram for rocks of the Goldenville horizon and surrounding stratigraphy.
- Figure 2.15** Molar element plots for rocks from the Goldenville horizon and surrounding stratigraphy.
- Figure 2.16.** Discrimination diagram plots for rocks of the Goldenville deposit.
- Figure 2.17** Boström-type plots for iron formation samples of the Goldenville horizon.
- Figure 2.18** Abundances of  $\text{Fe}_2\text{O}_3 + \text{MnO}$ ,  $\text{MnO}$ , and  $\text{Fe}_2\text{O}_3$  wt.% against  $\sum \text{REE}$ .
- Figure 2.19** Rare earth element budget versus key element ratio plots for rocks proximal and of the Goldenville horizon.
- Figure 2.20** Post-Archean Australian Shale (PAAS) normalized rare earth element and Y plots for Fe-rich rocks from the Goldenville horizon.
- Figure 2.21** a)  $\text{Ce}_n/\text{Ce}_n^*$ - $\text{Pr}_n/\text{Pr}_n^*$  plot; b)  $\text{Ce}_n/\text{Ce}_n^*$  versus  $\text{MnO}$ ; c)  $\text{Ce}_n/\text{Ce}_n^*$  versus  $\text{Fe}_2\text{O}_3$ ; and d)  $\text{Ce}_n/\text{Ce}_n^*$  versus  $\text{Y/Ho}$ .
- Figure 2.22** Base and transition metal induvial element plots vs  $(\text{Fe}+\text{Mn})/(\text{Fe}+\text{Mn}+\text{Al}+\text{Ti})$  ratios.
- Figure 2.23** Representative regional stratigraphy re-interpretated of the Baie Verte Peninsula.
- Figure 2.24** Representative hydrothermal plume with processes depicted for buoyant, non-buoyant plume, and overall sediment contribution. Inset of Fe-oxides versus Mn-oxides related to cerium (Ce) adsorption.

## LIST OF APPENDICES

**Appendix A:** Graphic Logs

- Appendix A.I** Abbreviations and legend for graphic logs
- Appendix A.II** Graphic logs from the 2016 drill program
- Appendix A.III** Graphic logs from the 1987/88 drill program

**Appendix B:** List of samples and methods used for rocks from the Goldenville Horizon and related stratigraphy

**Appendix C:** Petrography of rocks from the Goldenville Horizon and related stratigraphy

- Appendix C.I** Scans of petrographic thin sections

**Appendix D:** Quality Assurance and Quality Control (QA/QC)

- Appendix D.I** Precision and accuracy data abbreviations
- Appendix D.II** Precision and accuracy data for in house reference materials

**Appendix E:** Whole-rock geochemistry for rocks from the Goldenville Horizon and related stratigraphy

- Appendix E.I** Whole-rock geochemistry abbreviations
- Appendix E.II** Whole-rock geochemistry

**Appendix F:** Additional whole-rock geochemistry collected for rocks from the Goldenville Horizon and related stratigraphy

- Appendix F.I** Whole-rock geochemistry abbreviations, additional data
- Appendix F.II** Whole-rock geochemistry, additional data

## CHAPTER 1: Introduction and Overview

---

### 1.1 Introduction

The Baie Verte Peninsula (Fig. 1.1) has been the focus of mineral exploration and development for base metals (Cu, Zn), asbestos, and Au since 1867 (Hibbard, 1983; Evans, 2004; Skulski et al., 2010). The peninsula hosts numerous Cu- and Au-rich volcanogenic massive sulfide deposits, as well as orogenic gold deposits (Hibbard, 1983; Evans, 2004; Sparrow et al., 2017), where Au is hosted in both lower Ordovician ophiolitic rocks (e.g., Betts Cove and Pacquet complexes) and their volcanic cover sequences (Snooks Arm Group; Bédard, 1999; Castonguay et al., 2009). Significant Au mineralization is associated with fault zones and their splays (e.g., Baie Verte line and splays - the Scrape and Deer Cove thrusts) and is divided into either vein-hosted or altered wall rock-hosted mineralization (Dubé, 1990; Evans, 1999; Sparrow et al., 2017). The most common gold-only mineralization in the area is Au disseminated throughout altered wall rocks; particularly high Fe-Ti basalts and medium grained diabase/gabbro that hosts the Pine Cove deposit, and gabbro intrusions that host the Stog'er Tight and Argyle deposits, all of which have a spatial association to major faults (Dubé, 1990; Ybarra, 2019; Pawlukiewicz, 2020). Regionally extensive iron formations in the Baie Verte Peninsula also host orogenic Au, including the past producing Nugget Pond and Goldenville deposits (Dubé, 1990; Evans, 1999, 2004). The Nugget Pond deposit, associated with the Nugget Pond horizon, produced approximately 488,000 tonnes of ore that graded 9.61 g/t Au (Evans, 1999; Sparrow et al., 2017). The Goldenville deposit, associated with the Goldenville iron formation, and the focus of this study, produced 23

tonnes of ore between 1904-1906 (158 oz gold recovered), and more recently was the focus of an exploration campaign that resulted in drill hole intersections with Au grades of up to 1.42 g/t over 0.42 m (Sparrow et al., 2017).

The Goldenville deposit and surrounding stratigraphy are collectively known as the Goldenville horizon, and despite past mining and recent exploration, the deposit and horizon have not been studied with modern methods, and the chemistry and relationships of the iron formation to Au and base metal mineralization in the horizon are not well understood. Several models have been proposed as the source of gold for the Goldenville deposit, such as: 1) syngenetic gold, along with base metals, where gold is linked to seafloor exhalative horizons (i.e., syngenetic Au in iron formations; Fitzpatrick, 1981); 2) gold that was concentrated due to remobilization of original syngenetic Au (Snelgrove, 1935; Watson, 1947; Frew, 1971; Hibbard, 1983); or 3) related to epigenetic gold-enrichment due to wall rock sulfidation and veining associated with orogenic Au-bearing fluids interacting with the Fe-rich rocks (Evans, 2004). Previously, Fitzpatrick (1981) indicated that Au mineralization in the Goldenville iron formation was synchronous with the iron formation deposition (i.e., syngenetic), and along with previous workers (Snelgrove, 1935; Watson, 1947; Frew, 1971; Hibbard, 1983) he proposed that the gold-bearing quartz veins were a result of remobilization of gold that was previously deposited within the iron formation. In contrast, compared to similar deposits globally, most models for iron formation orogenic Au suggest they form from Au-bearing metamorphic fluids reacting with iron oxide-facies wall rock (e.g., Caddey, 1991; Peter, 2003; Morelli et al., 2010; Lambeck et al., 2011; Steadman et al., 2014; McNicoll et al., 2016).

In addition to being potential hosts of orogenic gold, iron formations and ferruginous cherty sediments are spatially associated with volcanogenic massive sulfide (VMS) deposits (Peter and Goodfellow, 1996; Spry et al., 2000; Konhauser et al., 2017). These VMS-related iron formations are referred to as exhalative-type (or Algoma-type), to emphasize their formation via exhalative hydrothermal vent processes (Gross, 1980; Bekker et al., 2014). Further, the Goldenville iron formation, occurring at a similar stratigraphic position as the end of Cu-Au-bearing Cambrian-Ordovician (~489-485 Ma) VMS activity (i.e., Ming deposit and Pacquet complex volcanism), and is interpreted to be a stratigraphic transition/marker unit within the Snooks Arm Group cover sequence (~470 Ma) (Skulski et al., 2009).

Across global studies of exhalative iron formations, it has been shown they form, in part, from mineral particles that precipitate in seawater and adsorb elements from the water column at the time of their formation (Bekker et al., 2014; Gourcerol et al., 2016). The redox-sensitive trace elements scavenged by these particles can result in a chemical signature (e.g., rare earth elements and Y patterns) retained in iron formations with potential to record ocean redox conditions within the basin of deposition. For this study, the Goldenville iron formation provides an opportunity to test the deep marine basin redox of the Humber seaway at the transition from the Cambrian to Ordovician. To be effective, however, particle-scavenged seawater signatures must be isolated from other contributors to bulk IF geochemical signatures, such as that of the hydrothermal fluid initially supplying dissolved Fe (and Mn) to the basin, and any volcaniclastic or terrigenous detritus.

While the regional tectonostratigraphic setting of the Goldenville iron formation is understood, its internal variations, lithogeochemistry, and thus the details of its origin, remain unknown. To better understand the Goldenville iron formation, this Master's study has four main objectives: 1) document the variations in the lithofaces and lithogeochemistry of the Goldenville iron formation and surrounding units; 2) evaluate the detrital, hydrogenous (signatures from seawater), and hydrothermal geochemical contributions to the iron formation as recorded by the lithogeochemistry of the iron formations; 3) evaluate the paleoredox conditions of the Humber seaway during deposition of the iron formation in the Cambrian-Ordovician (~489-485 Ma); and 4) document the spatial and genetic relationships between Au mineralization and the iron formation.

## 1.2 Site History

The study area is located within the Point Rousse project property owned by Anaconda Mining Inc., Baie Verte Peninsula (BVP), in UTM Zone 21 (NAD83) between latitudes  $49^{\circ}59'9.8''\text{N}$  and  $50^{\circ}00'13''\text{N}$  and longitudes  $56^{\circ}03'55''\text{W}$  and  $56^{\circ}01'49''\text{W}$  and sits 1.7 km northwest of Ming's Bight (Fig. 1.2; Evans, 1999; Sparrow et al., 2017). The area has producing Au mines within 8 km, including Stog'er Tight (642,000 t @ 3.02 g/t Au indicated resource and 53,000 t @ 5.63 g/t Au inferred resource), Argyle (436,800 t @ 2.53 g/t Au indicated and 500 t @ 2.77 g/t Au inferred), and the Pine Cove Stockpile (147,855 t @ 0.55 g/t Au probable) (Kuntz et al., 2021)..

The BVP has a rich history of mining and mineral exploration beginning with the Terra Nova Cu mine and subsequently the Tilt Cove and Betts Cove deposits (Evans,

2004). Gold mineralization was first discovered at the Goldenville Prospect by J.R. Stewart in 1903, which would later yield 158 oz of processed Au from 1904-1906 (Sparrow et al., 2017). No additional mining has occurred at the Goldenville deposit since the mine shafts were closed in 1906; however, exploration has continued along the Goldenville horizon and has resulted in the discovery of six new mineral occurrences (Sparrow et al., 2017).

Exploration of the Goldenville horizon has included four diamond drilling campaigns, in addition to prospecting, mapping, geophysics, soil sampling, and geochemical surveys. The U.S Borax and Chemical Corporation drilled one 209 m hole (historic DDH log provided by Anaconda Mining Inc.) in 1984; Granges Exploration Limited drilled eighteen holes (1673.52 m; historic DDH logs provided by Anaconda Mining Inc.) in 1987; Seaside Realty Limited carried out trenching and drilled eleven holes (198.0 m) in 1993 and 1994; and Anaconda Mining Inc. had a 14-hole drill program (Fig. 1.3, 1684.4 m) in 2016 (Evans, 2004; Sparrow et al., 2017). The U.S. Borax drill hole MPB-84-1 near Ming's Bight yielded two samples MPC-5 and MPC-6 with Au mineralization (0.057 g/t over 3.0 m and 0.028 g/t over 1.5 m, respectively; historic DDH log provided by Anaconda Mining Inc.). The drill program of Granges Exploration was drilled at the same location as the Goldenville Mine, whereas the Seaside Realty Limited program was drilled at the Corkscrew prospect 600 m east-north east along strike of the Goldenville deposit (Evans, 2004). Granges Exploration intersected significant Au grades proximal to the mine shaft, whereas the Corkscrew program returned minimal results except in hole M-97-27 (12.89 g/t over 1.8 m and 9.6 g/t over 1.0 m, respectively; Evans,

2004). The 2016 program of Anaconda Mining Inc. returned assays that included 1.22 g/t Au over 1.0 m (GV-16-07) and 1.42 g/t Au over 0.42 m (GV-16-09); however, abundant mineralization was not encountered during the program (Sparrow et al., 2017).

The Goldenville horizon varies in thickness. At the main shaft of the Goldenville Mine, the horizon ranges from 3.7 – 4.6 m, and southwest of the shaft, it increases to 7.0 m thick (Watson, 1947; Fitzpatrick, 1981). The surface exposure is limited, and not all the drill holes intersect the horizon. In lieu of direct surface exposure, the locations of the 2016 Anaconda Mining Inc. drill hole targets were planned using a combination of anomalous gold values from surface soil samples, magnetic lows in geophysical data related to potential magnetite destruction associated with mineralization, and any surface gold occurrences (Sparrow et al., 2017).

### **1.3 Regional Geology**

The Newfoundland Appalachians contains four tectonostratigraphic zones (Williams, 1979; Evans, 1999; Williams et al., 1999), from east to west: Humber, Dunnage, Gander, and Avalon zones (Fig. 1.1a). The Baie Verte Peninsula (Fig. 1.1) is positioned at the northern end of the Appalachian orogenic belt containing rocks of the Humber and Dunnage zones.

The Humber Zone represents the Neoproterozoic to Cambrian Laurentian cratonic margin, whereas the Dunnage Zone contains remnants of the Iapetus Ocean that was located between the Humber Zone and the rocks of the Gander and Avalon zones, which were crustal blocks that originated proximal to Gondwana (i.e., peri-Gondwanan; Williams and St-Julien, 1982; Hibbard, 1983; van Staal et al., 2007; van Staal and Barr,

2012). These two tectonostratigraphic zones record successive accretion of micro-continental blocks and related intra-oceanic arcs, back-arcs, ophiolite, and continental terranes throughout the Early Paleozoic to Middle Paleozoic (in age succession): Dashwoods, Taconic orogenesis; Ganderia, Salinic orogenesis; and Avalonia, Acadian orogenesis (van Staal et al., 2007; van Staal and Barr, 2012). The Dunnage Zone is subdivided into the peri-Laurentian Notre-Dame subzone and the peri-Gondwanan Exploits subzone, and comprised of abundant volcanic-derived sedimentary rocks, ophiolite suites, and mélanges of Late Cambrian to Middle Ordovician age (Williams et al., 1988; van Staal and Barr, 2012).

#### **1.4 Local Geology**

The Humber Zone and the Notre Dame subzone of the Dunnage Zone are separated by the discontinuous brittle-ductile Baie Verte line (BVL), a shear zone that contains ophiolite remnants along its length (Williams, 1979; Williams and St-Julien, 1982; Hibbard, 1983; Castonguay et al., 2014). West of the BVL lies the Neoproterozoic to early Paleozoic metasedimentary rocks of the Fleur de Lys Supergroup, and to the east is the peri-Laurentian Cambrian-Ordovician Baie Verte oceanic tract (BVOT) of the Notre Dame subzone (Williams, 1979; Hibbard, 1983; van Staal et al., 2007; Skulski et al., 2010).

The BVOT contains remnants of a variably preserved ophiolite sequences interpreted to represent vestiges of the Humber seaway that formed between Laurentia proper and rocks of Laurentian affinity (i.e., the Dashwoods microcontinent; Figs. 1.1-1.3; Skulski et al., 2010; van Staal and Barr, 2012). The ophiolitic rocks of the BVOT are

subdivided into four packages: 1) the Advocate Complex; 2) the Betts Cove Complex; 3) the Pacquet complex; and 4) the Point Rousse Complex (Skulski et al., 2010). The ophiolitic rocks have been subsequently overlain by volcano-sedimentary packages (Fig. 1.4): the Snooks Arm Group (cover to the Betts Cove Complex), the Point Rousse cover sequence, the Flatwater Pond Group, and the Shark Point Group (Skulski et al., 2010). The Advocate, Betts Cove, Pacquet, and the ophiolite member of the Point Rousse complexes are correlated based on similarities in lithology and stratigraphy; they are interpreted to represent Cambrian-Ordovician (488-485 Ma) partial to full ophiolite sequences (Hibbard, 1983; Piercy et al., 1997; Bédard, 1999; Skulski et al., 2010). The Point Rousse Complex includes an Ordovician volcanic cover sequence, and is correlated to the Snooks Arm Group (Hibbard, 1983; Bédard, 1999; Bédard et al., 2000; Skulski et al., 2010).

The Baie Verte Peninsula has experienced a complex deformation and metamorphic history, and the rocks in the Point Rousse area record a minimum of four deformation events (D<sub>1</sub>-D<sub>4</sub>; Castonguay et al., 2009). These events are related to regional deformation, including the Ordovician Taconic (D<sub>1</sub>), Silurian Salinic (D<sub>2</sub>-D<sub>3</sub>), and Devonian Acadian (D<sub>3</sub>-D<sub>4</sub>) deformation and metamorphic events (Hibbard, 1983; Dunning et al., 1990; Anderson et al., 2001; Castonguay et al., 2009). D<sub>1</sub> structures regionally are preserved in the Fleur de Lys Supergroup; however, later deformation has overprinted these structures (Anderson et al., 2001; Castonguay et al., 2014). The age of D<sub>1</sub> deformation is constrained by the base of the Advocate Complex, situated above the Fleur de Lys Supergroup, having amphibole and micas with <sup>40</sup>Ar/<sup>39</sup>Ar ages between 481

and 461 Ma (Castonguay et al., 2014). D<sub>2</sub> (428-420 Ma; Anderson et al., 2001; Castonguay et al., 2014), the main phase of metamorphism and deformation in the BVP, is interpreted to be responsible for burial of ophiolites and exhumation of the Fleur de Lys Supergroup during Silurian sinistral transpression localized along the BVL during the Silurian Salinic orogeny (Anderson et al., 2001; Castonguay et al., 2009). The D<sub>3</sub> fabrics in the region (post-388 Ma; Anderson et al., 2001) are attributed to Devonian extension and core complex formation (Anderson et al., 2001; Castonguay et al., 2009). The D<sub>4</sub> (ending ~370 Ma; Anderson et al., 2001) deformation is attributed to an overall transpressional to transtensional regime during the Acadian/Neoacadian orogeny (Anderson et al., 2001).

When present, D<sub>1</sub> structures are expressed as micaceous pervasive foliation, localized shear zones, and rare isoclinal folds preserved in the Fleur de Lys Supergroup that are attributed to ophiolite obduction of the BVOT during the Taconic orogeny (Castonguay et al., 2009, 2014). D<sub>2</sub> is responsible for the general north-dipping (30° to 40°; Tuach and Kennedy, 1978) units, S<sub>2</sub> foliation, and down-dip stretching lineations of the BVP and the meter-scale south-directed shear zones (Hibbard, 1983; Dunning et al., 1990; Castonguay et al., 2009; Sparrow et al., 2017). Post-D<sub>2</sub> and possible D<sub>3</sub>, extensional shear bands within the footwall of the Scrape thrust suggest normal sense reactivation that may be the cause of the low over high-grade relationship across the fault (Castonguay et al., 2009). D<sub>3</sub> fabrics are preserved in the 200-m thick Big Brook shear zone and the Baie Verte Line in the Ming's Bight Group and Paquet complex in addition to northward trending, shallowly inclined to recumbent asymmetric folding (Anderson et al., 2001;

Castonguay et al., 2009). In shear zone margins hosted in the Point Rousse Complex and Ming's Bight Group, D<sub>3</sub> fabrics transpose D<sub>1</sub>-D<sub>2</sub> structures, fabrics, and associated alteration (Anderson et al., 2001; Sparrow et al., 2017). Structures related to D<sub>1</sub>-D<sub>3</sub> are all affected by regional scale, north-northeast-trending anticlines and synclines during D<sub>4</sub> (F<sub>4</sub>; Sparrow et al., 2017). Generally, D<sub>4</sub> deformation is characterized by undulating to open, upright F<sub>4</sub> crossfolds and a weak vertical northeast-striking crenulation cleavage locally developed on S<sub>2</sub> surfaces, and variable styles in folding and plunges depending on the orientation of the preceding fabrics from D<sub>1</sub>-D<sub>3</sub> deformation (Tuach and Kennedy, 1978; Castonguay et al., 2009).

Orogenic gold mineralization throughout the BVP is spatially associated with major fault zones and their splays (Dubé, 1990; Evans, 1999, 2004). The D<sub>2</sub>-related Scrape thrust and Deer Cove sole thrust exhibit mineralization in their hanging walls yielding Re-Os pyrite geochronology and hydrothermal zircon ages around 420 Ma (Kirkwood and Dubé, 1992; Dubé et al., 1993; Castonguay et al., 2009; Kerr and Selby, 2012). Geochronological data and regional geological relationships to Silurian D<sub>2</sub> faults suggest that gold mineralization occurred with Silurian-Devonian orogenesis (Dubé et al., 1993; Ramezani et al., 2000; Kerr and Selby, 2012; Castonguay et al., 2014).

## 1.5 Stratigraphy

The Goldenville iron formation, at this locale, is positioned at the transition from the ophiolitic rocks of the Cambro-Ordovician Mount Misery Formation to the Early-Middle Ordovician Snooks Arm Group, the cover sequence to the Pacquet complex and the correlative Betts Cove Complex (Fig. 1.4; Bédard, 2000; Skulski et al., 2010).

The stratigraphy of the ophiolitic Betts Cove Complex (489 Ma) and the Snooks Arm Group (487-467 Ma) cover sequence in best preserved in the eastern part of the BVP (Figures 1.1 thru 1.3; Dunning and Krogh, 1985; Piercy et al., 1997; Bédard et al., 2000; Kessler and Bédard, 2000; Skulski et al., 2010). The ophiolite consists of a lower cumulate section, massive gabbros, sheeted dykes, pillowd boninites of the Betts Head Formation, and plagioclase phryic, pillowd island-arc tholeiitic basalts of the Mount Misery Formation (Fig. 1.3; Bédard et al., 2000; Skulski et al., 2010).

The Snooks Arm Group (ca. 479-467 Ma) cover sequence contains six distinct formations and members from oldest to youngest: 1) the Scrape Point Formation (900 m); 2) Bobby Cove Formation and included Prairie Hat Member (600 m); 3) Venam's Bight Formation (500 m); 4) Balsam Bud Cove Formation (800 m); and 5) Round Harbour Formation (500 m; Fig. 1.4; Hibbard, 1983; Bédard, 2000; Skulski et al., 2010; Pilote et al., 2015).

The Scrape Point Formation contains a basal conglomerate comprised of basalt clasts cemented with jasper, overlain by a discontinuous, magnetite iron formation and turbiditic rocks that are interbedded with red siltstones and volcaniclastic rocks (Sangster et al., 2007; Skulski et al., 2009). The remainder of the Scrape Point Formation consists of green sandstone-siltstone-mudstone turbidite units, and tuffaceous greywacke units that are interbedded with mafic tuffs and tholeiitic, high-Ti, plagioclase-phryic, commonly amygdaloidal pillow basalts (Bédard et al., 2000; Skulski et al., 2010). The overlying Bobby Cove Formation comprises basaltic to andesitic lava flows, conglomerates, sandstones, and purple to maroon mudstones, and contains the Prairie Hat Member

marker unit that consists of clinopyroxene-phyric crystal tuff, lapilli tuff, and tuff breccia (Bédard et al., 2000; Sangster et al., 2007; Skulski et al., 2009, 2010). This unit is overlain by the Venam's Bight Formation that consists of amygdaloidal, high-Ti, tholeiitic pillow basalts locally interbedded with hyaloclastite, pillow breccia, and red siliceous mudstone to ironstone (Bédard et al., 2000; Skulski et al., 2009, 2010). This unit is succeeded by felsic tuffs, siltstones, and shales of the Balsam Bud Cove Formation, which are overlain by high-Ti tholeiitic pillow basalts of the Round Harbour Formation, the uppermost unit of the Snooks Arm Group (Bédard et al., 2000; Skulski et al., 2009, 2010).

## 1.6 Orogenic Au

### 1.6.1 Baie Verte Orogenic Au Deposits

Orogenic Au mineralization in Newfoundland is epigenetic and spatially associated with Silurian and/or Devonian late-orogenic fault zones (Dubé, 1990; Swinden et al., 1990). In the Baie Verte Peninsula, there are syngenetic Au-bearing VMS deposits hosted within Cambro-Ordovician ophiolitic mafic rocks and ophiolite-associated felsic rocks (Dubé, 1990; Swinden et al., 1990; Weick, 1993; Brueckner et al., 2014; Pilote et al., 2014). In contrast, orogenic Au mineralization is associated with the Fe-Ti-rich units in the cover sequence rocks and second- and third-order fault splays off the Baie Verte Line (Ramezani, 1992; Ramezani et al., 2000; Ybarra, 2019; Pawlukiewicz, 2020). The Goldenville and Nugget Pond deposits are associated with splays and Fe-rich horizons that exhibits variable deformation and alteration (Swinden et al., 1990; Poulsen et al., 2000; Sangster et al., 2007).

### **1.6.2 Orogenic Au Deposits**

Orogenic gold deposits have numerous commonalities regardless of age or host-rock (e.g., Kerrich and Fyfe, 1981; Gebre-Mariam et al., 1995; Groves et al., 1998, 2003; Goldfarb et al., 2001, 2005). They are structurally-controlled, epigenetic deposits that form along convergent margins in accreted, translation, or collision zones, typically in the later stages of orogenic development (Fig. 1.5; McCuaig and Kerrich, 1998; Poulsen et al., 2000; Goldfarb et al., 2001, 2005; Groves et al., 2003; Goldfarb and Groves, 2015). Deposits are consistently located in metamorphosed fore-arc or back-arc settings where the country rocks exhibit a transition from greenschist to lower amphibolite facies (Groves et al., 1998, 2003; Goldfarb et al., 2001; Pitcairn et al., 2015 and references therein).

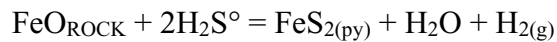
Despite being important sources of gold globally, the source of fluids and metals in orogenic Au deposits is still debated (Phillips et al., 1987; Pitcairn et al., 2014). Two main models have been proposed, including: 1) the magmatic-hydrothermal model; and 2) the metamorphic dehydration model. The metamorphic dehydration model is where metal-rich fluids are produced during accretion, translation, or collision related to crustal subduction that leads to prograde metamorphism from greenschist to amphibolite facies, leading to devolatilization of the down-going rocks in the accretionary complex (Fig. 1.6; Kerrich and Fyfe, 1981; Phillips et al., 1987; Goldfarb et al., 2005; Bierlein et al., 2006; Pitcairn et al., 2006, 2010, 2014; Phillips and Powell, 2010). The fluids are mobilized along major faults and/or deformed zones, often scavenging significant SiO<sub>2</sub>, CO<sub>2</sub>, K<sub>2</sub>O, H<sub>2</sub>O, S, Au, and other metals from the country-rock (Kerrich and Fyfe, 1981; Phillips and

Powell, 2010). The magmatic-hydrothermal model (Sillitoe and Bonham Jr, 1990; Spooner, 1993) suggests that magmatic activity could be a source for the fluids or the heat necessary for fluid circulation. Recently, McDivitt et al. (2017) has shown that many deposits exhibit both pre- and syn-orogenic veins with overlapping mineralization ages, suggesting that the models described prior are likely end-members and some deposits exhibit characteristics of both models with both influences from magmatic and metamorphic fluids.

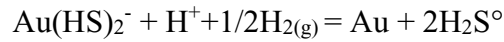
The composition of the fluids associated with orogenic Au deposits is relatively consistent through geologic time; fluid inclusions typically contain 5-20 mol% CO<sub>2</sub>, CH<sub>4</sub> and/or N<sub>2</sub>, 0.01-0.36 mol% H<sub>2</sub>S, neutral pH of 5.5, and 3-7 wt.% NaCl where Na>K>>Ca, Mg (Goldfarb and Groves, 2015). There is evidence in orogenic Au deposits of multiple pulses of fluids (e.g., multiple vein generations and/or fluid inclusion assemblages) during deposit formation, indicated by fluid chemistry and cross-cutting relationships (Ridley and Diamond, 2000). Thermodynamic data and estimated ore-fluid compositions indicate gold in orogenic fluids is soluble in HS<sup>-</sup> ligands, such as Au(HS)<sup>°</sup> or Au(HS)<sub>2</sub><sup>-</sup> where T<350°C, whereas AuCl<sub>2</sub><sup>-</sup> predominates where T>350°C (Seward, 1973; Mikucki, 1998; Robb, 2005; Williams-Jones et al., 2009).

In the metamorphic fluid model, metal-bearing fluids migrate through structural features such as shear zones, regional-scale faults, and splays until they encounter a depositional trap, be that rheological or chemical (Phillips et al., 1987; Peter et al., 2003b; Bierlein et al., 2006; Pitcairn et al., 2014). Generally, there are four known mechanisms for precipitation of Au from an aqueous solution: 1) a temperature drop in a localized

area; 2) pressure change results in fluid boiling and release of volatiles (i.e., phase separation); 3) chemical reaction between the fluid and reactive wall rock; and 4) chemical changes as a result of fluid mixing (Mikucki, 1998; Robb, 2005). Fluid interaction with reactive wall rock (3), particularly wall rock sulfidation, is an essential process for Au deposition related to iron formations and other Fe-rich rocks (Ridley et al., 1996; Mikucki, 1998; Williams-Jones et al., 2009):



and



In general,  $\text{Fe}^{3+}$ -bearing minerals are an effective way of reducing  $\text{HS}^-$  causing changes in the redox state allowing for gold to precipitate together with pyrite (Robb, 2005; Williams-Jones et al., 2009); thus, Fe-rich lithologies, including Fe-Ti-rich basalts, iron formations, Fe-rich sedimentary rocks, and/or ultramafic rocks are all common hosts to wall rock sulfidation-related Au deposits (Poulsen et al., 2000).

## **1.7 Overview of Exhalative Iron Formations**

Iron formations are described as sedimentary units composed of layered, bedded, or laminated rocks that contain >15% Fe, where Fe is hosted in oxides, silicates, carbonates, or some combination thereof (James, 1954). Iron formations are often further subdivided based on their dominant texture, into granular or banded, and/or their different depositional settings, such as continental margin iron formation (Superior-type) or exhalative iron formation related to seafloor hydrothermal venting (Algoma-type) (James,

1954; Gross, 1980; Bekker et al., 2014; Konhauser et al., 2017). Superior-type iron formations are formed by the precipitation of Fe-rich waters upwelling from suboxic marine basins to near-shore oxic waters, whereas exhalative-type iron formations represent Fe-rich sediment deposition from exhalative hydrothermal fluids venting into deeper submarine environments (Peter, 2003; Bekker et al., 2014).

Exhalative iron formations, in a “pure” state, are sedimentary rocks that form from the deposition of Fe-(Mn) oxides/oxyhydroxides, originating as dissolved  $\text{Fe}^{2+}$  and  $\text{Mn}^{2+}$  from a hydrothermal vent fluid after it interacts with seawater. Deep-water ( $>1000$  m) hydrothermal vent fluids often form plumes in seawater that can be subdivided into two distinct components: 1) a neutrally buoyant (laterally spreading) plume that can extend up to 10 km from the vent source; and 2) a buoyant (rising) plume that can reach up to a few hundred meters above the seafloor (Fig. 1.7; Baker, 1990; German et al., 1990; German and Von Damm, 2003; Peter, 2003; Bennett et al., 2008). Particulates measured at active vents found freshly formed sulphides concentrated within a few meters of the vent site and a significant reduction of those markers (e.g., Cu/Fe and Zn/Fe ratios) thereafter indicating a compositional difference in the plumes (Rudnicki, 1995). Active seafloor vents producing these hydrothermal sediments tend to be proximal to volcanic centers in back-arcs, spreading ridges, and continental rift settings in both modern and ancient environments, often forming hydrothermal sedimentary sequences that include varying particulate compositions from a variety of sources not attributed solely to plume segregation (Gross, 1980, 1983; Peter, 2003; Bennett et al., 2008; Gourcerol et al., 2016).

Iron formation mineralogy and geochemistry reflect the varying contributions from three sources: 1) detrital material (e.g., volcanic debris or continental sediments; Peter et al., 2003a); 2) hydrothermal plume material (i.e., minerals precipitated from the vent fluid itself; Peter and Goodfellow, 2003); and 3) hydrogenous components (i.e., elements scavenged from seawater; Bolhar et al., 2005). The proportion of detrital material in iron formations is evident from the presence of aluminosilicate minerals and their associated budget of insoluble elements (i.e. that are not readily sourced from hydrothermal fluids or dissolved in seawater and scavenged on hydrothermally derived mineral particles), and often have a more specific composition reflective of the surrounding host rocks (e.g., increasing abundances of Ti, Al, and Zr; Peter et al., 2003a; Bekker et al., 2014; Konhauser et al., 2017). The hydrothermal material in iron formations is most readily evident from Fe+Mn in excess of that structurally bound in detrital aluminosilicate minerals, in addition to any other elements originating from the hydrothermal fluid (e.g., Cu, Zn, Pb, Ba, Cd, and Hg; Boström and Peterson, 1966; Peter and Goodfellow, 2003; Peter et al., 2003a). Sulfide minerals precipitated in a hydrothermal plume tend to deposit very close to the source, whereas particulates of a lighter composition stay buoyant and disperse farther from the vent site (Fig. 1.7; Lupton and Craig, 1981; Baker, 1990; Rudnicki, 1995; Peter, 2003). The hydrogenous component is detected by specific signatures or increasing abundances of elements present in a soluble form in seawater (e.g., REE and Y, Mo, V, U) that are adsorbed onto Fe- and Mn-oxides in the water column (i.e., non-buoyant plume; Fig. 1.7) or on the seafloor (German et al., 1990; Bau and Dulski, 1996; Peter and Goodfellow, 2003;). The signatures and abundances of several elements dissolved in seawater are dependent on variables such as

fluid pH, T, and dissolved oxygen levels, such that the hydrogenous element component captured in iron formations can provide constraints on these parameters in ancient ocean basins (Bau et al., 1995; Alibo and Nozaki, 1999; Bau and Dulski, 1999).

The three components of iron formation can vary in relative proportions depending on the depositional conditions and proximity to different element sources, as well as the deployed geochemical sampling strategy. In exhalative iron formations, the hydrothermal component often comprises 40 to 90 % of the total composition (James, 1954; Spry et al., 2000; Peter, 2003). Samples with the highest relative abundance of hydrothermally derived minerals (e.g., Fe- and Mn-oxides, highest Fe and Mn concentration and lowest Al and Ti; Boström et al., 1972) are the most valuable for reconstructing the conditions of hydrothermal fluids and/or seawater composition (Bekker et al., 2014; Konhauser et al., 2017). As the abundance of detritus in iron formation increases (higher aluminosilicate mineral content and decreasing Fe and Mn with increasing Al and Ti; Boström et al., 1972), it can readily mask the hydrothermal and hydrogenous chemical signatures and can instead provide insights into the composition of the surrounding terrigenous sediment or local volcanic and sediment sources (James, 1954; Bhatia and Crook, 1986; Spry et al., 2000; Peter, 2003).

### **1.7.1 REE Proxies for Ancient Seawater Composition, Redox, and Hydrothermal Vent Fluid-Seawater Dynamics**

Seawater has diagnostic REE+Y signatures with light REE (LREE) depletion relative to heavy REE (HREE), and positive La, Gd, and Y anomalies, relative to REE+Y in shale. Shale composites are used as a proxy for an average exposed upper continental

crust composition and deployed for normalization of seawater and seawater chemical sediment/sedimentary rock since the upper crust is the dominant supply of soluble REE+Y to the oceans (Alibo and Nozaki, 1999). Carbonate complexes of the REE+Y ( $\text{MCO}_3^+$  or  $\text{M}(\text{CO}_3)^{2-}$ ) are the dominant aqueous species (Turner et al. 1981; Byrne & Sholkovitz, 1996, and references therein) in the oceans and the greater stability of HREE relative to LREE complexes leads to the shale-normalized LREE-depleted pattern typical of seawater (Goldberg et al., 1963; Elderfield & Greaves, 1982; Alibo & Nozaki, 1999). Similarly, the positive anomalies of La, Gd, and Y, arise from the greater aqueous stability of their complexes, as dictated by a more stable f-orbital electron configuration (Gd being half-filled) or lack of f-orbital (La, Y), compared to their respective neighboring REE (in terms identical charge and nearest ionic radii) that are preferentially scavenged by mineral surfaces and removed from solution (DeBaar et al., 1985; Zhang et al., 1994; Alibo and Nozaki, 1999). The positive anomaly of Y is commonly quantified using the Y/Ho ratio, where Ho is a geochemical “twin” of Y in terms of ionic charge and radii such that minimal changes in the ratio from chondritic values ( $\text{Y}/\text{Ho} \sim 27$  as a mass ratio; Pack et al. 2007) are observed in most igneous rocks, but a separation of these elements occurs readily in marine waters and produces superchondritic ratios (Bau, 1996; Douville et al., 1999). The positive anomalies of La and Gd are typically calculated as the excess La and Gd beyond what is predicted from a projection between or from the nearest neighboring non-anomalous REE on shale-normalized REE+Y plots (e.g., Lawrence and Kamber, 2006).

Another prominent REE anomaly typical of seawater is that of Ce, which separates from the other REE<sup>3+</sup> when it is oxidized to Ce<sup>4+</sup> via particle-interaction redox transformations that typically depend on the presence of Mn-(oxy)(hydr)oxide surfaces (Tostevin, 2021, and references therein). In oxygenated seawater, Ce is more readily removed from solution, producing strong negative anomalies in shale-normalized REE+Y patterns. In contrast, partially oxygenated water columns (e.g. redox-stratified with upper oxic waters overlying reducing bottom waters) can result in a range of neutral to positive Ce anomalies in bottom waters that result from the re-release of REE+Y scavenged on oxide particle surfaces higher in the oxidized areas of the water column as they are reductively dissolved in the water or sediment (De Baar et al., 1988; Bau et al., 1997; De Carlo & Green, 2002). Modern marine hydrogenetic Fe-Mn crusts, which grow slowly (a few mm/Myr) in fully oxygenated seawater, often feature the inverse pattern of seawater, including LREE>HREE enrichment, negative to positive Ce anomalies, and negative Y anomalies (i.e., chondritic to subchondritic Y/Ho ratios <25; Bau et al., 1996, 2014) that is similar to the patterns observed in deep anoxic waters of a redox-stratified water column. The aforementioned framework underlies the utility of Ce anomalies as paleo-redox proxy for ancient seawater when studying chemical sedimentary rocks.

High-temperature, metal-rich hydrothermal fluids (German and Von Damm, 2003) have contrasting REE+Y chemical signatures and abundances to the surrounding cold, oxidized ambient seawater (Michard, 1989; Bau and Dulski, 1999; Douville et al., 1999; Craddock et al., 2010). The REE have a wider range of normalized pattern slopes from flat to LREE-enriched that is controlled primarily by the pH and T of the

hydrothermal fluid, alongside the specific REE complexes (i.e. with F<sup>-</sup>, Cl<sup>-</sup>, SO<sub>4</sub><sup>2-</sup>) controlling their solubility, which, in turn, varies with tectonic environment (e.g. back-arc basin to mid-ocean ridge) (Bau and Dulski, 1999; Douville et al., 1999; Craddock et al., 2010). Importantly, the normalized REE+Y pattern of hydrothermal fluids also has a distinct lack of the positive La, Gd, and Y anomalies that are typical of seawater, as well as, often, a diagnostic, strong positive Eu anomaly (Michard et al., 1983; Klinkhammer et al., 1994; Douville et al., 1999) that stands in contrast to that of seawater. Europium, existing in either a divalent or trivalent form, has a Eu<sup>2+</sup>/Eu<sup>3+</sup>-redox equilibrium that is temperature dependent (Sverjensky, 1984; Bau, 1991). Hydrothermal vent fluids generally are acidic and reduced with high temperatures (>250°C) (e.g., Douville et al., 1999), favouring the solubility of Eu<sup>2+</sup> and development of a positive Eu anomaly in these fluids relative to those at lower T (e.g., Allen and Seyfried, 2005). Mixing of hydrothermal fluids with surrounding seawater occurs rapidly at the point of emanation from seafloor hydrothermal vents (e.g. Bau and Dulski, 1999) and the generation of abundant oxide particles in a hydrothermal plume (see Fig. 1.7; Rudnick, 1995) results in efficient scavenging of REE+Y in the surrounding deep marine environment, both in the water column and after deposition on the seafloor, such that these environments are an oceanic sink rather than a source of these elements (German et al., 1990). In turn, this also allows the geochemical measurement of oxide particles originating from hydrothermal vents to provide a proxy into the hydrothermal fluids, their dynamic mixing with seawater, and the conditions (e.g., redox-state) of the seawater.

The development and refinement of the application of REE+Y signatures as a proxy for ancient seawater and hydrothermal conditions has benefitted from an analysis of iron formation deposited in different environments (i.e. continental margin or exhalative iron formation) throughout geological time, under the premise that Fe-mineral (and other) particulates were passive scavengers of the seawater/marine pore water conditions at the time of their deposition (Bekker et al., 2010, 2014; Konhauser et al., 2017, and the references therein). For example, Archean iron formation of both types are generally devoid of Ce anomalies, and this has been taken as supporting evidence for a fully anoxic water column and an oxygen-poor atmosphere (Planavsky et al. 2010) in this eon, outside of highly localized marine oxygen “oases” (Anbar et al. 2007; Olson et al. 2013). Similarly, Archean iron formation, especially exhalative types, have very strong positive Eu anomalies (Danielson et al., 1992; Viehmann et al. 2015) that constitutes evidence for greater magmatic control on seawater chemistry relative to younger points in the Earth’s history, and that a greater budget of the REE (along with Fe and Mn) in the anoxic oceans was transported in soluble form from deep waters to shallow water environments (e.g., Alexander et al. 2008). In contrast, iron formation deposited during and after oxygenation of the atmosphere near the Archean-Proterozoic boundary contain positive Ce anomalies alongside a wider range of shale-normalized REE+Y pattern slopes and Y/Ho ratios; these features collectively point towards the more widespread development of redox-stratified marine waters (Fryer. 1977; Planavsky et al. 2010; Warke et al. 2020). With the exception of Neoproterozoic iron formation directly associated with glaciation (e.g., Baldwin et al. 2012), Mesoproterozoic and younger iron formation is typically directly associated with hydrothermal environments (i.e., associated with VMS)

(Bekker et al. 2010 and references therein). Nevertheless, such deposits from the Mesoproterozoic point to suboxic conditions reaching deep marine waters and the prevalence of marine redox-stratification (Slack et al., 2009) – information that is deciphered in large part by inferring REE+Y interaction with marine particulates. It is widely accepted that atmospheric oxygenation and deep marine oxygenation transitioned towards a near-modern state in the late Neoproterozoic into the Cambrian (Och and Shields-Zhou, 2012 and references therein), but the details of shallow vs. deep marine water redox are more complex and still poorly understood throughout the early Phanerozoic. For example, there is evidence that deep marine ferruginous (anoxic,  $\text{Fe}^{2+}$ -rich) conditions still dominated either locally or in punctuated intervals of the Cambrian (Li et al. 2018) and upwelled, deep marine  $\text{Fe}^{2+}$  sources are invoked by some to explain the origin of shallow marine ironstone deposits (Todd et al. 2019). As such, further study of the REE+Y geochemistry of early Phanerozoic exhalative iron formation has value not only in deciphering vent-proximal hydrothermal-seawater dynamics (Peter, 2003), but also contributes to our wider understanding of the oxygenation of deep marine environments through time.

### **1.7.2 Iron Formation and their Utility in VMS and Orogenic Au Exploration**

Exhalative-type iron formations and related ferruginous cherty sedimentary rocks are spatially associated with some volcanogenic massive sulfide (VMS) deposits, making them valuable stratigraphic horizons in exploration (Gross, 1980; Peter and Goodfellow, 1996; Spry et al., 2000). Many VMS deposits (e.g., Bathurst Camp deposits) have iron formations forming immediately in their hanging wall that, in many cases, extend

laterally, sometimes up to 12 km beyond the deposit (Lydon, 1984; Spry et al., 2000; Peter, 2003; Bekker et al., 2010). Iron formations can be used in the exploration for VMS deposits, in particular: 1) they often have distinctive thickness and geophysical magnetic signatures that vary with proximity to mineralization; 2) they exhibit distinct spatial distributions of mineral phases that can be used to decipher proximity to mineralization (e.g., more sulfides and higher Fe-oxide contents in iron formations proximal to mineralization, such as increased magnetite); 3) they exhibit variations in bulk chemistry and mineral chemistry with varying distance from mineralization (e.g., higher base metal values proximal to mineralization, and high compositional element ratios Fe/Ti, P/Ti, CO<sub>2</sub>/Ti, and Fe/Mn indicate close proximity); and 4) they exhibit variations in stable isotope compositions of bulk rock and mineral phases with varying distance to mineralization (Peter, 2003; Peter et al., 2003b; Peter and Goodfellow, 2003).

Exhalative-type iron formations are also associated with orogenic gold deposits (e.g., Homestake deposit; Caddey, 1991). In these cases, iron formations found proximal to major (and gold conduit) structures form chemically reactive rocks that allow Au(HS)<sub>2</sub><sup>-</sup> molecules in metamorphic-derived fluids to be destabilized resulting in wall rock sulfidation and Au deposition (Kerrick and Fyfe 1981, Phillips et al. 1987, Goldfarb et al. 2001, 2005, Phillips and Powell 2010, Groves et al. 2019). Often, these deposits have gold associated with pyrite that has replaced magnetite, which is spatially restricted to where quartz veins cross-cutting the iron formation (Kerswill, 1993). Like other orogenic gold environments, orogenic gold in iron formation settings is spatially associated with regional greenschist-amphibolite facies environments; crustal scale structures and their

splays; intersection of these structures with iron formations; and zones quartz veining with pyrite haloes indicative of wall rock sulfidation (Peter, 2003; Phillips and Powell 2010; Lambeck et al., 2011; Castonguay et al., 2015).

## 1.8 Thesis Objectives

Since the initial discovery of the Goldenville deposit, there has been limited research done on the horizon, and the chemistry, mineralogy, and relationships to Au and base metal mineralization in the iron formation are not fully understood. This study uses core-logging, petrography, and geochemistry to characterize the Goldenville iron formation and surrounding stratigraphy (i.e., Goldenville horizon). The research objectives of this thesis are as follows:

- document the stratigraphic and chemostratigraphic setting of the Goldenville horizon, nature of mineralization, and depositional setting of the iron formation;
- use the primary, immobile element geochemistry of the coherent mafic rocks in the footwall and hanging wall of the Goldenville deposit to establish the basalt stratigraphy and reconstruct the provenance of the volcaniclastic rocks, argillites, and the detrital material within the iron formation;
- use lithogeochemistry to document the detrital, hydrothermal, and hydrogenous footprint recorded in the Goldenville horizon and how it changes throughout the stratigraphy;

- use the REE+Y as a geochemical proxy to reconstruct the paleoredox conditions of the Humber seaway during deposition of the Goldenville horizon; and
- use field observations and lithogeochemistry to document any presence of base metal and gold mineralization associated with the ferruginous chert and iron formation of the Goldenville horizon to reevaluate how prospective the horizon is as an exploration target.

### **1.9 Co-authorship Statement**

This project was designed by Stephen Piercy, Michael Babechuk, and David Copeland. This research was done by the primary author and includes sample collection, core logging, sample preparation, and petrography. Scanning electron microscopy was done by the primary author under the guidance and supervision of Wanda Aylward at the Memorial University of Newfoundland. The primary editing of this research was done by Stephen Piercy and Michael Babechuk.

### **1.10 Presentation**

This work is presented as three chapters with accompanying figures, tables, and appendices. Chapter 1 introduces the project with necessary background information to understand the full body of work presented in the thesis. Chapter 2 contains the results of the research and includes lithofacies descriptions of the host stratigraphy, documentation of the mineralization, analytical methodology, and field, geochemical, and mineralogical results. The conclusions were the result of interpretations from graphic drill core logging, petrography, whole-rock lithogeochemistry and scanning electron microscope (SEM)

imaging. The goal of this chapter is for it to be eventually published in a peer reviewed journal. Chapter 3 is a summary of the findings of the research and outlines potential directions for future research. The accompanying appendices contain digitized drill hole logs, geochemical data, and photos of thin sections.

## References

- Alexander, B., Bau, M., Andersson, P. and Dulski, P., 2008. Continentally-derived solutes in shallow Archean seawater: rare earth element and Nd isotope evidence in iron formation from the 2.9 Ga Pongola: *Geochemica et Cosmochimica Acta*, v. 72, 378–394.
- Allen, D. and Seyfried Jr, W., 2005, REE controls in ultramafic hosted MOR hydrothermal systems: an experimental study at elevated temperature and pressure: *Geochemica et Cosmochimica Acta*, v. 69, p. 675–683.
- Alibo, D.S., and Nozaki, Y., 1999, Rare earth elements in seawater: Particle association, shale-normalization, and Ce oxidation: *Geochimica et Cosmochimica Acta*, v. 63, p. 363–372.
- Anbar, A.D., Duan, Y., Lyons, T.W., Arnold, G.L., Kendall, B., Creaser, R.A., Kaufman, A.J., Gordon, G.W., Scott, C., Garvin, J. and Buick, R., 2007, A whiff of oxygen before the great oxidation event?: *Science*, v. 317, p. 1903–1906.
- Anderson, S.D., Jamieson, R.A., Reynolds, P.H., and Dunning, G.R., 2001, Devonian Extension in Northwestern Newfoundland:  $^{40}\text{Ar}/^{39}\text{Ar}$  and U-Pb Data from the Ming's Bight Area, Baie Verte Peninsula: *The Journal of Geology*, v. 109, p. 191–211.
- Baker, E.T., 1990, Hydrothermal Plume Prospecting: Hydrographic and Geochemical Techniques: in *Gorda Ridge A Seafloor Spreading Center in the United States' Exclusive Economic Zone*, p. 155–167.
- Baldwin, G.J., Turner, E.C. and Kamber, B.S., 2012, A new depositional model for glaciogenic Neoproterozoic iron formation: insights from the chemostratigraphy and basin configuration of the Rapitan iron formation: *Canadian Journal of Earth Sciences*, v. 49, p. 455–476.
- Bau, M., 1996, Controls on the fractionation of isovalent trace elements in magmatic and aqueous systems: evidence from Y/Ho, Zr/Hf, and lanthanide tetrad effect: *Contributions to Mineralogy and Petrology*, v. 123, p. 323–333.
- Bau, M., 1991, Rare-earth element mobility during hydrothermal and metamorphic fluid-rock interaction and the significance of the oxidation state of europium: *Chemical*

*Geology*, v. 93, p. 219–230.

- Bau, M. and Dulski, P., 1999, Comparing yttrium and rare earths in hydrothermal fluids from the Mid-Atlantic Ridge: Implications for Y and REE behaviour during near-vent mixing and for the Y/Ho ratio of proterozoic seawater: *Chemical Geology*, v. 155, p. 77–90.
- Bau, M., and Dulski, P., 1996, Distribution of yttrium and rare-earth elements in the Penge and Kuruman iron-formations, Transvaal Supergroup, South Africa: *Precambrian Research*, v. 79, p. 37–55.
- Bau, M., and Dulski, P., 1999, Comparing yttrium and rare earths in hydrothermal fluids from the Mid-Atlantic Ridge: Implications for Y and REE behaviour during near-vent mixing and for the Y/Ho ratio of proterozoic seawater: *Chemical Geology*, v. 155, p. 77–90.
- Bau, M., Koschinsky, A., Dulski, P., and Hein, J.R., 1996, Comparison of the partitioning behaviours of yttrium, rare earth elements, and titanium between hydrogenetic marine ferromanganese crusts and seawater: *Geochimica et Cosmochimica Acta*, v. 60, p. 1709–1725.
- Bau, M., Dulski, P., and Moller, P., 1995, Yttrium and holmium in South Pacific seawater: vertical distribution and possible fractionation mechanisms: *Chemie der Erde - Geochemistry*, v. 55, p. 15.
- Bau, M., Möller, P. and Dulski, P., 1997, Yttrium and lanthanides in eastern Mediterranean seawater and their fractionation during redox-cycling: *Marine Chemistry*, v. 56, p. 123–131.
- Bau, M., Schmidt, K., Koschinsky, A., Hein, J., Kuhn, T., and Usui, A., 2014, Discriminating between different genetic types of marine ferro-manganese crusts and nodules based on rare earth elements and yttrium: *Chemical Geology*, v. 381, p. 9.
- Bédard, J.H., 1999, Petrogenesis of Boninites from the Betts Cove ophiolite, Newfoundland, Canada: Identification of subducted source components: *Journal of Petrology*, v. 40, p. 1853–1889.
- Bédard, J.H., Lauziere, K., Tremblay, A., Sangster, A., Douma, S.L., and Dec, T., 2000, Betts Cove ophiolite and its cover rocks, Newfoundland: *Bulletin of the Geological Survey of Canada*, v. 550, 76 p.
- Bekker, A., Planavsky, N.J., Krapež, B., Rasmussen, B., Hofmann, A., Slack, J.F., Rouxel, O.J., and Konhauser, K.O., 2014, Iron formations: Their origins and implications for ancient seawater chemistry: in *Treatise on Geochemistry: Second Edition*, v. 12, p. 561-628.
- Bekker, A., Slack, J.F., Planavsky, N., Krapez, B., Hofmann, A., Konhauser, K.O., and Rouxel, O.J., 2010, Iron formation: the sedimentary product of a complex interplay

- among mantle, tectonic, oceanic, and biospheric processes: *Economic Geology*, v. 105, p. 467–508.
- Bennett, S.A., Achterberg, E.P., Connelly, D.P., Statham, P.J., Fones, G.R., and German, C.R., 2008, The distribution and stabilisation of dissolved Fe in deep-sea hydrothermal plumes: *Earth and Planetary Science Letters*, v. 270, p. 157–167.
- Bhatia, M.R., and Crook, K.A.W., 1986, Trace element characteristics of graywackes and tectonic setting discrimination of sedimentary basins: *Contributions to Mineralogy and Petrology*, v. 92, p. 181–193.
- Bierlein, F.P., Groves, D.I., Goldfarb, R.J., and Dubé, B., 2006, Lithospheric controls on the formation of provinces hosting giant orogenic gold deposits: *Mineralium Deposita*, v. 40, p. 874–886.
- Bolhar, R., Kamber, B.S., Moorbat, S., Fedo, C.M. and Whitehouse, M.J., 2004, Characterisation of early Archaean chemical sediments by trace element signatures: *Earth and Planetary Science Letters*, v. 222, p. 43–60.
- Boström, K., Joensuu, O., Valdés, S. and Riera, M., 1972, Geochemical history of South Atlantic Ocean sediments since Late Cretaceous: *Marine Geology*, v. 12, p. 85–121.
- Boström, K., and Peterson, N.A., 1966, Precipitates from hydrothermal exhalations on the east pacific rise: *Economic Geology*, v. 61, p. 1258–1265.
- Brueckner, S.M., Piercy, S.J., Sylvester, P.J., Maloney, S., and Pilgrim, L., 2014, Evidence for syngenetic precious metal enrichment in an appalachian volcanogenic massive sulfide system: The 1806 Zone, Ming Mine, Newfoundland, Canada: *Economic Geology*, v. 109, p. 1611–1642.
- Byrne, R. and Sholkovitz, E., 1996, Marine chemistry and geochemistry of the lanthanides: *Handbook on the Physics and Chemistry of Rare Earths*, v. 23, p. 497–593.
- Caddey, S.S.W., 1991, The Homestake Gold Mine: an early Proterozoic iron-formation-hosted gold deposit, Lawrence County, South Dakota: *US Department of the Interior, US Geological Survey*, v. 1857-J1, 67 p.
- Castonguay, S., Dube, B., Mercier-Langevin, P., McNicoll, V., Oswald, W., Janvier, V. and Malo, M., 2015, Geological Controls of BIF-Hosted Gold Mineralization: Insights from the World-Class Musselwhite (Ontario) and Meadowbank (Nunavut) Deposits, Canada: *13th SGA Biennial Meeting on Mineral Resources in a Sustainable World–SGA*, p. 24–27.
- Castonguay, S., Skulski, T., van Staal, C., and Currie, M., 2009, New insights on the structural geology of the Pacquet Harbour group and Point Rousse complex, Baie Verte peninsula, Newfoundland: *Newfoundland and Labrador Department of Natural Resources, Geological Survey, Report*, v. 09-1, p. 147–158.
- Castonguay, S., van Staal, C.R., Joyce, N., Skulski, T., and Hibbard, J.P., 2014, Taconic

- metamorphism preserved in the Baie Verte Peninsula, Newfoundland Appalachians: Geochronological evidence for ophiolite obduction and subduction and exhumation of the leading edge of the Laurentian (Humber) margin during closure of the Taconic Seaway: *Geoscience Canada*, v. 41, p. 459–482.
- Craddock, P., Back, W., Seewald, J., Rouxel, O., Reeves, E. and Tivey, M., 2010, Rare earth element abundances in hydrothermal fluids from the Manus Basin, Papua New Guinea: Indicators of sub-seafloor hydrothermal processes in back-arc basins: *Geochemica et Cosmochimica Acta*, v. 74, p. 5494–5513.
- Danielson, A., Möller, P. and Dulski, P., 1992, The europium anomalies in banded iron formations and the thermal history of the oceanic crust: *Chemical Geology*, v. 97, p. 89–100.
- De Baar, H., Bacon, M., Brewer, P. and Bruland, K., 1985, Rare earth elements in the Pacific and Atlantic Oceans: *Geochemica et Cosmochimica Acta*, v. 49, p. 1943–1959.
- De Baar, H., German, C., Elderfield, H. and Van Gaans, P., 1988, Rare earth element distributions in anoxic waters of the Cariaco Trench: *Geochemica et Cosmochimica Acta*, v. 52, p. 1203–1219.
- De Carlo, E. and Green, W., 2002, Rare earth elements in the water column of Lake Vanda, McMurdo Dry Valleys, Antarctica: *Geochemica et Cosmochimica Acta*, v. 66, p. 1323–1333.
- Douville, E., Bienvenu, P., Charlou, J.-L., Donval, J.-P., Fouquet, Y., Appriou, P., and Gamo, T., 1999, Yttrium and rare earth elements in fluids from various deep-sea hydrothermal systems: *Geochemica et Cosmochimica Acta*, v. 63, p. 627–643.
- Dubé, B., 1990, A preliminary report on contrasting structural styles of gold-only deposits in western Newfoundland: *Geological Survey of Canada*, v. 90, p. 77–90.
- Dubé, B., Lauzière, K., and Poulsen, H.K., 1993, The Deer Cove deposit: an example of "thrust"-related breccia-vein type gold mineralization in the Baie Verte Peninsula, Newfoundland: *Geological Survey of Canada*, v. 93-1D, p. 10.
- Dunning, G.R., and Krogh, T.E., 1985, Geochronology of ophiolites of the Newfoundland Appalachians: *Canadian Journal of Earth Sciences*, v. 22, p. 1659–1670.
- Dunning, G.R., O'Brien, S.J., Colman-Sadd, S.P., Blackwood, R.F., Dickson, W.L., O'Neill, P.P., and Krogh, T.E., 1990, Silurian orogeny in the Newfoundland Appalachians: *The Journal of Geology*, v. 98, p. 895–913.
- Elderfield, H. and Greaves, M.J., 1982. The rare earth elements in seawater: *Nature*, v. 296, p. 214–219.
- Evans, D.T.W., 1999, Epigenetic gold mineralization, Baie Verte Peninsula, Newfoundland: *Newfoundland Department of Mines and Energy, Geological Survey*, v. 99-i, p. 98-1.

- Evans, D.T.W., 2004, Epigenetic gold occurrences, Baie Verte Peninsula, (NTS 12H/09, 16 and 12I/01), *Newfoundland: Government of Newfoundland and Labrador, Department of Natural Resources, Mineral Resource Report*, v. 11, p. 177.
- Fitzpatrick, D., 1981, Geology and mineral potential of upper ophiolitic rocks near Ming's Bight, Burlington Peninsula, Newfoundland: *Memorial University of Newfoundland*, p. 90.
- Frew, A., 1971, Petrographic and geochemical comparison of two gold-mineralized zones, Ming's Bight area, White Bay, Newfoundland: *Memorial University of Newfoundland*, p. 35.
- Fryer, B.J., 1977, Rare earth evidence in iron-formations for changing Precambrian oxidation states: *Geochimica et Cosmochimica Acta*, v. 41, p. 361-367.
- Gebre-Mariam, M., Hagemann, S.G., and Groves, D.I., 1995, A classification scheme for epigenetic Archaean lode-gold deposits: *Mineralium Deposita*, v. 30, p. 408–410.
- German, C.R., Klinkhammer, G.P., Edmond, J.M., Mura, A. and Elderfield, H., 1990. Hydrothermal scavenging of rare-earth elements in the ocean: *Nature*, v. 345, p. 516-518.
- German, C.R. and Von Damm, K.L., 2003. Hydrothermal processes: in *Treatise on Geochemistry, Second Edition*, v. 6, p. 181-222.
- Goldberg, E.D., Koide, M., Schmitt, R.A. and Smith, R.H., 1963, Rare-Earth distributions in the marine environment: *Journal of Geophysical Research*, v. 68, p. 4209–4217.
- Goldfarb, R.J., Baker, T., Dubé, B., Groves, D.I., Hart, C.J.R., and Gosselin, P., 2005, Distribution, character, and genesis of gold deposits in metamorphic terranes: *Society of Economic Geologists, One Hundredth Anniversary Volume*, p. 407-450.
- Goldfarb, R.J., and Groves, D.I., 2015, Orogenic gold: Common or evolving fluid and metal sources through time: *Lithos*, v. 233, p. 2–26.
- Goldfarb, R.J., Groves, D.I., and Gardoll, S., 2001, Orogenic gold and geologic time: a global synthesis: *Ore Geology Reviews*, v. 18, p. 75.
- Gourcerol, B., Thurston, P.C., Kontak, D.J., Côté-Mantha, O., and Biczok, J., 2016, Depositional setting of Algoma-type banded iron formation: *Precambrian Research*, v. 281, p. 47–79.
- Gross, G.A., 1980, A classification of iron formations based on depositional environments: *The Canadian Mineralogist*, v. 18, p. 215-222.
- Gross, G.A., 1983, Tectonic systems and the deposition of iron-formation: *Precambrian Research*, v. 20, p. 171–187.
- Groves, D.I., Goldfarb, R.J., Gebre-Mariam, M., Hagemann, S.G., and Robert, F., 1998, Orogenic gold deposits: A proposed classification in the context of their crustal

- distribution and relationship to other gold deposit types: *Ore Geology Reviews*, v. 13, p. 7–27.
- Groves, D.I., Goldfarb, R.J., Robert, F., and Hart, C.J.R., 2003, Gold deposits in metamorphic belts: overview of current understanding, outstanding problems, future research, and exploration significance: *Economic Geology*, v. 98, p. 29.
- Groves, D.I., Santosh, M., Deng, J., Wang, Q., Yang, L. and Zhang, L., 2019, A holistic model for the origin of orogenic gold deposits and its implications for exploration: *Mineralium Deposita*, v. 55, p. 275–292.
- Hibbard, J., 1983, Geology of the Baie Verte Peninsula, Newfoundland: *Mineral Development Division, Department of Mines and Energy, Government of Newfoundland and Labrador*, v. 2, p. 283.
- James, L., 1954, Sedimentary facies of iron-formation: *Economic Geology*, v. 49, p. 235–293.
- Kerr, A., and Selby, D., 2012, The timing of epigenetic gold mineralization on the Baie Verte Peninsula, Newfoundland, Canada: New evidence from Re-Os pyrite geochronology: *Mineralium Deposita*, v. 47, p. 325–337.
- Kerrick, R., and Fyfe, W.S., 1981, The gold—carbonate association: source of CO<sub>2</sub>, and CO<sub>2</sub> fixation reactions in Archaean lode deposits: *Chemical Geology*, v. 33, p. 265–294.
- Kerswill, J.A., 1993. Models for iron-formation-hosted gold deposits: *Geological Association of Canada Special Paper*, v. 40, p. 171–199.
- Kessler, L.G., and Bédard, J.H., 2000, Epiclastic volcanic debrites—evidence of flow transformations between avalanche and debris flow processes, Middle Ordovician, Baie Verte Peninsula, Newfoundland, Canada: *Precambrian Research*, v. 101, p. 135–161.
- Kirkwood, D., and Dubé, B., 1992, Structural control of sill-hosted gold mineralization: the Stog'er Tight gold deposit, Baie Verte Peninsula, northwestern Newfoundland: *Current research, Part D, Geological Survey of Canada Papers*, p. 211–221.
- Klinkhammer, G.P., Elderfield, H., Edmond, J.M., and Mitra, A., 1994, Geochemical implications of rare earth element patterns in hydrothermal fluids from mid-ocean ridges: *Geochimica et Cosmochimica Acta*, v. 58, p. 5105–5113.
- Konhauser, K.O., Planavsky, N.J., Hardisty, D.S., Robbins, L.J., Warchola, T.J., Haugard, R., Lalonde, S.V., Partin, C.A., Oonk, P.B.H., Tsikos, H. and Lyons, T.W., 2017, Iron formations: A global record of Neoarchaean to Palaeoproterozoic environmental history: *Earth-Science Reviews*, v. 172, p. 140–177.
- Kuntz, G., Robinson, J., McNeill, P., Bullock, K. and Budgell, C., 2021, NI 43-101 Mineral Resource and Mineral Reserve Update on the Point Rousse Project, Baie Verte, Newfoundland and Labrador, Canada, p. 217.

- Lambeck, A., Mernagh, T.P., and Wyborn, L., 2011, Are iron-rich sedimentary rocks the key to the spike in orogenic gold mineralization in the Paleoproterozoic? *Economic Geology*, v. 106, p. 321–330.
- Lawrence, M.G., and Kamber, B.S., 2006, The behaviour of the rare earth elements during estuarine mixing-revisited: *Marine Chemistry*, v. 100, p.147-161.
- Li, Z.Q., Zhang, L.C., Xue, C.J., Zheng, M.T., Zhu, M.T., Robbins, L.J., Slack, J.F., Planavsky, N.J. and Konhauser, K.O., 2018, Earth's youngest banded iron formation implies ferruginous conditions in the Early Cambrian ocean: *Scientific reports*, v. 8, p. 10.
- Lupton, J.E. and Craig, H., 1981, A Major Helium-3 Source at 15°S on the East Pacific Rise: *Science*, v. 214, p. 13–18.
- Lydon, J.W., 1984, Ore deposit models-8. Volcanogenic massive sulphide deposits Part I: a descriptive model: *Geological Survey of Canada*, v. 11, p. 195–202.
- McCuaig, T.C., and Kerrich, R., 1998, P-T-t-deformation-fluid characteristics of lode gold deposits: Evidence from alteration systematics: *Alteration and Alteration Processes Associated with Ore-forming Systems. Geological Association of Canada, Short Course Notes*, v. 12, p. 381–453.
- McDivitt, J.A., Lafrance, B., Kontak, D.J. and Robichaud, L., 2017, The Structural Evolution of the Missanabie-Renabie Gold District: Pre-orogenic Veins in an Orogenic Gold Setting and Their Influence on the Formation of Hybrid Deposits: *Economic Geology*, v. 112, p. 1959–1975.
- McNicoll, V., Dubé, B., Castonguay, S., Oswald, W., Biczok, J., Mercier-Langevin, P., Skulski, T., and Malo, M., 2016, The world-class Musselwhite BIF-hosted gold deposit, Superior Province, Canada: New high-precision U-Pb geochronology and implications for the geological setting of the deposit and gold exploration: *Precambrian Research*, v. 272, p. 133–149.
- Michard, A., 1989, Rare earth element systematics in hydrothermal fluids: *Geochimica et Cosmochimica Acta*, v. 53, p. 745–750
- Mikucki, E.J., 1998, Hydrothermal transport and depositional processes in Archean lode-gold systems: A review: *Ore Geology Reviews*, v. 13, p. 307–321.
- Morelli, R.M., Bell, C.C., Creaser, R.A., and Simonetti, A., 2010, Constraints on the genesis of gold mineralization at the Homestake Gold Deposit, Black Hills, South Dakota from rhenium–osmium sulfide geochronology: *Mineralium Deposita*, v. 45, p. 461–480.
- Och, L. and Shields-Zhou, G., 2012, The Neoproterozoic oxygenation event: environmental perturbations and biogeochemical cycling: *Earth-Science Reviews*, v. 110, p. 26–57.
- Olson, S., Kump, L. and Kasting, J., 2013, Quantifying the areal extent and dissolved

- oxygen concentrations of Archean oxygen oases: *Chemical Geology*, v. 362, p. 35–43.
- Pack, A., Russell, S., Shelley, J. and Van Zuilen, M., 2007, Geo-and cosmochemistry of the twin elements yttrium and holmium: *Geochemica et Cosmochimica Acta*, v. 71, p. 4592–4608.
- Pawlukiewicz, M., 2019. Hydrothermal reconstruction and lithogeochemistry of the Argyle orogenic gold deposit, Baie Verte, Newfoundland: *Memorial University of Newfoundland*, p. 426.
- Peter, J.M., 2003, Ancient iron formations: their genesis and use in the exploration for stratiform base metal sulphide deposits, with examples from the Bathurst Mining Camp: *Geochemistry of Sediments and Sedimentary rocks: Evolutionary Considerations to Mineral Deposit-forming Environments*, Geological Association of Canada, v. 4, p. 145–176.
- Peter, J.M., and Goodfellow, W.D., 2003, Hydrothermal sedimentary rocks of the Heath Steele Belt, Bathurst mining camp, New Brunswick; Part 3, Application of mineralogy and mineral and bulk compositions to massive sulfide exploration: *Economic Geology Monograph*, v. 11, p. 417–433.
- Peter, J.M., and Goodfellow, W.D., 1996, Mineralogy, bulk and rare earth element geochemistry of massive sulphide-associated hydrothermal sediments of the Brunswick Horizon, Bathurst Mining Camp, New Brunswick: *Canadian Journal of Earth Sciences*, v. 33, p. 252–283.
- Peter, J.M., Goodfellow, W.D., and Doherty, W., 2003a, Hydrothermal sedimentary rocks of the Heath Steele belt, Bathurst mining camp, New Brunswick: Part 2. Bulk and rare earth element geochemistry and implications for origin: *Economic Geology Monograph*, v. 11, p. 391–415.
- Peter, J.M., Kjarsgaard, I.M., Goodfellow, W.D., and McCutcheon, S.R., 2003b, Hydrothermal sedimentary rocks of the Heath Steele Belt, Bathurst mining camp, New Brunswick—Part 1. Mineralogy and mineral chemistry: Massive sulfide deposits of the Bathurst mining camp, New Brunswick, and northern Maine. *Economic Geology Monograph*, v. 11, p. 361–390.
- Phillips, G.N., Groves, D.I., and Brown, I.J., 1987, Source requirements for the Golden Mile, Kalgoorlie: Significance to the metamorphic replacement model for Archean gold deposits: *Canadian Journal of Earth Sciences*, v. 24, p. 1643–1651.
- Phillips, G.N., and Powell, R., 2010, Formation of gold deposits: A metamorphic devolatilization model: *Journal of Metamorphic Geology*, v. 28, p. 689–718.
- Piercey, S.J., Jenner, G.A., Wilton, D.H.C., Pereira, C.P.G., and Walsh, D.G., 1997, The stratigraphy and geochemistry of the southern Pacquet Harbour Group, Baie Verte Peninsula, Newfoundland; implications for mineral exploration: *Newfoundland and Labrador Department of Mines and Energy*, p. 119–139.

- Pilote, J.-L., Piercey, S.J., and Mercier-Langevin, P., 2014, Stratigraphy and hydrothermal alteration of the Ming Cu-Au volcanogenic massive-sulphide deposit, Baie Verte Peninsula, Newfoundland: *Geological Survey of Canada*, p. 18.
- Pilote, J.L., Piercey, S.J., and Mercier-Langevin, P., 2015, Volcanic architecture and alteration assemblages of the Ming Cu-Au-(Zn-Ag) VMS deposit, Baie Verte, Newfoundland and Labrador: *Implications for Au-enrichment processes and exploration, Geological Survey of Canada, Open File*, v. 7853, p. 197-210.
- Pitcairn, I.K., Craw, D., and Teagle, D.A.H., 2015, Metabasalts as sources of metals in orogenic gold deposits: *Mineralium Deposita*, v. 50, p. 373–390.
- Pitcairn, I.K., Craw, D., and Teagle, D.A.H., 2014, The gold conveyor belt: Large-scale gold mobility in an active orogen: *Ore Geology Reviews*, v. 62, p. 129–142.
- Pitcairn, I.K., Olivo, G.R., Teagle, D.A.H., and Craw, D., 2010, Sulfide evolution during prograde metamorphism of the Otago and Alpine Schists, New Zealand: *The Canadian Mineralogist*, v. 48, p. 1267–1295.
- Pitcairn, I.K., Teagle, D.A.H., Craw, D., Olivo, G.R., Kerrich, R., and Brewer, T.S., 2006, Sources of metals and fluids in orogenic gold deposits: insights from the Otago and Alpine Schists, New Zealand: *Economic Geology*, v. 101, p. 1525–1546.
- Planavsky, N., Bekker, A., Rouxel, O.J., Kamber, B., Hofmann, A., Knudsen, A., and Lyons, T.W., 2010, Rare earth element and yttrium compositions of Archean and Paleoproterozoic Fe formations revisited: New perspectives on the significance and mechanisms of deposition: *Geochimica et Cosmochimica Acta*, v. 74, p. 6387–6405.
- Poulsen, K.H., Robert, F., and Dubé, B., 2000, Geological classification of Canadian gold deposits: *Bulletin of the Geological Survey of Canada*, v. 540, p. 106.
- Ramezani, J., 1992, The geology, geochemistry and U-Pb geochronology of the Stog’er Tight gold prospect, Baie Verte Peninsula, Newfoundland: *Memorial University of Newfoundland*, p. 256.
- Ramezani, J., Dunning, G.R., and Wilson, M.R., 2000, Geologic setting, geochemistry of alteration, and U-Pb age of hydrothermal zircon from the Silurian Stog’er Tight gold prospect, Newfoundland Appalachians, Canada: *Exploration and Mining Geology*, v. 9, p. 171–188.
- Ridley, J.R., and Diamond, L.W., 2000, Fluid chemistry of orogenic lode gold deposits: *Reviews in Economic Geology, Society of Economic Geologists, Inc.*, v. 13, p. 141–162.
- Ridley, J., Mikucki, E.J., and Groves, D.I., 1996, Archean lode-gold deposits: fluid flow and chemical evolution in vertically extensive hydrothermal systems: *Ore Geology Reviews*, v. 10, p. 279–293.
- Robb, L.J., 2005, Introduction to ore-forming processes: John Wiley & Sons, p. 382.

- Rudnicki, M.D., 1995, Particle formation, fallout and cycling within the buoyant and non-buoyant plume above the TAG vent field: *Geological Society Special Publication*, v. 87, p. 387–396.
- Sangster, A.L., Douma, S.L., and Lavigne, J., 2007, Base metal and gold deposits of the Betts Cove Complex, Baie Verte Peninsula, Newfoundland: *Mineral Deposits of Canada: A Synthesis of Major Deposit-Types, District Metallogeny, the Evolution of Geological Provinces, and Exploration Methods: Geological Association of Canada, Mineral Deposits Division, Special Publication*, v. 5, p. 703–721.
- Seward, T.M., 1973, Thio complexes of gold and the transport of gold in hydrothermal ore solutions: *Geochimica et Cosmochimica Acta*, v. 37, p. 379–399.
- Sillitoe, R.H., and Bonham Jr, H.F., 1990, Sediment-hosted gold deposits: Distal products of magmatic-hydrothermal systems: *Geology*, v. 18, p. 157–161.
- Skulski, T., Castonguay, S., McNicoll, V., van Staal, C., Kidd, W., Rogers, N., Morris, W., Ugalde, H., Slavinski, H., and Spicer, W., 2010, Tectonostratigraphy of the Baie Verte oceanic tract and its ophiolite cover sequence on the Baie Verte Peninsula: *Newfoundland and Labrador Department of Natural Resources, Geological Survey*, v. 1, p. 315–337.
- Skulski, T., Castonguay, S., Van Staal, C.R., Rogers, N., Mcnicoll, V., Kerr, A., and Escayola, M., 2009, Baie Verte Peninsula: An Evolving Geological Story: *Geological Association of Canada, Newfoundland and Labrador Section Annual Field Trip Guide*, p. 76.
- Slack, J.F., Grenne, T., Bekker, A., Rouxel, O.J., and Lindberg, P.A., 2007, Suboxic deep seawater in the late Paleoproterozoic: evidence from hematitic chert and iron formation related to seafloor-hydrothermal sulfide deposits, central Arizona, USA: *Earth and Planetary Science Letters*, v. 255, p. 243–256.
- Snelgrove, A.K., 1935, Geology of gold deposits of Newfoundland. *Newfoundland Department of Natural Resources: Bulletin*, v. 2, p. 46.
- Sparrow, B., Barrett, S., Copeland, D., and Walsh, M., 2017, Assessment report on prospecting and drilling on the Point Rousse Project- Goldenville Prospect, Licences 018925M (6th year) and 018926M (6th year), 015582M (8th year), and 018617M (6th year) NTS Sheets 12H/16 and 12I/01 Newfoundland and Labrador Canada, p. 481.
- Spooner, E.T.C., 1993, Magmatic sulphide/volatile interaction as a mechanism for producing chalcophile element enriched, Archean Au-quartz, epithermal Au Ag and Au skarn hydrothermal ore fluids: *Ore Geology Reviews*, v. 7, p. 359–379.
- Spry, P.G., Peter, J.M., and Slack, J.F., 2000, Meta-exhalites as exploration guides to ore: *Reviews in Economic Geology, Society of Economic Geologists, Inc.*, v. 11, p. 163–201.

- Steadman, J.A., Large, R.R., Davidson, G.J., Bull, S.W., Thompson, J., Ireland, T.R., and Holden, P., 2014, Paragenesis and composition of ore minerals in the Randalls BIF-hosted gold deposits, Yilgarn craton, Western Australia: Implications for the timing of deposit formation and constraints on gold sources: *Precambrian Research*, v. 243, p. 110–132.
- Sverjensky, D.A., 1984, Europium redox equilibria in aqueous solution: *Earth and Planetary Science Letters*, v. 67, p. 70–78.
- Swinden, S., McBride, D., and Dubé, B., 1990, Preliminary geological and mineralogical notes on the Nugget Pond gold deposit, Baie Verte Peninsula, Newfoundland: *Newfoundland Department of Mines and Energy Report of Activities, Mineral Development Division*, p. 201–215.
- Todd, S., Pufahl, P., Murphy, J. and Taylor, K., 2019, Sedimentology and oceanography of early Ordovician ironstone, Bell Island, Newfoundland: Ferruginous seawater and upwelling in the Rheic Ocean: *Sedimentary Geology*, v. 379, p. 15.
- Tostevin, R. 2021, Cerium Anomalies and Paleoredox: *Cambridge University Press*, p. 6454.
- Tuach, J., and Kennedy, M.J., 1978, The geologic setting of the Ming and other sulfide deposits, Consolidated Rambler Mines, Northeast Newfoundland: *Economic Geology*, v. 73, p. 192–206.
- Turner, D., Whitfield, M. and Dickson, A. 1981. The equilibrium speciation of dissolved components in freshwater and sea water at 25 C and 1 atm pressure: *Geochemica et Cosmochimica Acta*, v. 45, p. 855–881.
- van Staal, C.R., and Barr, S.M., 2012, Lithospheric architecture and tectonic evolution of the Canadian Appalachians and associated Atlantic margin: *Tectonic Styles in Canada: The LITHOPROBE Perspective: Geological Association of Canada Special Paper*, v. 49, p. 55.
- van Staal, C.R., Whalen, J.B., McNicoll, V.J., Pehrsson, S., Lissenberg, C.J., Zagorevski, A., Van Breemen, O., and Jenner, G.A., 2007, The Notre Dame arc and the Taconic orogeny in Newfoundland: *Geological Society of America Memoirs*, v. 200, p. 511–552.
- Viehmann, S., Bau, M., Hoffmann, J. and Muenker, C., 2015, Geochemistry of the Krivoy Rog Banded Iron Formation, Ukraine, and the impact of peak episodes of increased global magmatic activity on the trace element composition of Precambrian seawater: *Precambrian Research*, v. 270, p. 165–180.
- Warke, M., Strauss, H. and Schröder, S., 2020, Positive cerium anomalies imply pre-GOE redox stratification and manganese oxidation in Paleoproterozoic shallow marine environments: *Precambrian Research*, v. 344, p. 105–767.
- Watson, K.D.P., 1947, Geology and mineral deposits of the Baie Verte-Mings Bight area,

- Newfoundland: *Geological Survey of Newfoundland*, v. 21, p. 209.
- Weick, R.J., 1993, Petrography and stable isotope geochemistry of alteration and mineralization in the Rambler volcanogenic massive sulphide deposit, Baie Verte, Newfoundland: *Memorial University of Newfoundland*, p. 209.
- Williams-Jones, A.E., Bowell, R.J., and Migdisov, A.A., 2009, Gold in solution: *Elements*, v. 5, p. 281–287.
- Williams, H., 1979, Appalachian Orogen in Canada: *Canadian Journal of Earth Sciences*, v. 16, p. 792–807.
- Williams, H., Colman-Sadd, S.P., and Swinden, H.S., 1988, Tectonostratigraphic subdivisions of central Newfoundland: *Current Research, Part B. Geological Survey of Canada Paper*, v. 88-1B, p. 91-98.
- Williams, H., Dehler, S.A., Grant, A.C., and Oakey, G.N., 1999, Tectonics of Atlantic Canada: *Geoscience Canada*, v. 26, p. 51-70.
- Williams, H., and St-Julien, P., 1982, The Baie Verte-Brompton line: early Paleozoic continent-ocean interface in the Canadian Appalachians: in *Major Structural Zones and Faults of the Northern Appalachians*, *Geological Association of Canada*, v. 24, p. 177–208.
- Ybarra, S., 2019, Hydrothermal alteration and lithogeochemistry of the Pine Cove orogenic gold deposit, Baie Verte Peninsula, Newfoundland, Canada: *Memorial University of Newfoundland*, p. 250.
- Zhang, J., Amakawa, H. and Nozaki, Y., 1994, The comparative behaviors of yttrium and lanthanides in the seawater of the North Pacific: *Geophysical Research Letters*, v. 21, p. 2677–2680.

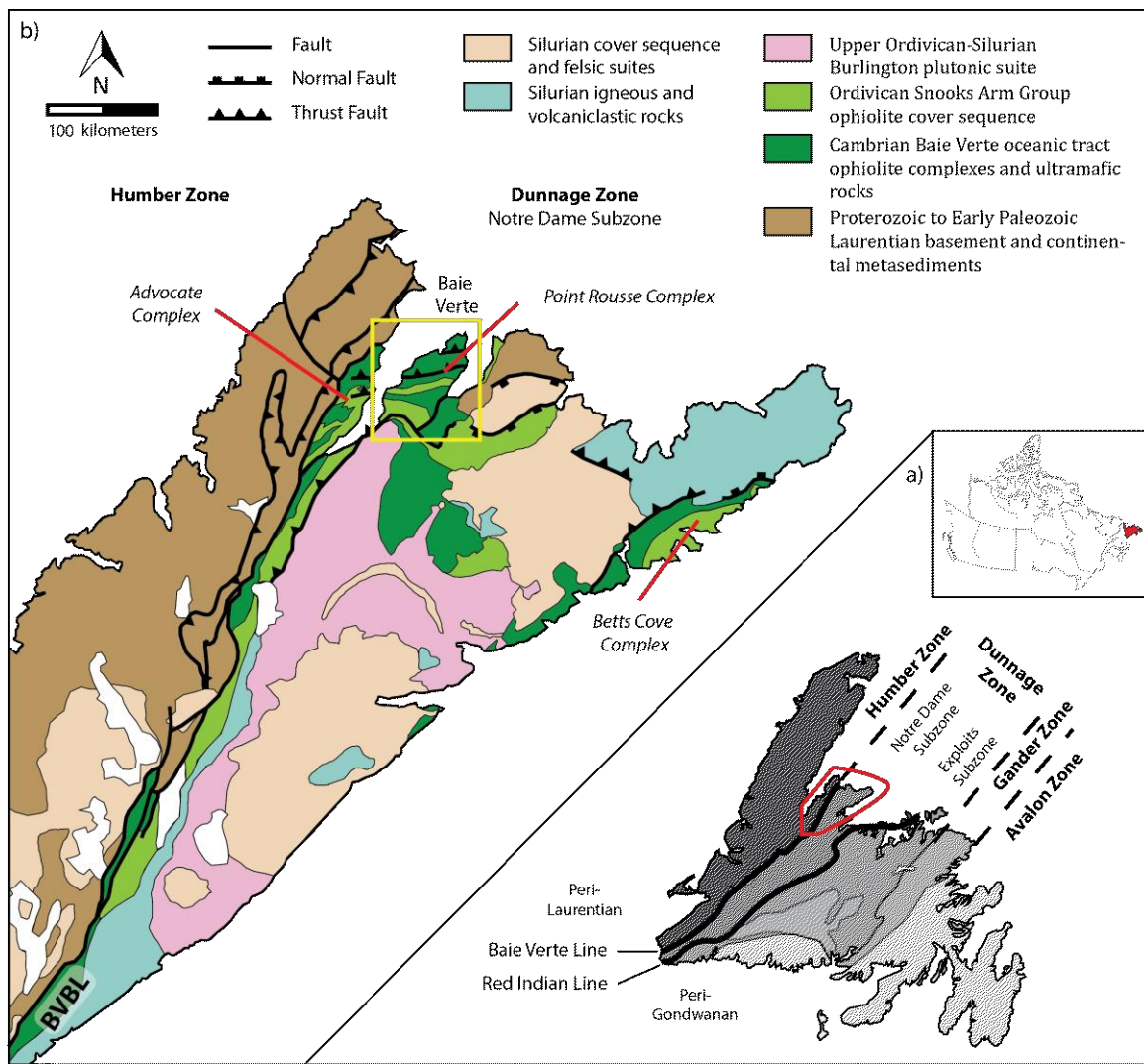


**Figure 1.1.** a) Simplified map of the tectonostratigraphic terranes of Newfoundland (modified after Williams, 1979 and Skulski et al., 2010) with an inset showing the area of 1.1b, the location of the Baie Verte Peninsula in Newfoundland. b) Geology map of the Baie Verte Peninsula (modified after Skulski et al., 2010) with yellow box showing the location in Figure 1.2.

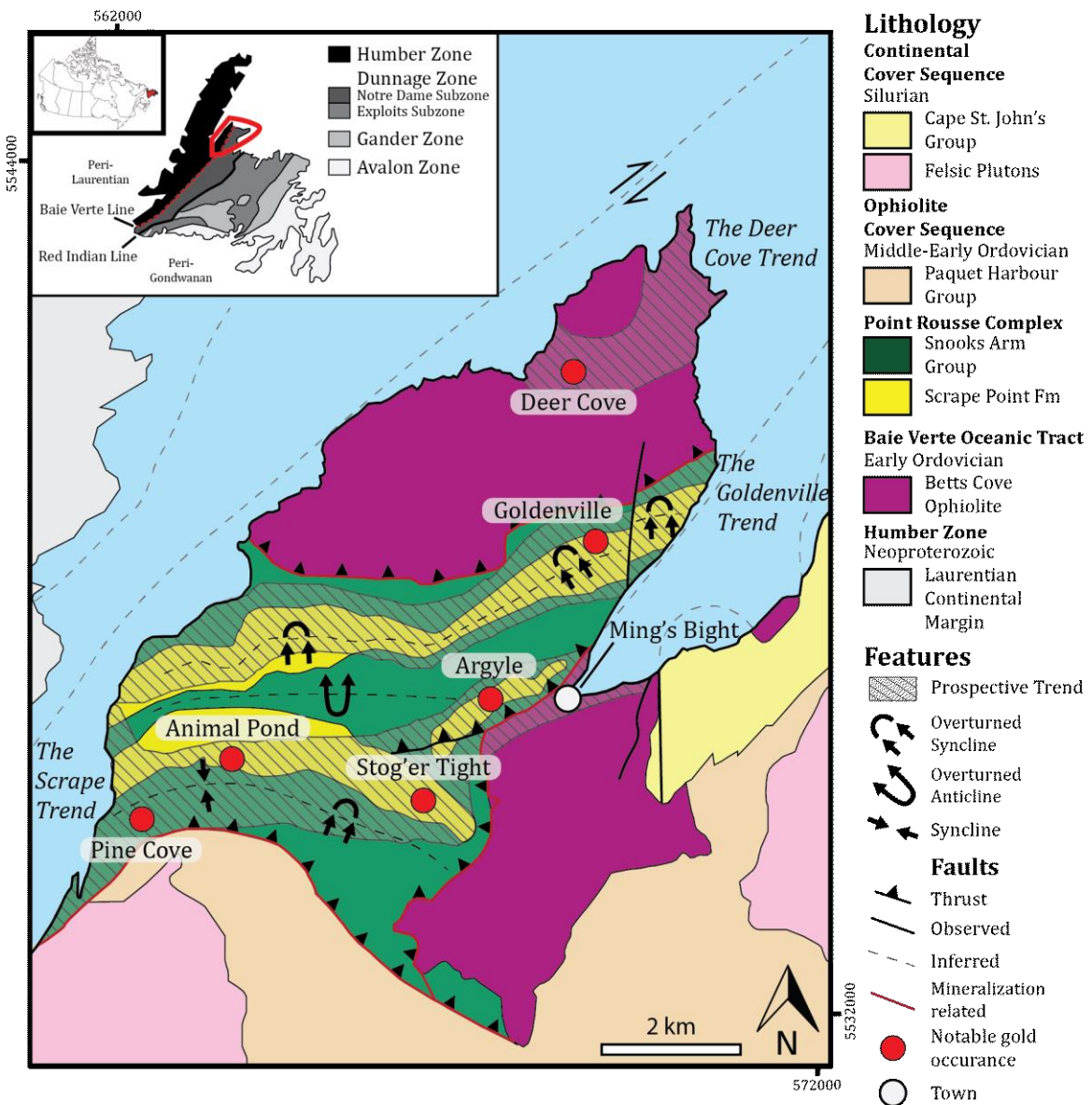


**Figure 1.2.** Simplified geology map of the Point Rousse project on the Baie Verte Peninsula with notable gold deposits and VMS occurrences. Modified from Skulski et al. (2010) and Anaconda Mining's Assessment Report on the Point Rousse Project by Sparrow et al. (2017).

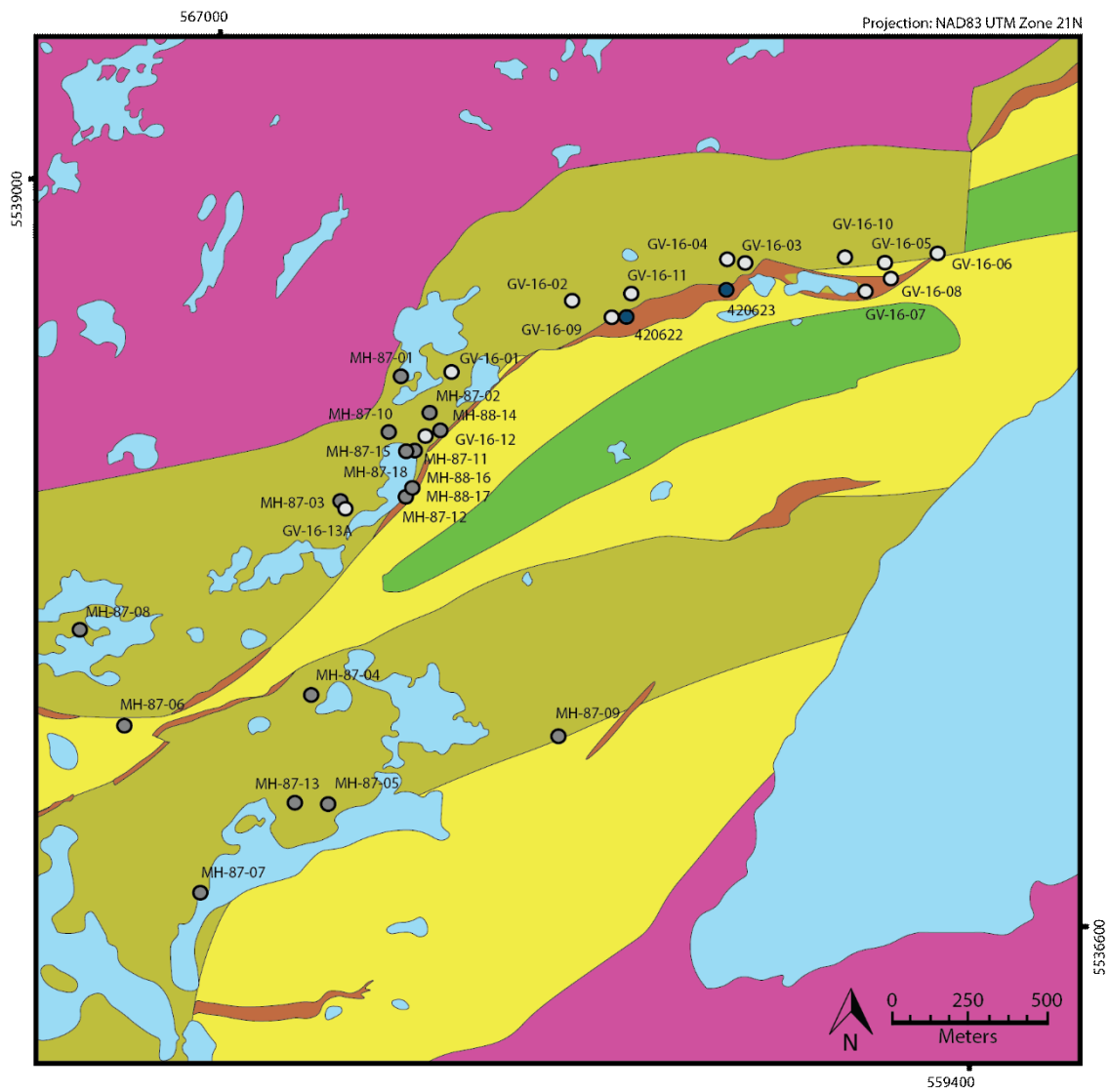


**Figure 1.3.** Simplified geologic map of the Goldenville mine area with logged drill holes and surface samples (Appendix A). Modified from Skulski et al. (2010; 2015) and Anaconda Mining Inc. (unpublished mapping).

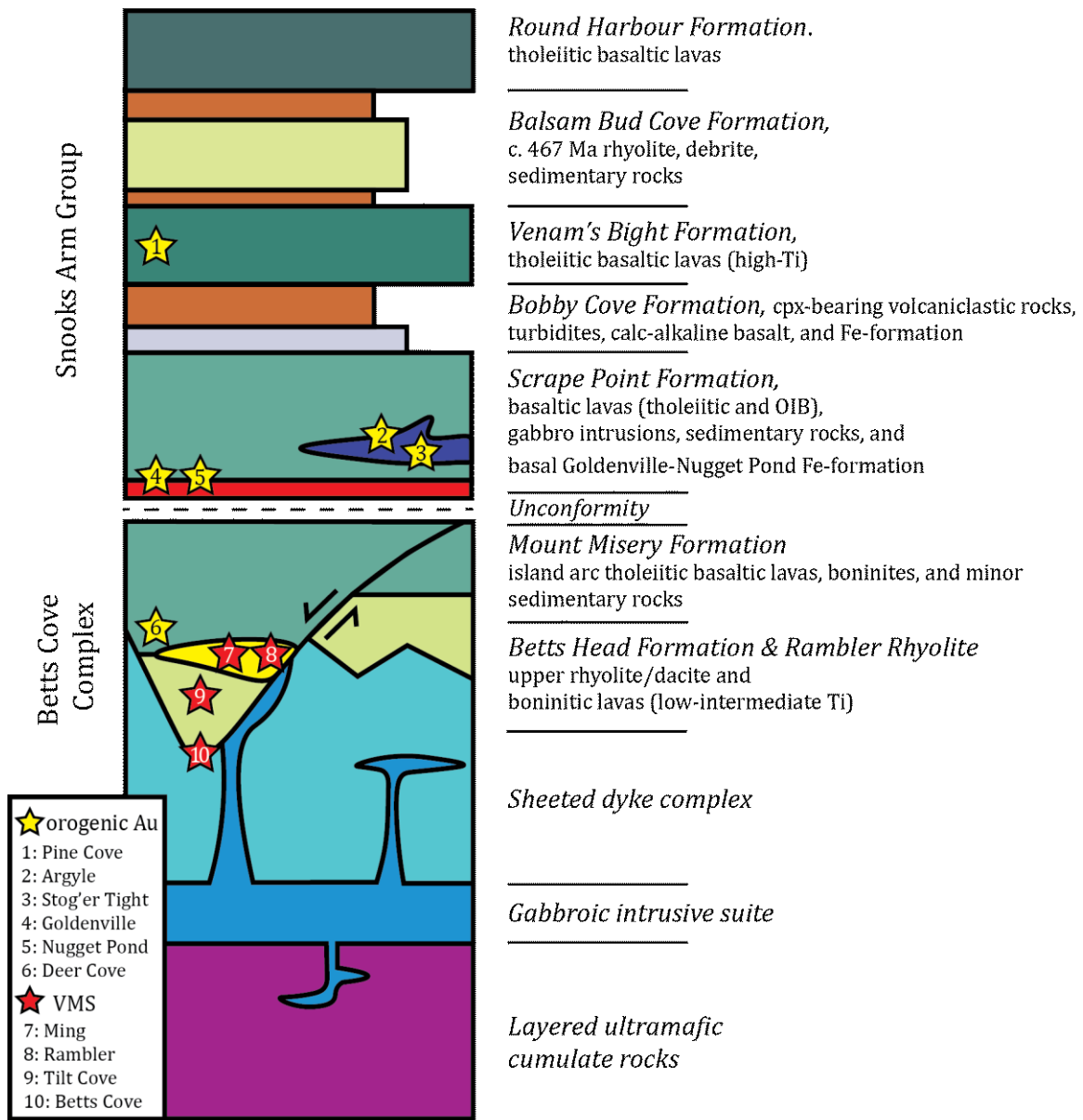


**Figure 1.4.** Regional stratigraphy of the Baie Verte Peninsula. Mineral deposits are symbolized by stars, and include orogenic Au and VMS deposits. Modified after Bédard et al. (2000), Kessler and Bédard (2000), and Skulski et al. (2009).

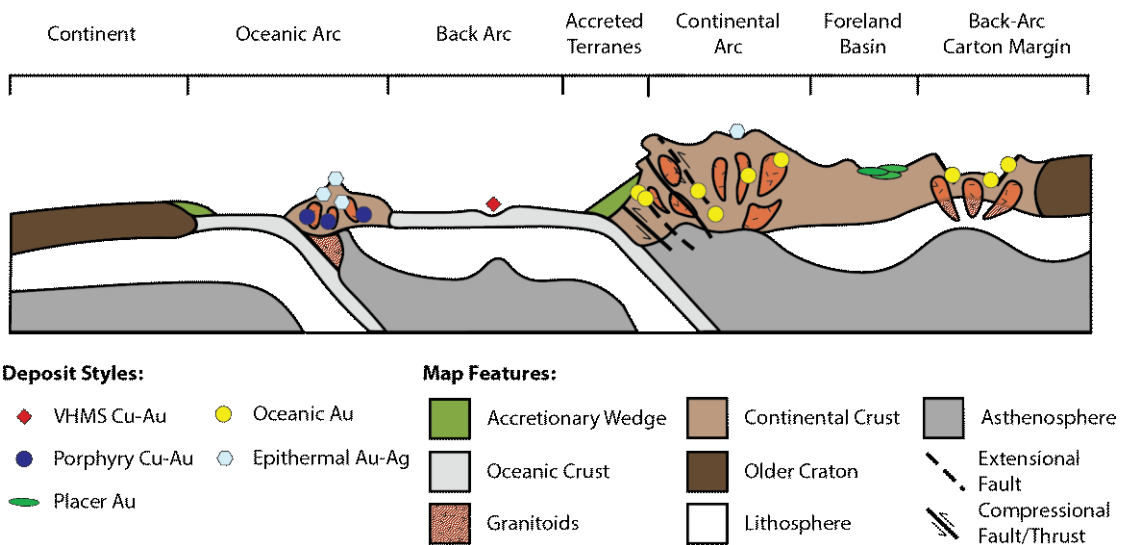


**Figure 1.5.** Representative cross-section of the tectonic settings in which gold deposits are formed. Orogenic gold, symbolized by yellow circles, are found in deformed forearc and backarc settings, and sheared margins of continental arc batholiths. Modified after Goldfarb and Groves (2015).

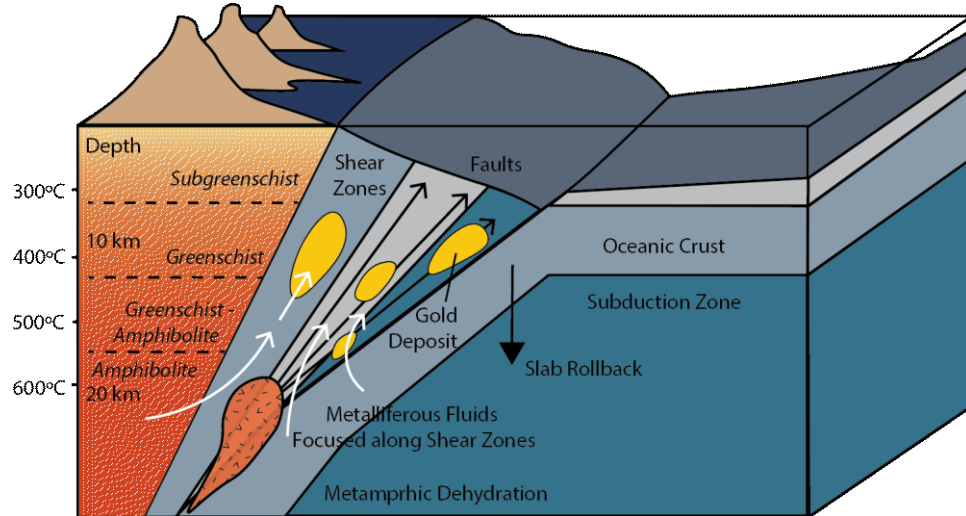


**Figure 1.6.** Schematic of fluid flow into accreted ocean arc, where fluid is derived from prograde metamorphism of the subducting slab and associated sedimentary, or other overlying material. Modified after Kerrich et al. (2005).

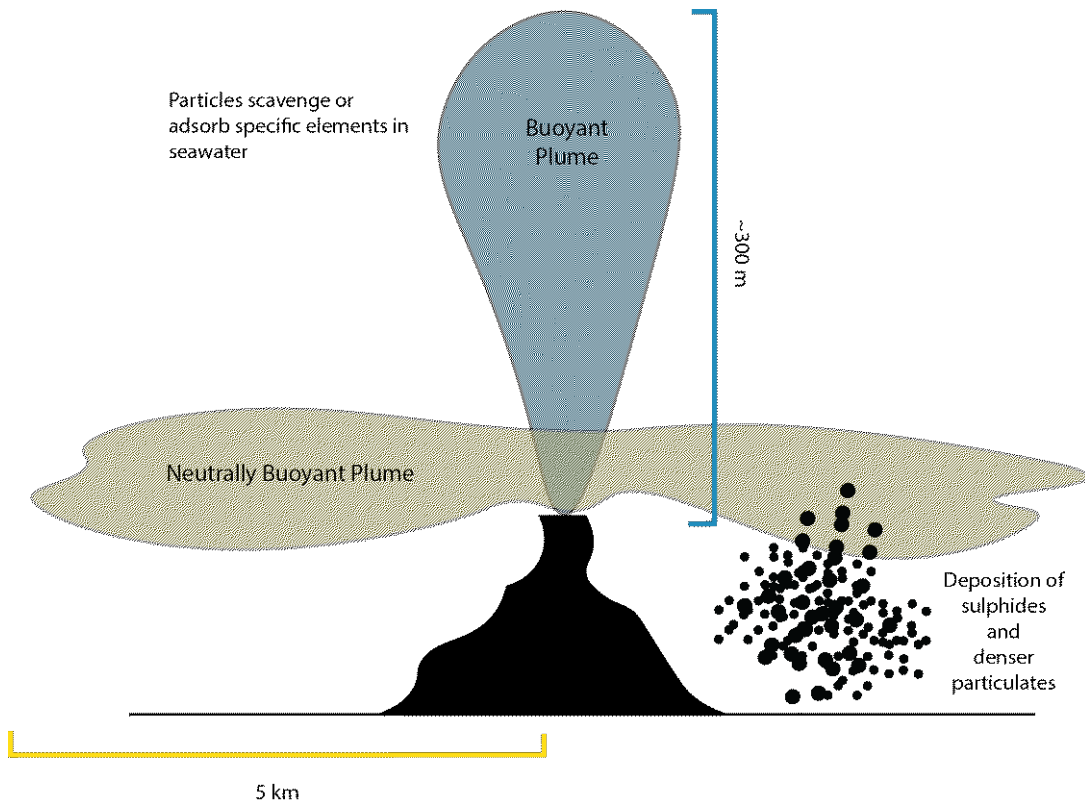


**Figure 1.7.** Schematic breakdown of the buoyant and non-buoyant plume associated with a hydrothermal vent and the associated processes occurring within each. Modified after Rudnicki (1995) and Peter, (2003).

## **Chapter 2: Origin and Genesis of the Goldenville Iron Formations Associated with Base Metals and Orogenic Au, Baie Verte, Newfoundland, Canada**

---

### **2.1 Abstract**

The Goldenville iron formation (IF), within the Point Rousse complex, Baie Verte Peninsula, Newfoundland, hosts the Goldenville Au deposit and produced 23 tonnes of ore between 1904-1906 (158 oz gold recovered). The Goldenville IF marks the end of Cambrian-Ordovician (~489-485 Ma) Au-rich VMS activity and is considered to be correlative with the Nugget Pond IF, with both iron formations believed to form a marker unit between the Mount Misery Formation and the overlying Snooks Arm Group cover sequence (~470 Ma). The redox-sensitive element geochemistry of exhalative IF also has utility as an ancient deep seawater paleo-redox proxy, such that the Goldenville IF has potential to reveal new insights regarding the oxygenation of the Cambrian-Ordovician Humber seaway. Despite its economic, stratigraphic, and geological importance, the Goldenville IF has received very little textural-mineralogical-geochemical focus.

The Goldenville horizon is a laterally discontinuous, fine-grained, and laminated unit within argillites, volcaniclastic rocks, and basalt flows of the Mount Misery Formation footwall and Scrape Point Formation hanging wall. Immobile element (e.g., Zr, Ti, Th, La, and Sc) signatures of the interbedded argillites and volcaniclastic rocks indicate derivation from intra-oceanic island arc sources. Chemostratigraphy places the Goldenville horizon deposition synchronous with the Mount Misery Formation, whereas the Nugget Pond horizon represents post-Mount Misery deposition.

The Goldenville iron formation can be subdivided into groups with compositional and lithogeochemical signatures that reflect varying contributions from sedimentary/volcanic detritus, hydrothermal fluids, and elements hydrogenously scavenged from seawater. The samples with the greatest hydrothermally sourced element abundance (highest Fe+Mn relative to Al+Ti) have post-Archean Australian Shale (PAAS) normalized REE+Y patterns with a range of Ce anomalies from negative to positive ( $\text{Pr}_{\text{sn}}/\text{Pr}_{\text{sn}}^* = 0.79-1.22$ ). However, the samples with a positive Ce anomaly have the highest Mn abundances, and thus the full range of Ce anomalies can be reconciled under the same inferred bottom water redox conditions if hydrothermal oxide particles scavenged REE from fully oxygenated seawater (negative Ce anomalies) and the Mn-rich samples specifically record the preferential scavenging of  $\text{Ce}^{4+}$  by Mn-(oxy)(hydr)oxides in the water column, and possibly after deposition (local positive Ce anomaly development). This interpretative model is similar to observations from some modern hydrothermal environments and would imply bottom waters in the Humber seaway were fully oxygenated in the Cambrian-Ordovician.

Gold mineralization in and proximal to the IF was younger and associated with Silurian  $\text{Au}(\text{HS})_2^-$ -bearing hydrothermal fluids. Pyrite with gold inclusions suggests that orogenic Au-bearing fluids interacted with  $\text{Fe}^{3+}$ -bearing minerals within IF, resulting in wall rock sulfidation and the co-precipitation of gold and pyrite. Due to the stratigraphic re-positioning of the Goldenville horizon, the iron formation may not be as favorable of an exploration target as the Nugget Pond horizon at this location.

## 2.2 Introduction

Exhalative (i.e., “Algoma-type”) iron formations are interpreted to reflect formation from the precipitation and deposition of iron-rich minerals on the seafloor (James, 1954; Gross, 1980; Bekker et al., 2014). These iron formations typically consist of variable quantities of 1) hydrothermal-exhalative material occurring as layered magnetite and/or hematite interbedded with chert; 2) hydrogenous contributions represented by elements scavenged from seawater onto hydrothermal materials and 3) detrital material (e.g., volcaniclastic debris; Boström and Peterson, 1969; Peter and Goodfellow, 2003). Exhalative iron formations are often spatially and temporally associated with seafloor massive sulfide deposits, and in the ancient record are found directly in contact and extending outwards laterally from volcanogenic massive sulfide (VMS) (e.g., Brunswick #12, New Brunswick; Peter and Goodfellow, 2003). Exhalative iron formations have also been document as hosts for younger orogenic Au mineralization (e.g., Homestake-type orogenic Au; Caddey, 1991). The spatial association of iron formations with VMS and orogenic Au deposits make iron formation a potentially valuable tool in exploration for both types of deposits.

The Baie Verte Peninsula (BVP) in north-central Newfoundland hosts both Cu-Au-rich VMS deposits and orogenic Au deposits (Hibbard, 1983; Skulski et al., 2009, 2010; van Staal and Barr, 2012). The Goldenville iron formation within the Point Rousse Complex of the BVP produced 23 tonnes of ore between 1904-1906 (158 oz gold recovered; Sparrow et al., 2017). It is coeval with the end of Cambrian-Ordovician (~489-485 Ma) Au-rich VMS activity (i.e., Rambler VMS deposits and Pacquet complex

volcanism) and previous authors have suggested that it represents a regional marker unit in the Baie Verte Peninsula between the underlying ophiolitic Mount Misery Formation and the overlying Snooks Arm Group ophiolite cover sequence (~470 Ma) (Hibbard, 1983; Bédard, 1999; Castonguay et al., 2009). The unit has significant exploration potential due to its timing in relation to VMS activity and as a host for younger, Silurian-Devonian orogenic Au mineralization at Goldenville. Thus, field, mineralogical, and geochemical characterization of the iron formation is critical for understanding its stratigraphic significance and potential as a host for base metal and orogenic Au mineralization. Further, iron formations are critical records of ancient seafloor hydrothermal activity that have potential to preserve the ocean redox conditions at the time of formation (Bekker et al., 2014; Gourcerol et al., 2016). The Goldenville iron formation provides an opportunity to capture oceanic oxygen conditions in the Humber seaway during the transition from the Cambrian into the Ordovician, where the ocean conditions are poorly constrained (~489-485 Ma; Landing, 2012a, 2012b; Tripathy et al. 2014, Azmy et al. 2015).

Despite the geological importance of the Goldenville iron formation and surrounding sedimentary units (collectively referred to as the Goldenville horizon), the unit has had very little modern geological, mineralogical, or lithogeochemical study. This chapter has four main objectives: 1) to document the variations in the lithofacies and lithogeochemistry of the Goldenville iron formation and surrounding units to place them in a regional and tectonostratigraphic context; 2) evaluate the hydrothermal, hydrogenous, and detrital geochemical contributions to the iron formation; 3) evaluate the paleoredox

conditions of the Humber seaway, from the perspective of REE+Y signatures, at the time of deposition (Cambrian-Ordovician ~489-485 Ma); and 4) evaluate the spatial relationship between base metal and Au mineralization in the iron formation.

### 2.3 Tectonic and Regional Setting

The Newfoundland Appalachians contain four tectonostratigraphic zones (Williams, 1979; Williams et al., 1999), from west to east: the Humber, Dunnage, Gander, and Avalon zones (Fig. 2.1a). The Goldenville deposit is located in the BVP, comprised of rocks from both the Humber and Dunnage zones, which are separated by the Baie Verte-Brompton Line, also referred to as the Baie Verte Line (BVBL/BVL; Fig. 2.1b), a discontinuous brittle-ductile shear zone (Williams and St-Julien, 1982).

The BVL separates Neoproterozoic to Cambrian rocks of the Humber zone to the west and predominantly Cambrian-Ordovician rocks of the Notre Dame subzone of the Dunnage zone to the east (Fig. 2.1b). The Humber zone, west of the BVL in Newfoundland, contains ancient continental margin strata of Laurentia and consists of polydeformed metasedimentary rocks of the Fleur de Lys Supergroup (Hibbard, 1983; Castonguay et al., 2009, 2014; Skulski et al., 2010; van Staal et al., 2013). The Dunnage zone east of the BVL consists of intra-oceanic arc, back-arc, ophiolite, and continental terranes. The Dunnage zone is further subdivided into peri-Gondwanan Exploits subzone and peri-Laurentian Notre Dame subzone that formed near the Gondwanan and Laurentian margins, respectively (Fig. 2.1b; Williams, 1979; Williams et al., 1988; van Staal et al., 2007; van Staal and Barr, 2012). These two subzones are separated by the Red Indian Line, a crustal-scale fault that defines a zone of tectonic mélange comprised of

Lower Ordovician and Cambrian rocks that formed due to arc-arc collision during the later stages of the Taconic orogen (Zagorevski et al., 2006; van Staal et al., 2007; van Staal and Barr, 2012).

## **2.4 Regional Geologic and Stratigraphic Setting of the Goldenville Horizon**

Four ophiolite sequences of the Baie Verte oceanic tract (BVOT) make up part of the BVP, and are interpreted to be the remnants of the Humber seaway that formed between Laurentia proper and rocks of Laurentian affinity (i.e., the Dashwoods microcontinent; Figs. 2.1 and 2.2; Hibbard, 1983; Waldron and van Staal, 2001; Skulski et al., 2010; van Staal and Barr, 2012). These ophiolite rocks are subdivided into four groups: 1) the Advocate Complex; 2) the Betts Cove Complex; 3) the Pacquet complex; and 4) the Point Rousse Complex (Skulski et al., 2010), which are overlain by younger Ordovician and Silurian volcano-sedimentary sequences: the Snooks Arm Group (cover to the Betts Cove Complex), the Point Rousse cover sequence, the Flatwater Pond Group, and the Shark Point Group (Skulski et al., 2010).

The stratigraphy of the ophiolitic rocks and their cover sequences are best preserved within the Betts Cove Complex (489 Ma) and Snooks Arm Group (487-467 Ma) in the eastern part of the BVP (Fig. 2.3; Dunning and Krogh, 1985; Piercy et al., 1997; Bédard et al., 2000; Kessler and Bédard, 2000; Skulski et al., 2010). The ophiolite consists of a lower cumulate section, massive gabbros, sheeted dykes, pillowd boninites of the Betts Head Formation, and island-arc tholeiitic basalts of the Mount Misery Formation (Fig. 2.3; Bédard et al., 2000; Skulski et al., 2010). The Betts Head Formation are further subdivided into: 1) low-Ti boninites that are aphyric with localized

phenocrysts of olivine, orthopyroxene, chromite,  $\pm$  clinopyroxene; and 2) intermediate-Ti boninites that are aphyric with phenocrysts of clinopyroxene or plagioclase (Bédard et al., 2000; Skulski et al., 2010). The Mount Misery Formation stratigraphically overlying the Betts Head Formation contains plagioclase-phyric, pillowd, island-arc tholeiitic basalts (Bédard et al. 2000; Skulski et al., 2010).

The Snooks Arm Group (ca. 479-467 Ma) cover sequence is divided into five distinct formations and members from oldest to youngest: 1) the Scrape Point Formation (900 m thick); 2) Prairie Hat Member of the Bobby Cove Formation and the remainder of the Bobby Cove Formation (600 m thick); 3) Venam's Bight Formation (500 m thick); 4) Balsam Bud Cove Formation (800 m thick); and 5) Round Harbour Formation (500 m thick, Fig. 2.3; Hibbard, 1983; Bédard, 2000; Skulski et al., 2010; Pilote et al., 2015).

The Goldenville horizon, considered to be analogous to the Nugget Pond horizon, is interpreted to mark the angular unconformity marking the transition from the basaltic lavas of the Cambro-Ordovician Mount Misery Formation in the ophiolitic rocks to the Early-Middle Ordovician Snooks Arm Group cover sequence (Fig. 2.3; Hibbard, 1983; Bédard, 1999; Bédard et al., 2000; Skulski et al., 2009, 2010). The Scrape Point Formation contains a basal conglomerate comprised of basalt clasts cemented with jasper, overlain by a discontinuous, magnetite-dominated iron formation (i.e., Nugget Pond horizon and the previously correlated Goldenville Horizon), and turbiditic rocks that are interbedded with red siltstones and volcaniclastic units (Sangster et al., 2007; Skulski et al., 2009). The remainder of the Scrape Point Formation consists of green sandstone-siltstone-mudstone turbidite units, and tuffaceous greywacke units that are interbedded

with mafic tuffs and tholeiitic, high-Ti, plagioclase-phyric, commonly amygdaloidal pillow basalts (Bédard et al., 2000; Skulski et al., 2010). The overlying Bobby Cove Formation, comprises basaltic to andesitic lava flows, conglomerates, sandstones, and purple to maroon mudstones, and contains the Prairie Hat Member marker unit that consists of clinopyroxene-phyric crystal tuff, lapilli tuff and tuff breccia (Bédard et al., 2000; Sangster et al., 2007; Skulski et al., 2009, 2010). The Bobby Cove Formation is overlain by the Venam's Bight Formation, which consists of amygdaloidal, high-Ti, tholeiitic pillow basalts locally interbedded with hyaloclastite, pillow breccia, and red siliceous mudstone to ironstone (Bédard et al., 2000; Skulski et al., 2009, 2010). This unit is succeeded by a series of felsic tuffs, siltstones, and shales of the Balsam Bud Cove Formation, which are followed by high-Ti tholeiitic pillow basalts of the Round Harbour Formation, the uppermost unit of the Snooks Arm Group (Skulski et al., 2009, 2010).

Rocks of the Point Rousse Complex (PRC) were subject to at least four phases of regional deformation throughout the Ordovician to Silurian ( $D_1$ - $D_4$ ; Castonguay et al., 2009). The first deformation event ( $D_1$ , between 481 and 461 Ma; Castonguay et al., 2014), is regionally preserved in the Fleur de Lys Supergroup; however, later deformation has overprinted these structures (Anderson et al., 2001; Castonguay et al., 2014). Generally, this first phase of deformation has been attributed to ophiolite obduction and diachronous arc-continent collision during the Taconic orogeny (Williams, 1979; Tremblay et al., 1997; Anderson et al., 2001; van Staal et al., 2007; Castonguay et al., 2009). The second ( $D_2$ , 428-420 Ma; Dunning and Krogh, 1985; Anderson et al., 2001; Castonguay et al., 2014), and main phase of metamorphism and deformation in the BVP,

is interpreted to be responsible for burial of ophiolites and exhumation of the Fleur de Lys Supergroup during Silurian sinistral transpression localized along the BVL during the Salinic orogeny (Anderson et al., 2001; Castonguay et al., 2009). D<sub>2</sub> events are responsible for meter-scale south-directed shear zones, such as the Scrape thrust, that emplace the PRC over the Pacquet complex (Hibbard, 1983; Dunning et al., 1990; Castonguay et al., 2009). D<sub>3</sub> fabrics in the region (post-388 Ma; Anderson et al., 2001) are attributed to Devonian extension and core complex formation (Castonguay et al., 2009). D<sub>4</sub> deformation (ending ~370 Ma; Anderson et al., 2001) is attributed to an overall transpressional to transtensional regime during the Acadian orogeny (Castonguay et al., 2014). Despite the localized extensive deformation, the rocks of the Dunnage Zone in the Baie Verte Peninsula have preserved tectono-stratigraphy and have only been affected up to greenschist-facies metamorphism (Hibbard, 1983; Tuach and Kennedy, 1978; Anderson et al., 2001; Castonguay et al., 2009; Skulski et al., 2009, 2010).

## 2.5 Lithofacies

### 2.5.1 Igneous and Clastic Sedimentary Lithofacies

Stratigraphy, lithofacies, mineralization, alteration, and other observations of the rocks proximal to the Goldenville horizon were documented using graphic logs created from drill core (Fig. 2.4 and Appendix A). Lithofacies classifications described below are used in cross-sections and stratigraphic columns shown in Figures 2.5 and 2.6, with examples shown in photographs in Figures 2.7-2.9. Igneous rocks are classified as coherent (e.g., flows or intrusions) or as clastic with clastic rocks further subdivided according to Fisher's (1966) non-genetic, grain sized classification for volcaniclastic

rocks that was recently updated by White and Houghton (2006). The stratigraphy described here is part of the Mount Misery Formation of Betts Cove Complex and the Scrape Point Formation of the Snooks Arm Group.

*Massive mafic flows, pillow lavas, and breccias:* mafic rocks consist of coherent flows and associated breccias. Coherent rocks are massive to pillowed, amygdaloidal with quartz ± calcite and chlorite infill, localized varioles, and retain hyaloclastite in pillow margins (Figs. 2.7a-d); the rocks are light grey to green and contain minor breccia at the pillow margins that are partly to fully replaced by chlorite, epidote, calcite, and/or quartz (Figs. 2.7c and d). Localized breccia occurrences contain angular clasts of the basalt and pillow fabrics within a fine-grained matrix with consistent replacement by chlorite, epidote, calcite, and/or quartz mineral assemblage to the surrounding lithology. The coherent rocks are locally cross-cut by quartz-carbonate veins < 4 cm to mm-scale veinlets. There are no significant lithological differences in the basalt flows above or below the Goldenville horizon (Fig. 2.6).

*Mafic volcaniclastic rocks:* mafic volcaniclastic rocks, primarily lapilli tuff and lapillistone, are found throughout the stratigraphy but occur primarily in the footwall to the Goldenville horizon and are often found in contact to the iron formation (Fig. 2.6). The lapilli tuff is predominantly matrix-supported with sub-rounded to elongated clasts of mafic material that are aligned parallel to sediment laminations (Fig. 2.7e). Clast-supported, lapillistone zones are less abundant and contain moderately-sorted angular clasts (5 – 20 mm) of basalt. The lapillistone grades into more matrix-supported lapilli tuff that is well-sorted with rounded clasts (5 - 10 mm) of basalt. Ash-sized material

within the volcaniclastic rocks is very fine-grained and grey to green; the clasts and ash are partially to fully replaced by black to green chlorite and epidote.

*Mafic intrusive rocks:* mafic intrusive rocks, primarily gabbro and diabase, are found in the stratigraphy cross-cutting units in the hanging wall and the footwall of the Goldenville iron horizon (Figs. 2.5 and 2.6). The gabbroic rocks (< 1 m to 5 m wide) are coarse-grained, light tan to light grey and contain leucoxene and disseminated pyrite (Fig. 2.7f). The diabase dykes (< 1 m), cross-cutting the mafic flows and gabbro, are fine- to medium-grained, variably grey to light green, locally amygdaloidal (partially to fully filled by calcite and/or quartz) and very rarely contain pyrite mineralization. The gabbroic intrusive rocks are sericite altered with cross-cutting mm-scale carbonate-quartz veinlets, whereas the diabase dykes are variably chlorite altered and are cross-cut by mm-scale epidote and carbonate-quartz veinlets. All the intrusive rocks logged in this study exhibit sharp boundaries with surrounding lithologies.

*Argillites:* the argillite lithofacies is stratigraphically below and interbedded with the iron formation (Figs. 2.5-2.6). This unit varies from maroon to light and dark green (Figs. 2.7g and h) and is predominantly fine-grained and well-laminated multicolored argillite (1 to 3 cm in thickness); complete turbidite sequence with graded bedding is locally present. The argillites contain variable quantities of laminated quartz, magnetite, and disseminated cubic to clotted pyrite. Vugs, veins (up to 4 cm), and veinlets (1 to 4 mm) of chlorite and carbonate, with lesser epidote, quartz, and albite that cross-cut laminations.

## 2.5.2 Iron Formation Lithofacies

The Goldenville iron formation (IF) in drill hole occurs as continuous intervals up to 8 meters or as multiple thinner lenses that can be as thin as few centimeters (drill core thickness; Figs. 2.5-2.6). The iron formation, red to maroon in color, is laminated, magnetic, and locally contains jasper chert nodules and detrital volcaniclastic material (Fig. 2.8a-f). The horizon is subdivided into three categories based on magnetite content: massive magnetite-rich iron formations dominated by magnetite (>45% mag), argillite with semi-massive magnetite (15-45% mag), and argillite with disseminated magnetite (<15% mag).

*Massive magnetite-rich IF* contains alternating layers of magnetite with detrital volcaniclastic (ash) material (Figs. 2.8c and d). Predominant minerals include euhedral to anhedral fine-grained magnetite and fine-grained chlorite. Magnetite occurs as monomineralic layers with lesser chlorite dominant layers. Chlorite within magnetite-rich layers occurs as fine-grained interlocking grains parallel to layering. Lesser minerals include hematite, sericite, epidote, and vein-hosted carbonate. Hematite occurs on the margins of magnetite grains and very rarely as its own isolated grains.

*Argillite with semi-massive magnetite* contains alternating layers of detrital material and magnetite, chlorite forms monomineralic layers and is intergrown with magnetite, forming most of the matrix of the rock. Banding, or distinct layers is characteristic of this unit, similar to the magnetite-rich IF. Magnetite is euhedral to subhedral, fine-grained with minor bladed grains. Lesser minerals include hematite, carbonate, sericite, ilmenite, epidote, and trace rutile. Rutile and ilmenite, absent in the

previous subgroup, are found along grain boundaries of the magnetite often associated with hematite.

*Argillite with disseminated magnetite* contains alternating layers of detrital material with sparse magnetite (<15%), and dominated by sericite, carbonate, quartz, and chlorite. Banding, or distinct layers of a substantial composition (i.e., layers composed of >50% of one mineral) is less evident in this subgroup relative to the massive magnetite-rich IF and argillite with semi-massive magnetite groups. Sericite occurs as thin, bladed grains with chlorite interstitial to the sericite. Sericite can also form monomineralic layers. Accessory minerals include magnetite, hematite, and epidote.

Lithologically, the subgroup of iron-bearing rocks are intercalated or within cm of each other. They are also commonly interbedded with light to medium grey detrital (ash) material (Figs. 2.8c and d). Milky white quartz-carbonate veins (2-6 cm) that commonly contain albite and iron carbonate cross-cut the iron formation horizon (Fig. 2.8f). Quartz in veins occurs as large grains that are intergrown, are anhedral to subhedral, and intergrown with carbonate grains. Chert nodules occur throughout the horizon. Mineralogically, all three subgroups of the Goldenville horizon contain magnetite, secondary hematite (via martitization of magnetite) with chlorite and epidote interpreted to be alteration products of the volcaniclastic detritus.

*Mineralization:* in the Goldenville iron formation there are two styles of mineralization present in drill core: 1) quartz-carbonate vein associated pyrite (Fig. 2.8f); and 2) laminated sulfide-magnetite±hematite mineralization (Fig. 2.8g). The laminated mineralization contains laminations that are mm-scale and up to 6 cm with locally graded

beds of sulfide and is similar to primary Cambro-Ordovician VMS-style exhalative mineralization found elsewhere on the peninsula (Figs. 2.8g; e.g., Ming deposit). Laminated mineralization contains pyrite and magnetite with lesser chalcopyrite and accessory galena, bornite, and covellite. Pyrite within laminated mineralization is euhedral to subhedral, fractured, and often contain inclusions filled with magnetite, chalcopyrite, and galena. Chalcopyrite and galena is found associated with fine-grained laminated pyrite mineralization and parallel with the surrounding iron formation laminations. Chalcopyrite is predominantly associated with Fe-minerals (e.g., magnetite) and pyrite occurring as: inclusions within pyrite grains; along fractures of pyrite and/or magnetite; and along pyrite and/or magnetite margins (Fig. 2.9b-e). Bornite and covellite are also found spatially associated with chalcopyrite (Fig. 2.9c) within fine-grained laminated mineralization, and replacing chalcopyrite that is interstitial and along the edges of pyrite grains (Fig. 2.9c). Galena is found only associated with pyrite and occurs as inclusions, along fractures, and margins of pyrite grains (Fig. 2.9e-f); notably, galena can only be seen using a scanning electron microscope (SEM).

Quartz-carbonate vein association mineralization consists of coarser grained (>3 mm) euhedral pyrite grains that are found in the selvages of cross-cutting quartz-carbonate veins that are replacing magnetite and/or the edges of chert nodules (Fig. 2.8h and Fig. 2.9a). Gold mineralization is rare within the Goldenville iron formation (see 2.6.2.4); however, when present gold is spatially associated with carbonate-quartz veins and clotted, coarse-grained pyrite (Fig. 2.9d). This pyrite and gold association is

interpreted to have formed from wall rock sulfidation related to Silurian-Devonian orogenic Au mineralization (Figs. 2.8h and 2.9a; e.g., Evans, 2004).

Pyrite mineralization is found elsewhere in the stratigraphy occurring as: 1) pyrite replacement in amygdalites (synvolcanic?; Fig. 2.7c); 2) within pillows and along their rims/rinds/cooled margins (synvolcanic?; Fig. 2.7b); 3) disseminated throughout coarse-grained intrusive rocks (magmatic sulfides?); and 4) less abundantly throughout argillite and lapilli tuff units (diagenetic pyrite?).

## 2.6 Lithogeochemistry

### 2.6.1 Sampling, Analytical Methods, and QA/QC

A total of 115 lithogeochemical samples were analyzed from both outcrop and across 23 diamond drill holes within the Goldenville area (Fig. 2.4). Sampling was focused on significant changes in alteration style/type or lithology (i.e., geologic contacts). Additionally, sampling of the iron formation was targeted for representative samples and where applicable a larger sample was taken to include intervals of mixed material (e.g., localized ash layers). Samples that had evidence of faulting, veining, and shearing were avoided. All drill core samples that were analyzed were collected from the 2016 drill holes from Anaconda Mining Inc. These holes were chosen because they were the freshest core available targeting the Goldenville horizon and contained continuous stratigraphy.

Rock samples were sent to ALS Minerals Laboratories in Vancouver, British Columbia where they were crushed using steel plates and pulverized to a homogenous powder with agate mills to minimize potential metal contamination (e.g., Piercey, 2014).

These were measured for major and trace elements using a combined lithogeochemical characterization package including 1) major elements ( $\text{SiO}_2$ ,  $\text{TiO}_2$ ,  $\text{Al}_2\text{O}_3$ ,  $\text{Fe}_2\text{O}_{3T}$ ,  $\text{Cr}_2\text{O}_3$ ,  $\text{BaO}$ ,  $\text{MnO}$ ,  $\text{MgO}$ ,  $\text{CaO}$ ,  $\text{Na}_2\text{O}$ ,  $\text{K}_2\text{O}$ ,  $\text{P}_2\text{O}_5$ ) a lithium metaborate fusion followed by subsequent dissolution of the bead in an acid and analysis by inductively coupled plasma atomic emission spectroscopy (ICP-AES) ((ME-MS81 package accompanied by ME-ICP06 method; FUS-ICP-AES), 2) trace elements (HFSE: Zr, Hf, Nb, Ta, Th; LFSE: Cs, Rb, Sr; and REE: Y, La, Ce, Pr, Nd, Sm, Eu, Gd, Tb, Dy, Ho, Er, Tm, Yb, Lu) underwent fusion followed by subsequent inductively coupled plasma-mass spectrometry (ICP-MS) (ME-MS81 package; FUS-ICP-MS), and 3) LOI by ignition by gravimetric finished in a furnace (OA-GRA05 method, GRAV). The samples were sent to Ontario Geoscience Laboratories (OGL) in Sudbury, Ontario to obtain metals and volatile elements/metalloids (Li, Be, Ni, Co, Sc, Cu, Pb, Zn, Cd, In, Sn, Mo, Ag, Tl, Sb) and were determined by 4 acid digestion and an ICP-MS finish (IMC-100 method; AD-ICP-MS) with ore grade samples were done by four acid digestion and analysis by ICP-AES (e.g., Zn-OG62, Ag-OG62 in ME-OG62 method; AD-ICP-MS), Additional trace elements were collected at OGL, however, this data was not utilized due to digestion issues (IAC-100 method; AD-ICP-AES; Appendix F). All samples underwent gold preparation using a fire assay (FA) pre-preparation (30g), with an ICP-AES finish (Au-ICP21 method; FA-ICP-AES). The same samples were sent to Geoscience Laboratories for  $\text{CO}_2$  and S by combustion infrared spectrometry (COM-IR).

Accuracy and precision of the major and trace element analyses were monitored using an internal basalt reference material (SLV-MC) and the iron ore certified reference

material IOC-1 from Natural Resources Canada (NRCan)/Canada Centre for Mineral and Energy Technology (CANMET). The latter was selected for its high-Fe matrix that is closer to that of the Goldenville iron formation than silicate reference materials. The former was selected as a basalt reference as the surrounding stratigraphy was primarily mafic volcanic sourced. These reference materials were measured every 20 samples alongside unknowns for QA/QC monitoring (Appendix D). Accuracy is determined by calculating the % relative difference (%RD: ([mean value of the standard selected for this study-reference value of the standard]/[mean value of the standard selected for this study])x100) of the mean gathered from this study to a reference value. Precision is estimated using a relative standard deviation (%RSD) using in-house reporting for SLV-MC and NRCan/CANMET certified values for IOC-1 where available.

The estimated precision for major elements based on SLV-MC (n=4) using a relative standard deviation (%RSD: ([1 standard deviation of value from this study]/[mean value from this study])x100) was <3%. In a similar manner, the estimated precision for trace element abundances is <10%, except for Yb (11.31%). Metal abundances have estimated precision values <10%, except for Cd, and Ag (11.71% and 24%, respectively). Estimated precision for metalloids and volatile elements is <4% for Li and >10% for CO<sub>2</sub>, S, and Sb (58.22%, 65.33%, and 15.93%, respectively). Values outside of the 10% are attributed to concentrations near the limit of detection. Accuracy of SLV-MC from this study compared well with unpublished in-house data determined with the same methods; a %RD for all major and trace elements was < 10% for all major element oxides, trace elements, and metalloids (Appendix D).

The estimated precision for major elements based on IOC-1 (n=4) using a relative standard deviation (%RSD) is <8%, except for TiO<sub>2</sub> and K<sub>2</sub>O (22.22% and 47.14%, respectively), which was attributed to the low concentrations of these elements as a result of the high-Fe composition. Precision estimates for trace elements, calculated in similar manner, is generally over 10% (Appendix D), due to concentrations near the limit of detection. Where above the detection limit of metals, are <10%, except for V, Zn, Ag, Be, and Ga (15.07%, 19.25%, 54.71%, and 11.24%, respectively), due to concentrations near the limit of detection. Estimated precision for metalloids and volatile elements is <10% except for CO<sub>2</sub>, S, Sb, and Li (66.65%, 198.24%, 21.75%, and 10.35%, respectively). Accuracy of IOC-1 (n=4) from this study compare well with NRCAN/CANMET certified values with given %RD values for major oxides is <10% except for K<sub>2</sub>O (86.67%), attributed to concentrations near the limit of detection. Trace element values, where available, compare to certified values with %RD values <10, except for V (24.09%).

## 2.6.2 Results

Representative major and trace element data for each lithofacies (see section 2.5) is summarized in Table 1, whereas the full dataset used in this work for all samples is reported in Appendix E.

### 2.6.2.1 Alteration, metamorphism, and element mobility

The BVP has undergone greenschist facies metamorphism and has undergone multiple episodes of hydrothermal alteration (Tuach and Kennedy, 1978; Castonguay et al., 2009, 2014), which influences what elements can be used for understanding primary geochemical signatures vs secondary alteration/metamorphism-related signatures. Despite

sampling to avoid secondary veins and contacts, all samples have undergone some degree of alteration and/or metamorphism such that several major elements (e.g., SiO<sub>2</sub>, Na<sub>2</sub>O, K<sub>2</sub>O, CaO) and other low field strength element (LFSE; e.g., Cs, Rb, Ba, Sr) are likely to have been mobilized during alteration and metamorphism. Coherent mafic rocks plotted on the chlorite-carbonate-pyrite index (CCPI; [(100(MgO + FeO))/(MgO + FeO + Na<sub>2</sub>O + K<sub>2</sub>O)]) vs Hashimoto alteration index (AI; [(100(K<sub>2</sub>O + MgO))/(K<sub>2</sub>O + MgO + Na<sub>2</sub>O + CaO)]) box plot show minor carbonate, chlorite, and epidote alteration related to hydrothermal processes (Fig. 2.10; Ishikawa et al., 1976; Large et al., 2001), which is consistent with field and petrographic observations of the rocks (e.g., chlorite-epidote ± quartz, calcite; Appendix A and B). The sedimentary and Goldenville horizon samples plotted on the same figure show a similar pattern consistent with hydrothermal processes, which is also consistent with field observations (e.g., chlorite-epidote ± quartz, calcite; Fig. 2.10). Goldenville horizon samples in the magnetite-rich and argillite with semi-massive magnetite subgroups plotting on the very top of the figure is reflective of the sulphide (e.g., pyrite) and Fe-rich (e.g., magnetite) composition (Fig. 2.10). The elements, Al<sub>2</sub>O<sub>3</sub>, TiO<sub>2</sub>, high field strength elements (HFSE; e.g., Zr, Hf, Nb, Ta, Th), and REE are typically immobile under greenschist-facies conditions and used to interpret the primary igneous/sedimentary rocks in this study (e.g., MacLean and Barrett, 1993). To further test for any obvious effects of element mobility on inter-element ratios of the latter elements, plots of alteration indices (Al<sub>2</sub>O<sub>3</sub>/Na<sub>2</sub>O alteration index of Spitz and Darling, 1978) vs key petrogenetic ratios (e.g., Nb/Y, Ti/V, Zr/Y) were constructed to test for any potential influences of hydrothermal alteration/metamorphism (Fig. 2.11). No correlations are observed, supporting the assumption that Al<sub>2</sub>O<sub>3</sub>, TiO<sub>2</sub>, other HFSE, and REE were

immobile, with changes in absolute abundance as a result of mass change, but at constant inter-element ratios (e.g., Spitz and Darling, 1978; MacLean and Barrett, 1993).

#### *2.6.2.2 Mafic volcanic rocks:*

Immobile trace element ratios and REE systematics of the coherent basaltic samples proximal to the Goldenville horizon show there are two distinct geochemical suites, suite 1 and suite 2 (Figs. 2.12 and 2.13); the basalts in these suites show no discernable differences in drill core.

*Suite 1:* the majority of the basalt samples ( $n = 43$  of 48) fall into suite 1 (Table 1). Rocks in this group have  $\text{TiO}_2$  values  $<0.78$  wt.%. These samples also have Nb/Y values indicating they are subalkaline and Zr/Ti values that indicate compositions that range from basaltic to andesitic with the majority showing basaltic affinities (Figs. 2.12a and 2.13a). This suite has arc-like low Ti/V values ( $<20$ ) values that straddle the line between low-Ti island arc tholeiites/boninite (IAT/B, respectively) and IAT (Fig. 2.12b). Both Zr/Y and La/Yb ratios of suite 1 samples show that suite 1 has a tholeiitic affinity with a few samples plotting in the transitional field (Figs. 2.12c and d).

Primitive mantle-normalized multi-element plots (PM; Sun and McDonough, 1989) for suite 1 are shown in Figure 2.13a. The samples show LREE depletion relative to HREE ( $\text{La}_n/\text{Sm}_n = 0.36\text{-}1.23$  [ $n = \text{normalized to primitive mantle values of Sun and McDonough, (1989)}$ ]), with only two samples (348909 and 348094) that have  $\text{La}_n/\text{Sm}_n$  values over 1 (1.13 and 1.23, respectively; Appendix E). This suite has negative Nb anomalies relative to Th and La ( $\text{Nb}_n/\text{Th}_n = 0.03\text{-}0.39$ ) and lower Nb relative to suite 2 ( $\text{Nb} = 0.3\text{-}1.5$  ppm). The values of  $\text{TiO}_2$  and  $\text{Al}_2\text{O}_3$ , along with the HFSE-REE features

above are similar to modern island-arc tholeiites (IAT; Fig. 2.13c; Stolz et al., 1990; Shinjo et al., 2000). On an igneous Th/Yb – Nb/Yb plot, to indicate potential mantle sources for basalts, suite 1 basalts plot with Th/Yb and plot within the volcanic arc array, akin to island-arc tholeiitic rocks (Fig. 2.14).

*Suite 2:* a small subset of samples ( $n = 5$  of 48) that occurs in the uppermost hanging wall to the Goldenville iron formation comprise suite 2. These samples contain higher  $\text{Fe}_2\text{O}_{3T}$  (13.00-15.45 wt.% relative to 5.87-11.95 wt.% of suite 1) and  $\text{TiO}_2$  (2.89-4.10 wt.%) contents. Rocks in this suite have  $\text{Zr}/\text{TiO}_2$  and  $\text{Nb}/\text{Y}$  ratios that straddle values for subalkalic to weakly alkalic basalts (Fig. 2.12a). The higher  $\text{TiO}_2$  values relative to suite 1, results in suite 2 having  $\text{Ti}/\text{V}$  ratios that plot in the OIB field with one sample overlapping the OIB-MORB line in the Ti-V space (Fig. 2.12b).

On primitive mantle-normalized multi-element plots (PM; Fig. 2.13b; Sun and McDonough, 1989), suite 2 samples have slopes that are slightly enriched relative to primitive mantle and have LREE enrichment ( $\text{La}_n/\text{Sm}_n = 1.15-1.36$ ). This suite has positive Nb anomalies relative to Th and La ( $\text{Nb}_n/\text{Th}_n = 1.24-1.64$ ) and higher Nb values ( $\text{Nb} = 15.4-26.6 \text{ ppm}$ ). Notably, there is enrichment in Zr and Hf relative to Nd and Sm in combination with high Nb/Y (Fig. 2.12a) indicating a potential enriched mantle component in their genesis similar to enriched-mid ocean ridge basalts (E-MORB; Fig. 2.13c; Sun and McDonough, 1989). On an igneous Th/Yb – Nb/Yb plot, to indicate potential mantle source, suite 2 rocks plot with a Nb/Yb enrichment relative to suite 1 and are proximal to the E-MORB node (Fig. 2.14).

### *2.6.2.3 Clastic sedimentary rock geochemistry and provenance*

Selected features of the major and trace element data for the volcaniclastic ( $n = 20$ ) and argillite ( $n = 10$ ) samples are shown in Figures 2.15 and 2.16. The iron formation and basalt lithofacies are plotted for reference, as they are the local rocks from which the clastic sedimentary rocks may have been derived (i.e., their provenance). The volcaniclastic and argillite rocks contain predominantly  $\text{SiO}_2$  (41.9-61.9 wt.% and 38.9-77.8 wt.%, respectively),  $\text{Al}_2\text{O}_3$  (11.95-17.35 wt.% and 3.91-16.7 wt.%, respectively), and  $\text{Fe}_2\text{O}_{3T}$  (5.97-17.15 wt.% and 9.64-13.9 wt.%, respectively; mean and  $2\sigma$  in Table 1; Appendix E). Argillite samples contain a greater range of  $\text{TiO}_2$  concentrations (0.15-3.59 wt.%) relative to volcaniclastic samples (0.28-2.23 wt.%).

On the molar A-CN-K-FM ternary plot (Fig. 2.15a; Nesbitt and Young, 1984; Nesbitt, 2003), the volcaniclastic rocks and argillite samples cluster together proximal to the coherent mafic rocks of suites 1 and 2. Additionally, the volcaniclastic and argillite samples have similar Nb/Y, Ti/V, and Zr/Y ratios to the coherent mafic rocks (Fig. 2.11), implying provenance from the mafic rocks. Further, the argillite with disseminated magnetite samples plot in the same area as these clastic dominated samples implying similar provenance from mafic rocks. The A-CN-K-FM plot is also useful in illustrating the Fe-rich composition of magnetite-rich IF and argillite with semi-massive magnetite Goldenville samples, which plot closer to the Fe-Mg apex than any of the other lithofacies (Fig. 2.15a).

On the A-CN-K ternary plot (Fig. 2.15b; Nesbitt and Young, 1984; Nesbitt, 2003), the majority of the samples plot along the  $\text{Al}_2\text{O}_3$  and  $\text{CaO}+\text{Na}_2\text{O}$  edge of the diagram,

consistent with the mafic provenance for the sedimentary rocks. While most samples cluster along the A-CN join, a subset of samples trend towards the A-K join. These samples also have elevated chemical index of alteration (CIA; [CIA =  $100 \times \text{Al}_2\text{O}_3 / (\text{Al}_2\text{O}_3 + \text{Na}_2\text{O} + \text{K}_2\text{O} + \text{CaO})$ ]) values  $>50$ , higher than values typical for fresh mafic rocks, which tend to have CIA values  $\sim 35-50$  (Babechuk et al., 2014; Nesbitt et al., 1992); these features are consistent with greater alteration and accompanying increase of clay minerals in these samples. Samples trending toward A-K join, consisting of argillite with disseminated magnetite, have a minimal Fe-Mg component, as illustrated previously (Fig. 2.15a).

The data for the mafic volcanic rocks, volcaniclastic rocks, argillite, and argillite with disseminated magnetite, are plotted on immobile element provenance plots in Figures 2.14 and 2.16. In samples dominated by a clastic component (e.g., samples indicated by high Al), immobile elements can be used in evaluating provenance (Taylor and McLennan, 1985; Bhatia and Crook, 1986; Nesbitt and Markovics, 1997; McLennan et al., 2003). In the ternary La-Th-Sc space, the basalt, volcaniclastic, and argillite samples plot along a similar trend indicating the detrital component in the latter two groups is from the local mafic rocks (Fig 2.16a). In a Th-La plot, the volcaniclastic samples cluster within the ocean island arc field and a similar grouping is seen in the ternary La-Th-Sc (Figs. 2.16a) where the samples fall along a trendline from the coherent volcanic rocks at the Sc apex towards the La apex within with ocean island arc field (Fig. 2.16b). On the igneous Th/Yb – Nb/Yb plot (Fig 2.14) the volcaniclastic rocks plot in two groups: one with the suite 1 IAT affinity rocks and a second group still within the arc

array, but intermediate between suite 1 and suite 2 rocks with higher Th/Yb, indicating a calc-alkalic like detrital source that may have been derived from the volcaniclastic rocks. On the Th/Yb – Nb/Yb plot, the magnetite-rich IF and argillite with semi-massive magnetite samples follow a similar trend, however, the argillite with semi-massive magnetite samples cluster with the second more calc-alkaline volcaniclastic grouping (Fig. 2.14). Argillite with disseminated magnetite samples overlap suite 2 mafic rocks, volcaniclastic rocks, and argillite rocks on immobile element provenance plots indicating the groups have similar detritus sources (i.e., local mafic suites; Fig. 2.14 and 2.16a-b).

#### *2.6.2.4 Iron formation geochemistry and REE+Y characteristics*

The iron formation lithofacies are subdivided into 3 groups based on a combination of field relationships and Fe-Mn-Al-Ti systematics. Iron formations are considered to have >15wt% Fe as per James (1954), and the only group within the Goldenville horizon meeting that criteria is the massive magnetite-rich IF (n=6) which contains high  $\text{Fe}_2\text{O}_{3T}$  wt.% (53.80-68.80; average = 62.58), high Fe/Al molar ratios (10.80-23.57; average = 13.62), and high  $(\text{Fe}+\text{Mn})/(\text{Fe}+\text{Mn}+\text{Al}+\text{Ti})$  ratios (0.91-0.96; average = 0.92). The second subgroup, argillite with semi-massive magnetite (n=10), has lesser Fe with lower  $\text{Fe}_2\text{O}_{3T}$  wt.% (15.15-41.10; average = 28.30), lower Fe/Al molar ratios (1.15-4.37; average = 2.50), and lower  $(\text{Fe}+\text{Mn})/(\text{Fe}+\text{Mn}+\text{Al}+\text{Ti})$  ratios (0.56-0.81; average = 0.71). The third subgroup, argillite with disseminated magnetite (n=14), has the lowest  $\text{Fe}_2\text{O}_{3T}$  wt.% (12.50-20.40; average = 11.02), Fe/Al molar ratios (0.24-0.78; average = 0.82), and  $(\text{Fe}+\text{Mn})/(\text{Fe}+\text{Mn}+\text{Al}+\text{Ti})$  ratios (0.19-0.40; average = 0.34) of all samples in the Goldenville horizon.

The major element composition of the Goldenville horizon magnetite-rich IF and argillite with semi-massive magnetite subgroups is dominated by  $\text{Fe}_2\text{O}_{3T}$  and  $\text{SiO}_2$  (11.6-36.2 wt.% and 37.0-58.6 wt.%, respectively; Table 2). The  $\text{MnO}$  and  $\text{Al}_2\text{O}_3$  is higher in the argillite with semi-massive magnetite samples (1.99-7.44 wt.% and 6.94-10.35 wt.%, respectively) relative to the magnetite-rich IF samples (0.37-1.45 wt.% and 1.73-4.94 wt.%; Fig. 2.17c). The composition of the argillite with disseminated magnetite ( $n=14$ ) group has a lower concentration of  $\text{Fe}_2\text{O}_{3T}$  with more variable  $\text{SiO}_2$  (38.9-77.8 wt.%), and generally the highest  $\text{Al}_2\text{O}_3$  (3.91-16.7 wt.%) relative to the magnetite-rich IF and argillite with semi-massive magnetite groups. The  $\text{MnO}$  within the argillite with disseminated magnetite group is the lowest relative to the other groups (0.36-0.68 wt.%).

The Al-Ti-Fe-Mn relationships of the Goldenville horizon lithofacies (Section 2.5.2) are illustrated further on  $\text{Fe}/\text{Ti}$  vs  $\text{Al}/\text{Al}+\text{Fe}+\text{Mn}$  and Fe-Al-Mn ternary Boström-type plots (Fig. 2.17a-b) and in Fe-Mn spaces (Figure 2.17c). In these plots, the  $\text{Al}+\text{Ti}$  and  $\text{Fe}+\text{Mn}$  components are proxies for the elements derived from detrital and hydrothermal sources, respectively. The Fe-Al-Mn (Fig. 2.17a) and  $\text{Fe}/\text{Ti}$  vs.  $\text{Al}/\text{Al}+\text{Fe}+\text{Mn}$  (Fig. 2.17b) plots show the 3 sub-divisions of Goldenville horizon samples into the magnetite-rich IF (greatest hydrothermal component,  $\geq 80\%$  hydrothermal components), argillite with semi-massive magnetite (intermediate hydrothermal and detrital component, between 35 and 70 % hydrothermal components), and argillite with disseminated magnetite (greatest detrital component). This effectively illustrates the Goldenville horizon contains true IF (magnetite-rich IF), an argillite with elevated Fe (argillite with disseminated magnetite), and the mixture of these two end member units

(argillite with semi-massive magnetite). A plot of  $\text{Fe}_2\text{O}_{3T}$  wt.% vs.  $\text{MnO}$  wt.% (Fig. 2.17c) illustrates that both the magnetite-rich IF and argillite with disseminated magnetite groups have significant  $\text{MnO}$ , but the latter group has much higher  $\text{MnO}$  contents (also seen in a deviation from the Al-Fe join towards the Mn apex in Fig. 2.17a).

The Goldenville horizon samples have  $\Sigma\text{REE}$  contents where magnetite-rich IF (98.21-215.22 ppm) and argillite with disseminated magnetite (80.43-217.17 ppm) have similar ranges, whereas argillite with semi-massive magnetite generally have higher  $\Sigma\text{REE}$  contents (203.38-314.09 ppm). These units have higher total REE values relative to surrounding lithologies, specifically the suite 1 mafic volcanic rocks (53.42-86.51 ppm) and the volcaniclastic rocks (30.05-149.83 ppm); they have similar  $\Sigma\text{REE}$  values to the suite 2 mafic volcanic rocks (176.92-291.19 ppm) and argillite (70.26-249.25 ppm) samples. On plots of  $\Sigma\text{REE}$  vs.  $\text{MnO}$  wt.% and  $\text{Fe}_2\text{O}_{3T}$  wt.%, and multiple observations can be made (Fig. 2.18). Firstly, samples with the highest  $\Sigma\text{REE}$  have the highest  $\text{MnO}$  (Fig. 2.18b), notably the argillite with semi-massive magnetite samples. Secondly, abundances of  $\Sigma\text{REE}$  in the surrounding lithology relative to  $\text{MnO}$  are similar to the values found in the Goldenville horizon, (Fig. 2.18b), indicating that  $\text{MnO}$  could be important for overall  $\Sigma\text{REE}$  abundances.

On plots of  $\Sigma\text{REE}$  vs. elements indicative of detrital material (e.g., Nb, Ti, and Zr), two important observations are apparent. First, the majority of the argillite with disseminated magnetite samples overlap suite 2 volcanic rocks, volcaniclastic rocks, and argillites, suggesting that the detritus in these samples is from the local units (Fig. 2.19). A minor population of argillite with disseminated magnetite samples have higher REE

abundances decoupled from the aforementioned array. Second, the argillite with semi-massive magnetite and magnetite-rich IF samples plot with distinct horizontal arrays with low Nb and Zr consistent with minimal detrital REE-HFSE contributions.

The rare earth element and yttrium (REE+Y) data for the Goldenville horizon are shown in post-Archean Australian Shale (PAAS)-normalized (Pourmand et al., 2012) plots in Figure 2.20. The ratios  $Tb_{sn}/Yb_{sn}$  and  $Pr_{sn}/Tb_{sn}$  ( $sn$  = shale normalized) are used as MREE/HREE and LREE/MREE monitors, respectively, where values  $> 1$  in either ratio indicate MREE enrichment over HREE and LREE enrichment over MREE, respectively and values  $< 1$  the opposite. The magnetite-rich IF REE patterns (Fig. 2.20a) are depleted in LREE ( $Pr_{sn}/Tb_{sn} = 0.37\text{-}0.62$ ) and slightly enriched in MREE ( $Tb_{sn}/Yb_{sn} = 0.96\text{-}1.13$ ) relative to PAAS values and have absent to negative Ce anomalies (Fig. 2.21a). The Bau and Dulski (1996)  $Ce_{sn}/Ce_{sn}^*$ - $Pr_{sn}/Pr_{sn}^*$  cross-plot in Figure 2.21a show that the Ce anomalies are true negative Ce anomalies ( $Pr_{sn}/Pr_{sn}^* > 1$ ;  $Pr_{sn}/Pr_{sn}^* = 1.03\text{-}1.22$ ). The argillite with semi-massive magnetite patterns (Fig. 2.20b) are flatter with less LREE/MREE depletion compared to the magnetite-rich IF group ( $Pr_{sn}/Tb_{sn} = 0.43\text{-}0.81$ ) and more MREE enrichment ( $Tb_{sn}/Yb_{sn} = 0.95\text{-}1.26$ ) and have positive Ce anomalies ( $Pr_{sn}/Pr_{sn}^* < 1$ ;  $Pr_{sn}/Pr_{sn}^* = 0.77\text{-}0.89$ ; Fig. 2.21a). The argillite with disseminated magnetite REE patterns (Fig. 2.20c) show this group has the greatest LREE depletion ( $Pr_{sn}/Tb_{sn} = 0.18\text{-}0.70$ ) of the Goldenville horizon with variable MREE/HREE slopes ( $Tb_{sn}/Yb_{sn} = 0.59\text{-}1.37$ ). Ce anomalies, along with the REE patterns, of the argillite with disseminated magnetite subgroup have some overlapping patterns with the magnetite-rich

IF and argillite with semi-massive magnetite subgroups with both small negative Ce anomalies and positive Ce anomalies ( $\text{Pr}_{\text{sn}}/\text{Pr}_{\text{sn}}^* = 0.79\text{-}1.04$ ; Fig. 2.21).

The magnetite-rich IF and argillite with semi-massive magnetite groups of the Goldenville horizon have small positive Eu anomalies ( $\text{Eu}_{\text{sn}}/\text{Eu}_{\text{sn}}^*>1$ ;  $(\text{Eu}_{\text{sn}} = \text{Sm}_{\text{sn}}^{2*}/\text{Tb}_{\text{sn}})^{1/3}$ ; Lawrence et al. 2006) (1.13-1.35 and 1.21-1.52, respectively), whereas the argillite with disseminated magnetite samples have either negligible or positive Eu anomalies, similar to the surrounding iron formation (0.98-1.63).

The Y/Ho mass ratios are sub-chondritic ( $\text{Y}/\text{Ho} < 27$ ; Bau, 1996; Pack et al. 2007) in both the magnetite-rich IF (22.3-24.2) and argillite with semi-massive magnetite (19.1-23.2) samples, whereas the argillite with disseminated magnetite (22.2-30.8) samples have a wider range from sub-chondritic to super-chondritic (Fig. 2.21d;  $\text{Y}/\text{Ho} \sim 27$ ; Bau, 1996). These Y/Ho values are relatively consistent with values in the surrounding lithologies - suite 1 (22.2-30.7), suite 2 (24.5-27.2), volcaniclastic rock (23.2-28.5), and argillite (21.1-30.5) samples.

#### *2.6.2.5 Goldenville horizon transition, base, and precious metal distribution*

The variations in abundances of selected base and transition metals (V, Ni, Pb, Cu, Co, Zn, Au) in the Goldenville and surrounding units are illustrated in plots of individual elements vs.  $(\text{Fe}+\text{Mn})/(\text{Fe}+\text{Mn}+\text{Al}+\text{Ti})$  ratios to separate out the iron formation samples with the clearest evidence for sulfide mineralization (Fig. 2.22).

The concentrations for most base and transition metals within the Goldenville horizon are similar to concentrations found in the surrounding lithology (Table 2). Within

the Goldenville horizon itself, concentrations of V, Ni, Pb, and Co are consistent throughout each subgroup (Table 2.2; Fig. 2.22a-c). Copper concentrations are slightly enriched in the magnetite-rich IF and argillite with semi-massive magnetite (7.4-1185 ppm and 10.3-207.0 ppm, respectively) subgroups relative to the argillite with disseminated magnetite (8.6-672.0 ppm; Fig. 2.22d). Zinc concentrations have some higher values in the argillite with semi-massive magnetite (91-326 ppm) relative to magnetite-rich IF samples (73.0-265 ppm); however, both subgroups are enriched relative to argillite with disseminated magnetite (46-135 ppm; Fig. 2.22e).

Gold concentrations of the Goldenville horizon and surrounding stratigraphy varies from values near detection limit (0.001 ppm) to 0.515 ppm, reflective of the limited gold found in thin section and SEM (Fig. 2.9d; Fig. 2.22f). Au values beyond the background value (0.001-0.009 ppm) are found throughout the Goldenville horizon, correlating with the higher sulfidation seen in the Fe-rich rocks (i.e., pyrite mineralization; Fig. 2.22f). The samples with the highest Au values occurred in samples collected from depths of 20.9 meters to 119.9 meters indicating there is no one Goldenville horizon lens that is preferential to gold concentrations (Fig. 2.22f; Appendix E). Additionally, these samples came from six different drill holes indicating in no one place the gold concentrated within the Goldenville horizon as observed from the available data.

## **2.7 Discussion**

### **2.7.1 Stratigraphic Relationships Relative to the Goldenville Iron Formation**

The Goldenville horizon is interpreted to mark the Cambrian-Ordovician (~488 Ma; Dunning and Krogh, 1985) transition from the Betts Cove ophiolite complex to the Snooks Arm Group cover sequence (Skulski et al., 2010). This transition is distinguished by a 40-60 m thick unit composed of a local basal conglomerate cemented by jasper (e.g., the Kidney Pond conglomerate in the Flatwater Pond area; Fly Pond and equivalents elsewhere on the peninsula), turbidites, and a jasper-magnetite iron formation (Nugget Pond and Goldenville horizon), which lies in sub-conformable contact with the underlying Betts Cove Complex (Bédard, 1999; Skulski et al., 2009). In the type locality the footwall of the Nugget Pond horizon consists of island arc tholeiitic basalts of the Mount Misery Formation, whereas the hanging wall comprises Fe-Ti-rich tholeiitic basalts of the Scrape Point Formation (Bédard, 1999; Bédard et al., 2000; Skulski et al., 2009). The Scrape Point Formation signatures is found in the upper 75 meters of the drill holes logged as a part of this work. Signatures of the Mount Misery Formation are found above and below Scrape Point Formation signatures indicating a more complex relationship including intercalated units, folded units, and or a faulted relationship at this locale (Fig. 2.23).

In the Goldenville area, the footwall basalts (suite 1) to the iron formation have island arc tholeiite (IAT) affinities similar to the Mount Misery Formation (Figures 2.10-2.13); however, the majority of the hanging wall samples also are IAT (suite 1), which differs from the type locality in the Betts Cove Complex. At this location, suite 2 rocks

have niobium values greater than primitive ocean-arc tholeiitic basalts ( $\text{Nb} = \sim 3$  ppm), giving a possible classification as Nb-enriched basalts (NEB; Pearce 2008; Hastie et al., 2011). Further, the suite 2 rocks with Fe-Ti enrichment (Figs. 2.10-2.13) that are similar to the Scrape Point Formation (e.g., Jenner and Fryer, 1980; Coish, 1989; and Bédard et al., 2000) are located in the upper part of the hanging wall of the Goldenville horizon and not directly at the hanging wall contact as seen in the type locality for the Nugget Pond horizon (Fig. 2.6). Furthermore, in the Nugget Pond type locality, the footwall contains the Kidney Pond conglomerate with clasts of the Mount Misery Formation, whereas the hanging wall is absent of breccia or hyaloclastite (Bédard et al., 2000). This relationship is in contrast with the Goldenville horizon, which contains basaltic hyaloclastite in both its footwall and hanging wall (Fig. 2.6).

These observations suggest that the Nugget Pond and Goldenville iron formations may not be correlative units as previously suggested, and that in the BVP the presence of iron formation alone is not a universal stratigraphic marker marking the transition from the Betts Cove Complex and Snooks Arm cover sequence (Fig. 2.21). These iron formations represent stratigraphically distinct horizons where the Goldenville horizon exists lower in the stratigraphy representing hydrothermal activity synchronous with deposition of the Mount Misery Formation, whereas the Nugget Pond horizon reflects hydrothermal activity post-Mount Misery Formation but before deposition of the Snooks Arm cover sequence.

## **2.7.2 Evaluating Detrital, Hydrothermal, and Hydrogenous Components in the Goldenville horizon**

Exhalative iron formation mineralogy and geochemistry reflects the varying contributions from detrital material (e.g., volcanic debris or continental sediments), elements precipitated from hydrothermal vent fluids, and elements scavenged from seawater on the surface of minerals precipitated in the water column and after deposition on the seafloor (Boström and Peterson, 1966; Gross, 1980, 1983; Rudnicki, 1995; German and Von Damm, 2003; Bolhar et al., 2005). The latter of these can potentially provide insight into the oxygenation state of the ocean within the basin at the time of iron formation deposition (e.g., Danielson et al., 1992; Slack et al., 2009; Och and Shields-Zhou, 2012). The relative contributions of detritus, hydrothermal fluids, and seawater scavenged elements in the lithogeochemical signatures of the Goldenville iron formation will be evaluated below.

On a Boström-type plot, adopting the East Pacific Rise metalliferous sediment mixing line, the Goldenville horizon has variable hydrothermal inputs with the magnetite-rich IF having  $\geq 80\%$  hydrothermal components, the argillite with semi-massive magnetite between 35 and 70 %, and the argillite with disseminated magnetite dominated by detritus (Fig. 2.17b). The presence of detritus in the iron formations is not surprising given their bounding stratigraphy (Fig. 2.6) and associated evidence for a volcanically active basin. The samples with the highest  $(Fe+Mn)/(Fe+Mn+Al+Ti)$  ratios generally correspond to those with the highest abundance of magnetite, which occurs in fine-grained laminae. These laminae, interbedded with laminated sulfide-rich zones (pyrite,

chalcopyrite, and galena; Fig. 2.9), are common features in exhalative iron formations (Rudnicki, 1995; Peter, 2003; Peter et al., 2003). The pyrite and lesser chalcopyrite and galena are interpreted to represent settling from hydrothermal vent fluids (Fig. 2.8c, g, and h; e.g., Boström, 1973). There is also minor enrichment in Cu and Zn in the magnetite-rich IF and argillite with semi-massive magnetite samples relative to argillite with disseminated magnetite, reflecting hydrothermal Cu-Zn addition and consistent with the observed mineralogy of the Fe-rich samples (Fig. 2.22d and e).

On discrimination diagrams using the aforementioned elements (Fig. 2.16), the Goldenville horizon sedimentary rocks show mixed provenance where there is overlap in the trends between the argillite with disseminated magnetite and the remaining Goldenville horizon groups (magnetite-rich IF and argillite with semi-massive magnetite) suggesting similar detritus sources. Detritus-rich samples also overlap the suite 1 basalts and the volcaniclastic rocks, with minor exceptions, in Th-La-Sc and Th-La space (Fig. 2.16a-b), and have low TiO<sub>2</sub> contents, both of which are consistent with derivation of the detritus in the iron formations from the Mount Misery Formation flows and volcaniclastic rocks. In Th/Yb-Nb/Yb space (Fig. 2.16c) many iron formations overlap the volcaniclastic samples and cluster with the suite 1 and Mount Misery Formation volcanic rocks; however, a subset, including many of the argillite with semi-massive and disseminated magnetite samples have higher Th/Yb requiring a more Th-rich source, potentially indicating a more felsic or continental crustal component in these samples. This can likely be attributed to a felsic contribution from the volcanic ash within the

volcaniclastic rock unit that often occurs interbedded with the iron formation, in addition to clays found within both units.

Rare earth elements and Y can be controlled by both detrital minerals and adsorption of a dissolved fraction of these elements from seawater, hydrothermal fluids, or a mixture of both on hydrothermally derived oxide particles (Klinkhammer et al., 1983; German et al., 1990; Bau and Dulski, 1996). However, an issue with deciphering hydrothermal and/or hydrogenous REE+Y signatures in iron formation is that even small percentages (<3%) of detrital material can overprint them due to the generally high REE abundance in detritus compared to chemical precipitates (Shimizu and Masuda, 1977; Bau, 1993; Kamber and Webb, 2001). Therefore, detritus-rich samples are expected to have limited utility for reconstructing preserved REE+Y patterns that reflect hydrothermal fluids or seawater. While the Goldenville horizon samples all have some influence of detrital material, as indicated by the  $(\text{Fe}+\text{Mn})/(\text{Fe}+\text{Mn}+\text{Al}+\text{Ti})$  ratios (Fig. 2.17b), decoupling of the total REE budget from detritus control lines (Fig 2.17) for the magnetite-rich IF (<20% detritus) and argillite with semi-massive magnetite (30-65% detritus) groups suggests a dominant role of oxide-scavenged REE despite the relatively high proportion of detritus. This is interpreted to be a result of the mafic rock-dominated detritus sources that are generally poor in REE, but the REE enrichment in the magnetite-rich IF and argillite with semi-massive magnetite groups could also implicate significant residence time of hydrothermally-derived oxide particles in the water column and/or continued scavenging of dissolved REE on mineral surfaces after deposition on the seafloor (Fig. 2.19; Piper, 1974; Byrne and Kim, 1990; Mills et al., 2001; Menendez et

al., 2017). Similarly, the Ce anomalies preserved in these sample groups cannot be controlled by detritus since the main detritus sources (i.e. as represented by the argillites, volcaniclastic rocks, and volcanic rocks) generally do not have measurable Ce anomalies ( $\text{Pr}_{\text{sn}}/\text{Pr}_{\text{sn}}^*$ : 0.73-1.11, average 0.93) and the separation of Ce from other LREE requires a  $\text{Ce}^{3+}/\text{Ce}^{4+}$  redox transition in low-T aqueous environments that typically involves Mn-(oxy)(hydr)oxides (Bau, 1999; Ohta and Kawabe, 2001; Tostevin 2021). In other words, the Ce anomalies record a hydrogenous signature despite the high proportion of detritus, and it is argued below that both groups (argillite with semi-massive magnetite samples with positive Ce anomalies; magnetite-rich IF samples with negative Ce anomalies) are important to deciphering seawater oxygenation at the time of IF deposition.

### **2.7.3 Evaluating Cerium for Paleoredox; Inferring Conditions in the Humber Seaway throughout the Cambrian-Ordovician**

The magnetite-rich IF group of the Goldenville horizon has the lowest detrital contribution and these samples have a range of neutral to true negative Ce anomalies ( $\text{Pr}_{\text{sn}}/\text{Pr}_{\text{sn}}^*$ : 1.03-1.22). The presence of negative Ce anomalies is similar to patterns observed in modern vent-proximal deep oceans waters (e.g. Klinkhammer et al. 1983) and suggests that the Fe-particles scavenged REE+Y from oxygenated seawater that was depleted in Ce relative to La and Pr due to oxidation of  $\text{Ce}^{3+}$  to  $\text{Ce}^{4+}$  and its preferential retention on oxide-minerals that are stable throughout the full water column, similar to the modern open oceans (e.g., Alibo and Nozaki, 1999). In contrast, the lower Fe (but higher Mn) argillite with semi-massive magnetite group of the Goldenville horizon has significantly greater detrital input, but all samples have positive Ce anomalies ( $\text{Pr}_{\text{sn}}/\text{Pr}_{\text{sn}}^*$ :

0.77-0.89). Positive Ce anomalies are observed in modern redox-stratified water bodies where Ce<sup>4+</sup> preferentially scavenged on oxide minerals is re-released upon reductive dissolution of the oxides below a water column redoxcline (De Baar et al., 1988; Bau et al., 1997; De Carlo & Green, 2002). Positive Ce anomalies are a common feature of Paleoroterozoic-Mesoproterozoic (exhalative and continental margin) iron formation (Planavsky et al. 2010; Slack et al. 2007, 2009) where these signatures are widely adopted as evidence for redox-stratified open ocean waters at the time. Interpreting the argillite with semi-massive magnetite group samples in a similar manner (i.e., as recording evidence for reducing bottom waters underlying an oxic upper water column) presents an apparent redox paradox for the ancient seawater conditions recorded by the Goldenville samples. Specifically, if both groups of samples are considered passive recorders of near-vent deep ocean water REE+Y budgets, the negative Ce anomalies in the magnetite-rich IF samples would suggest fully oxygenated bottom water conditions where Mn-(oxy)(hydr)oxides were stabilized to the point of delivery to the seafloor, whereas the argillite with semi-massive magnetite samples would suggest suboxic to anoxic bottom waters where Mn-(oxy)(hydr)oxides were undergoing reductive dissolution and releasing Ce back to the water column. The two sample groups are intercalated and/or in close physical proximity (within cm) to one another, such that it is unlikely that they record oceanic conditions with significant time gaps between them or even different topographical depressions/areas that are likely to record different highly localized redox conditions (Ohta and Kawabe, 2001; Tostevin 2021).

The apparent redox paradox generated by both positive and negative Ce anomalies can be reconciled by the argillite with semi-massive magnetite samples recording a localized particle scavenging signature controlled by mineralogy rather than a wider suboxic to anoxic basin signature, which appears to be revealed through the  $\text{Fe}_2\text{O}_3$ - $\text{MnO}$ -Ce relationships of the samples. The significant correspondence of the higher Mn abundance with the positive Ce anomalies in the argillite with semi-massive magnetite samples suggests that these samples record preferential accumulation of Ce onto Mn-oxide particle surfaces. Manganese particles, relative to Fe particles, have a strong preferential adsorptive affinity for Ce following oxidation of  $\text{Ce}^{3+}$  to  $\text{Ce}^{4+}$  (e.g., Calvert and Pedersen, 1993; Alibo and Nozaki, 1999; Ohta and Kawabe, 2001; Tostevin, 2021) such that the more Mn-rich samples are interpreted to have been deposited in an oxygenated environment where dissolved Mn (sourced primarily from hydrothermal fluids; Cowen et al., 1986; Hannington et al., 1995; German and Von Damm, 2003 ) accumulated more Ce relative to the other LREE and also relative to the Fe-rich samples. The inferred Mn-(oxy)(hydr)oxide-dominated scavenging process could have produced the positive Ce anomalies within a fully oxygenated deep water column, similar to what is observed in some suspended oceanic particulates and hydrogenetic crusts and nodules on the modern seafloor (Sholkovitz et al., 1994; Bau et al., 2014). This model is comparable to one from Otake et al. (2021) for ferruginous sedimentary rocks from the VMS deposits of the Hokuroku district where some Mn-rich samples (containing a mixture of Mn-oxides, carbonates, and silicates, with the latter two groups interpreted to have formed by partial reduction of Mn-oxides) retained positive Ce anomalies in a vent-proximal hydrothermal environment.

While the Ce anomaly variations in the Goldenville samples can be explained as a hydrogenous signature of dissolved REE scavenged from oxic deep waters, several other REE+Y features of the samples present complications to this interpretation. The negative Ce anomalies of the magnetite-rich IF samples are best explained as a signature of oxic seawater, but other features expected of a shale-normalized REE+Y pattern in oxic water are absent (i.e., positive La, Gd, and Y anomalies, magnitude of LREE>HREE depletion). The typical seawater REE+Y pattern features are also absent in the argillite with semi-massive magnetite samples with positive Ce anomalies. In the case of both sample groups, an important factor could be that the dissolved REE+Y budget of the water scavenged by oxide particles was a mixture of ambient oxic seawater and hydrothermally sourced REE+Y devoid of seawater anomalies (German et al., 1990; Bau and Dulski, 1996; Menendez et al., 2017). In this case, the hydrothermal fluid would have to be assumed to have been low-T since all samples also do not have the strong positive Eu anomalies that are characteristic of high-T hydrothermal fluids (Fig. 2.20; Michard et al., 1983; Klinkhammer et al., 1994; Douville et al., 1999). An additional factor is that during adsorption of REE+Y to the surface of Fe- and Mn-(oxy)(hydr)oxides, features such as the LREE>HREE depletion in the dissolved budget of seawater can be gradually erased due to the preferential adsorption of LREE>HREE on the oxide surfaces (Slack et al., 2007; Ohta and Kawabe, 2001). Finally, the high detritus content, especially for the argillite with semi-massive magnetite samples, can still be a contributor to the overall sample REE+Y budgets that is still a mixture between a hydrogenous/hydrothermal component and the detritus component. Considering this factor amplifies the magnitude of the Ce anomalies likely to be associated with only the hydrogenous/hydrothermal REE+Y

budget of the samples. However, more detailed assessment of an end-member hydrogenous/hydrothermal signature by calculating out a detritus component or undertaking a more targeting extraction of hydrothermal mineral-dominated sub-samples was beyond the scope of this work.

Independent of the complications evident in the full REE+Y patterns of the Goldenville horizon subgroups, the preferred interpretation of the Ce anomalies would require that the bottom waters into which the hydrothermal fluids vented at the time of forming the exhalative units had sufficient O<sub>2</sub> to form Mn-(oxy)(hydr)oxides and sustain Ce as Ce<sup>4+</sup> (e.g., Tostevin 2021). In other words, the implication is that the Humber seaway was fully oxygenated down to bottom waters in the Cambrian-Ordovician. The Cambrian and Ordovician were times where the Earth experienced large-scale biological and climate changes, the emergence of planktonic graptolites, conodonts, new trilobite groups, and warmer oceanic conditions (Webby et al., 2003; Landing, 2012a, 2012b; Terfelt et al., 2014). Despite the indication that ocean conditions were suitable for a sustained biodiversification there have been very few studies to define the redox state across the Cambrian-Ordovician boundary (Landing, 2012a, 2012b; Azmy et al., 2015). For example, Dictyonema shales in Norway indicate anoxic waters at deposition, whereas shales of the Global Stratotype Section and Point (GSSP) at Green Point, western Newfoundland indicate reducing conditions at deposition (Berry et al., 1986; Tripathy et al., 2014; Azmy et al., 2015). Additionally, studies on mudstones along the Laurentian continental slope that suggest periods of very low oxygen (i.e., dysoxic) with intervals of anoxic conditions (Landing 2012a and references therein). A recent model by Tripathy et

al. (2014) suggests that conditions at the margins of Laurentia and Baltica were anoxic, whereas basins with colder water (e.g., Avalonia) were less reducing. Based on stratigraphic relations outlined above the Goldenville horizon has to be between 488-483 Ma of the late Cambrian to early Ordovician (Fig. 2.3; Dunning and Krogh, 1985; Ramezani et al., 2000; Skulski et al., 2010). Thus, the evidence of the Ce anomalies and inferred stabilization of Mn-(oxy)(hydr)oxides from this study, implying that the peri-Laurentian Humber seaway that hosted the Goldenville horizon was oxygenated in the late Cambrian to early Ordovician (~488-483 Ma), contradicts the more anoxic conditions suggested previously (e.g., Tripathy et al., 2014, Azmy et al., 2015). The perspective from the Goldenville horizon is from the deep marine environment, whereas most previous studies made inferences from shallow marine environments; the contradicting results appear to point to more complicated redox architecture in ocean basins at the time, rapid swings in redox-state, proxy biases in different depositional environments, or some combination of all of these factors. The presence of banded iron formation distal from any VMS deposit in the Cambrian (Li et al. 2018) suggests ferruginous (and thus anoxic) bottom water conditions may have prevailed in the lead up to the depositional timeframe of the Goldenville horizon. Further assessment of oceanic redox in the Cambrian and Ordovician (and into the younger Phanerozoic) will benefit from further research that considers the perspective offered from deep marine deposits such as exhalative iron formations.

#### **2.7.4 Implications for Exploration; Au and Base Metal Mineralization**

Iron formations are spatially associated with some VMS deposits and orogenic Au deposits globally. For example, many deposits in the Bathurst Mining Camp have laterally extensive iron formations that occur immediately in the hanging wall to massive sulfides and at a similar stratigraphic level regionally (e.g., Peter, 2003). In the case of orogenic Au deposits, some consist of structurally hosted deposits hosted in both veins and iron formations where the iron formations are interpreted to have provided an Fe-rich host rock that destabilized  $\text{Au}(\text{HS})_2^-$  molecules in hydrothermal fluids via wall rock sulfidation leading to the precipitation of Au (e.g., Phillips and Powell, 2010).

Previously, Fitzpatrick (1981) indicated the Au mineralization in the Goldenville iron formation was synchronous with the iron formation deposition (i.e., syngenetic). Together with previous workers (Snelgrove, 1935; Watson, 1947; Frew, 1971; Hibbard, 1983), it was proposed that the gold-bearing quartz veins were a result of remobilization of gold that was previously deposited within the iron formation (Evans, 1999, 2004). A syngenetic origin as proposed is inconsistent with several features documented more fully in this study. In particular, mineralization is structurally controlled and consists of gold that is hosted by iron formation but spatially associated with coarse grained annealed pyrite with magnetite inclusions found along the selvages of cross-cutting quartz veins, indicative of wall-rock sulfidation (Fig. 2.8f). The Goldenville horizon is also spatially associated with the Scrape thrust, a splay off the BVL, and shares a spatial association and similar hydrothermal footprint to other orogenic Au deposits in the peninsula found along that same structure (Figs. 2.1-2.3; Kirkwood and Dubé, 1992; Bédard, 1999; Evans,

2004; Skulski et al., 2010). Collectively, the latter features are more consistent with the gold having been introduced during regional metamorphism and deformation, rather than from syngenetic VMS-related gold and subsequent remobilization.

The results of this study demonstrate that the Goldenville horizon was deposited entirely within the Mount Misery Formation in the late Cambrian to early Ordovician (~488-483 Ma; Fig. 2.3; Dunning and Krogh, 1985; Skulski et al., 2010) and is stratigraphically below the Nugget Pond horizon, but stratigraphically above the ~487 Ma Ming Cu-Zn-Ag-Au VMS deposit (Skulski et al., 2009, 2010). Laminated, fine-grained Cu-Zn bearing sulfide mineralization (e.g., Cu and Zn; Fig. 2.20d and e) with chalcopyrite, galena, sphalerite) and hydrothermal lithogeochemical signatures of the iron formation are consistent with the Goldenville horizon having formed as an exhalative VMS horizon (e.g., Peter, 2003); it is possible that it represents a hydrothermal sedimentary unit distal to VMS in the Rambler-Ming district. Gold in the Goldenville horizon, however, was not related to a VMS event and appears to be orogenic.

The work herein demonstrates that the Goldenville and Nugget Pond horizons represent distinct stratigraphic units, both of which host orogenic Au mineralization; however, there is a marked difference in historic gold production from these horizons with the Nugget Pond horizon having produced more gold than the Goldenville horizon (Evans, 2004; Sparrow et al., 2017). Further work will be needed to determine why the Nugget Pond horizon was more Au-productive and to evaluate whether this is a function of genetic processes or an artifact reflecting variable levels of exploration and development.

## 2.8 Conclusion

The key conclusions for the Goldenville horizon and this work include:

- 1) The Goldenville iron formation is hosted within basalts with IAT affinities interpreted to be the Mount Misery Formation. They are stratigraphically below the transition from IAT basalts to those with E-MORB signatures interpreted to the Scrape Point Formation. Given that the Nugget Pond horizon is at the stratigraphic contact between IAT of the Mount Misery Formation and overlying MORB-like rocks of the Scrape Point Formation, it suggests that the Goldenville iron formation and Nugget Pond horizons are not stratigraphically equivalent and that the Goldenville horizon is stratigraphically below the Nugget Pond horizon.
- 2) Iron-rich rocks in the Goldenville horizon are subdivided based on their Fe-Mn-Al contents, into iron formations, Fe-rich argillites, and argillites with disseminated magnetite. The Fe-Mn features of the Fe-rich rocks influenced the REE systematics of the rocks where Mn-rich rocks have positive Ce anomalies on shale normalized REE plots and Fe-rich rocks have negative Ce anomalies. Iron formations with low Mn have negative Ce anomalies consistent with adsorption from oxic seawater. Manganese-rich rocks have positive Mn anomalies, which are traditionally interpreted to reflect anoxic/suboxic ocean conditions; however, we suggest that this positive anomaly is from preferential adsorption of Ce by Mn and the subsequent stabilization of Ce as  $Ce^{4+}$  in Mn-rich layers. Both features

indicate that the Goldenville iron formation interacted with oxygenated water in the Humber seaway, indicating oxygenated bottom waters during the Cambrian-Ordovician (~488-483 Ma).

- 3) Regional structures, regional greenschist-facies metamorphism and wall rock sulfidization relationships between quartz veins and the iron formation indicate that the gold mineralization in the Goldenville deposit was epigenetic and not synchronous with iron formation deposition as previously suggested.
- 4) Results in this study demonstrate that the Goldenville horizon is stratigraphically below the Nugget Pond horizon, and is likely at a stratigraphic position above the Ming VMS deposit. However, additional work will be needed to assess why the two horizons have varying Au and base metal mineralization.

## References

- Alibo, D.S., and Nozaki, Y., 1999, Rare earth elements in seawater: Particle association, shale-normalization, and Ce oxidation: *Geochimica et Cosmochimica Acta*, v. 63, p. 363–372.
- Anderson, S.D., Jamieson, R.A., Reynolds, P.H., and Dunning, G.R., 2001, Devonian extension in Northwestern Newfoundland:  $^{40}\text{Ar}/^{39}\text{Ar}$  and U-Pb Data from the Ming's Bight Area, Baie Verte Peninsula: *The Journal of Geology*, v. 109, p. 191–211.
- Azmy, K., Kendall, B., Brand, U., Stouge, S., and Gordon, G.W., 2015, Redox conditions across the Cambrian-Ordovician boundary: Elemental and isotopic signatures retained in the GSSP carbonates: *Palaeogeography, Palaeoclimatology, Palaeoecology*, v. 440, p. 440–454.
- Babechuk, M.G., Widdowson, M. and Kamber, B.S., 2014. Quantifying chemical weathering intensity and trace element release from two contrasting basalt profiles, Deccan Traps, India: *Chemical Geology*, v. 363, p. 56-75.
- Bau, M., 1996, Controls on the fractionation of isovalent trace elements in magmatic and

- aqueous systems: Evidence from Y/Ho, Zr/Hf, and lanthanide tetrad effect: *Contributions to Mineralogy and Petrology*, v. 123, p. 323–333.
- Bau, M., 1993, Effects of syn- and post-depositional processes on the rare-earth element distribution in Precambrian iron-formations: *European Journal of Mineralogy*, v. 5, p. 257–268.
- Bau, M., 1999, Scavenging of dissolved yttrium and rare earths by precipitating iron oxyhydroxide: experimental evidence for Ce oxidation, Y-Ho fractionation, and lanthanide tetrad effect: *Geochimica et Cosmochimica Acta*, v. 63, p. 67–77.
- Bau, M., and Dulski, P., 1996, Distribution of yttrium and rare-earth elements in the Penge and Kuruman iron-formations, Transvaal Supergroup, South Africa: *Precambrian Research*, v. 79, p. 37–55.
- Bau, M., Möller, P. and Dulski, P., 1997, Yttrium and lanthanides in eastern Mediterranean seawater and their fractionation during redox-cycling: *Marine Chemistry*, v. 56, p. 123–131.
- Bau, M., Schmidt, K., Koschinsky, A., Hein, J., Kuhn, T., and Usui, A., 2014, Discriminating between different genetic types of marine ferro-manganese crusts and nodules based on rare earth elements and yttrium: *Chemical Geology*, v. 381, p. 9.
- Bédard, J.H., 1999, Petrogenesis of boninites from the Betts Cove Ophiolite, Newfoundland, Canada: Identification of subducted source components: *Journal of Petrology*, v. 40, p. 1853–1889.
- Bédard, J.H., Lauziere, K., Tremblay, A., Sangster, A., Douma, S.L., and Dec, T., 2000, Betts Cove ophiolite and its cover rocks, Newfoundland: *Current Research, Bulletin of the Geological Survey of Canada*, v. 550, 76 p.
- Bekker, A., Planavsky, N.J., Krapež, B., Rasmussen, B., Hofmann, A., Slack, J.F., Rouxel, O.J., and Konhauser, K.O., 2014, Iron formations: Their origins and implications for ancient seawater chemistry: in *Treatise on Geochemistry: Second Edition*, v. 12, p. 561–628.
- Berry, W.B.N., Wilde, P., Quinby-Hunt, M.S., and Orth, C.J., 1986, Trace element signatures in Dictyonema Shales and their geochemical and stratigraphic significance: *Norsk Geologisk Tidsskrift*, v. 66, p. 45–51.
- Bhatia, M.R., and Crook, K.A.W., 1986, Trace element characteristics of graywackes and tectonic setting discrimination of sedimentary basins: *Contributions to Mineralogy and Petrology*, v. 92, p. 181–193.
- Bolhar, R., Kamber, B.S., Moorbat, S., Fedo, C.M. and Whitehouse, M.J., 2004, Characterisation of early Archaean chemical sediments by trace element signatures: *Earth and Planetary Science Letters*, v. 222, p. 43–60.
- Boström, K., 1973, The origin and fate of ferromanganoan active ridge sediments.

Stockholm contributions in geology: *Acta Universitatis Stockholmensis*, v. 27, p. 149–243.

- Boström, K., and Peterson, N.A., 1966, Precipitates from hydrothermal exhalations on the east pacific rise: *Economic Geology*, v. 61, p. 1258–1265.
- Boström, K., and Peterson, N.A., 1969, The origin of aluminum-poor ferromanganan sediments in areas of high heat flow on the East Pacific Rise: *Marine Geology*, v. 7, p. 427–447.
- Byrne, R.H. and Kim, K.H., 1990, Rare earth element scavenging in seawater: *Geochimica et Cosmochimica Acta*, v. 54, p. 2645–2656.
- Caddey, S.S.W., 1991, The Homestake Gold Mine: an early Proterozoic iron-formation-hosted gold deposit, Lawrence County, South Dakota: *US Department of the Interior, US Geological Survey*, v. 1857-JI, 67 p.
- Calvert, S.E., and Pedersen, T.F., 1993, Geochemistry of recent oxic and anoxic marine sediments: Implications for the geological record: *Marine Geology*, v. 113, p. 67–88.
- Castonguay, S., Skulski, T., van Staal, C., and Currie, M., 2009, New insights on the structural geology of the Pacquet Harbour group and Point Rousse complex, Baie Verte peninsula, Newfoundland: *Current Research, Newfoundland and Labrador Department of Natural Resources, Geological Survey, Report*, v. 09-1, p. 147–158.
- Castonguay, S., van Staal, C.R., Joyce, N., Skulski, T., and Hibbard, J.P., 2014, Taconic metamorphism preserved in the Baie Verte Peninsula, Newfoundland Appalachians: Geochronological evidence for ophiolite obduction and subduction and exhumation of the leading edge of the Laurentian (Humber) margin during closure of the Taconic Seaway: *Geoscience Canada*, v. 41, p. 459–482.
- Coish, R.A., 1989, Boninitic lavas in Appalachian ophiolites: a review: *Boninites and Related Rock*, p. 264–287.
- Cowen, J.P., Massoth, G.J. and Baker, E.T., 1986, Bacterial scavenging of Mn and Fe in a mid-to far-field hydrothermal particle plume: *Nature*, v. 322, p. 169–171.
- Danielson, A., Möller, P., and Dulski, P., 1992, The europium anomalies in banded iron formations and the thermal history of the oceanic crust: *Chemical Geology*, v. 97, p. 89–100.
- De Baar, H., German, C., Elderfield, H. and Van Gaans, P., 1988, Rare earth element distributions in anoxic waters of the Cariaco Trench: *Geochemica et Cosmochimica Acta*, v. 52, p. 1203–1219.
- De Carlo, E. and Green, W., 2002, Rare earth elements in the water column of Lake Vanda, McMurdo Dry Valleys, Antarctica: *Geochemica et Cosmochimica Acta*, v. 66, p. 1323–1333.
- Douville, E., Bienvenu, P., Charlou, J.-L., Donval, J.-P., Fouquet, Y., Appriou, P., and

- Gamo, T., 1999, Yttrium and rare earth elements in fluids from various deep-sea hydrothermal systems - evidence for heat extraction from magma chambers or cracking fronts? *Geochemica et Cosmochimica Acta*, v. 63, p. 627–643.
- Dunning, G.R., and Krogh, T.E., 1985, Geochronology of ophiolites of the Newfoundland Appalachians: *Canadian Journal of Earth Sciences*, v. 22, p. 1659–1670.
- Dunning, G.R., O'Brien, S.J., Colman-Sadd, S.P., Blackwood, R.F., Dickson, W.L., O'Neill, P.P., and Krogh, T.E., 1990, Silurian orogeny in the Newfoundland Appalachians: *The Journal of Geology*, v. 98, p. 895–913.
- Evans, D.T.W., 1999, Epigenetic gold mineralization, Baie Verte Peninsula, Newfoundland: *Current Research, Newfoundland Department of Mines and Energy, Geological Survey, Report 98-1*, p. 35-51.
- Evans, D.T.W., 2004, Epigenetic gold occurrences, Baie Verte Peninsula, (NTS 12H/09, 16 and 12I/01), *Current Research, Newfoundland: Government of Newfoundland and Labrador, Department of Natural Resources, Mineral Resource Report*, v. 11, p. 177.
- Fisher, R. V., 1966, Rocks composed of volcanic fragments and their classification: *Earth-Science Reviews*, v. 1, p. 287–298.
- Fitzpatrick, D., 1981, Geology and mineral potential of upper ophiolitic rocks near Ming's Bight, Burlington Peninsula, Newfoundland: *Memorial University of Newfoundland, Doctoral Dissertation*, 90 p.
- Frew, A., 1971, Petrographic and geochemical comparison of two gold-mineralized zones, Ming's Bight area, White Bay, Newfoundland: *Memorial University of Newfoundland, Unpublished B.Sc. Thesis*, 35 p.
- German, C.R., Klinkhammer, G.P., Edmond, J.M., Mura, A. and Elderfield, H., 1990. Hydrothermal scavenging of rare-earth elements in the ocean: *Nature*, v. 345, p. 516–518.
- German, C.R., and Von Damm, K.L., 2003, Hydrothermal Processes: in *Treatise on Geochemistry vol. 6, The Oceans and Marine Geochemistry*, p. 181–222.
- Gourcerol, B., Thurston, P.C., Kontak, D.J., Côté-Mantha, O., and Biczok, J., 2016, Depositional setting of Algoma-type banded iron formation: *Precambrian Research*, v. 281, p. 47–79.
- Gross, G.A., 1980, A classification of iron formations based on depositional environments: *The Canadian Mineralogist*, v. 18, p.215-222.
- Gross, G.A., 1983, Tectonic systems and the deposition of iron-formation: *Precambrian Research*, v. 20, p. 171–187.
- Hannington, M.D., Tivey, M.K., Larocque, A.C., Petersen, S., and Rona, P.A., 1995, The occurrence of gold in sulfide deposits of the hydrothermal field, Mid-Atlantic Ridge:

- The Canadian Mineralogist*, v. 33, p. 1285–1310.
- Hastie, A.R., Mitchell, S.F., Kerr, A.C., Minifie, M.J. and Millar, I.L., 2011, Geochemistry of rare high-Nb basalt lavas: Are they derived from a mantle wedge metasomatised by slab melts?: *Geochimica et Cosmochimica Acta*, v. 75, p. 5049–5072.
- Hibbard, J., 1983, Geology of the Baie Verte Peninsula, Newfoundland: *Mineral Development Division, Department of Mines and Energy, Government of Newfoundland and Labrador*, v. 2, p. 283.
- Ishikawa, Y., Sawaguchi, T., Iwaya, S., and Horiuchi, M., 1976, Delineation of prospecting targets for Kuroko deposits based on modes of volcanism of underlying dacite and alteration halos: *Mining Geology*, v. 26: p. 105–117.
- James, L., 1954, Sedimentary facies of iron-formation: *Economic Geology*, v. 49, p. 235–293.
- Jenner, G.A., and Fryer, B.J., 1980, Geochemistry of the upper Snooks Arm Group basalts, Burlington Peninsula, Newfoundland: evidence against formation in an island arc: *Canadian Journal of Earth Sciences*, v. 17, p. 888–900.
- Kamber, B.S., and Webb, G.E., 2001, The geochemistry of late Archaean microbial carbonate: Implications for ocean chemistry and continental erosion history: *Geochimica et Cosmochimica Acta*, v. 15, p. 2509–2525
- Kessler, L.G., and Bédard, J.H., 2000, Epiclastic volcanic debrites-evidence of flow transformations between avalanche and debris flow processes, Middle Ordovician, Baie Verte Peninsula, Newfoundland, Canada: *Precambrian Research*, v. 101, p. 135–161.
- Kirkwood, D., and Dubé, B., 1992, Structural control of sill-hosted gold mineralization: the Stog'er Tight gold deposit, Baie Verte Peninsula, northwestern Newfoundland: *Current Research, Part D, Geological Survey of Canada Papers*, p. 211–221.
- Klinkhammer, G.P., Elderfield, H., Edmond, J.M., and Mitra, A., 1994, Geochemical implications of rare earth element patterns in hydrothermal fluids from mid-ocean ridges: *Geochimica et Cosmochimica Acta*, v. 58, p. 5105–5113.
- Klinkhammer, G., Elderfield, H. and Hudson, A., 1983, Rare earth elements in seawater near hydrothermal vents: *Nature*, v. 305, p. 185–188.
- Landing, E., 2012a, The great American Carbonate bank in Eastern Laurentia: Its births, deaths, and linkage to paleoceanic oxygenation (Early Cambrian–Late Ordovician): *AAPG Memoir*, v. 98, p. 451–492.
- Landing, E., 2012b, Time-specific black mudstones and global hyperwarming on the Cambrian-Ordovician slope and shelf of the Laurentia palaeocontinent: *Palaeogeography, Palaeoclimatology, Palaeoecology*, v. 367–368, p. 256–272.

- Large, R.R., Gemmell, J.B., and Paulick, H., 2001, The alternation box plot: A simple approach to understanding the relationship between alteration mineralogy and lithogeochemistry associated with volcanic-hosted massive sulfide deposits: *Economic Geology*, v. 96, p. 957–971.
- Lawrence, M.G., Greig, A., Collerson, K.D., and Kamber, B.S., 2006, Rare earth element and yttrium variability in South East Queensland waterways: *Aquatic Geochemistry*, v. 12, p. 39–72.
- Li, Z.Q., Zhang, L.C., Xue, C.J., Zheng, M.T., Zhu, M.T., Robbins, L.J., Slack, J.F., Planavsky, N.J. and Konhauser, K.O., 2018, Earth's youngest banded iron formation implies ferruginous conditions in the Early Cambrian ocean: *Scientific Reports*, v. 8, p. 10.
- Lode, S., Piercey, S.J. and Squires, G.C., 2016, Role of metalliferous mudstones and detrital shales in the localization, genesis, and paleoenvironment of volcanogenic massive sulphide deposits of the Tally Pond volcanic belt, central Newfoundland, Canada: *Canadian Journal of Earth Sciences*, v. 53, p. 387-425.
- MacLean, W.H., and Barrett, T.J., 1993, Lithogeochemical techniques using immobile elements: *Journal of Geochemical Exploration*, v. 48, p. 109–133.
- McLennan, S.M., 1989, Archean sedimentary rocks and the Archean mantle: *Workshop on the Archean Mantle*, p. 57.
- McLennan, S.M., Bock, B., Hemming, S.R., Hurowitz, J.A., Lev, S.M., and McDaniel, D.K., 2003, The roles of provenance sedimentary processes in the geochemistry of sedimentary rocks: in *Geochemistry of Sediments and Sedimentary Rocks: Evolutionary Considerations to Mineral Deposit Forming Environments*, p. 7–31.
- Menendez, A., James, R.H., Roberts, S., Peel, K. and Connelly, D., 2017, Controls on the distribution of rare earth elements in deep-sea sediments in the North Atlantic Ocean: *Ore Geology Reviews*, v. 87, p. 100-113.
- Michard, A., Albarède, F., Michard, G., Minster, J.F., and Charlou, J.L., 1983, Rare-earth elements and uranium in high-temperature solutions from east pacific rise hydrothermal vent field (13 °N): *Nature*, v. 303, p. 795–797.
- Mills, R.A., Wells, D.M. and Roberts, S., 2001, Genesis of ferromanganese crusts from the TAG hydrothermal field: *Chemical Geology*, v. 176, p. 283-293.
- Nesbitt, H.W., 2003, Petrogenesis of siliciclastic sediments and sedimentary rocks: *Geochemistry of Sediments and Sedimentary Rocks: Evolutionary Considerations to Mineral Deposit Forming Environments*, p. 39-51.
- Nesbitt, H.W., and Markovics, G., 1997, Weathering of granodioritic crust, long-term storage of elements in weathering profiles, and petrogenesis of siliciclastic sediments: *Geochimica et Cosmochimica Acta*, v. 8, p. 1653-1670.
- Nesbitt, H.W., Martini, I.P. and Chesworth, W., 1992, Diagenesis and metasomatism of

- weathering profile, with emphasis on Precambrian paleosols: in *Weathering, Soils & Paleosols: Developments in Earth Surface Processes* 2, p. 127-152.
- Nesbitt, H.W. and Young, G.M., 1984, Prediction of some weathering trends of plutonic and volcanic rocks based on thermodynamic and kinetic considerations: *Geochimica et Cosmochimica Acta*, v. 48, p. 1523-1534.
- Och, L. and Shields-Zhou, G., 2012, The Neoproterozoic oxygenation event: environmental perturbations and biogeochemical cycling: *Earth-Science Reviews*, v. 110, p. 26–57.
- Ohta, A., and Kawabe, I., 2001, REE(III) adsorption onto Mn dioxide ( $\delta\text{-MnO}_2$ ) and Fe oxyhydroxide: Ce(III) oxidation by  $\delta\text{-MnO}_2$ : *Geochimica et Cosmochimica Acta*, v. 65, p. 695–703.
- Otake, T., Yamada, R., Suzuki, R., Nakamura, S., Ito, A., Shin, K.C. and Sato, T., 2021, Large Fe isotope fractionations in sulfide ores and ferruginous sedimentary rocks from the Kuroko volcanogenic massive sulfide deposits in the Hokuroku district, northeast Japan: *Geochimica et Cosmochimica Acta*, v. 295, p. 49-64.
- Pack, A., Russell, S., Shelley, J. and Van Zuilen, M., 2007, Geo-and cosmochemistry of the twin elements yttrium and holmium: *Geochemica et Cosmochimica Acta*, v. 71, p. 4592–4608.
- Pearce, J.A., 1996, A User's Guide to Basalt Discrimination Diagrams. Trace element geochemistry of volcanic rocks: applications for massive sulphide exploration: *Geological Association of Canada, Short Course Notes*, v. 39, p. 21–40.
- Pearce, J.A., 2008, Geochemical fingerprinting of oceanic basalts with applications to ophiolite classification and the search for Archean oceanic crust: *Lithos*, v. 100, p. 14-48.
- Peter, J.M., 2003, Ancient iron formations: their genesis and use in the exploration for stratiform base metal sulphide deposits, with examples from the Bathurst Mining Camp: *Geochemistry of Sediments and Sedimentary Rocks: Evolutionary Considerations to Mineral Deposit Forming Environments*, p. 145–176.
- Peter, J.M., Goodfellow, W.D., and Doherty, W., 2003, Hydrothermal sedimentary rocks of the Heath Steele belt, Bathurst mining camp, New Brunswick: Part 2. Bulk and rare earth element geochemistry and implications for origin: *Economic Geology Monograph*, v. 11, p. 391-415.
- Peter, J.M., Kjarsgaard, I.M., Goodfellow, W.D., and McCutcheon, S.R., 2003b, Hydrothermal sedimentary rocks of the Heath Steele Belt, Bathurst mining camp, New Brunswick—Part 1. Mineralogy and mineral chemistry: Massive sulfide deposits of the Bathurst mining camp, New Brunswick, and northern Maine: *Economic Geology Monograph*, v. 11, p. 361–390.
- Phillips, G.N., and Powell, R., 2010, Formation of gold deposits: A metamorphic

- devolatilization model: *Journal of Metamorphic Geology*, v. 28, p. 689-718.
- Piercey, S.J., 2014, Modern analytical facilities 2. A review of quality assurance and quality control (QA/QC) procedures for lithogeochemical data: *Geoscience Canada*, v. 41, p. 75–88.
- Piercey, S.J., Jenner, G.A., Wilton, D.H.C., Pereira, C.P.G., and Walsh, D.G., 1997, The stratigraphy and geochemistry of the southern Pacquet Harbour Group, Baie Verte Peninsula, Newfoundland; implications for mineral exploration: *Current Research, Newfoundland and Labrador Department of Mines and Energy*, p. 119-139.
- Pilote, J.L., Piercey, S.J., and Mercier-Langevin, P., 2015, Volcanic architecture and alteration assemblages of the Ming Cu-Au-(Zn-Ag) VMS deposit, Baie Verte, Newfoundland and Labrador: *Current Research, Implications for Au-enrichment processes and exploration, Geological Survey of Canada, Open File*, v. 7853, p. 197-210.
- Piper, D.Z., 1974, Rare earth elements in the sedimentary cycle: a summary: *Chemical Geology*, v. 14, p. 285-304.
- Planavsky, N., Bekker, A., Rouxel, O.J., Kamber, B., Hofmann, A., Knudsen, A., and Lyons, T.W., 2010, Rare earth element and yttrium compositions of Archean and Paleoproterozoic Fe formations revisited: New perspectives on the significance and mechanisms of deposition: *Geochimica et Cosmochimica Acta*, v. 74, p. 6387–6405.
- Pourmand, A., Dauphas, N. and Ireland, T.J., 2012, A novel extraction chromatography and MC-ICP-MS technique for rapid analysis of REE, Sc and Y: Revising CI-chondrite and Post-Archean Australian Shale (PAAS) abundances: *Chemical Geology*, v. 291, p. 38-54.
- Ramezani, J., Dunning, G.R., and Wilson, M.R., 2000, Geologic setting, geochemistry of alteration, and U-Pb age of hydrothermal zircon from the Silurian Stog’er Tight gold prospect, Newfoundland Appalachians, Canada: *Exploration and Mining Geology*, v. 9, p. 171–188.
- Ross, P.S. and Bédard, J.H., 2009, Magmatic affinity of modern and ancient subalkaline volcanic rocks determined from trace-element discriminant diagrams: *Canadian Journal of Earth Sciences*, v. 46, p. 823-839.
- Rudnicki, M.D., 1995, Particle formation, fallout and cycling within the buoyant and non-buoyant plume above the TAG vent field: *Geological Society Special Publication*, v. 87, p. 387–396.
- Sangster, A.L., Douma, S.L., and Lavigne, J., 2007, Base metal and gold deposits of the Betts Cove Complex, Baie Verte Peninsula, Newfoundland: *Mineral Deposits of Canada: A Synthesis of Major Deposit-Types, District Metallogeny, the Evolution of Geological Provinces, and Exploration Methods: Geological Association of Canada, Mineral Deposits Division, Special Publication*, v. 5, p. 703–721.

- Shervais, J.W., 1982, Ti-V plots and the petrogenesis of modern and ophiolitic lavas: *Earth and Planetary Science Letters*, v. 59(1), p. 101-118.
- Shimizu, H. and Masuda, A., 1977, Cerium in chert as an indication of marine environment of its formation: *Nature*, v. 266, p. 346-348.
- Shinjo, R., Woodhead, J.D., and Hergt, J.M., 2000, Geochemical variation within the northern Ryukyu Arc: Magma source compositions and geodynamic implications: *Contributions to Mineralogy and Petrology*, v. 140, p. 263–282.
- Sholkovitz, E.R., Landing, W.M. and Lewis, B.L., 1994, Ocean particle chemistry: the fractionation of rare earth elements between suspended particles and seawater: *Geochimica et Cosmochimica Acta*, v. 58, p. 1567-1579.
- Skulski, T., Castonguay, S., Kidd, W.S.F., McNicoll, V.J., van Staal, C.R. and Hibbard, J.P., 2015, Geology, Baie Verte and parts of Fleur de Lys, Newfoundland and Labrador, NTS 12-H/16 and part of NTS 12-I/1: *Current Research, Canadian Geoscience Map*, v. 159, 21 p.
- Skulski, T., Castonguay, S., McNicoll, V., van Staal, C., Kidd, W., Rogers, N., Morris, W., Ugalde, H., Slavinski, H., and Spicer, W., 2010, Tectonostratigraphy of the Baie Verte oceanic tract and its ophiolite cover sequence on the Baie Verte Peninsula: *Current Research, Newfoundland and Labrador Department of Natural Resources, Geological Survey, Report*, p. 315–337.
- Skulski, T., Castonguay, S., Van Staal, C.R., Rogers, N., Mcnicoll, V., Kerr, A., and Escayola, M., 2009, Baie Verte Peninsula: An Evolving Geological Story: *Geological Association of Canada, Newfoundland and Labrador Section Annual Field Trip Guide*, 76 p.
- Slack, J.F., Grenne, T. and Bekker, A., 2009, Seafloor-hydrothermal Si-Fe-Mn exhalites in the Pecos greenstone belt, New Mexico, and the redox state of ca. 1720 Ma deep seawater: *Geosphere*, v. 5, p. 302–314.
- Slack, J.F., Grenne, T., Bekker, A., Rouxel, O.J., and Lindberg, P.A., 2007, Suboxic deep seawater in the late Paleoproterozoic: evidence from hematitic chert and iron formation related to seafloor-hydrothermal sulfide deposits, central Arizona, USA: *Earth and Planetary Science Letters*, v. 255, p. 243–256.
- Snelgrove, A.K., 1935, Geology of gold deposits of Newfoundland: *Newfoundland Department of Natural Resources: Bulletin*, v. 2, p. 46.
- Sparrow, B., Barrett, S., Copeland, D., and Walsh, M., 2017, Assessment report on prospecting and drilling on the Point Rousse Project- Goldenville Prospect, Licences 018925M (6th year) and 018926M (6th year), 015582M (8th year), and 018617M (6th year) NTS Sheets 12H/16 and 12I/01, Assessment Report, Newfoundland and Labrador Canada, p. 481.
- Spitz, G., and Darling, R., 1978, Major and minor element lithogeochemical anomalies

- surrounding the Louvem Copper Deposit, Val D'or, Quebec. Lithogeochemical: *Canadian Journal of Earth Sciences*, v. 15, p. 1161–1169.
- Stolz, A.J., Varne, R., Davies, G.R., Wheller, G.E., and Foden, J.D., 1990, Magma source components in an arc-continent collision zone: the Flores-Lembata sector, Sunda arc, Indonesia: *Contributions to Mineralogy and Petrology*, v. 105, p. 585–601.
- Sun, S. -s., and McDonough, W.F., 1989, Chemical and isotopic systematics of oceanic basalts: implications for mantle composition and processes: *Geological Society, London, Special Publications*, v. 42, p. 313–345.
- Taylor, S., and McLennan, S., 1985, The Continental Crust: Its Composition and Evolution: *Blackwell, Oxford*, 312 p.
- Terfelt, F., Eriksson, M.E., and Schmitz, B., 2014, The Cambrian-Ordovician transition in dysoxic facies in Baltica - diverse faunas and carbon isotope anomalies: *Palaeogeography, Palaeoclimatology, Palaeoecology*, v. 394, p. 59–73.
- Tostevin, R. 2021, Cerium Anomalies and Paleoredox: Cambridge University Press, p. 6454.
- Tuach, J., and Kennedy, M.J., 1978, The geologic setting of the Ming and other sulfide deposits, Consolidated Rambler Mines, Northeast Newfoundland: *Economic Geology*, v. 73, p. 192–206.
- Tremblay, A., Bédard, J.H. and Lauzière, K., 1997, Taconian obduction and Silurian exhumation of the Betts Cove ophiolite, Canadian Appalachians: *The Journal of Geology*, v. 105, p. 701-716.
- Tripathy, G.R., Hannah, J.L., Stein, H.J., and Yang, G., 2014, Re-Os age and depositional environment for black shales from the Cambrian-Ordovician boundary, Green Point, western Newfoundland: *Geochemistry, Geophysics, Geosystems*, v. 15, p. 1021–1037.
- Tuach, J., and Kennedy, M.J., 1978, The geologic setting of the Ming and other sulfide deposits, Consolidated Rambler Mines, Northeast Newfoundland: *Economic Geology*, v. 73, p. 192–206.
- van Staal, C.R., and Barr, S.M., 2012, Lithospheric architecture and tectonic evolution of the Canadian Appalachians and associated Atlantic margin: in *Percival, J. A., Cook, F. A. and Clowes, R. M., eds., Tectonic styles in Canada: The LITHOPROBE perspective: Geological Association of Canada Special Paper*, v. 49, p. 55.
- van Staal, C.R., Chew, D.M., Zagorevski, A., McNicoll, V., Hibbard, J., Skulski, T., Castonguay, S., Escayola, M.P., and Sylvester, P.J., 2013, Evidence of late Ediacaran hyperextension of the Laurentian Iapetan margin in the Birchy Complex, Baie Verte Peninsula, Northwest Newfoundland: Implications for the opening of Iapetus, formation of Peri- Laurentian microcontinents and Taconic – Grampi orogenesis: *Geoscience Canada*, v. 40, p. 94–118.
- van Staal, C.R., Whalen, J.B., McNicoll, V.J., Pehrsson, S., Lissenberg, C.J., Zagorevski,

- A., Van Breemen, O., and Jenner, G.A., 2007, The Notre Dame arc and the Taconic orogeny in Newfoundland: *Geological Society of America Memoirs*, v. 200, p. 511–552.
- Waldron, J.W.F., and van Staal, C.R., 2001, Taconian orogeny and the accretion of the Dashwoods block: A peri-Laurentian microcontinent in the Iapetus Ocean: *Geology*, v. 29, p. 811–814.
- Watson, K.D.P., 1947, Geology and mineral deposits of the Baie Verte-Mings Bight area: *Princeton University, Doctoral Dissertation*.
- Webby, B., Paris, F., and Droser, M., 2003, The Great Ordovician Biodiversification Event: *Columbia University Press*, v. 61, p. 1–40.
- White, J.D.L., and Houghton, B.F., 2006, Primary volcaniclastic rocks: *Geology*, v. 34, p. 677–680.
- Williams, H., 1979, Appalachian orogen in Canada: *Canadian Journal of Earth Sciences*, v. 16, p. 792–807.
- Williams, H., Colman-Sadd, S.P., and Swinden, H.S., 1988, Tectonostratigraphic subdivisions of central Newfoundland: *Current Research, Part B. Geological Survey of Canada Paper*, v. 88-1B, p. 91–98.
- Williams, H., Dehler, S.A., Grant, A.C., and Oakey, G.N., 1999, Tectonics of Atlantic Canada: *Geoscience Canada*, v. 26, p. 51–70.
- Williams, H., and St-Julien, P., 1982, The Baie Verte-Brompton line: early Paleozoic continent-ocean interface in the Canadian Appalachians: in *Major Structural Zones and Faults of The Northern Appalachians, Geological Association of Canada, Special Paper*, v. 24, p. 177–207.
- Winchester, J.A. and Floyd, P.A., 1977, Geochemical discrimination of different magma series and their differentiation products using immobile elements: *Chemical Geology*, v. 20, p. 325–343.
- Zagorevski, A., Rogers, N., van Staal, C.R., McNicoll, V., Lissenberg, C.J., and Valverde-Vaquero, P., 2006, Lower to Middle Ordovician evolution of peri-Laurentian arc and backarc complexes in Iapetus: Constraints from the Annieopsquotch accretionary tract, central Newfoundland: *Bulletin of the Geological Society of America*, v. 118, p. 324–342.

**Table 2.1** Summary of geochemical characteristics of simplified lithologies

Simplified Lithology			Basalt - Suite 1		Basalt- Suite 2		Volcaniclastic		Argillite		Mag-rich IF		Arg w/ SMM		Arg w/ DSM	
Mean			Mean	2 $\sigma$	Mean	2 $\sigma$	Mean	2 $\sigma$	Mean	2 $\sigma$	Mean	2 $\sigma$	Mean	2 $\sigma$	Mean	2 $\sigma$
Number of Samples			n = 43		n = 5		n = 20		n = 10		n = 6		n = 10		n = 14	
SiO <sub>2</sub>	%	FUS-ICP-AES	50.40	9.41	42.74	2.78	50.46	11.55	49.92	10.68	22.49	18.08	48.14	11.65	55.13	20.21
TiO <sub>2</sub>	%	FUS-ICP-AES	0.52	0.24	3.48	1.11	0.80	0.94	1.74	1.81	0.18	0.12	0.42	0.15	0.93	1.87
Al <sub>2</sub> O <sub>3</sub>	%	FUS-ICP-AES	15.62	2.92	14.37	1.19	15.28	2.97	14.57	2.58	3.81	2.26	9.26	5.29	14.25	10.14
Fe <sub>2</sub> O <sub>3T</sub>	%	FUS-ICP-AES	9.20	3.24	14.30	2.13	9.46	5.52	11.87	2.89	62.58	11.60	28.30	19.91	10.99	5.53
MnO	%	FUS-ICP-AES	0.11	0.10	0.21	0.07	0.13	0.10	0.48	0.87	0.81	0.80	3.30	3.70	0.34	0.65
MgO	%	FUS-ICP-AES	6.09	3.06	5.75	1.08	6.58	3.67	5.04	3.11	1.52	1.11	2.96	1.73	3.59	4.51
CaO	%	FUS-ICP-AES	8.08	5.78	8.65	2.75	6.75	5.58	6.97	4.59	4.37	3.16	2.54	3.31	4.52	3.77
Na <sub>2</sub> O	%	FUS-ICP-AES	2.83	2.16	2.20	1.27	2.78	3.61	2.66	3.33	0.36	1.20	1.37	4.73	3.19	4.90
K <sub>2</sub> O	%	FUS-ICP-AES	0.39	1.21	0.48	1.21	0.76	1.23	0.75	2.13	0.24	0.43	0.47	0.75	1.50	2.62
P <sub>2</sub> O <sub>5</sub>	%	FUS-ICP-AES	0.04	0.04	0.66	0.48	0.10	0.15	0.23	0.26	2.23	1.87	0.38	0.56	0.21	0.32
Cr <sub>2</sub> O <sub>3</sub>	%	FUS-ICP-AES	0.01	0.03	0.01	0.01	0.03	0.07	0.01	0.01	0.01	0.02	0.01	0.01	0.02	0.04
BaO	%	FUS-ICP-AES	0.01	0.01	0.01	0.02	0.01	0.01	0.02	0.05	0.01	0.01	0.01	0.01	0.03	0.05
LOI	%	GRAV	6.57	7.24	6.54	3.09	6.67	5.66	5.77	4.78	0.84	3.59	3.87	4.93	5.37	4.41
Total	%		99.89	1.80	99.42	1.04	99.80	1.75	100.06	1.21	99.46	1.18	99.80	1.47	100.07	1.79
CO <sub>2</sub>	%	COM-IR	3.70	7.32	3.35	2.85	3.59	4.78	2.62	4.31	1.89	3.96	2.32	4.74	3.42	3.53
S	%	COM-IR	0.16	0.54	0.27	0.67	0.27	1.02	0.05	0.07	0.06	0.11	0.06	0.15	0.07	0.23
Li	ppm	AD-ICP-MS	17.45	13.29	16.58	17.46	20.17	16.55	13.24	8.48	4.70	4.59	11.72	7.67	12.45	11.64
Be	ppm	AD-ICP-MS	0.26	0.20	1.29	0.68	0.54	0.56	1.09	1.16	0.89	0.96	1.57	1.06	0.91	0.72
Sc	ppm	AD-ICP-MS	35.92	8.21	30.82	3.19	31.04	13.82	30.01	20.36	7.45	5.25	11.86	2.71	31.39	23.33
V	ppm	FUS-ICP-MS	295.00	116.98	347.40	71.65	230.85	149.09	263.10	177.52	224.67	132.36	112.10	66.61	212.50	208.50
Co	ppm	AD-ICP-MS	35.80	14.34	46.54	11.90	34.47	20.69	32.65	17.33	58.47	41.42	27.87	12.14	34.35	25.25
Ni	ppm	AD-ICP-MS	48.93	50.69	54.16	44.87	72.61	125.95	43.61	32.44	52.32	26.02	93.89	60.84	52.99	67.86
Cu	ppm	AD-ICP-MS	72.72	83.24	43.78	39.31	100.46	414.76	143.58	690.43	313.67	868.51	100.88	200.77	172.27	445.62
Zn	ppm	AD-ICP-MS	85.44	59.55	121.00	22.72	85.35	82.46	101.90	57.90	135.00	150.66	209.20	152.24	100.93	77.70
Ga	ppm	FUS-ICP-MS	15.45	4.66	23.28	4.67	15.88	3.96	19.02	11.40	6.45	3.97	13.23	2.03	17.65	7.50
Rb	ppm	FUS-ICP-MS	6.18	20.39	7.96	20.71	12.34	24.65	16.27	46.66	5.98	11.87	11.41	19.26	37.51	73.11
Sr	ppm	FUS-ICP-MS	133.85	138.12	233.50	284.60	144.93	142.78	200.93	286.23	75.50	106.95	56.14	147.25	120.21	123.48
Y	ppm	FUS-ICP-MS	14.09	7.28	37.28	19.15	17.36	14.54	32.53	20.12	33.20	19.71	32.67	14.35	27.76	23.20
Zr	ppm	FUS-ICP-MS	29.07	17.27	300.60	152.99	76.75	100.83	139.90	151.07	26.50	19.46	76.60	19.56	115.21	154.24

**Table 2.1 (continued)** Summary of geochemical characteristics of simplified lithologies

Simplified Lithology			Basalt - Suite 1		Basalt- Suite 2		Volcaniclastic		Argillite		Mag-rich IF		Arg w/ SMM		Arg w/ DSM	
Mean			Mean	2σ	Mean	2σ	Mean	2σ	Mean	2σ	Mean	2σ	Mean	2σ	Mean	2σ
Number of Samples			n = 43		n = 5		n = 20		n = 10		n = 6		n = 10		n = 14	
Nb	ppm	FUS-ICP-MS	0.67	0.48	20.38	10.34	3.18	5.81	6.59	9.58	2.23	1.50	6.62	1.79	4.68	9.53
Mo	ppm	AD-ICP-MS	0.38	0.64	1.41	1.31	0.53	2.07	0.80	1.68	0.38	0.34	1.04	2.36	0.65	1.16
Ag	ppm	AD-ICP-MS	0.04	0.04	0.03	0.03	0.04	0.06	0.06	0.19	0.14	0.44	0.07	0.14	0.06	0.10
Cd	ppm	AD-ICP-MS	0.08	0.13	0.15	0.03	0.07	0.07	0.09	0.10	0.06	0.07	0.06	0.06	0.09	0.13
In	ppm	AD-ICP-MS	0.06	0.03	0.10	0.04	0.05	0.04	0.09	0.05	0.24	0.15	0.15	0.05	0.08	0.04
Sn	ppm	AD-ICP-MS	0.30	0.16	2.00	1.25	0.70	0.73	1.55	1.43	1.07	0.58	2.14	0.82	1.19	1.45
Sb	ppm	AD-ICP-MS	0.80	0.85	1.07	1.54	1.03	1.57	1.48	2.14	0.61	1.11	0.84	1.42	0.71	0.62
Cs	ppm	AD-ICP-MS	0.17	0.30	0.19	0.08	0.17	0.23	0.29	0.55	0.08	0.07	0.12	0.14	0.33	0.52
La	ppm	FUS-ICP-MS	1.76	1.50	23.10	11.57	5.84	9.04	11.74	15.73	19.80	12.63	33.86	12.39	11.89	19.01
Ce	ppm	FUS-ICP-MS	4.13	3.18	56.78	29.37	13.81	20.89	33.27	59.55	32.08	18.61	104.74	33.79	32.20	56.86
Pr	ppm	FUS-ICP-MS	0.60	0.38	7.85	4.36	1.81	2.60	3.84	4.27	5.82	3.75	8.68	2.34	3.63	5.05
Nd	ppm	FUS-ICP-MS	3.08	1.84	35.00	19.20	7.88	10.64	17.45	17.90	23.75	15.19	33.86	11.28	15.53	19.84
Sm	ppm	FUS-ICP-MS	1.23	0.68	8.36	4.78	2.28	2.36	4.91	4.22	6.04	3.82	7.51	2.59	4.24	4.79
Eu	ppm	FUS-ICP-MS	0.43	0.22	2.74	1.36	0.75	0.72	1.51	1.29	1.51	1.02	1.88	0.75	1.15	1.22
Gd	ppm	FUS-ICP-MS	1.79	0.88	8.18	3.88	2.77	2.63	5.65	4.05	6.97	4.34	7.78	2.42	4.77	4.43
Tb	ppm	FUS-ICP-MS	0.33	0.17	1.25	0.70	0.47	0.41	0.92	0.61	1.12	0.72	1.22	0.42	0.80	0.74
Dy	ppm	FUS-ICP-MS	2.36	1.12	7.38	4.29	2.98	2.58	5.91	3.81	6.94	4.37	7.48	3.13	5.16	4.76
Ho	ppm	FUS-ICP-MS	0.55	0.28	1.45	0.82	0.67	0.56	1.28	0.77	1.44	0.87	1.52	0.62	1.10	0.94
Er	ppm	FUS-ICP-MS	1.72	0.87	4.04	2.23	2.01	1.68	3.65	2.26	4.16	2.44	4.25	1.83	3.16	2.72
Tm	ppm	FUS-ICP-MS	0.26	0.14	0.56	0.29	0.30	0.24	0.53	0.33	0.57	0.28	0.59	0.26	0.46	0.39
Yb	ppm	FUS-ICP-MS	1.70	1.00	3.58	1.99	1.97	1.51	3.48	1.89	3.60	2.05	3.65	1.45	3.08	2.46
Lu	ppm	FUS-ICP-MS	0.27	0.15	0.52	0.28	0.30	0.24	0.50	0.30	0.49	0.23	0.51	0.21	0.49	0.43
Hf	ppm	FUS-ICP-MS	0.94	0.51	6.48	3.19	2.04	2.29	3.47	3.43	0.58	0.54	1.94	0.67	3.07	3.71
Ta	ppm	FUS-ICP-MS	0.15	0.12	1.32	0.71	0.30	0.38	0.52	0.56	0.23	0.10	0.51	0.24	0.45	0.69
Au	ppm	FA-ICP-AES	0.00	0.01	0.00	0.00	0.01	0.01	0.01	0.03	0.04	0.11	0.04	0.13	0.09	0.33
Tl	ppm	AD-ICP-MS	0.08	0.14	0.06	0.12	0.09	0.14	0.16	0.37	0.05	0.04	0.09	0.12	0.23	0.33
Pb	ppm	AD-ICP-MS	1.96	2.25	3.74	5.45	49.24	405.29	11.90	27.17	10.72	26.12	37.56	72.58	10.15	36.58
Bi	ppm	FUS-ICP-MS	<0.47	<0.47	<0.47	<0.47	1.09	<0.47	<0.47	<0.47	<0.47	<0.47	0.72	0.20	0.80	0.62
Th	ppm	FUS-ICP-MS	0.38	0.79	1.23	0.88	1.44	2.63	2.15	5.09	1.35	1.30	6.00	2.17	2.72	6.43
U	ppm	FUS-ICP-MS	0.29	0.40	0.49	0.26	0.76	1.44	0.90	0.86	1.76	1.44	1.87	1.11	1.06	2.78

**Table 2.2** Summary of geochemical characteristics of the Goldenville Horizon

Lithology	Mean	FUS-ICP-AES	Magnetite-rich IF				Argillite w/ semi-massive magnetite				Argillite w/ disseminated magnetite						
			Mean n = 6	2σ	min	max	Mean n = 10	2σ	min	max	Mean n = 14	2σ	min	max			
SiO <sub>2</sub> (%)	%	FUS-ICP-AES	22.49	18.08	11.60	-	36.20	47.64	11.77	37.00	-	58.60	51.83	9.83	43.80	-	60.20
TiO <sub>2</sub>	%	FUS-ICP-AES	0.18	0.12	0.08	-	0.25	0.40	0.11	0.34	-	0.51	1.05	1.88	0.31	-	3.70
Al <sub>2</sub> O <sub>3</sub>	%	FUS-ICP-AES	3.81	2.26	1.73	-	4.94	8.53	2.34	6.94	-	10.35	15.89	5.02	12.50	-	20.40
Fe <sub>2</sub> O <sub>3T</sub>	%	FUS-ICP-AES	62.58	11.60	53.90	-	68.80	28.30	19.21	15.15	-	41.10	11.02	5.87	6.18	-	15.00
MnO	%	FUS-ICP-AES	0.81	0.80	0.37	-	1.45	3.62	3.19	1.99	-	7.44	0.36	0.68	0.08	-	1.32
MgO	%	FUS-ICP-AES	1.52	1.11	0.62	-	2.25	3.16	1.18	2.12	-	3.98	3.98	4.26	0.97	-	6.79
CaO	%	FUS-ICP-AES	4.37	3.16	3.34	-	7.52	2.52	3.48	0.71	-	5.21	4.62	4.01	1.73	-	7.91
Na <sub>2</sub> O	%	FUS-ICP-AES	0.36	1.20	0.03	-	1.56	0.70	1.58	0.03	-	1.89	3.62	4.63	0.15	-	8.13
K <sub>2</sub> O	%	FUS-ICP-AES	0.24	0.43	0.03	-	0.56	0.49	0.77	0.05	-	1.23	1.65	2.65	0.03	-	4.44
P <sub>2</sub> O <sub>5</sub>	%	FUS-ICP-AES	2.23	1.87	0.65	-	3.37	0.38	0.58	0.16	-	1.14	0.17	0.28	0.04	-	0.56
Cr <sub>2</sub> O <sub>3</sub>	%	FUS-ICP-AES	0.01	0.02	0.00	-	0.02	0.01	0.01	0.01	-	0.02	0.02	0.04	0.00	-	0.06
BaO	%	FUS-ICP-AES	0.01	0.01	0.01	-	0.01	0.01	0.01	0.01	-	0.02	0.03	0.05	0.01	-	0.07
LOI	%	GRAV	0.84	3.59	-0.80	-	3.79	3.99	5.12	1.32	-	8.44	5.62	4.50	2.26	-	10.30
Total	%		99.46	1.18	98.76	-	100.09	99.76	1.53	98.57	-	101.31	99.88	1.52	98.52	-	101.25
CO <sub>2</sub>	%	COM-IR	1.89	3.96	0.31	-	4.89	2.38	4.98	0.02	-	6.87	3.44	3.78	0.51	-	7.04
S	%	COM-IR	0.06	0.11	0.01	-	0.13	0.06	0.15	0.01	-	0.25	0.08	0.25	0.01	-	0.47
Li (ppm)	ppm	AD-ICP-MS	4.70	4.59	1.80	-	7.40	11.72	7.67	7.10	-	20.40	12.45	11.64	4.70	-	23.30
Be	ppm	AD-ICP-MS	0.89	0.96	0.25	-	1.69	1.57	1.06	0.62	-	2.39	0.91	0.72	0.26	-	1.50
Sc	ppm	AD-ICP-MS	7.45	5.25	3.10	-	10.90	11.86	2.71	9.50	-	14.30	31.39	23.33	12.50	-	43.90
V	ppm	FUS-ICP-MS	224.67	132.36	134.00	-	309.00	112.10	66.61	79.00	-	185.00	212.50	208.50	51.00	-	384.00
Co	ppm	AD-ICP-MS	58.47	41.42	22.30	-	76.90	27.87	12.14	14.10	-	35.00	34.35	25.25	10.20	-	50.40
Ni	ppm	AD-ICP-MS	52.32	26.02	30.60	-	67.50	93.89	60.84	58.30	-	136.00	52.99	67.86	13.10	-	127.00
Cu	ppm	AD-ICP-MS	313.67	868.51	7.40	-	1185.00	100.88	200.77	9.30	-	317.00	172.27	445.62	8.60	-	672.00
Zn	ppm	AD-ICP-MS	135.00	150.66	72.00	-	265.00	209.20	152.24	91.00	-	326.00	100.93	77.70	46.00	-	211.00
Ga	ppm	FUS-ICP-MS	6.45	3.97	2.80	-	8.60	13.23	2.03	11.00	-	14.80	17.65	7.50	10.20	-	22.90
Rb	ppm	FUS-ICP-MS	5.98	11.87	0.60	-	14.30	11.41	19.26	1.30	-	29.40	37.51	73.11	0.60	-	140.00
Sr	ppm	FUS-ICP-MS	75.50	106.95	22.70	-	157.50	56.14	147.25	8.20	-	214.00	120.21	123.48	41.10	-	234.00
Y	ppm	FUS-ICP-MS	33.20	19.71	22.80	-	46.80	32.67	14.35	23.30	-	43.80	27.76	23.20	13.30	-	54.00
Zr	ppm	FUS-ICP-MS	26.50	19.46	16.00	-	45.00	76.60	19.56	66.00	-	97.00	115.21	154.24	25.00	-	268.00
Nb	ppm	FUS-ICP-MS	2.23	1.50	1.40	-	3.50	6.62	1.79	5.30	-	8.20	4.68	9.53	0.70	-	18.00

**Table 2.2** (continued) Summary of geochemical characteristics of the Goldenville Horizon

Lithology	Mean		Magnetite-rich IF				Argillite w/ semi-massive magnetite				Argillite w/ disseminated magnetite						
			Mean n = 6	2σ	min	max	Mean n = 10	2σ	min	max	Mean n = 14	2σ	min	max			
Mo	ppm	AD-ICP-MS	0.38	0.34	0.21	-	0.68	1.04	2.36	0.11	-	3.82	0.65	1.16	0.06	-	1.77
Ag	ppm	AD-ICP-MS	0.14	0.44	0.02	-	0.58	0.07	0.14	0.01	-	0.25	0.05	0.10	0.01	-	0.18
Cd	ppm	AD-ICP-MS	0.06	0.07	0.03	-	0.12	0.06	0.06	0.03	-	0.13	0.08	0.13	0.01	-	0.24
In	ppm	AD-ICP-MS	0.24	0.15	0.18	-	0.37	0.15	0.05	0.11	-	0.18	0.08	0.04	0.05	-	0.12
Sn	ppm	AD-ICP-MS	1.07	0.58	0.60	-	1.40	2.14	0.82	1.50	-	2.80	1.19	1.45	0.40	-	2.20
Sb	ppm	AD-ICP-MS	0.61	1.11	0.22	-	1.73	0.84	1.42	0.28	-	2.50	0.71	0.62	0.26	-	1.24
Cs	ppm	AD-ICP-MS	0.05	0.07	0.03	-	0.12	0.09	0.15	0.03	-	0.22	0.31	0.52	0.03	-	1.03
La	ppm	FUS-ICP-MS	19.80	12.63	10.00	-	26.80	33.86	12.39	23.00	-	43.70	11.89	19.01	2.10	-	27.90
Ce	ppm	FUS-ICP-MS	32.08	18.61	18.90	-	42.30	104.74	33.79	70.60	-	128.50	32.20	56.86	5.30	-	87.60
Pr	ppm	FUS-ICP-MS	5.82	3.75	3.04	-	8.03	8.68	2.34	6.41	-	10.05	3.63	5.05	0.81	-	7.24
Nd	ppm	FUS-ICP-MS	23.75	15.19	13.70	-	33.60	33.86	11.28	24.50	-	40.80	15.53	19.84	4.00	-	28.60
Sm	ppm	FUS-ICP-MS	6.04	3.82	3.86	-	8.83	7.51	2.59	5.77	-	8.92	4.24	4.79	1.34	-	7.82
Eu	ppm	FUS-ICP-MS	1.51	1.02	0.88	-	2.30	1.88	0.75	1.37	-	2.50	1.15	1.22	0.46	-	2.44
Gd	ppm	FUS-ICP-MS	6.97	4.34	4.29	-	9.62	7.78	2.42	5.96	-	9.57	4.77	4.43	2.09	-	8.98
Tb	ppm	FUS-ICP-MS	1.12	0.72	0.73	-	1.60	1.22	0.42	0.82	-	1.51	0.80	0.74	0.32	-	1.54
Dy	ppm	FUS-ICP-MS	6.94	4.37	4.56	-	9.79	7.48	3.13	4.75	-	9.12	5.16	4.76	2.22	-	10.80
Ho	ppm	FUS-ICP-MS	1.44	0.87	0.96	-	2.00	1.52	0.62	1.04	-	1.90	1.10	0.94	0.52	-	2.14
Er	ppm	FUS-ICP-MS	4.16	2.44	2.81	-	6.18	4.25	1.83	2.78	-	5.36	3.16	2.72	1.54	-	6.41
Tm	ppm	FUS-ICP-MS	0.57	0.28	0.41	-	0.75	0.59	0.26	0.40	-	0.74	0.46	0.39	0.26	-	0.90
Yb	ppm	FUS-ICP-MS	3.60	2.05	2.56	-	5.09	3.65	1.45	2.53	-	4.64	3.08	2.46	1.65	-	5.83
Lu	ppm	FUS-ICP-MS	0.49	0.23	0.37	-	0.63	0.51	0.21	0.35	-	0.62	0.49	0.43	0.27	-	0.97
Hf	ppm	FUS-ICP-MS	0.58	0.54	0.30	-	1.10	1.94	0.67	1.60	-	2.60	3.07	3.71	0.60	-	6.00
Ta	ppm	FUS-ICP-MS	0.23	0.10	0.20	-	0.30	0.51	0.24	0.30	-	0.70	0.45	0.69	0.10	-	1.40
Au	ppm	FA-ICP-AES	0.04	0.11	0.00	-	0.15	0.04	0.13	0.00	-	0.20	0.09	0.33	0.00	-	0.52
Tl	ppm	AD-ICP-MS	0.04	0.06	0.01	-	0.07	0.07	0.12	0.01	-	0.16	0.20	0.34	0.01	-	0.56
Pb	ppm	AD-ICP-MS	10.72	26.12	2.30	-	36.70	37.56	72.58	4.40	-	123.00	10.15	36.58	2.80	-	73.40
Bi	ppm	FUS-ICP-MS	<0.47	<0.47	0.00	-	0.00	0.72	0.20	0.65	-	0.79	0.80	0.62	0.57	-	1.15
Th	ppm	FUS-ICP-MS	1.35	1.30	0.92	-	2.65	6.00	2.17	4.69	-	8.05	2.72	6.43	0.31	-	9.63
U	ppm	FUS-ICP-MS	1.76	1.44	1.21	-	3.09	1.87	1.11	1.12	-	3.06	1.06	2.78	0.13	-	5.55

**Table 2.2** (continued) Summary of geochemical characteristics of the Goldenville Horizon

Lithology		Magnetite-rich IF				Argillite w/ semi-massive magnetite				Argillite w/ disseminated magnetite						
		Mean n = 6	2σ	min	max	Mean n = 10	2σ	min	max	Mean n = 14	2σ	min	max			
Fe/Ti	(molar)	334.40	250.51	231.07	-	577.46	62.88	53.15	27.63	-	97.30	12.91	11.41	3.41	-	22.17
Fe/Al	(molar)	13.62	10.05	10.32	-	23.57	2.64	2.30	1.15	-	4.37	0.54	0.33	0.24	-	0.78
Pr <sub>sn</sub> /Pr <sub>sn</sub> *		1.14	0.16	1.03	-	1.21	0.82	0.09	0.77	-	0.89	0.94	0.15	0.74	-	1.04
MREE/HREE	(Tb <sub>sn</sub> /Yb <sub>sn</sub> )	1.04	0.12	0.96	-	1.13	1.14	0.16	0.95	-	1.26	0.87	0.47	0.57	-	1.37
LREE/MREE	(Pr <sub>sn</sub> /Tb <sub>sn</sub> )	0.46	0.18	0.37	-	0.62	0.64	0.24	0.43	-	0.81	0.37	0.35	0.18	-	0.70

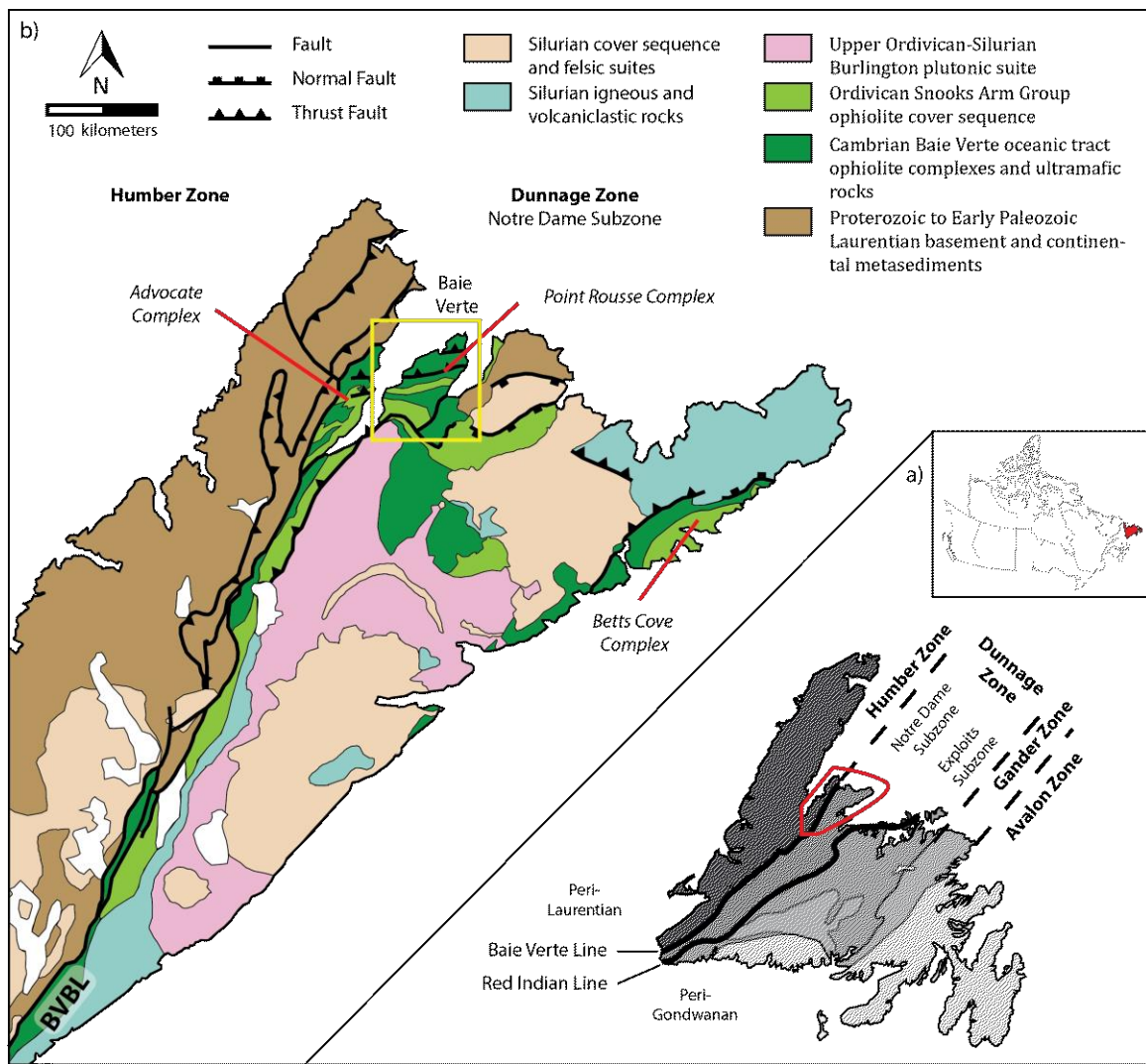


**Figure 2.1.** a) Simplified map of the tectonostratigraphic terranes of Newfoundland (modified after Williams, 1979 and Skulski et al., 2010) with an inset showing the area of 2.1b, the location of the Baie Verte Peninsula in Newfoundland. b) Geology map of the Baie Verte Peninsula (modified after Skulski et al., 2010) with yellow box showing the location shown in Figure 1.2.

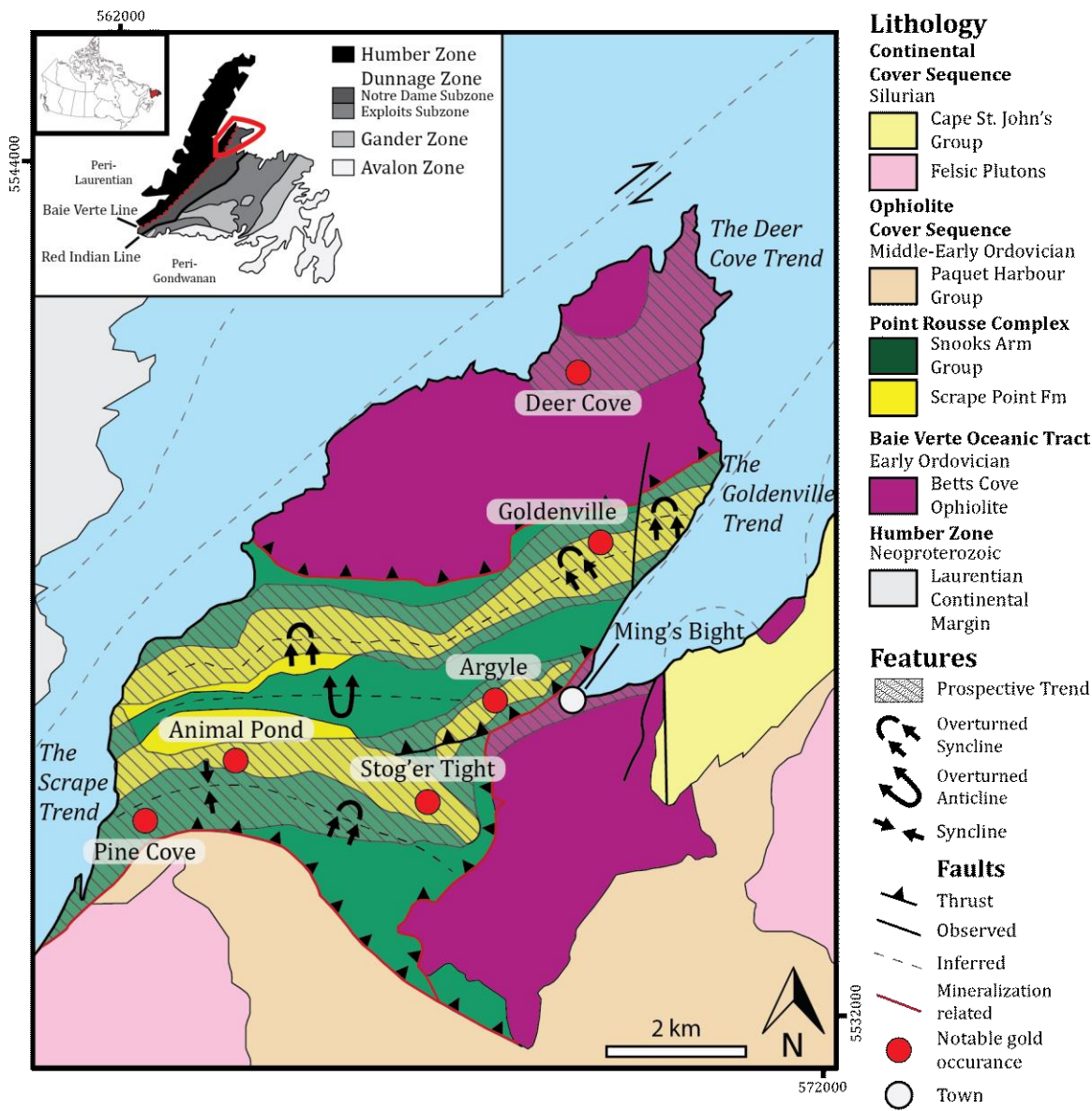


**Figure 2.2.** Simplified geology map of the Point Rousse peninsula with notable gold deposits and VMS occurrences. Modified from Skulski et al. (2010) and Anaconda Mining's Assessment Report on the Point Rousse Project by Sparrow et al. (2017).

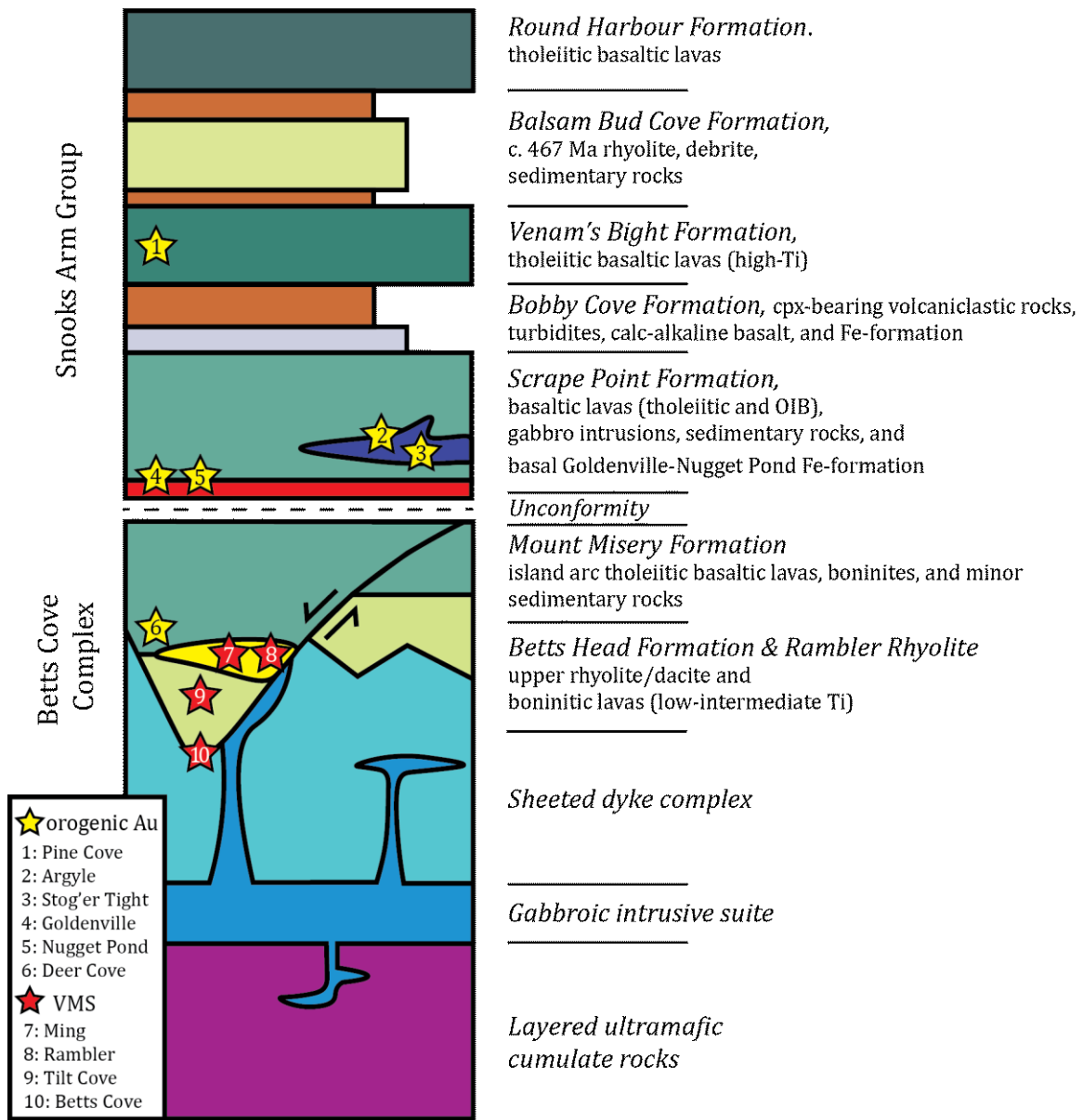
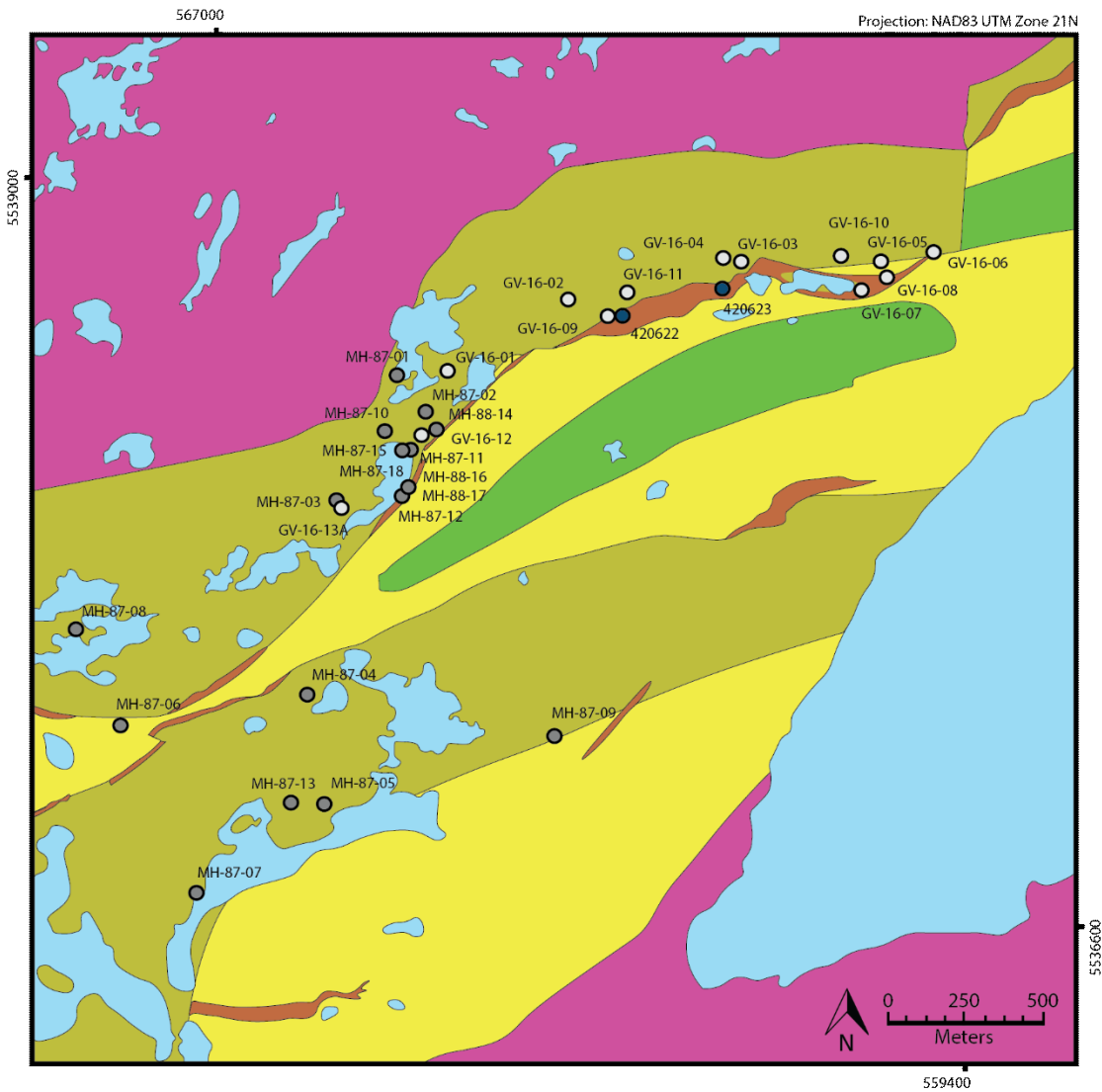
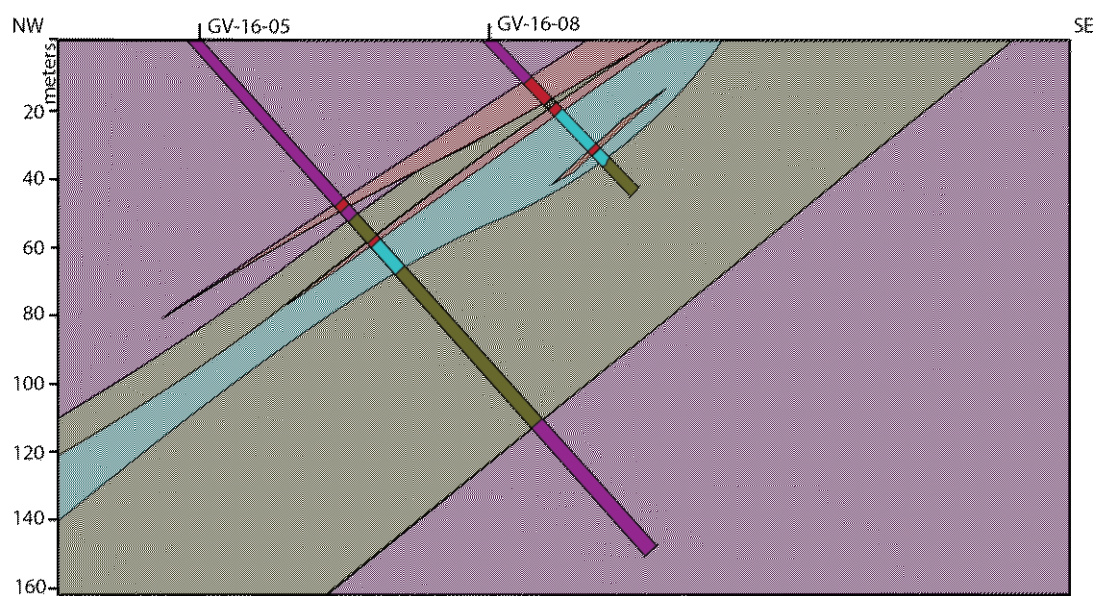
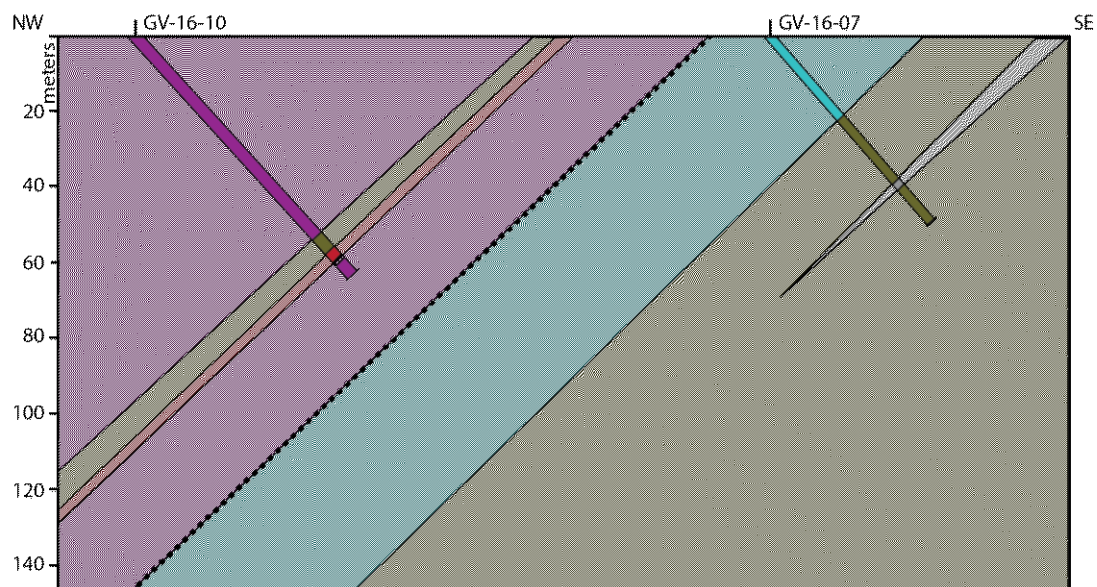
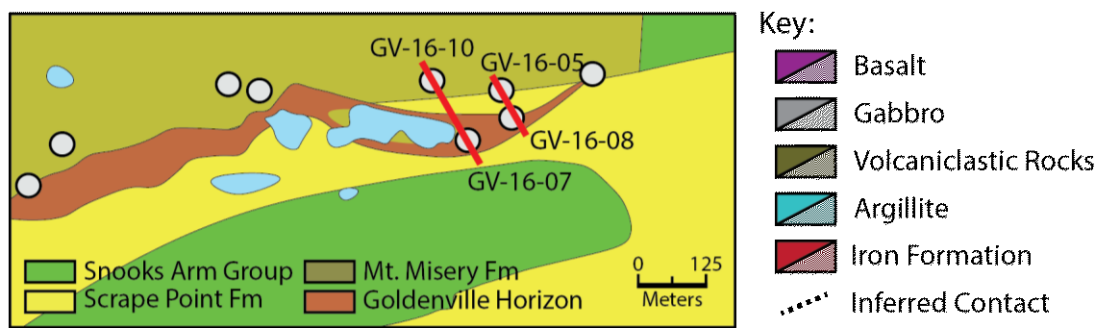


**Figure 2.3.** Regional stratigraphy of the Baie Verte Peninsula. Mineral deposits are symbolized by stars and include orogenic Au and VMS deposits. Modified after Bédard et al. (2000), Kessler and Bédard (2000), and Skulski et al. (2009).

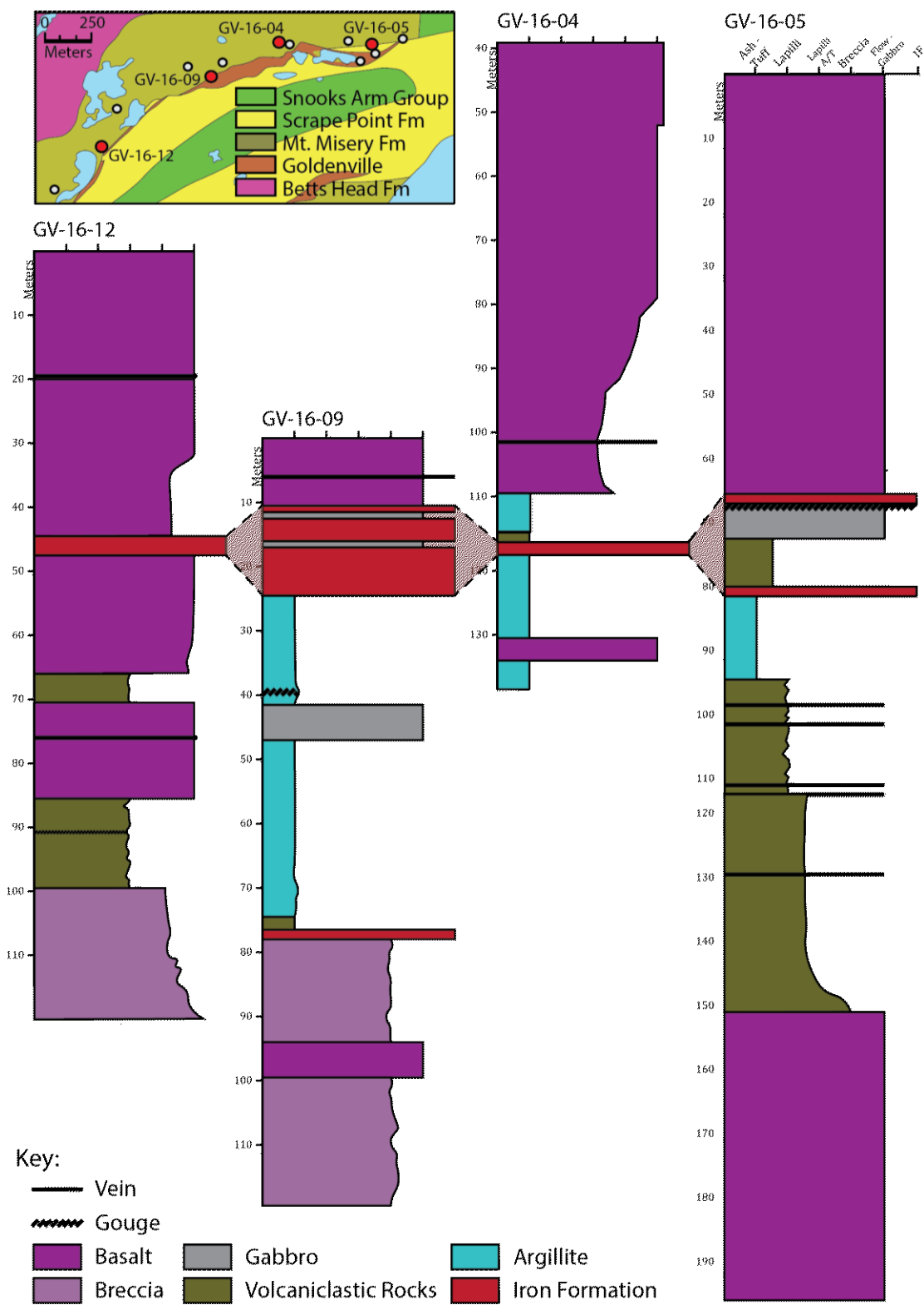


Features	Lithology	
● MH DDH (pre-2016)	Ophiolite Cover Sequence (Middle-Early Ordovician)	Baie Verte Oceanic Tract (Early Ordovician)
● GV DDH (2016)	Point Rousse Complex	
● GV Hand Sample (2019)	● Snooks Arm Group	● Mt. Misery Fm
■ Waterbody	● Scrape Point Fm	■ Betts Head Fm
	● Goldenville Horizon (Scrape Point Fm)	

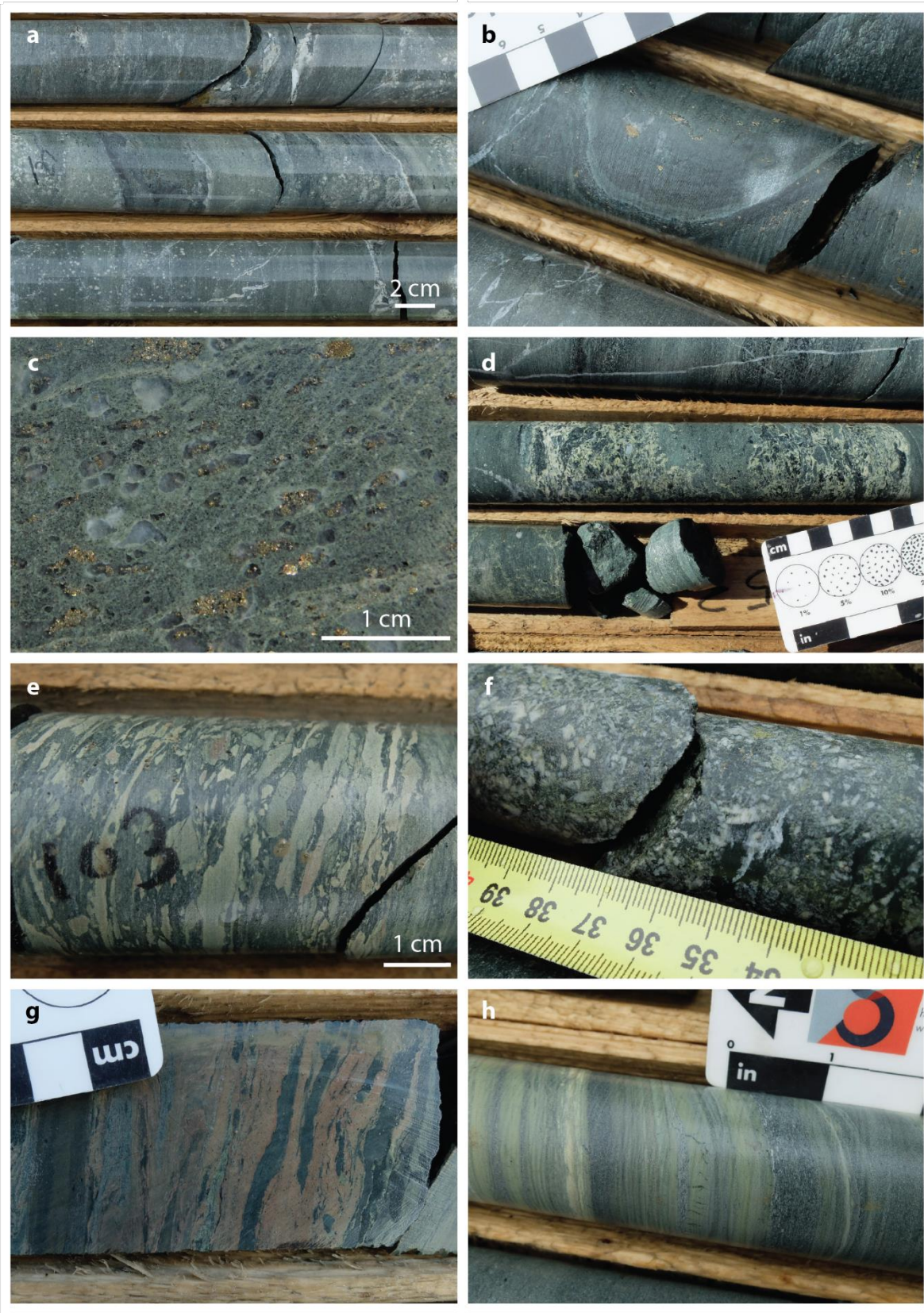
**Figure 2.4.** Simplified geological map of the Goldenville mine area with logged drill holes and surface samples (Appendix A). Modified from Skulski et al. (2010; 2015) and Anaconda Mining Inc. (unpublished mapping).



**Figure 2.5. (above)** Representative cross-sections through the Goldenville iron formation with inset map highlighted sections. Inset is from Figure 2.4.

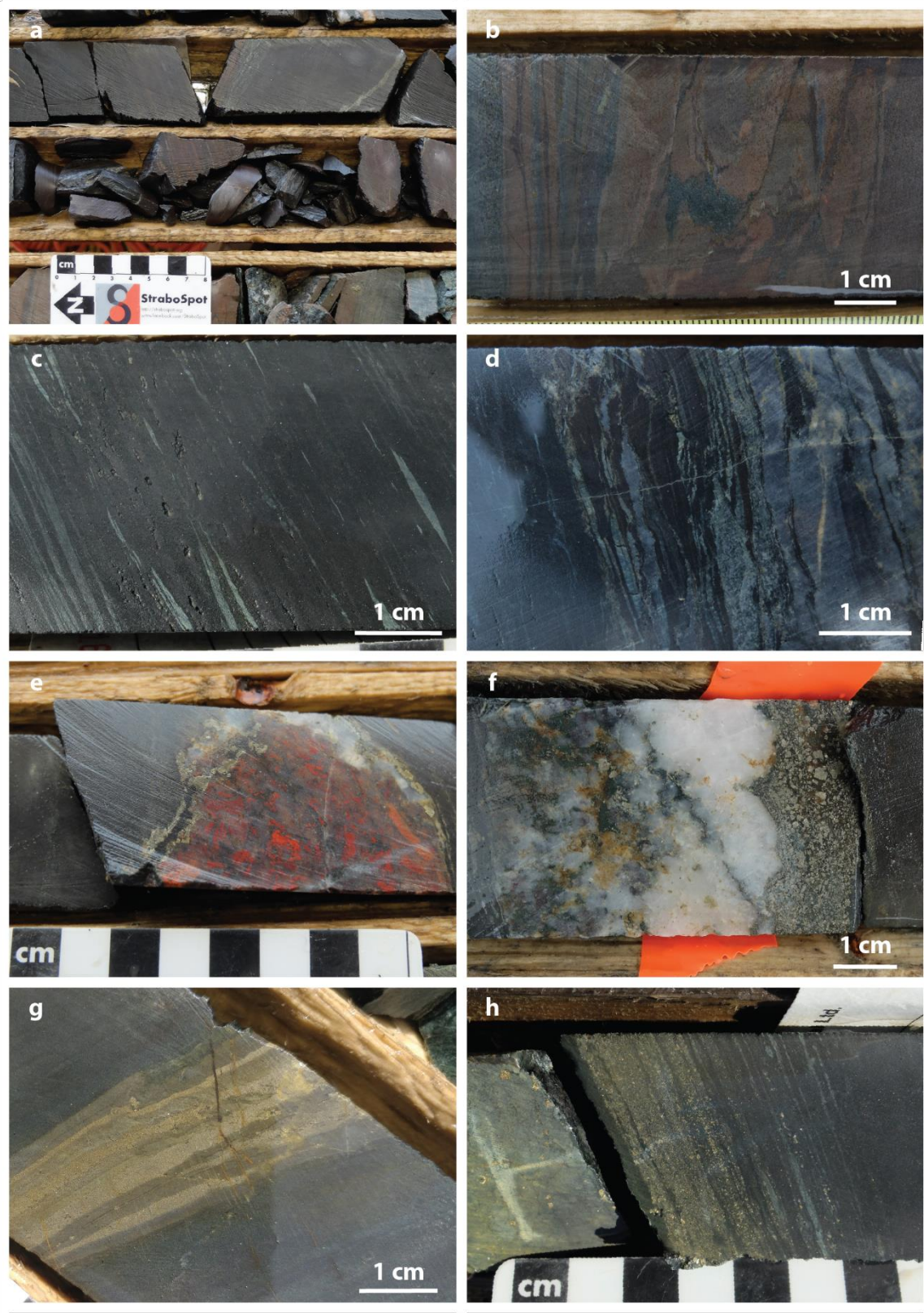


**Figure 2.6. (above)** Graphic logs of select drill holes from the Goldenville deposit showing the stratigraphy and variations in lithology of the Goldenville horizon. Inset is from Figure 2.4 with the drill holes shown in red.



**Figure 2.7. (above)** Representative volcanic, volcaniclastic, and sedimentary units in the Goldenville horizon stratigraphy. a) Representative image of massive mafic flow. b) Pillow lava with well-preserved cooling margins and disseminated pyrite. c) Amygdules with partial to full replacement by chlorite, epidote, calcite, quartz, and/or pyrite. d) Hyaloclastite with matrix replacement by chlorite, epidote, calcite, and quartz. e) Volcaniclastic unit with sub-rounded and elongated clasts of what? in a fine-grained matrix. f) Coarse-grained mafic intrusive rock with minor sericite alteration. g) Fine-grained, laminated, light maroon to green argillite with lenses of black chlorite and epidote. h) Fine-grained, laminated green argillite with graded partial to full turbidite sequences.

**Figure 2.8. (below)** Iron formation and associated mineralization from the Goldenville horizon. a) Representative fine-grained, well-laminated, dark brown to maroon iron-rich horizon. b) Fine-grained, maroon to grey interbedded sediments and iron formation featuring syn-sedimentary folding. c) Laminated iron formation interbedded with light grey detrital (ash and carbonate). d) Cherty opaque lenses interlaminated within the magnetite-rich iron formation. e) Chert and jasper nodule with pyrite along its edges in an iron formation. f) Quartz-albite vein with graded clotted pyrite along edge typical of orogenic-Au style mineralization. g) Very fine-grained exhalative style pyrite. h) Fine-grained graded exhalative style pyrite interbedded with detrital light grey ash and black chlorite.



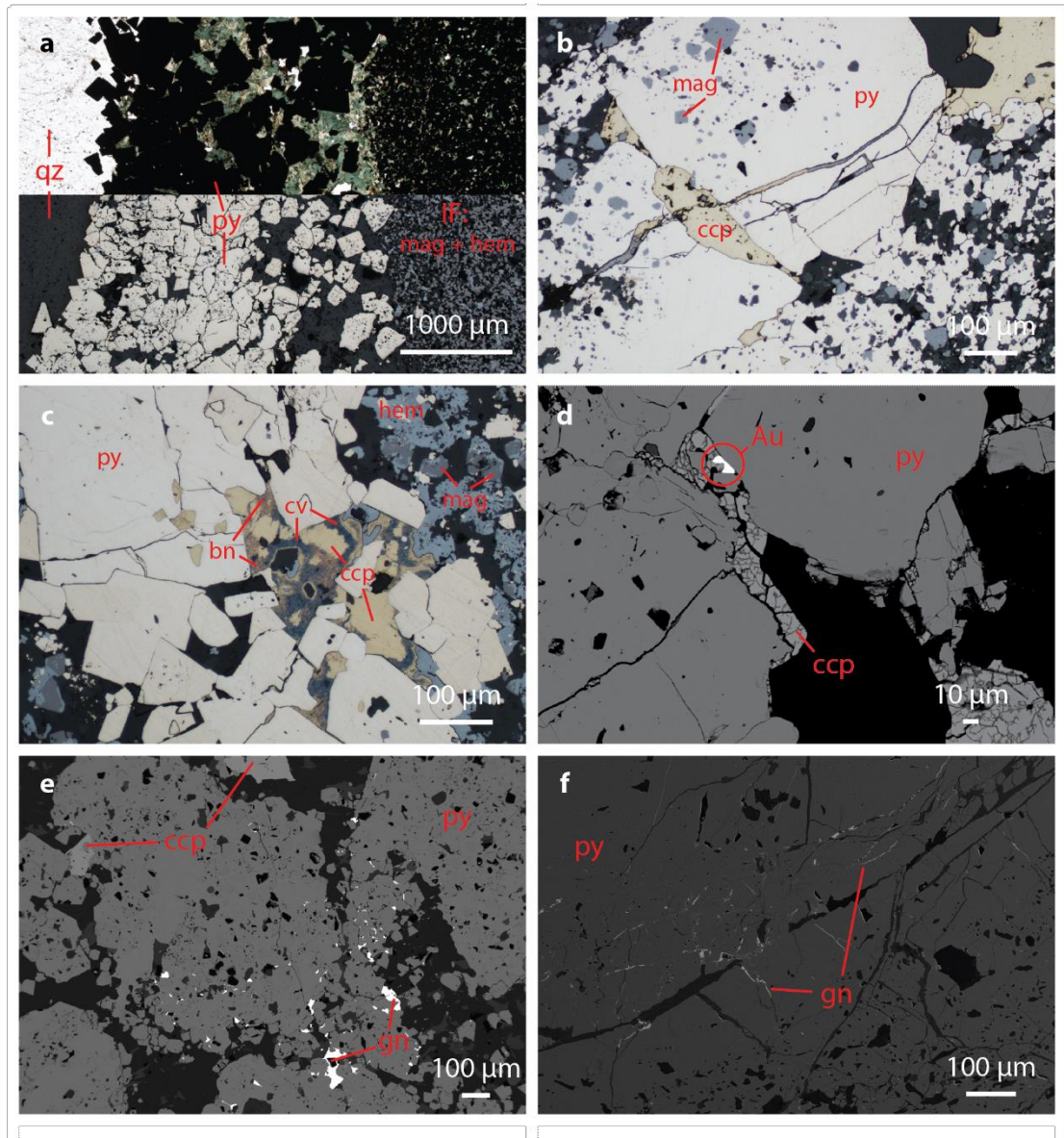


**Figure 2.9. (above)** Photomicrographs and backscatter electron (BSE)-scanning electron microscope (SEM) images of mineralization within the Goldenville iron formation. a) Split image of pyrite mineralized against a quartz vein and magnetite rich iron formation shown in plane polarized light (PPL; top) and reflected light (RL; bottom). b) Euhedral pyrite grain with magnetite inclusions and interstitial chalcopyrite (RL). c) Euhedral pyrite with chalcopyrite featuring bornite and covellite (RL). d) BSE-SEM image of gold and chalcopyrite along the edge of pyrite grains. e) BSE-SEM image of pyrite with chalcopyrite and galena infilling voids. f) BSE-SEM image of pyrite grain with galena infilling fractures.

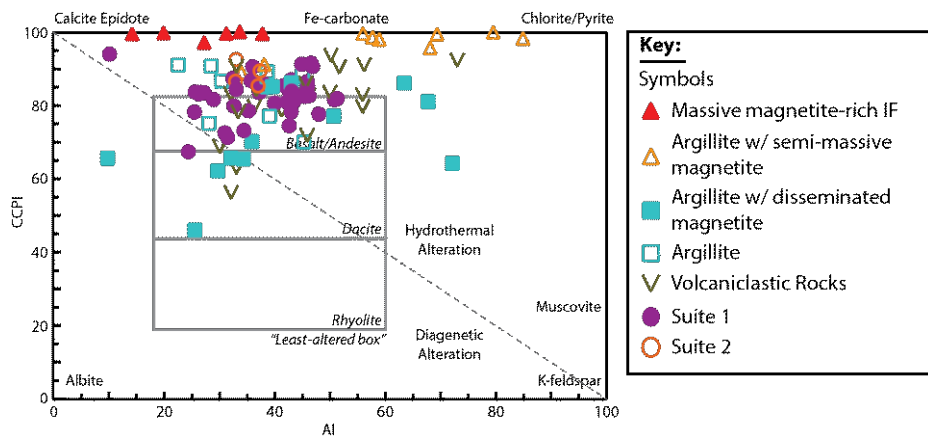


**Figure 2.10.** Alteration box plot for Goldenville horizon and surrounding stratigraphy—Hashimoto alteration index (AI; Ishikawa et al., 1976) vs. chlorite-carbonate-pyrite index (CCPI; Large et al., 2001).

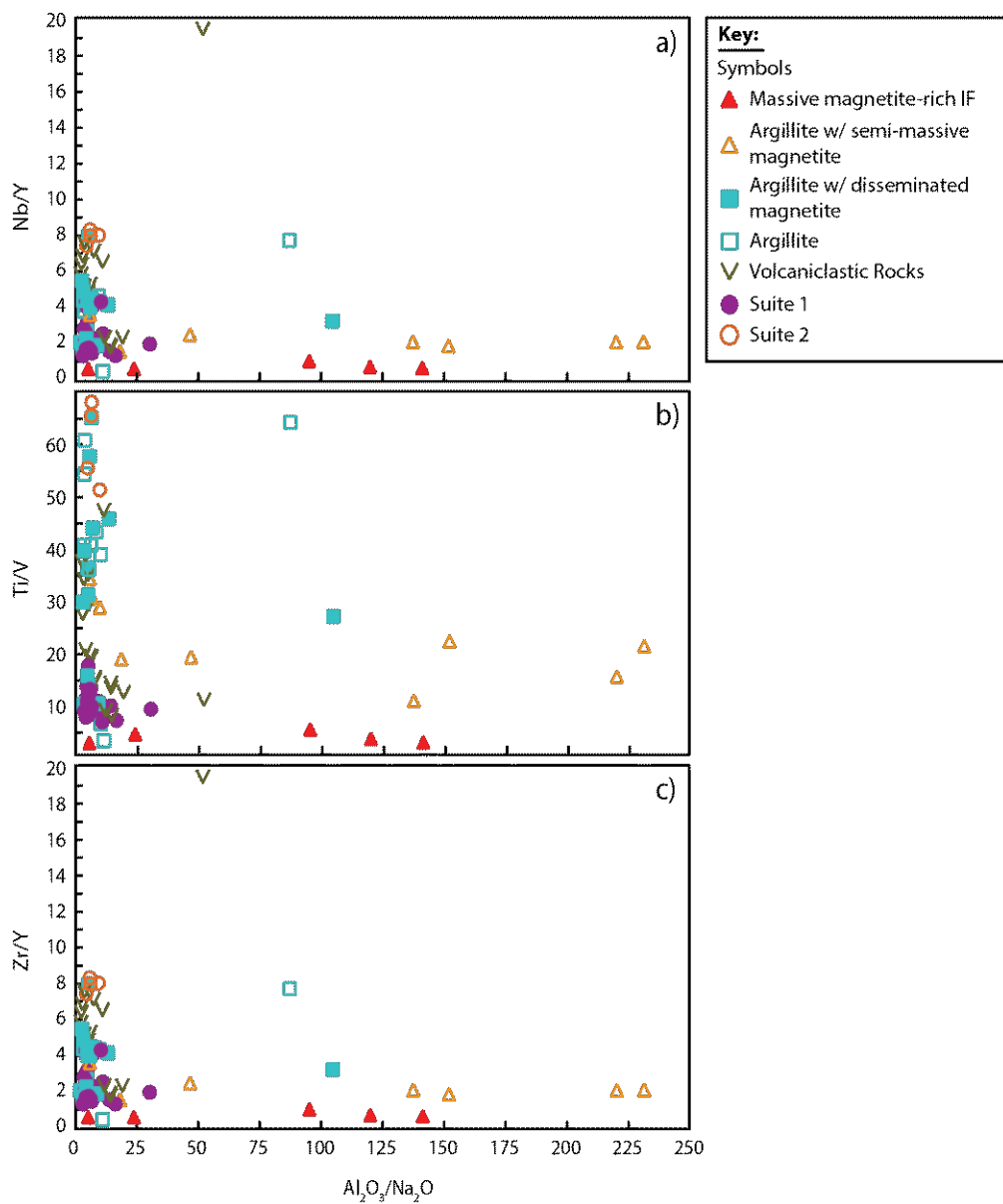


**Figure 2.11.** Key element ratios for the Goldenville horizon and surrounding stratigraphy against the  $\text{Al}_2\text{O}_3/\text{Na}_2\text{O}$  alteration index (Spitz and Darling, 1978). a) incompatible Nb/Y element ratio, b) compatible Ti/V element ratio; and c) incompatible Zr/Y element ratio. Further details provided in the text.

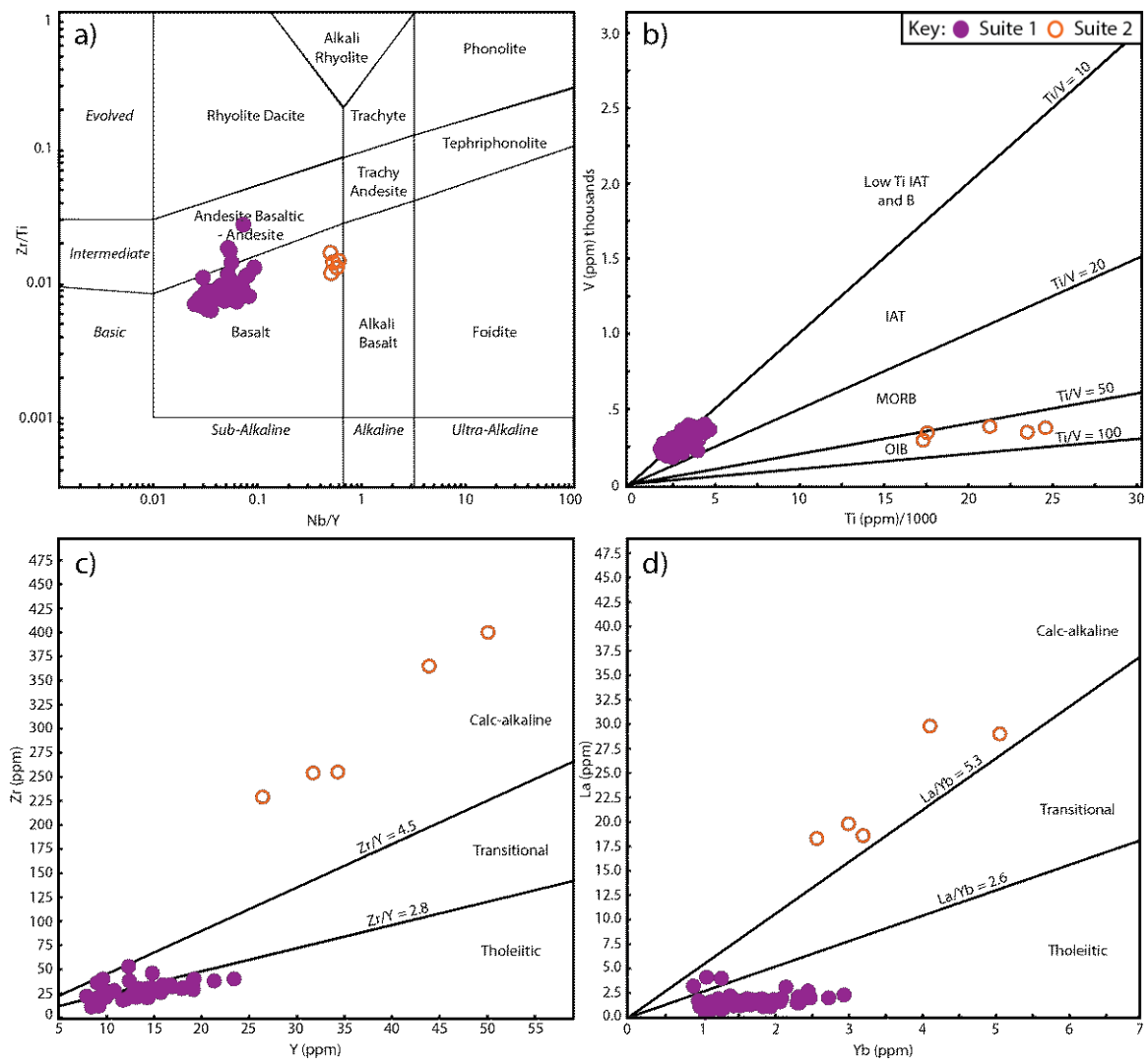


**Figure 2.12.** Discrimination diagrams for the differing basalt suites of the Goldenville deposit. a) Zr/TiO<sub>2</sub> vs. Nb/Y discrimination diagram from Winchester and Floyd (1977), revised by Pearce (1996). b) Ti-V plot of Shervais (1982); B, boninite; IAT, island arc tholeiite; MORB, mid-ocean ridge basalt; OIB, ocean island basalt. c-d) Zr vs Y and La vs Yb after Ross and Bédard (2009).

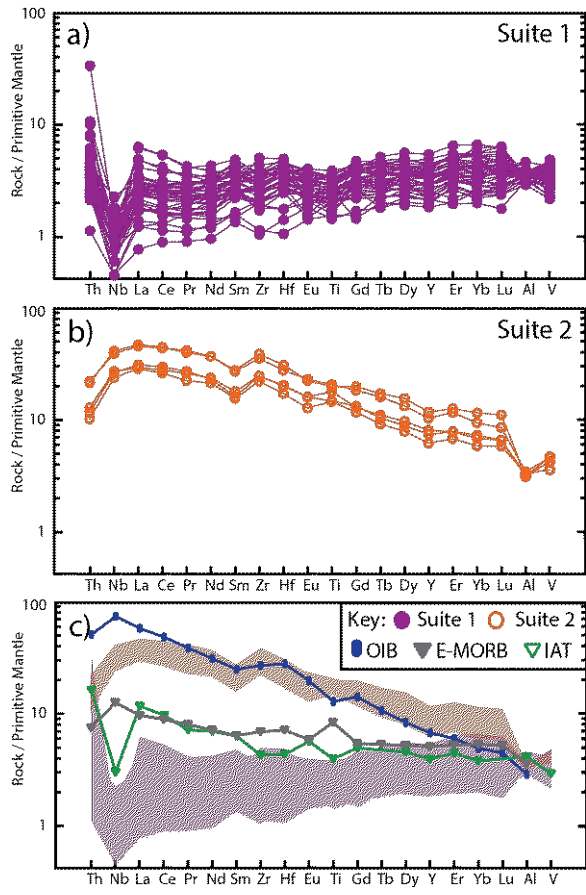


**Figure 2.13.** a-b) Primitive mantle-normalized trace element plots for the two geochemical suites of the mafic rocks proximal to the Goldenville horizon. c) Typical ocean island basalt (OIB; Sun and McDonough, 1989), enriched-mid ocean island basalt (E-MORB; Sun and McDonough, 1989) and island arc tholeiite (IAT; Stolz et al., 1990) are shown for comparison. Primitive mantle-normalized values are from Sun and McDonough, (1989).

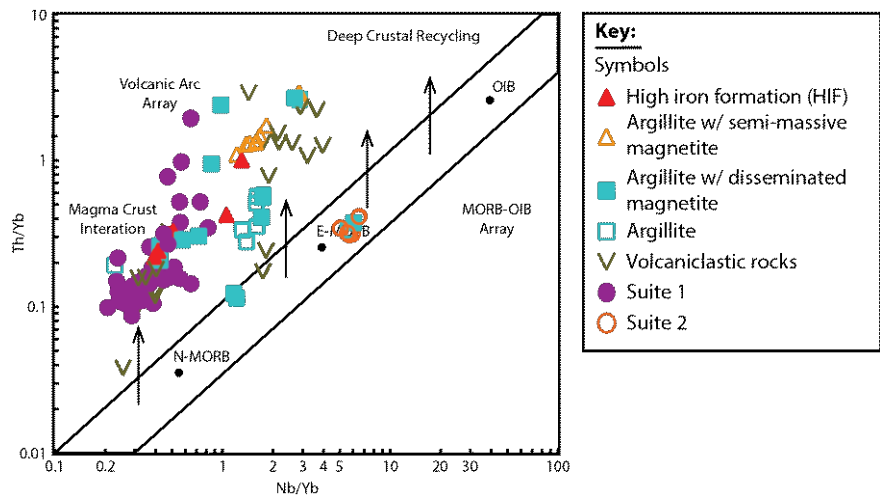


**Figure 2.14.** Th/Yb vs Nb/Yb diagram for rocks of the Goldenville horizon and surrounding stratigraphy showing grouping relationships of volcaniclastic rocks and argillite rocks relative to the basalts in the stratigraphy. Modified after Pearce (2008)

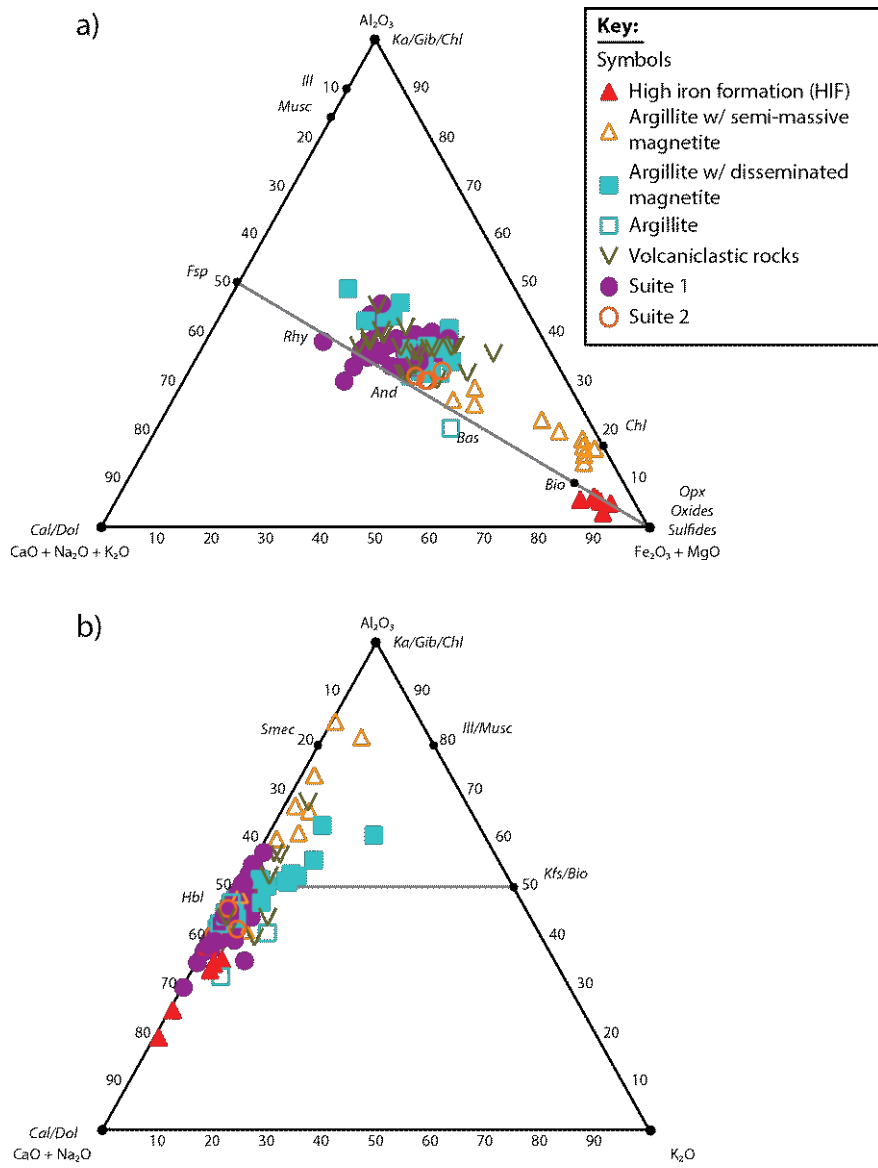


**Figure 2.15.** Molar element plots for rocks from the Goldenville horizon and surrounding stratigraphy. a)  $(\text{CaO} + \text{Na}_2\text{O}) + \text{K}_2\text{O}$ - $\text{Al}_2\text{O}_3$ - $(\text{Fe}_2\text{O}_3 + \text{MgO})$  and b)  $(\text{CaO} + \text{Na}_2\text{O})$ - $\text{Al}_2\text{O}_3$ - $(\text{K}_2\text{O})$  plots of Nesbitt and Young, (1984) and Nesbitt (2003).

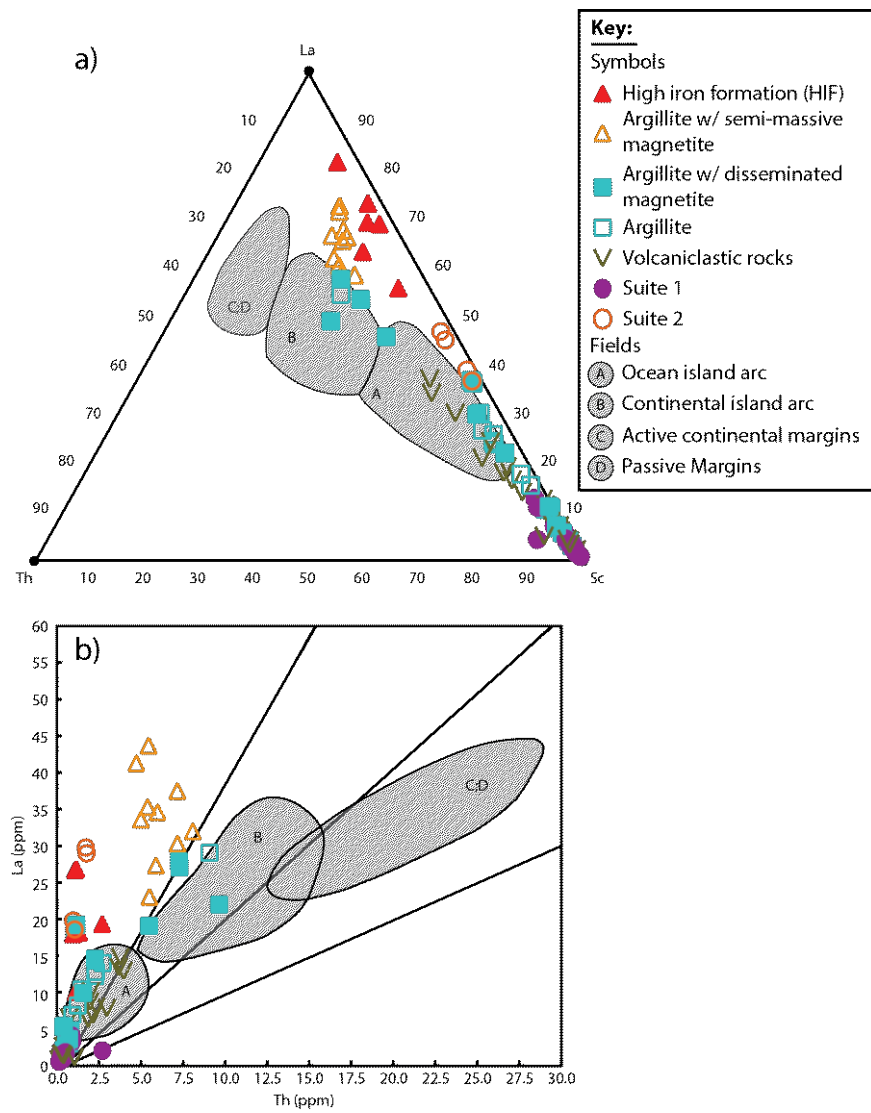


**Figure 2.16.** Discrimination diagram plots for rocks of the Goldenville horizon and surrounding stratigraphy. a-b) immobile element sediment provenance plots modified after Bhatia and Crook (1986) showing fields for various tectonic settings; iron formation samples plotted for comparison. A, ocean island arc; B, continental island arc; C, active continental margins; D, passive margins.

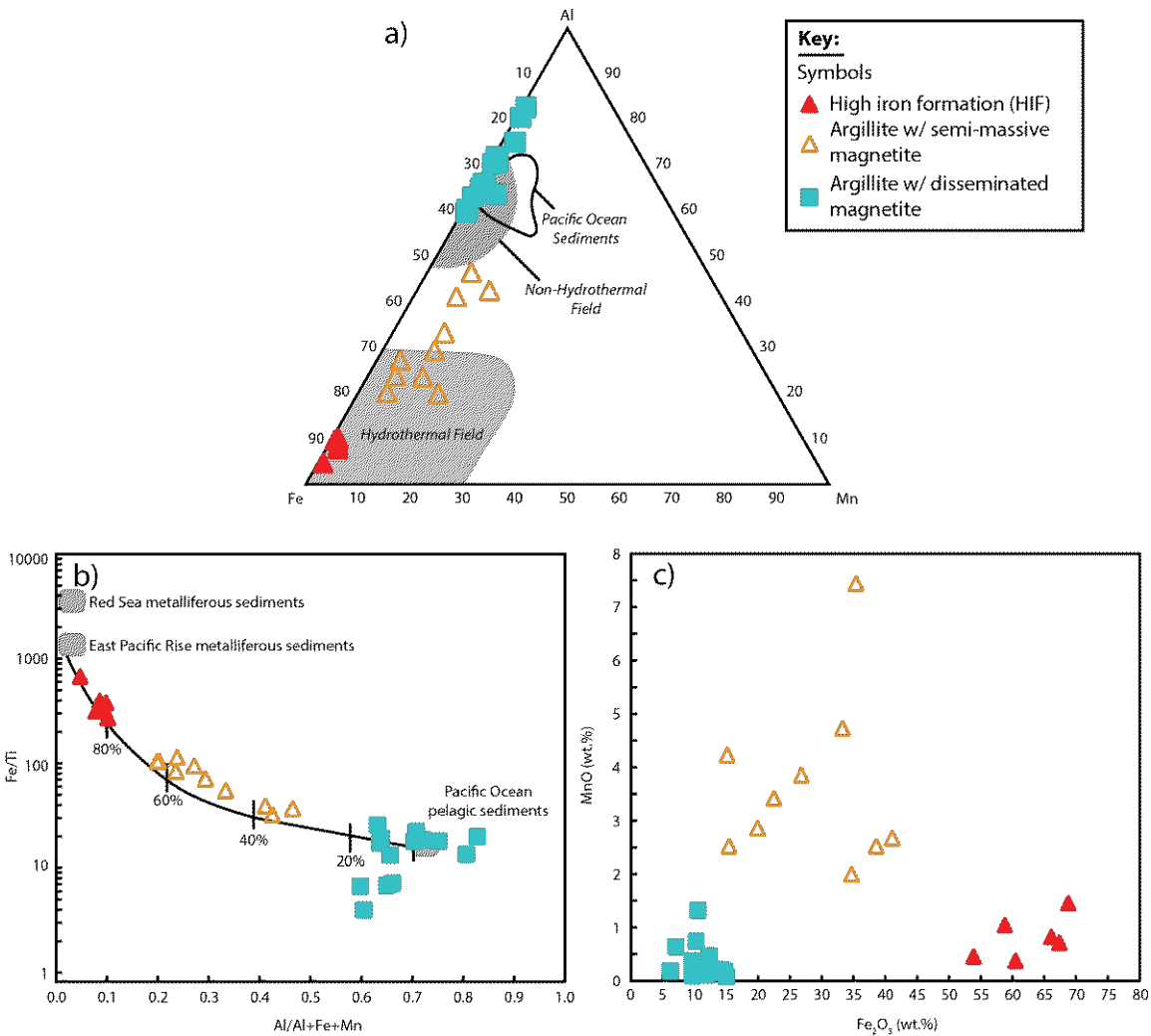


**Figure 2.17.** Boström-type plots for iron formation samples of the Goldenville horizon. a) Molar Fe-Al-Mn diagram showing relative contribution of hydrothermal versus detrital material for samples of the Goldenville horizon. b) Molar Fe/Ti-Al/(Al+Fe+Mn) Böstrom-type diagram with a mixing line between EPR metalliferous sediments and PO pelagic sediments reproduced as presented in plots of Boström (1973) due to the close fit of Goldenville horizon sample data. Diagrams modified from Boström (1973). c) Fe<sub>2</sub>O<sub>3</sub>-MnO illustrating the populations of the Goldenville horizon subgroups.

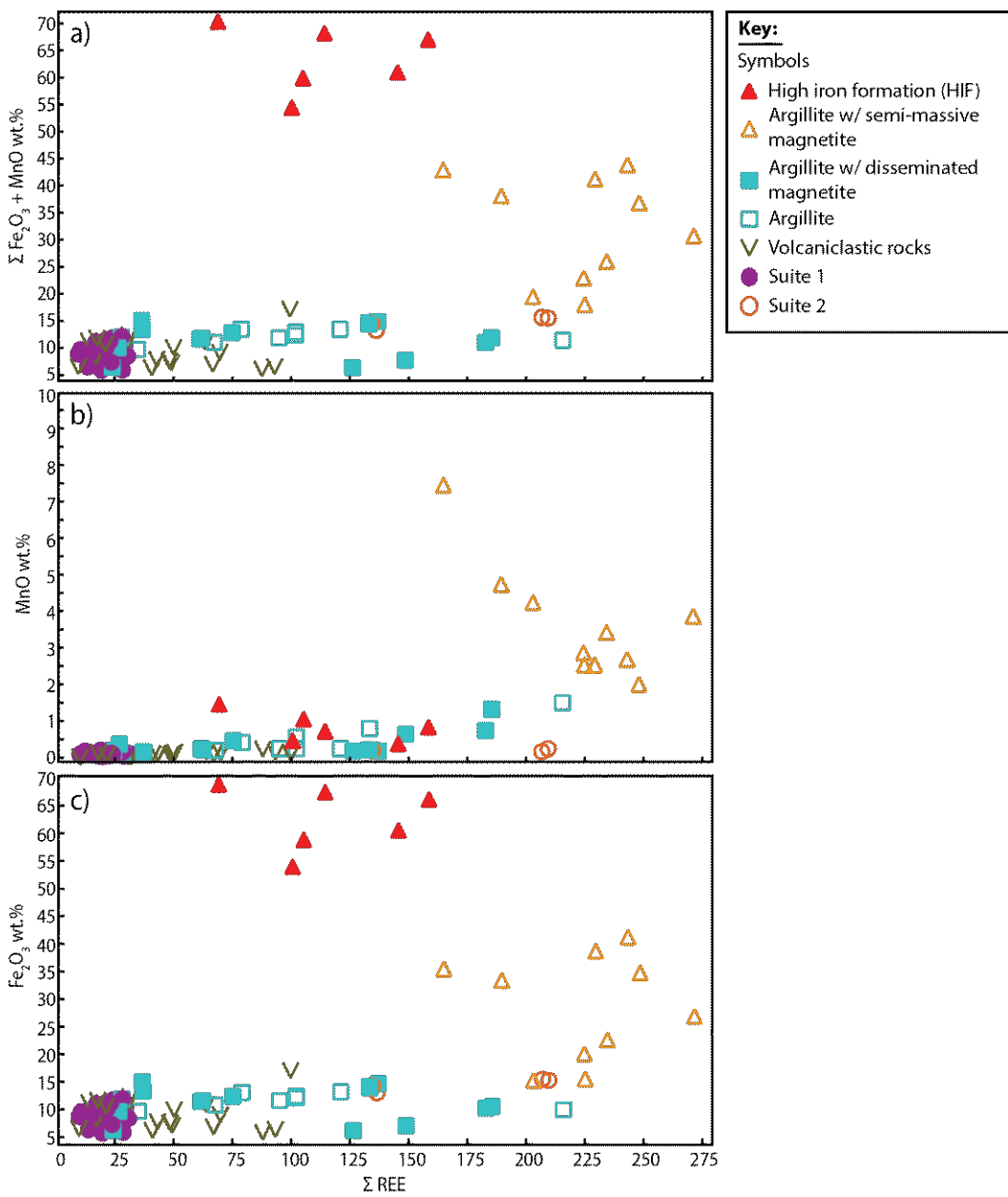


**Figure 2.18.** Abundances of  $\text{Fe}_2\text{O}_3 + \text{MnO}$ ,  $\text{MnO}$ , and  $\text{Fe}_2\text{O}_3$  wt.% in the rocks of the Goldenville horizon and surrounding stratigraphy plotted against  $\sum \text{REE}$ .

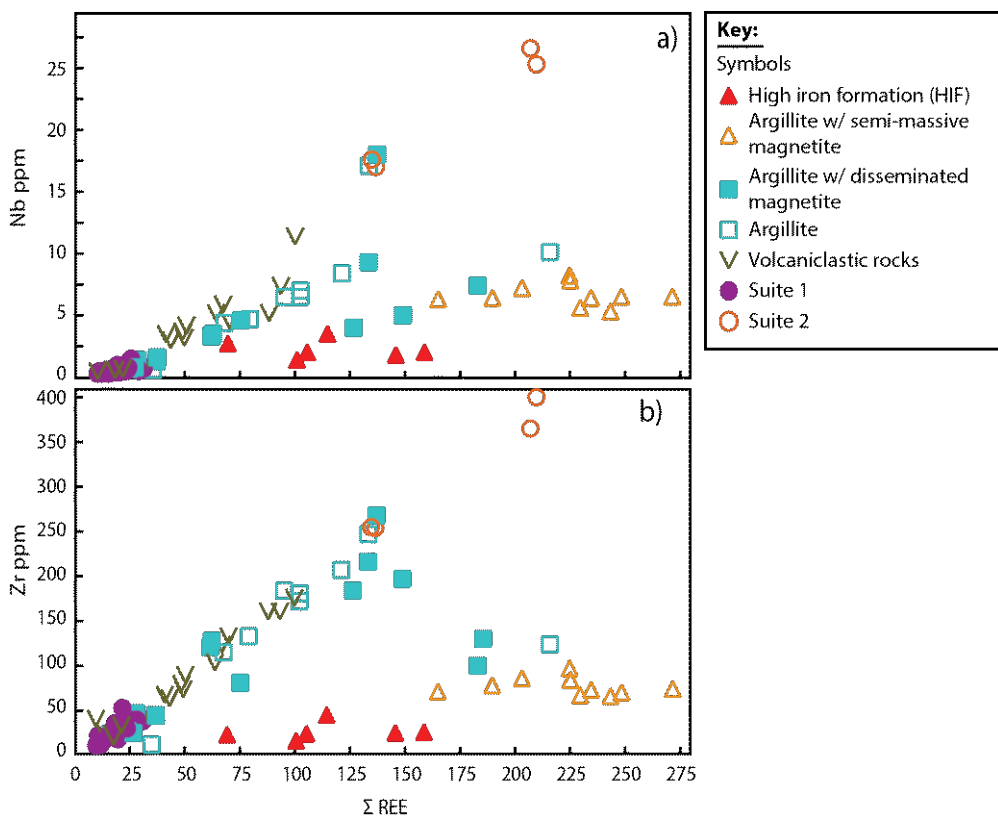


**Figure 2.19.** Total abundance of the rare earth elements ( $\Sigma$ REE) against Zr and Nb for lithologies of the Goldenville horizon and surrounding lithologies. The correlation between REE and elements indicative of detritus like Zr and Nb, suggest that REE budget in the Goldenville horizon subgroups is dominated by detritus and that the detritus is similar to the composition of the surrounding units. Further details provided in the text.

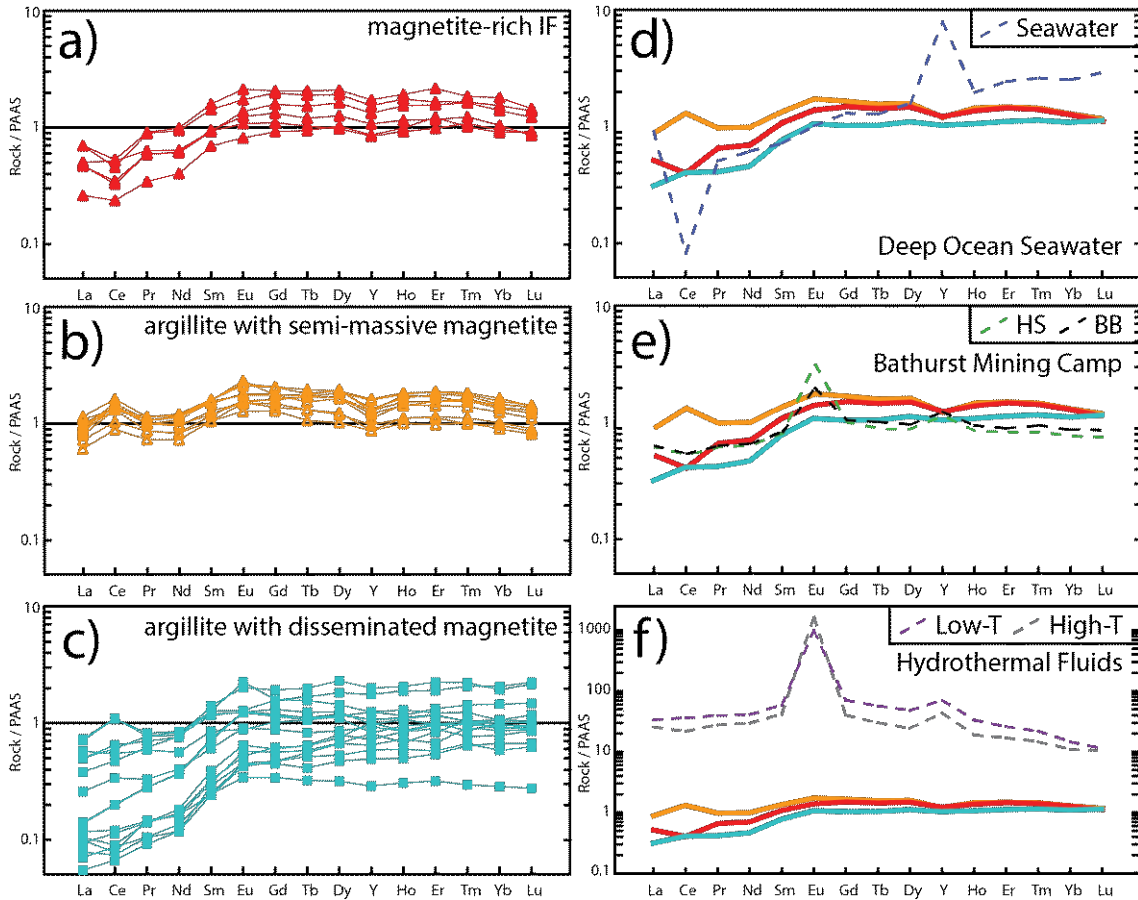


**Figure 2.20.** Post-Archean Australian Shale (PAAS) normalized rare earth element and Y plots for Fe-rich rocks from the Goldenville horizon: a) magnetite-rich, b) argillite with semi-massive magnetite and c) argillites with disseminated magnetite. PAAS values are from Pourmand et al. (2012). d-f) shows the average of each of the Goldenville horizon subgroups plotted against d) modern seawater from Alibo and Nozaki (1999), e) averages of the Bathurst mining camp hydrothermal sedimentary rocks values from Peter et al. (2003), BB = Brunswick Belt, HS = Heath Steele belt; and f) averages of the high-temperature ( $>250^{\circ}\text{C}$ , Broken Spur vent site at  $29^{\circ}\text{N}$  Mid-Atlantic Ridge) and low-temperature ( $<110^{\circ}\text{C}$ , TAG hydrothermal mound at  $26^{\circ}\text{N}$  Mid-Atlantic Ridge) hydrothermal fluid values from Bau and Dulski (1999).

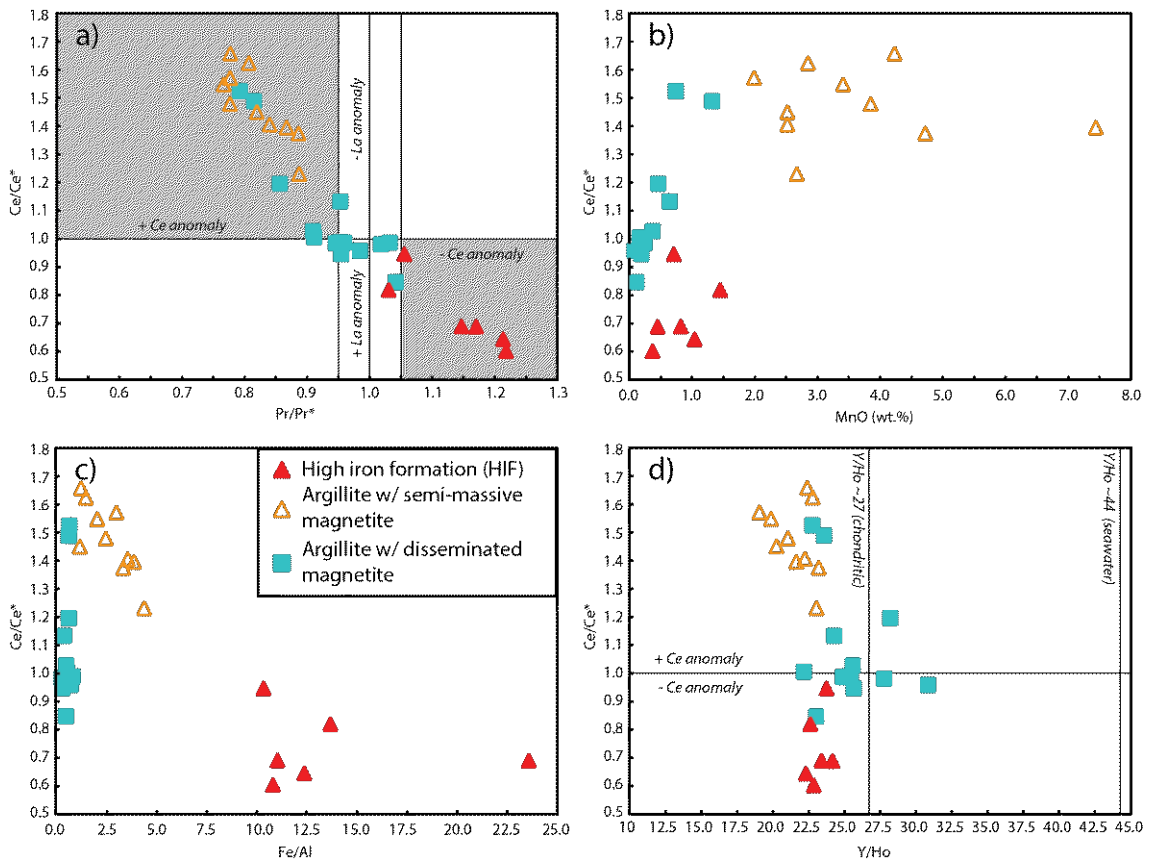


**Figure 2.21.** a)  $\text{Ce}_{\text{sn}}/\text{Ce}_{\text{sn}}^*$ - $\text{Pr}_{\text{sn}}/\text{Pr}_{\text{sn}}^*$  plot ( $\text{Ce}_{\text{sn}}/\text{Ce}_{\text{sn}}^* = \text{Ce}_{\text{sn}}/(0.5\text{La}_{\text{sn}}+0.5\text{Pr}_{\text{sn}})$ ;  $\text{Pr}_{\text{sn}}/\text{Pr}_{\text{sn}}^* = \text{Pr}_{\text{sn}}/(0.5\text{Ce}_{\text{sn}}+0.5\text{Nd}_{\text{sn}})$ ) demonstrating that the argillite with semi-massive magnetite samples have true positive Ce anomalies, whereas the magnetite-rich IF samples have true negative anomalies. Diagram after Bau and Dulski (1996) and Kamber and Webb (2001). b)  $\text{Ce}_{\text{sn}}/\text{Ce}_{\text{sn}}^*$ , calculated as  $(\text{Pr}_{\text{sn}}^*(\text{Pr}_{\text{sn}}/\text{Nd}_{\text{sn}})^2$ , versus MnO illustrating that the most positive Ce anomalies are associated with higher MnO concentrations. c)  $\text{Ce}_{\text{sn}}/\text{Ce}_{\text{sn}}^*$  versus  $\text{Fe}_2\text{O}_3$  illustrating negative Ce anomalies are associated with higher  $\text{Fe}_2\text{O}_3$  concentrations. d)  $\text{Ce}_{\text{sn}}/\text{Ce}_{\text{sn}}^*$  versus Y/Ho showing Y/Ho ratios are consistent for the samples within the Goldenville horizon (modified after Piercey et al., 2018). REE<sub>n</sub> = PAAS-normalized REE values McLennan (1989).

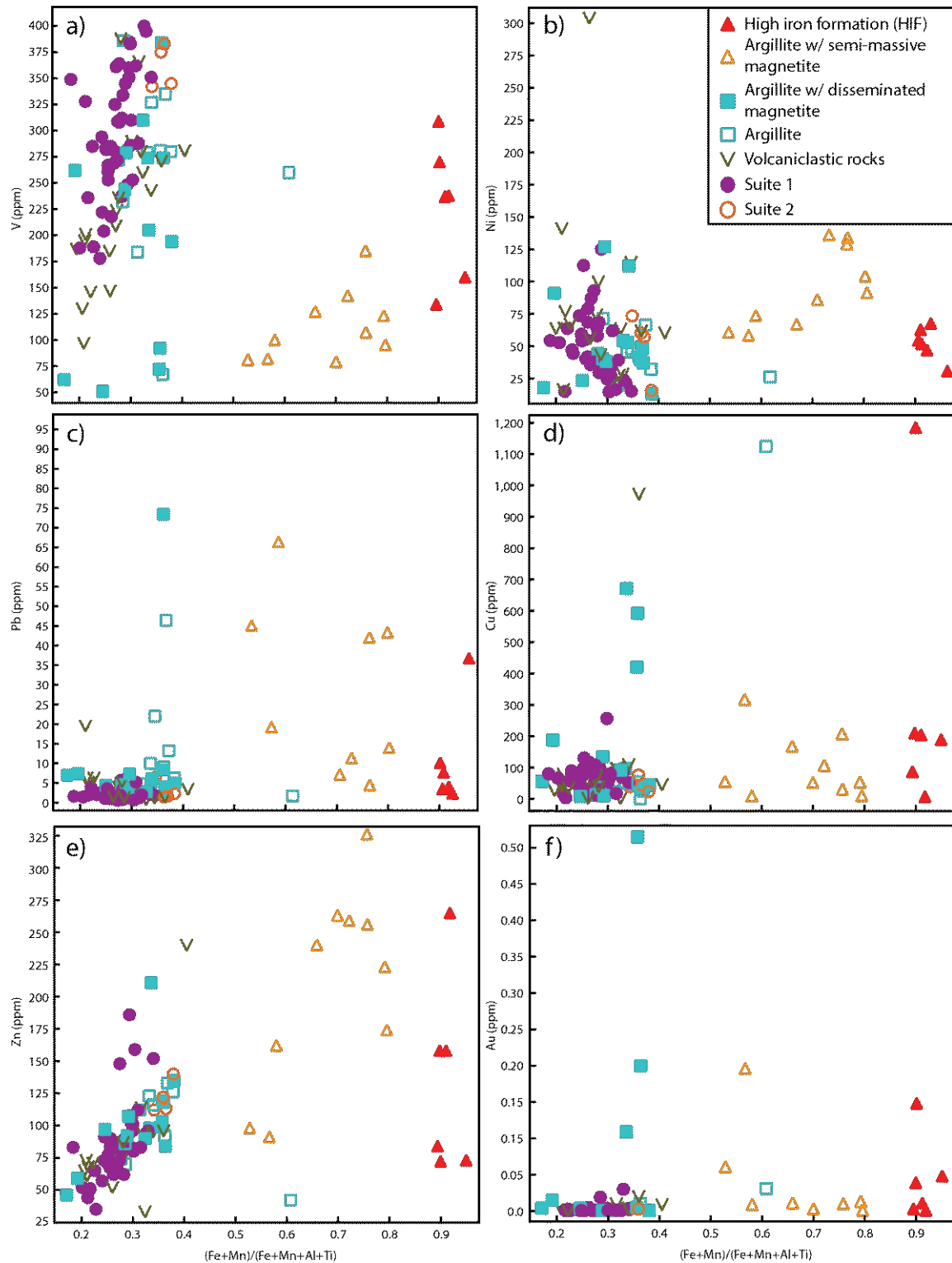


**Figure 2.22. (above)** Abundances of selected base and transition metals (V, Ni, Pb, Cu, Zn, Au) in the rocks proximal and in the Goldenville horizon plotted against  $(\text{Fe}+\text{Mn})/(\text{Fe}+\text{Mn}+\text{Al}+\text{Ti})$  molar ratios.

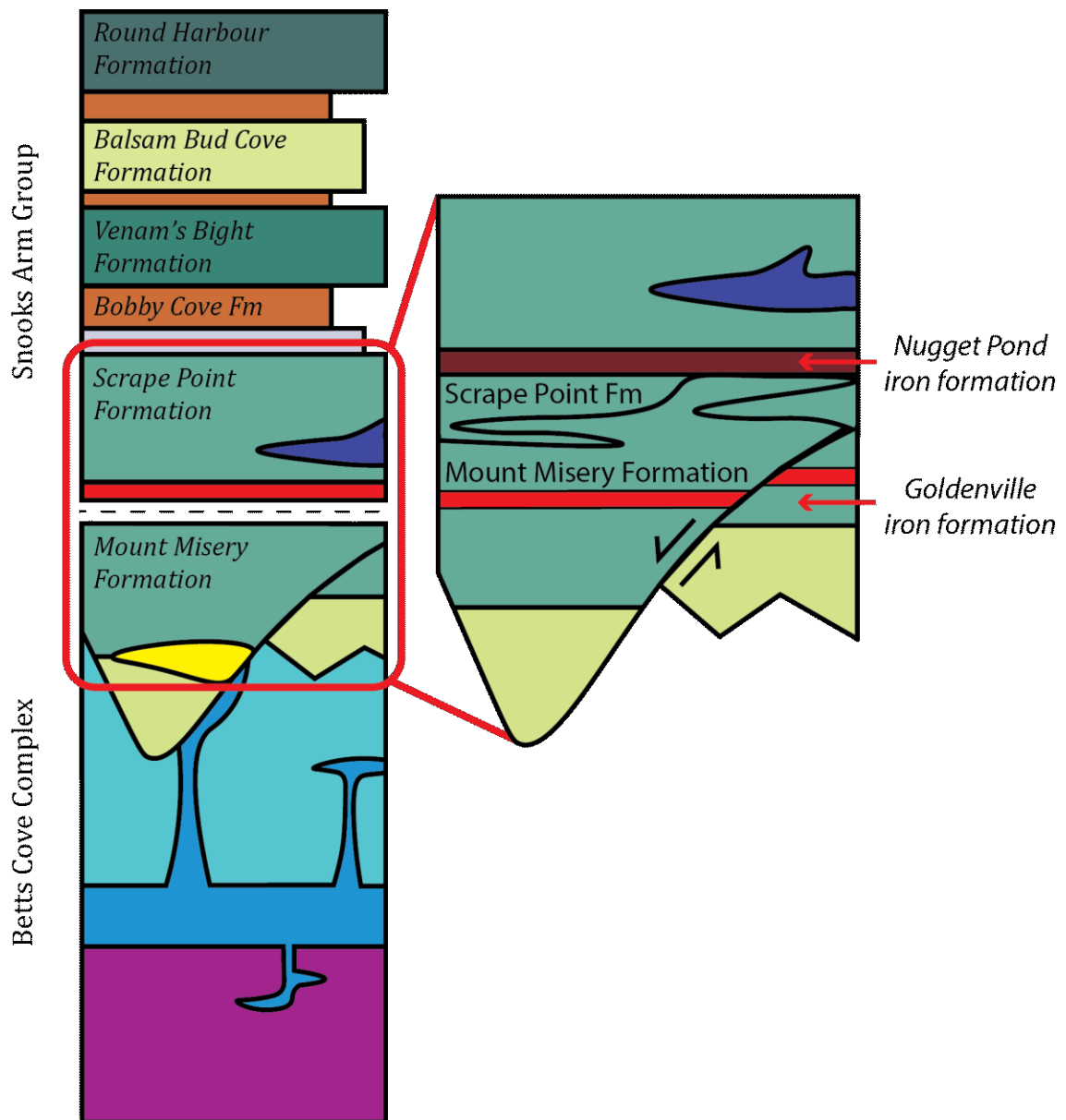


**Figure 2.23.** Representative regional stratigraphy re-interpreted of the Baie Verte Peninsula using the results of this study. Modified from Figure 2.3 after Bédard et al., (2000); Kessler and Bédard (2000); and Skulski et al., (2009).

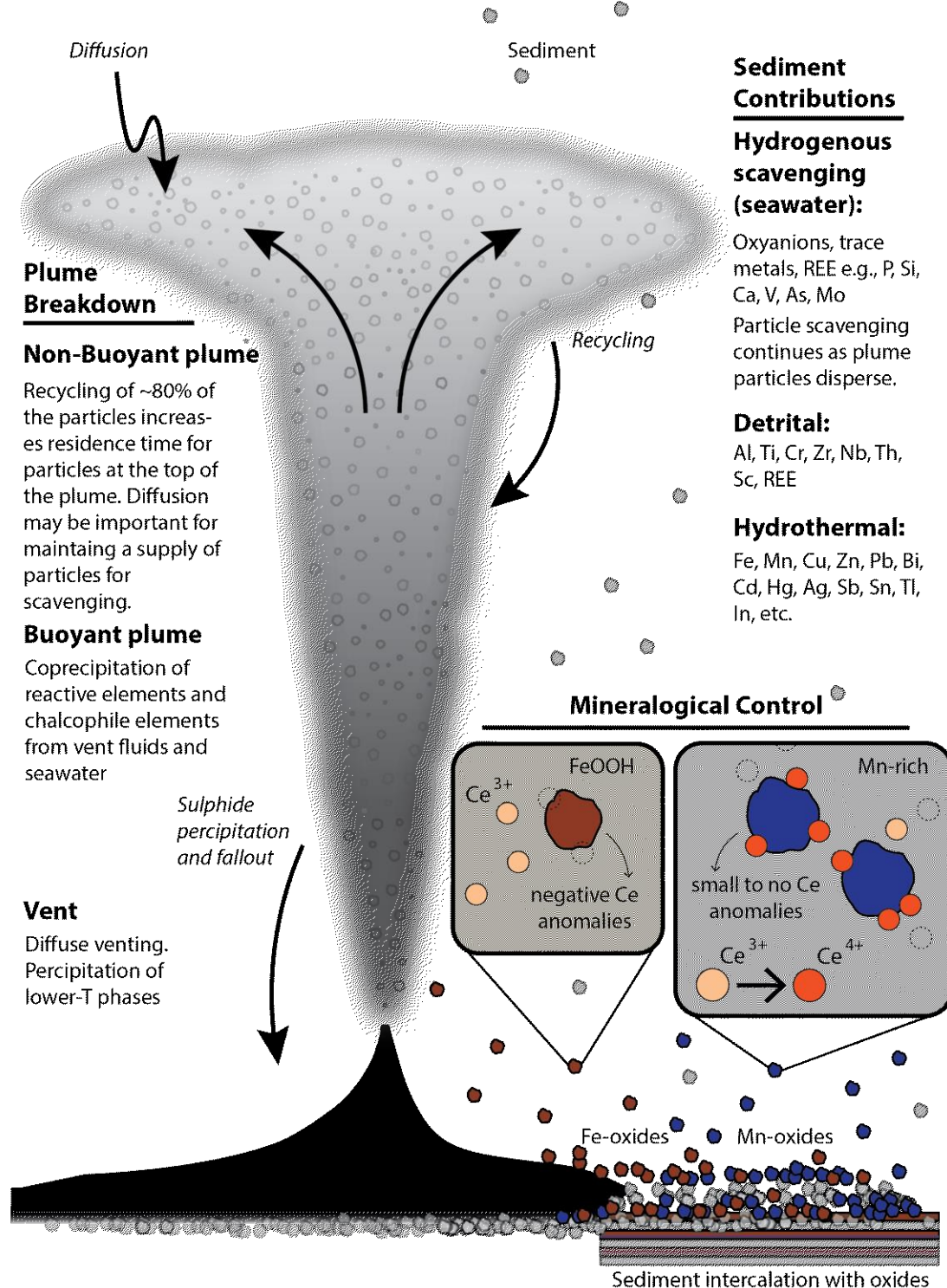


**Figure 2.24. (above)** Representative hydrothermal plume with processes depicted for buoyant, non-buoyant plume, and overall sediment contribution. Inset showing mineralogical control of Fe-oxides versus Mn-oxides related to Ce adsorption while suspended in the water column. Modified from; Rudnicki (1995); Peter (2003); and Lode et al., (2016).

## **Chapter 3: Summary and Future Research**

---

### **3.1 Summary**

The Goldenville Au deposit is hosted by an iron formation (Goldenville horizon) belonging to the Mount Misery Formation of the Snooks Arm Group, Baie Verte Peninsula, Newfoundland, Canada. The Goldenville horizon includes the iron formation and associated Fe-rich sedimentary units, and is an ideal unit to study the stratigraphy, exhalative sediments attributed to a hydrothermal plume, ocean paleoredox conditions at the time of deposition within the Cambrian-Ordovician (~489-485 Ma), and relationships to base metal and Au mineralization. Furthermore, the Goldenville iron formation has been considered analogous to the Nugget Pond iron formation, a horizon defining the transition between the ophiolite (Betts Cove Complex) and the cover sequence (Snooks Arm Group), and host to the past-producing Nugget Pond gold deposit. Early interpretations of the stratigraphic position of the Goldenville deposit produced exploration programs guided by mineralization relationships at Nugget Pond rather than defined geochemical characteristics unique to the Goldenville iron formation. This study was designed to test whether the Goldenville and Nugget Pond horizons are stratigraphically similar and also elucidate the mineralization styles and potential paleoredox of the Humber seaway during the Cambrian-Ordovician. The major conclusions from this thesis are as follows:

- 1) The Goldenville horizon is hosted within and contains footwall basalts with IAT geochemical affinities interpreted to be the Mount Misery Formation. Whereas the uppermost hanging wall contains E-MORB affinities interpreted to

be the Scrape Point Formation. This locale represents a transition that is intercalated to transitional with signatures both being present within cm of each other in the hanging wall;

- 2) The re-evaluated stratigraphic position of the Goldenville horizon within the Mount Misery Formation indicates that: 1) the Nugget Pond and Goldenville iron formations are not stratigraphically equivalent; and 2) given that there are multiple iron formations, the presence of an iron formation alone can not be used as a distinct marker horizon between the Mount Misery Formation and the overlying Snooks Arm Group;
- 3) The Goldenville horizon rocks contain = a dominate role of oxide-scavenged REE material despite having enough detrital material (>3%) that would otherwise overprint primary seawater signatures, thus allowing the use of REE to evaluate redox conditions at the time of deposition. Oxide features of the Goldenville horizon influenced the REE systematics where Mn-rich rocks have positive Ce anomalies on shale normalized REE plots and Fe-rich rocks have negative Ce anomalies. This is a result of preferential adsorption of Ce by Mn and the subsequent stabilization of Ce as  $Ce^{4+}$  in Mn-rich layers in oxygenated bottom waters; and
- 4) Gold, observed in a limited quantity, occurred along the edges of quartz veins associated with Fe-rich wall rock within the Goldenville horizon. It is interpreted that this relationship could represent epigenetic gold rather than syngenetic gold, typical of iron formation-hosted Orogenic Au deposits.

### **3.2 Future Research**

The results from this study on the Goldenville iron formation provide interesting opportunities for further academic work to improve understanding of the stratigraphy, geochemistry, and metallogeny of the Baie Verte Peninsula. Potential future research topics to expand this work include:

- 1) Redefining the regional relationship and evaluating the contact between the Mount Misery and Scrape Point formations. Results of this study show that the contact between the two units is not universally as distinct as previously thought and further geochemical work on this transition is recommended. Given that the Goldenville and Nugget Pond horizons may not be a regional marker unit as previously suggested, it is critical to understand the stratigraphic relationships between the Mount Misery and Scrape Point formations regionally. This has implications for both base metal and gold exploration and is required so as to provide a more accurate framework for focused exploration;
- 2) A comparative study between the hydrothermal vent related sediments of the Goldenville horizon and VMS deposits at the same stratigraphic level of the in the Baie Verte Peninsula to define and establish their relationship, if any. Further regional evaluation coupled with detailed lithogeochemistry to define areas with minimal time spent in the water column to pinpoint the closest extent to a vent are needed to establish if the Goldenville horizon could represent exhaust from the systems. Characterizing the relationship between

the Goldenville horizon could further define the horizon as a vectoring tool for vent-proximal and vent-distal signatures related to concealed VMS mineralization and add to its' use as an exploration tool;

- 3) Further comparative stratigraphic, geochemical, and microanalytical work is needed to elucidate the differences between the Nugget Pond and Goldenville iron formations. Understanding the key differences between a past-producing iron formation (e.g., Nugget Pond) to, in relation, barren iron formation (e.g., Goldenville) may help evaluate whether genetic processes or exploration/development intensity explain the differences in gold production from these two iron formations;
- 4) Previous work on the Goldenville horizon by numerous researchers has suggested that gold is syngenetic. Additional petrography of the Goldenville horizon zones that host gold mineralization is suggested to elucidate the hypothesis the gold is syngenetic as suggested by this study. Furthermore, these findings should be compared to petrography of gold mineralization of the Nugget Pond horizon to complement further work as suggested in 3);
- 5) Given new information that the Nugget Pond iron formation represents a younger iron formation than the Goldenville, it is possible to evaluate the ocean redox evolution within the Humber seaway as it evolved by comparing the evolution of redox sensitive trace elements in both iron formations. Critical to this, however, will be establishment of better age constraints (using high precision U-Pb geochronology) on both the Goldenville horizon and Nugget

Pond horizon in order to calibrate redox results to other coeval environments globally; and

- 6) Detailed high-precision geochemical analysis of sub-sampled detrital poor zones, chert-rich horizons, and hematite-rich units within the iron formation to obtain REE signatures and other paleo-redox proxies (e.g., Mo, V, and U) that are not obscured by detrital signatures. This would allow for a more definitive interpretation of the paleoredox conditions of the Humber seaway.

## **Appendices**

---

### **Appendix A. Graphic Logs**

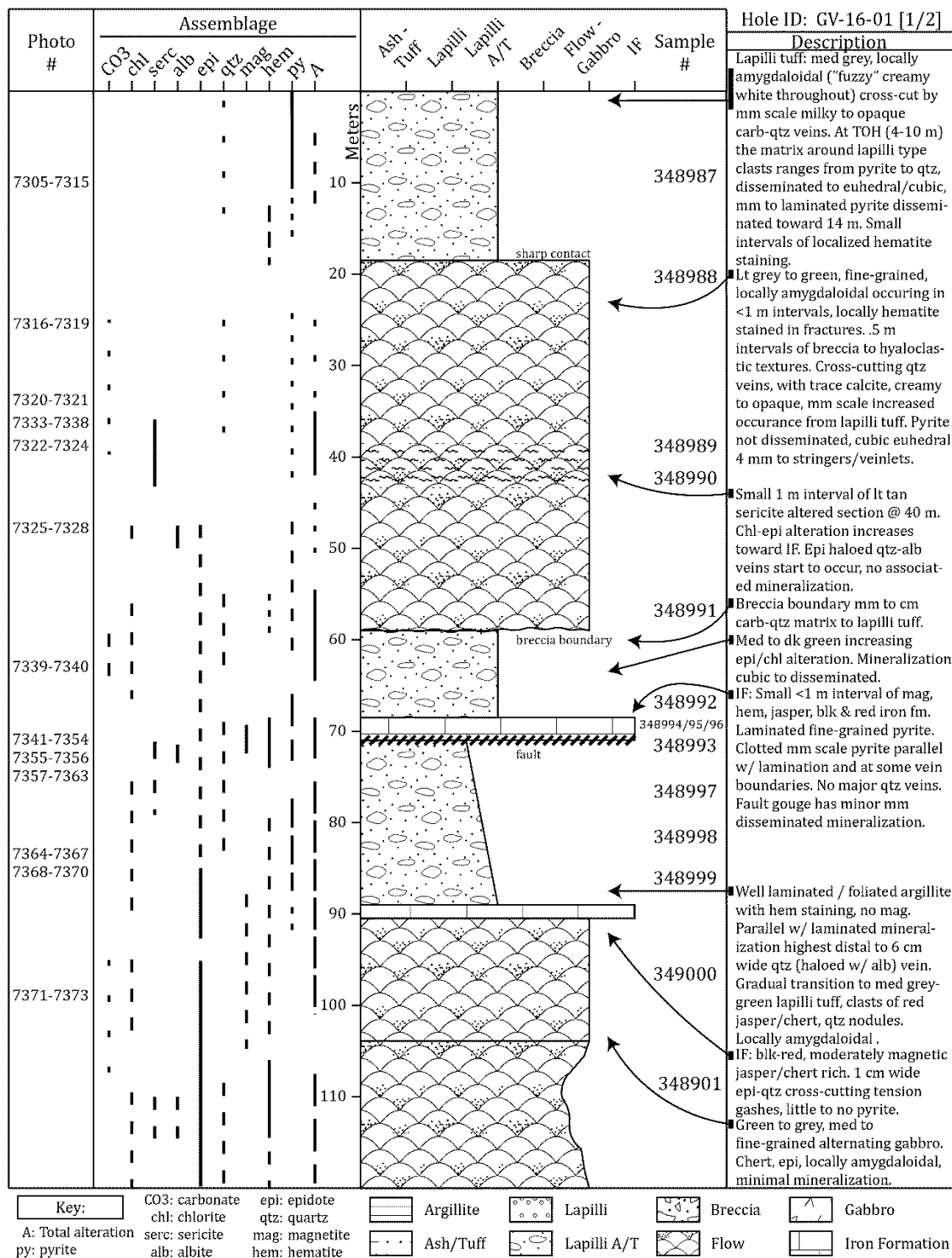
## Appendix A.I Abbreviations and legend for graphic logs

Alteration:		Lithology		
—	Strong		Argillite	
- - -	Moderate			Pillow Basalt to Basalt Flow
....	Weak			
CO3:	Carbonate		Ash/Tuff	
chl:	Chlorite			Gabbro / Intrusion
serc:	Sericite		Lapilli	
alb:	Albite			IF: Iron Formation
epi:	Epidote		Lapilli Ash/Tuff (Lapilli A/T)	
qtz:	Quartz			Significantly Altered/ Foliated
mag:	Magnetite/general magnetism			
hem:	Hematite		Breccia	
py:	Pyrite			Fault
A:	Total alteration			— Dyke, Sill, or thin unit

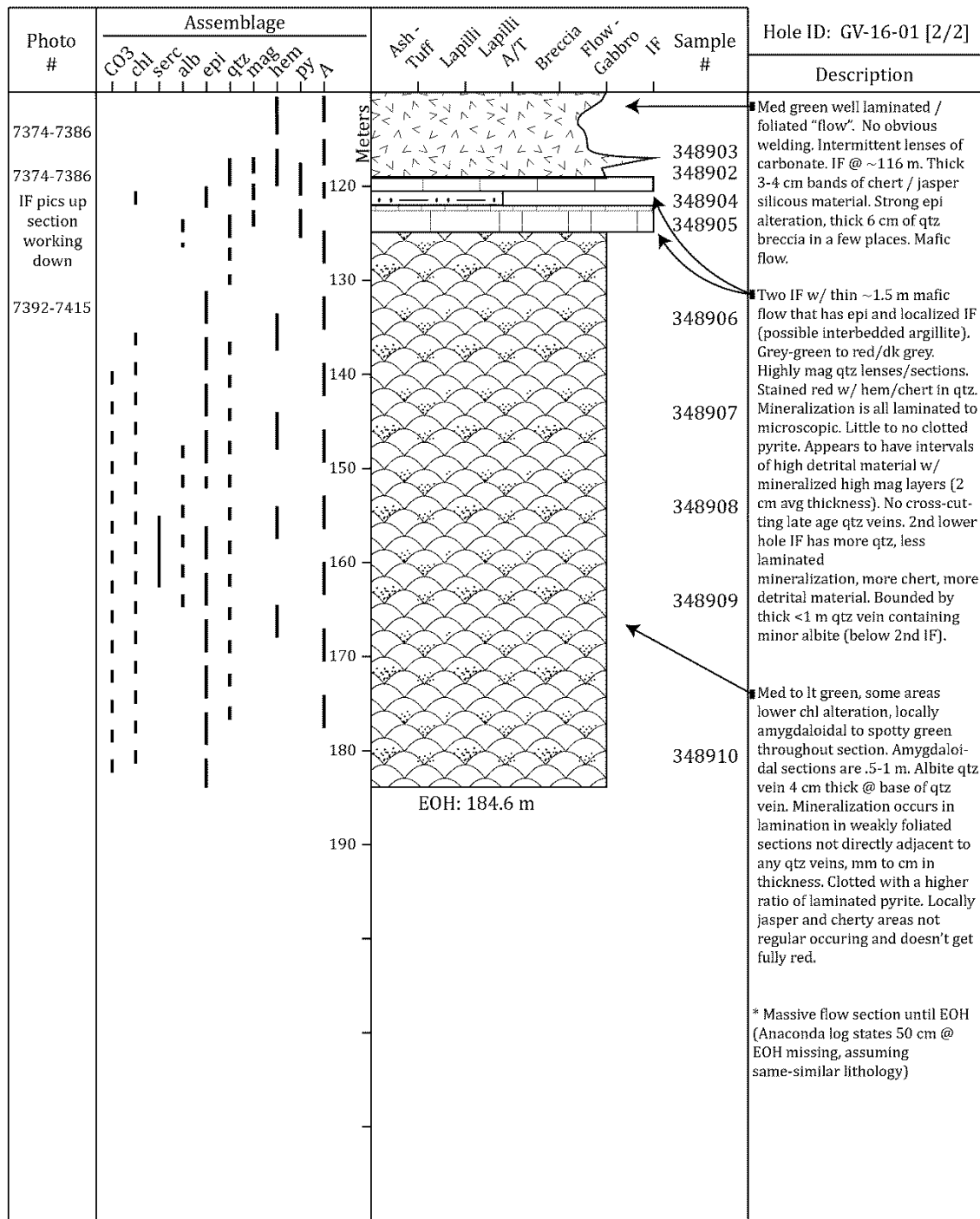
### Abbreviations:

TOH: Top of Hole	TOS: Top of Section
EOH: End of Hole	EOS: End of Section
Dk: Dark	Alt: Alteration/ altered
Med: Medium	cal/calc: Calcite
Lt: Light	carb: Carbonate
w/: With	blk: Black
w/in: Within	bwn: Brown
m: Meter	fm: Formation
cm: Centimeter	lg: Large
mm: Millimeter	

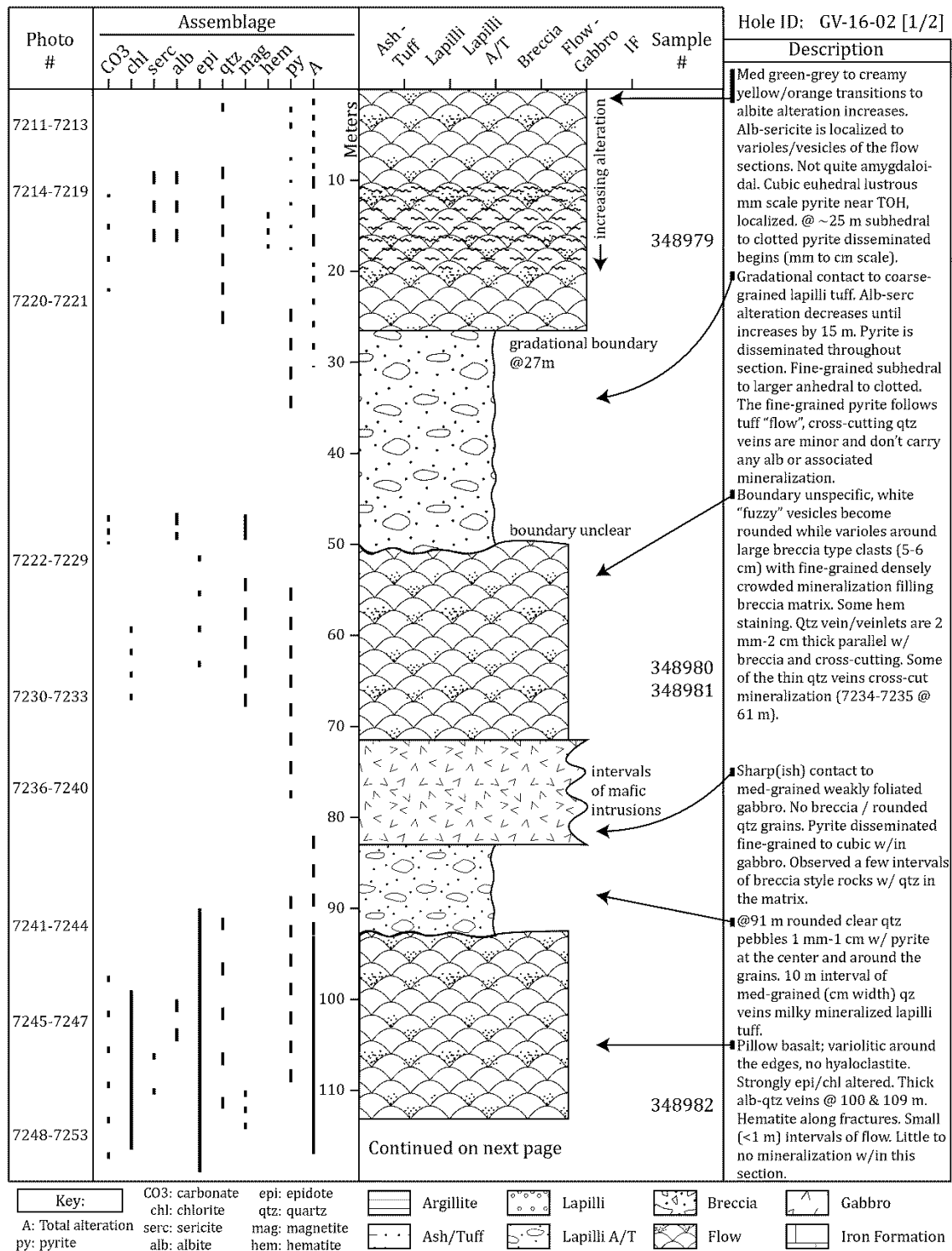
## Appendix A.II Graphic logs from the 2016 drill program



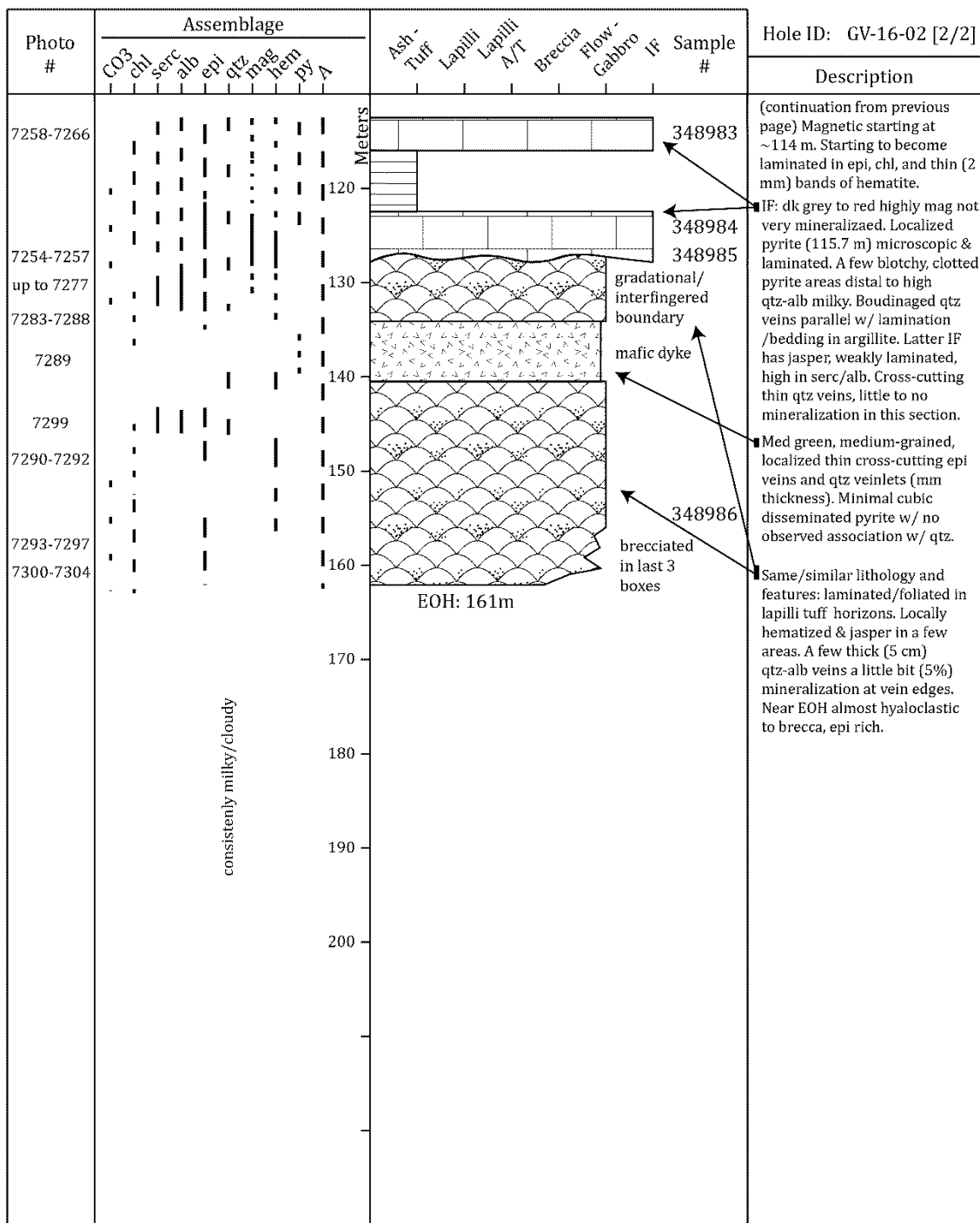
## Appendix A.II (continued) Graphic logs from the 2016 drill program



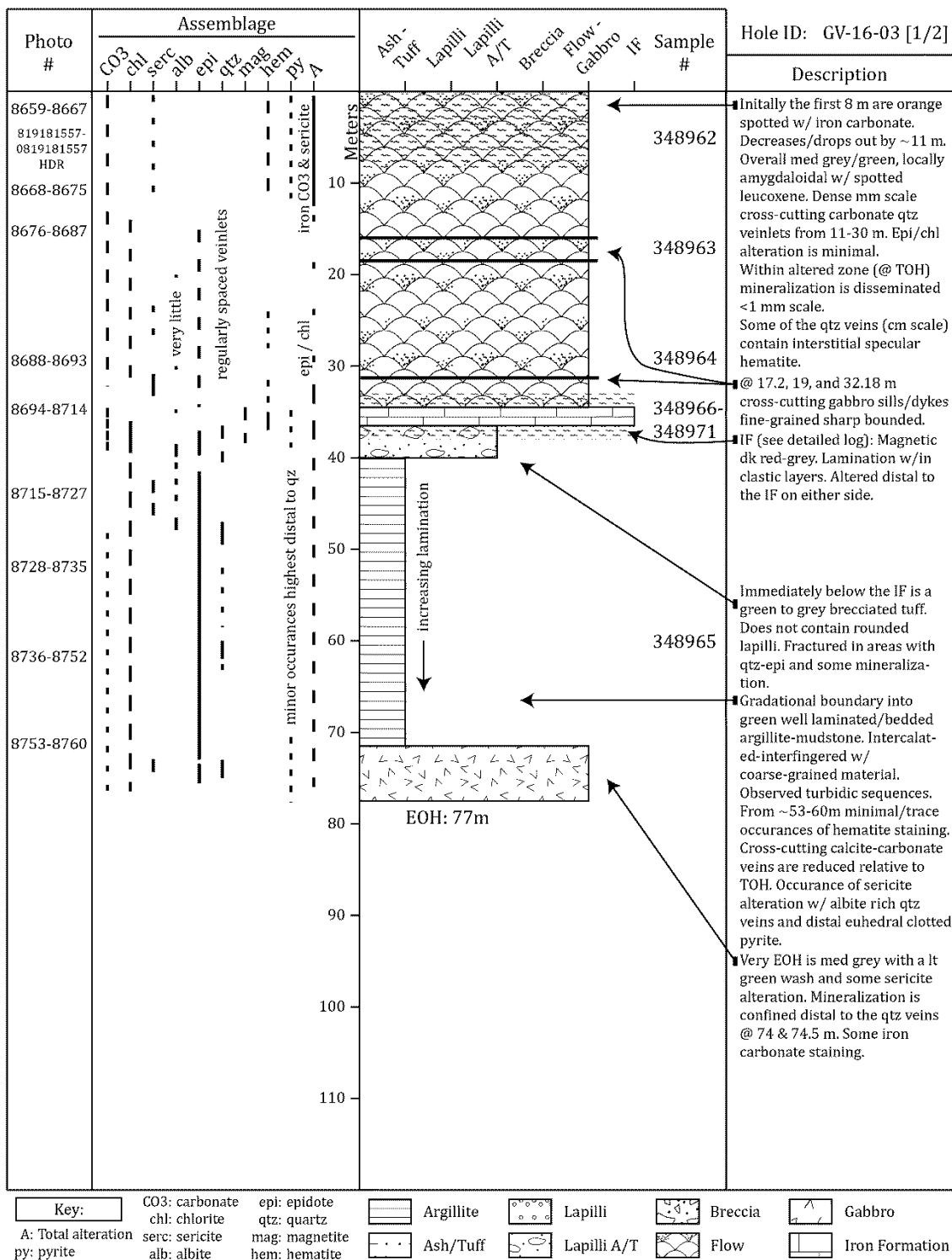
## Appendix A.II (continued) Graphic logs from the 2016 drill program



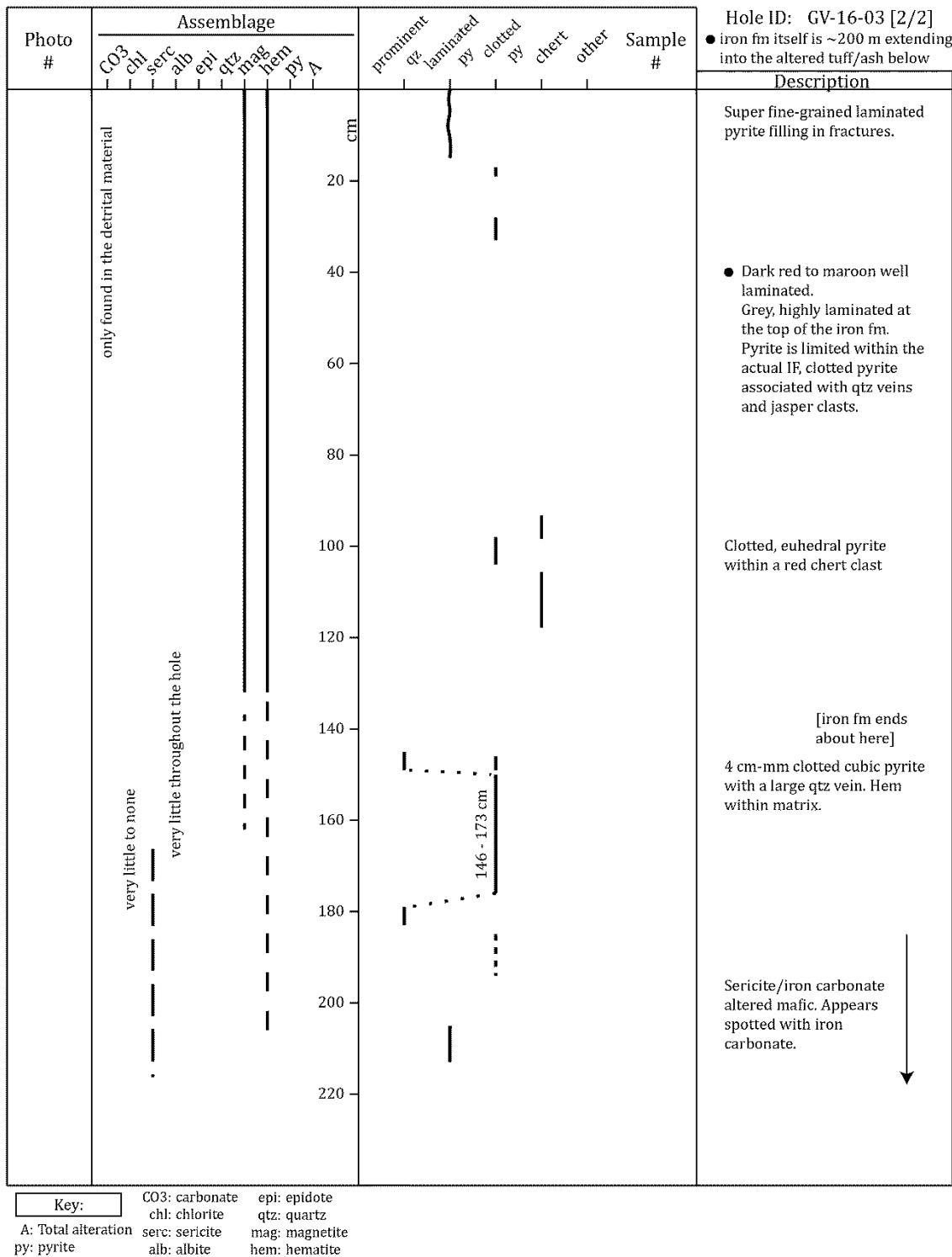
**Appendix A.II (continued) Graphic logs from the 2016 drill program**



## Appendix A.II (continued) Graphic logs from the 2016 drill program



## **Appendix A.II (continued) Graphic logs from the 2016 drill program**



Key:

CO<sub>3</sub>: carbonate

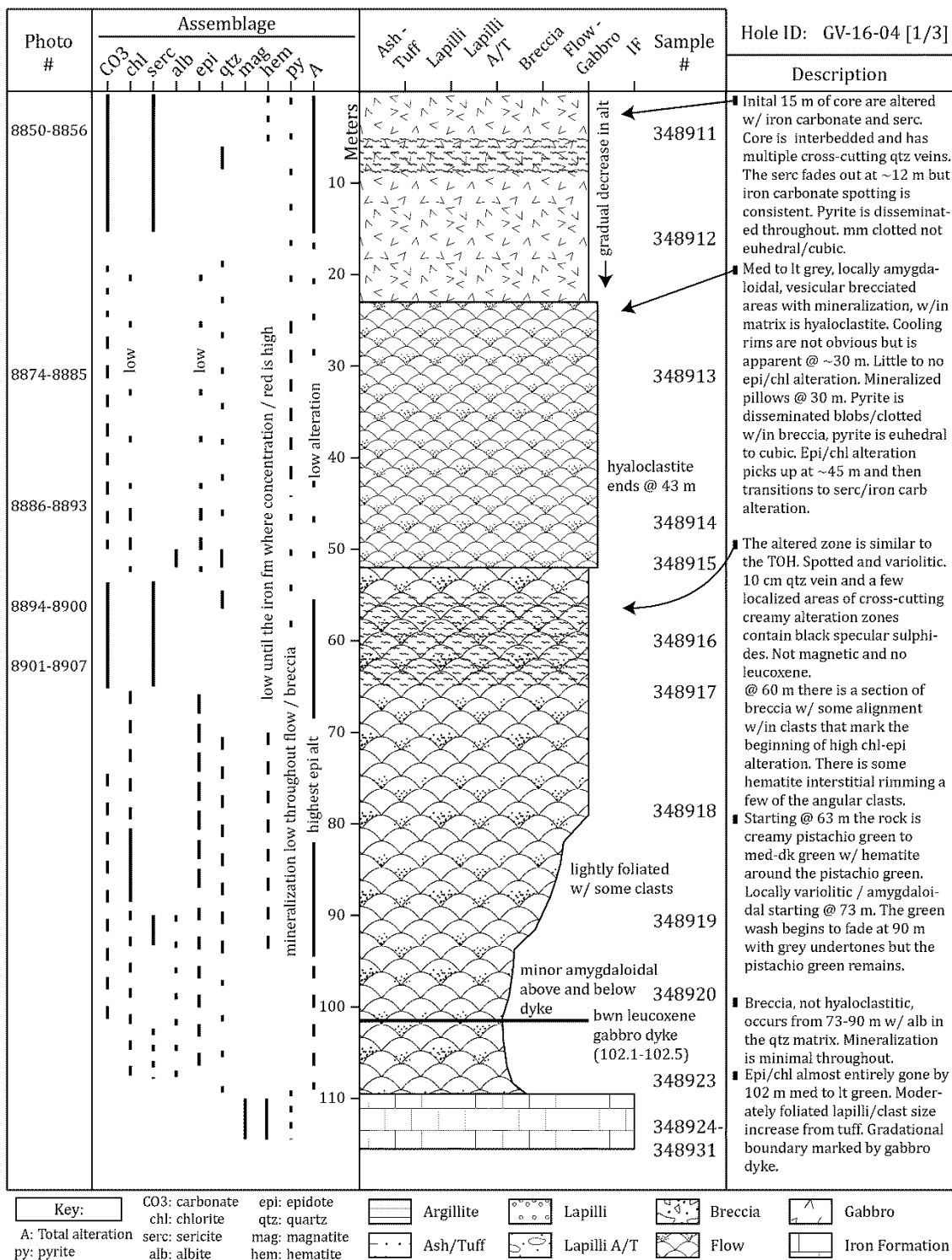
### epidote

A: Total alteration  
by: pyrite

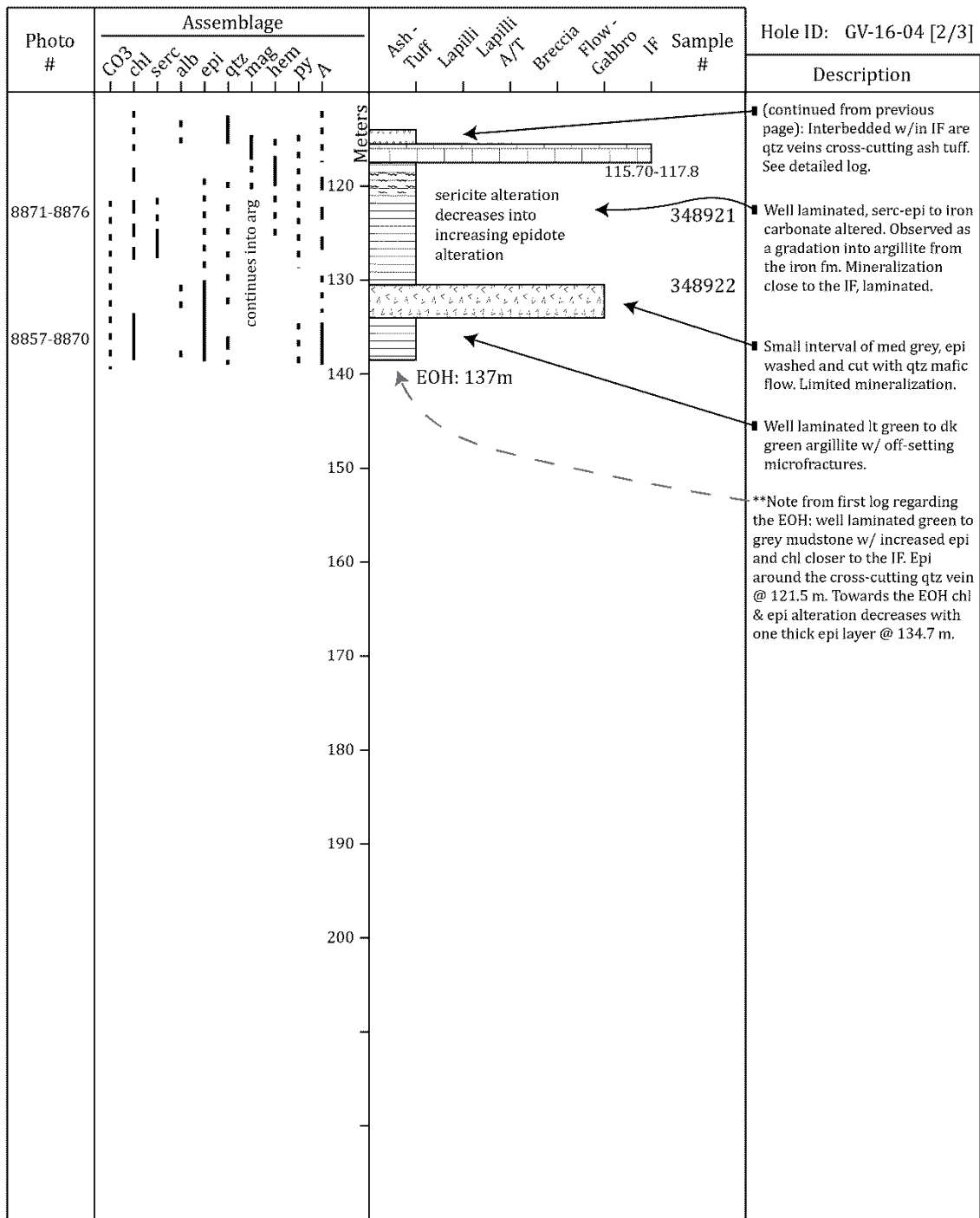
chl: chlorite  
serc: sericite  
alb: albite

quartz  
magnetite  
hematite

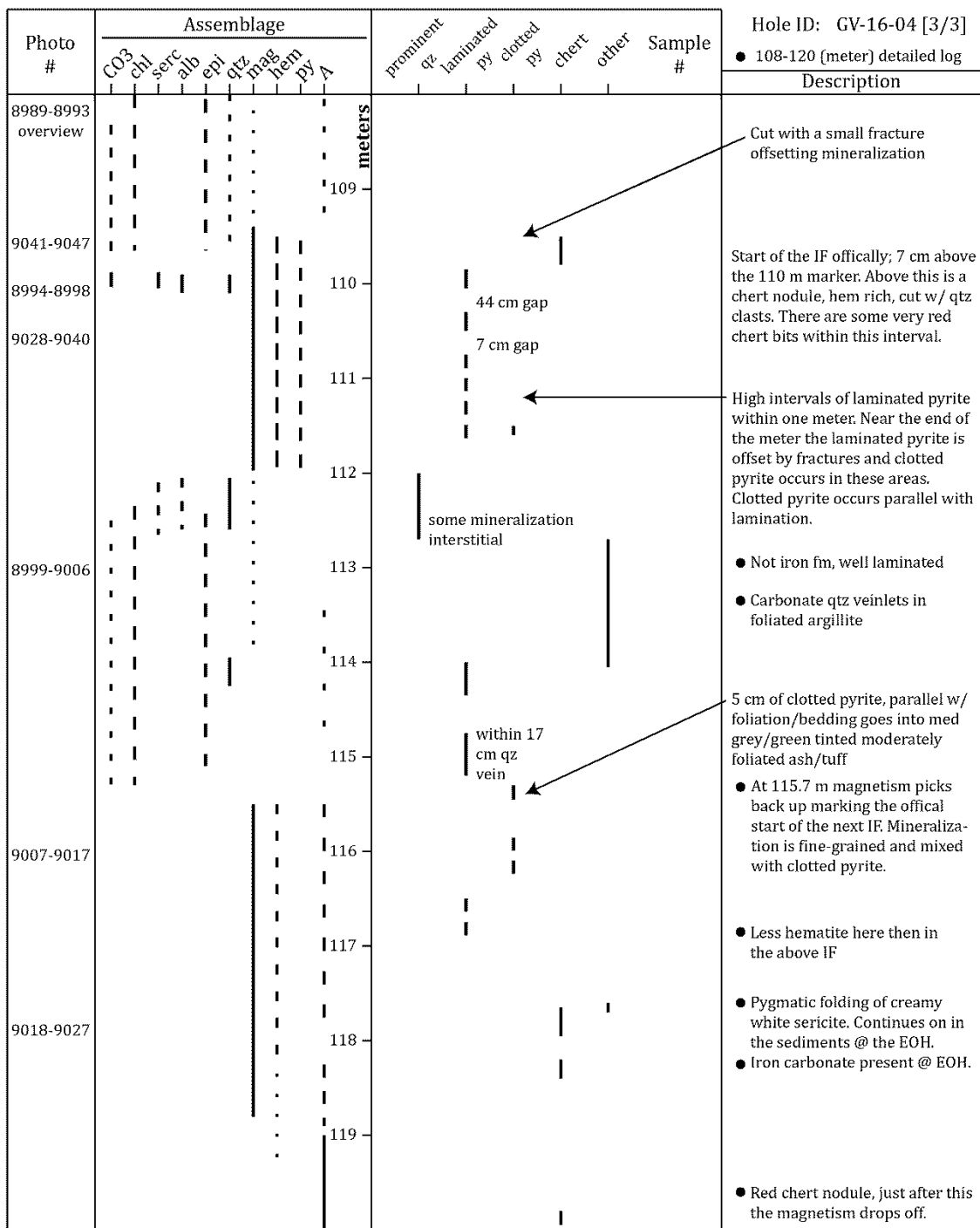
## Appendix A.II (continued) Graphic logs from the 2016 drill program



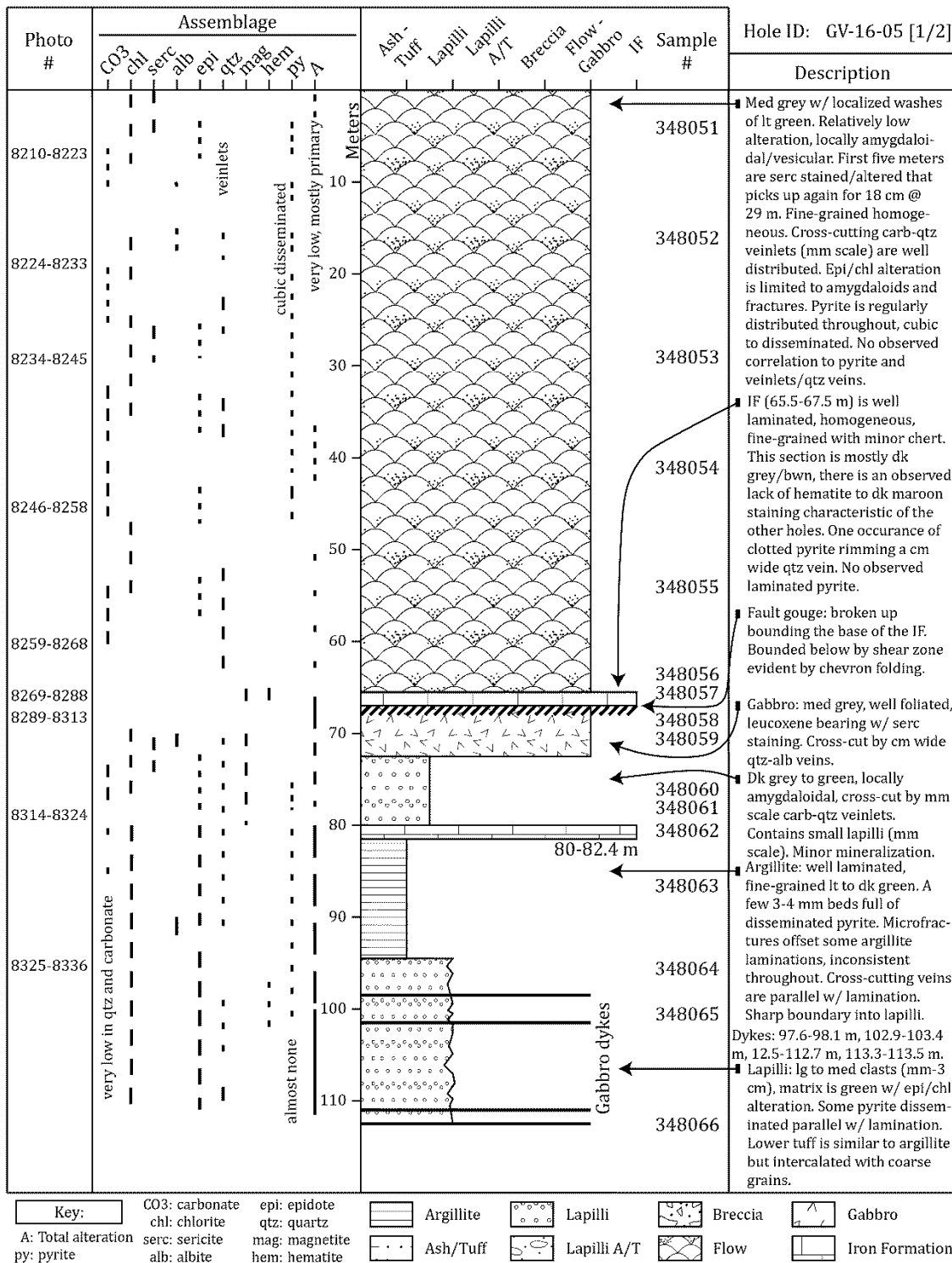
## **Appendix A.II (continued) Graphic logs from the 2016 drill program**



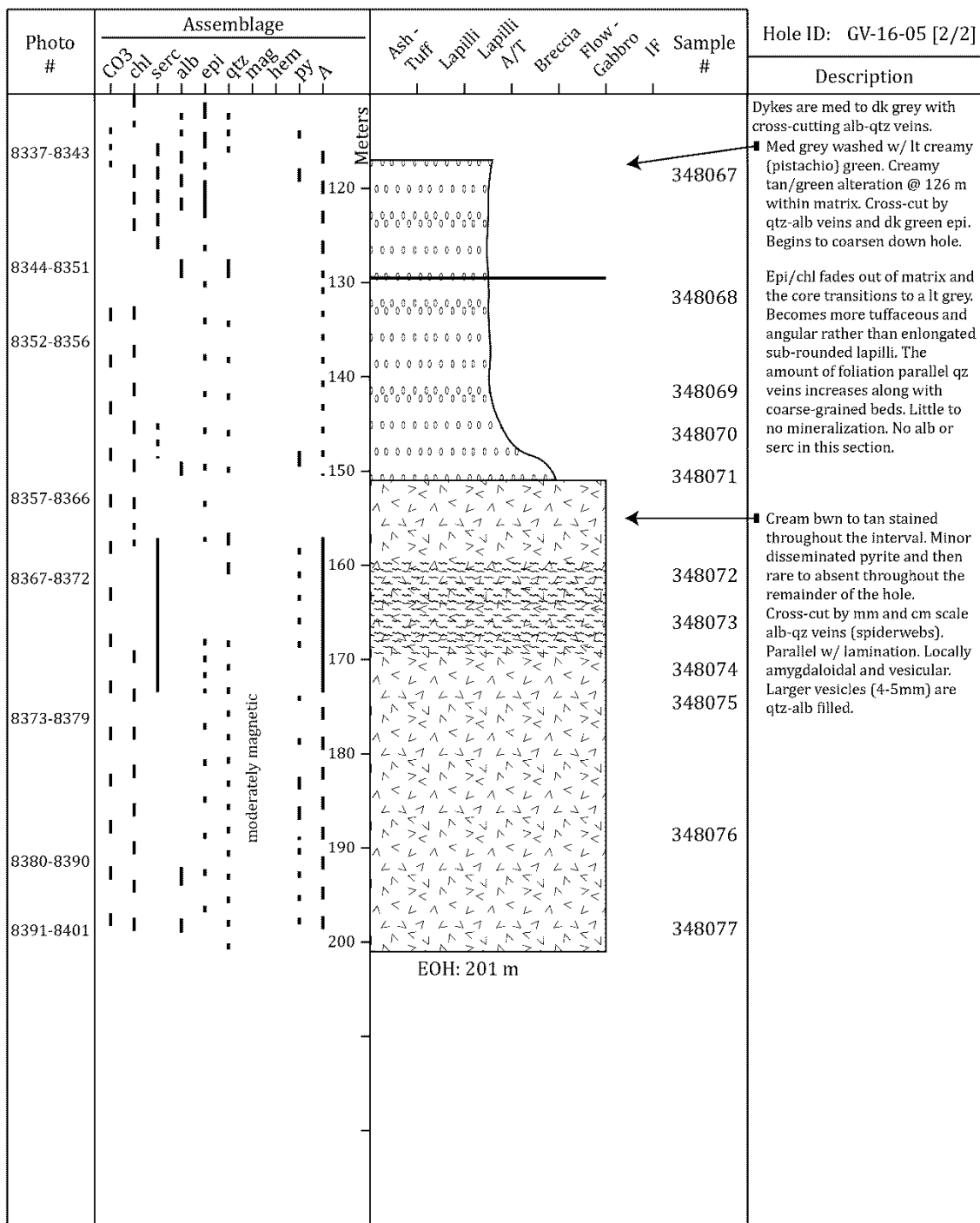
## Appendix A.II (continued) Graphic logs from the 2016 drill program



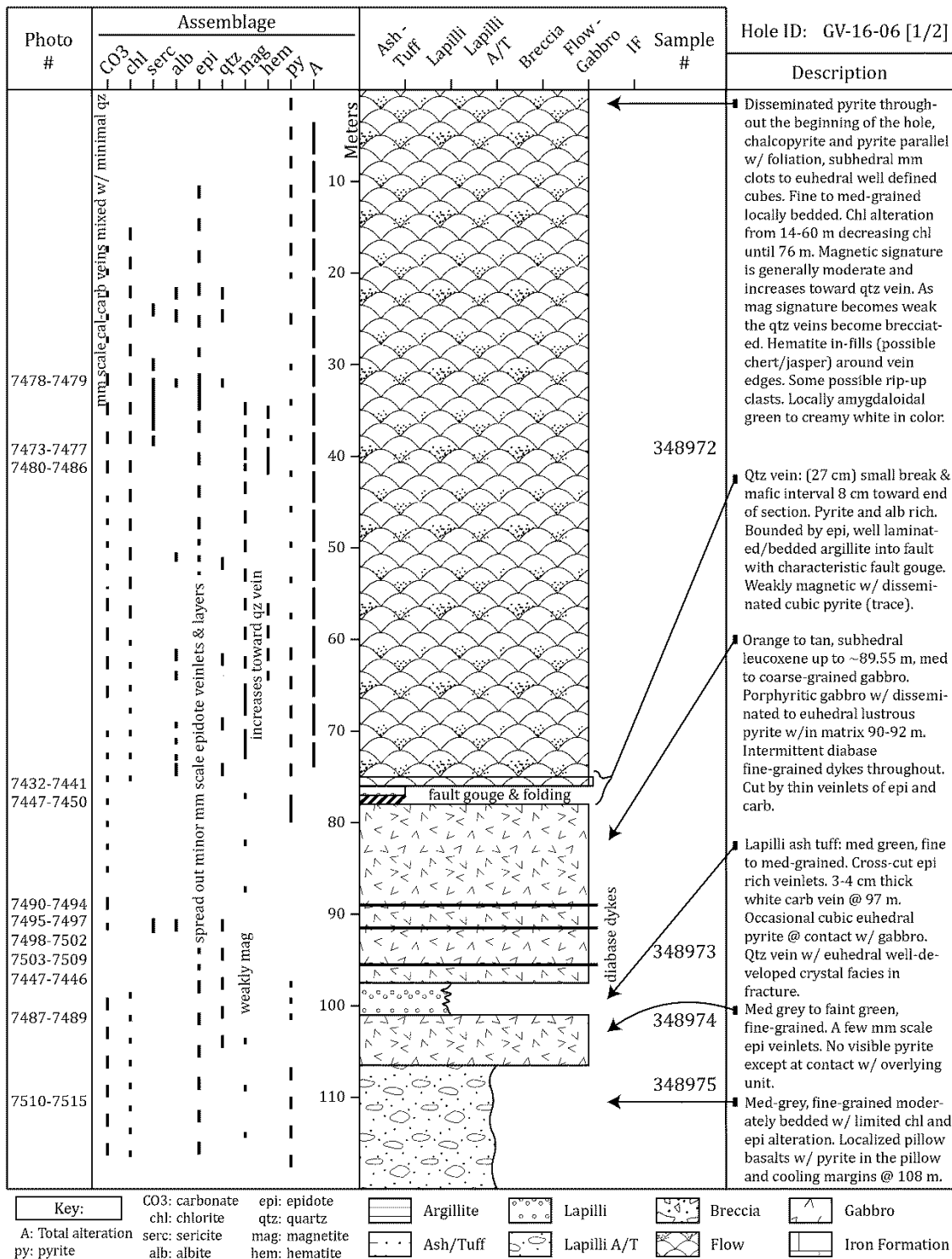
## Appendix A.II (continued) Graphic logs from the 2016 drill program



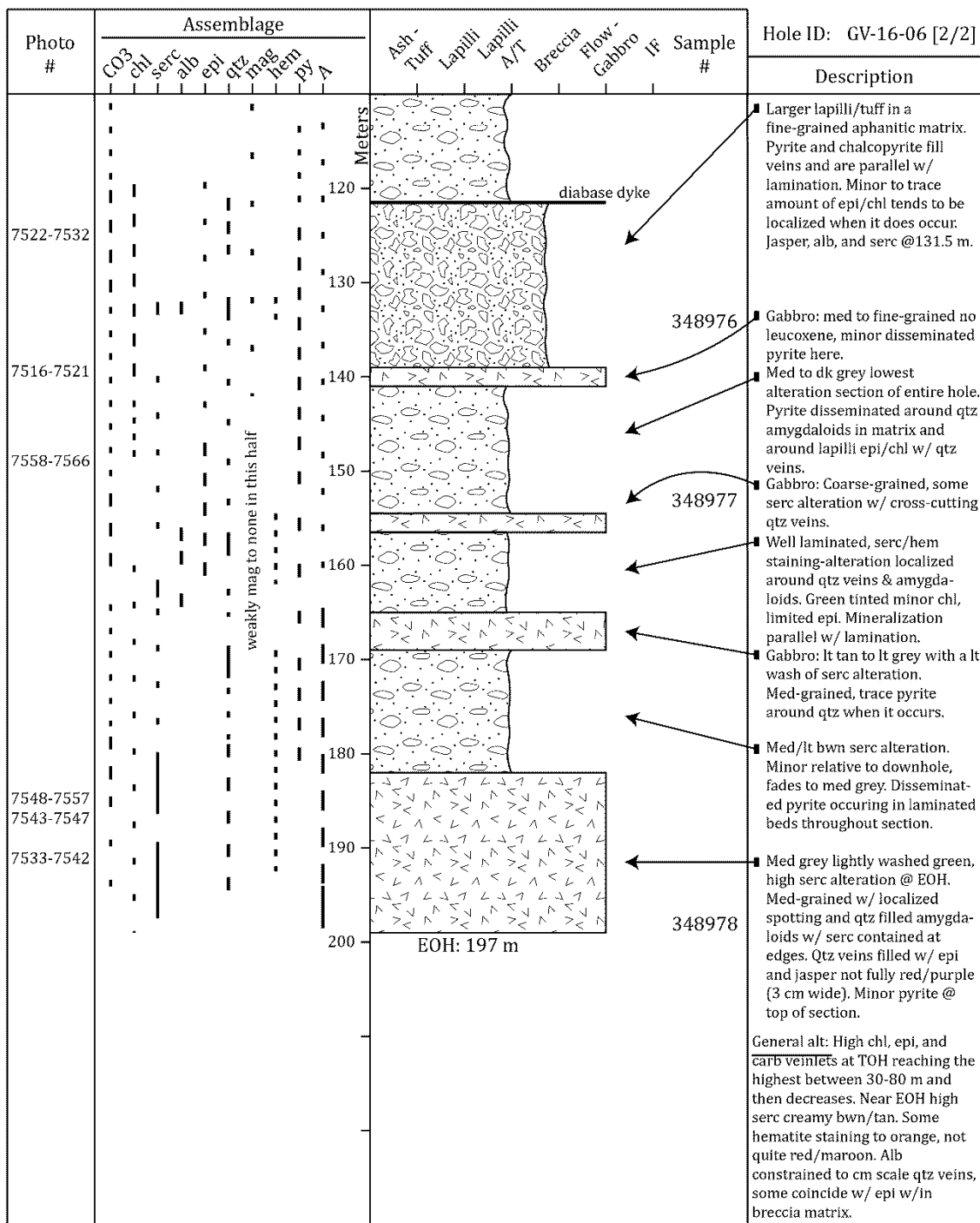
## Appendix A.II (continued) Graphic logs from the 2016 drill program



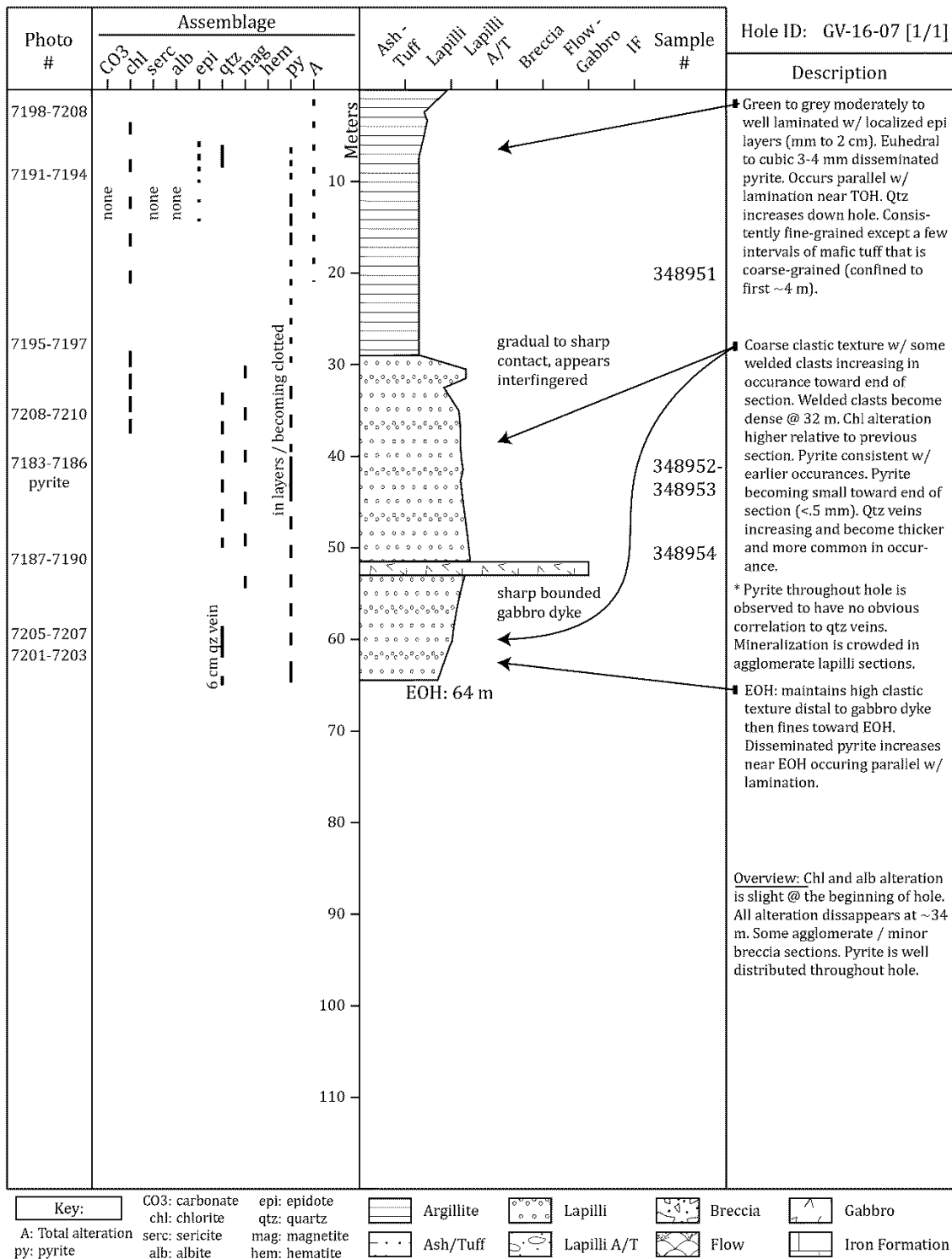
## Appendix A.II (continued) Graphic logs from the 2016 drill program



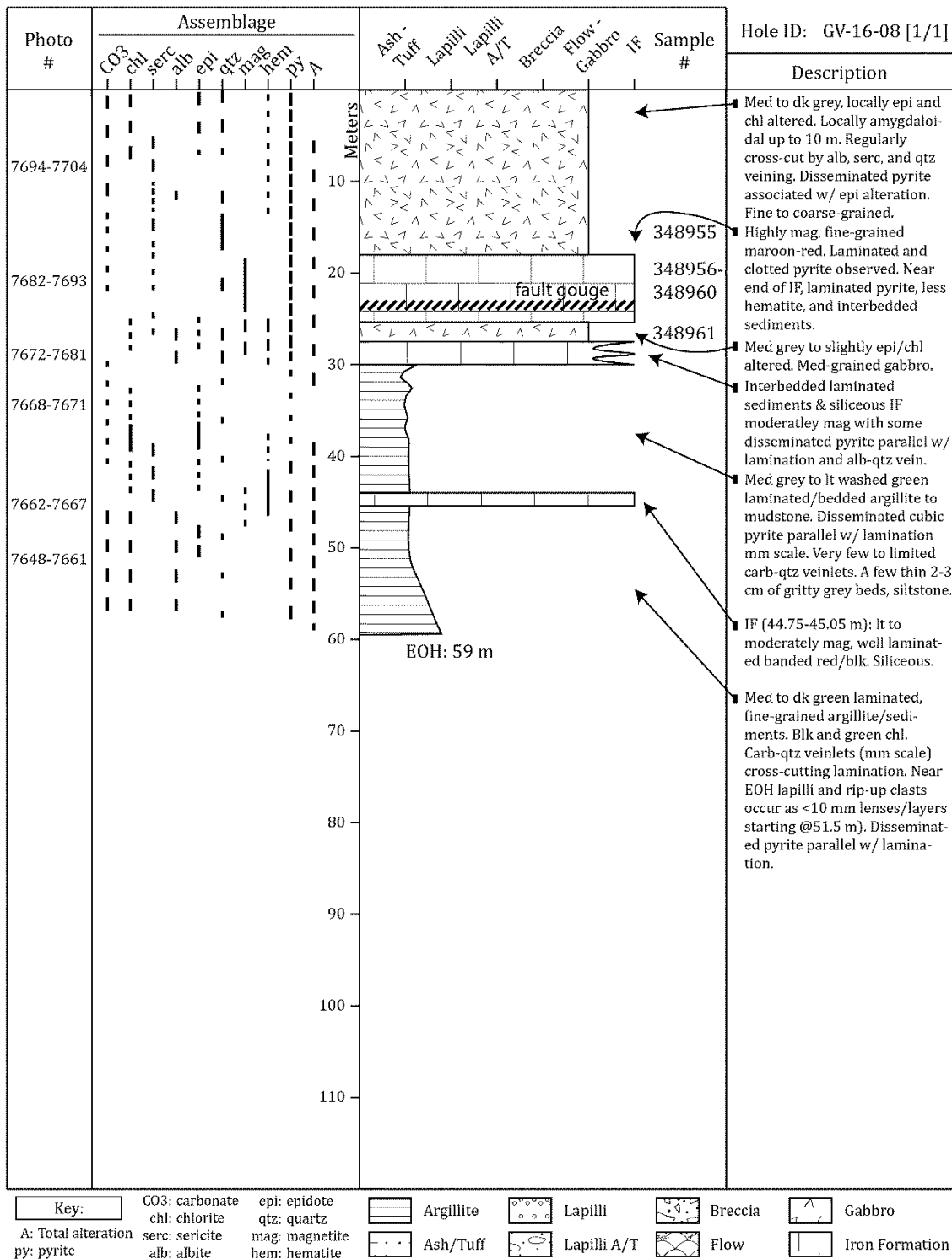
## Appendix A.II (continued) Graphic logs from the 2016 drill program



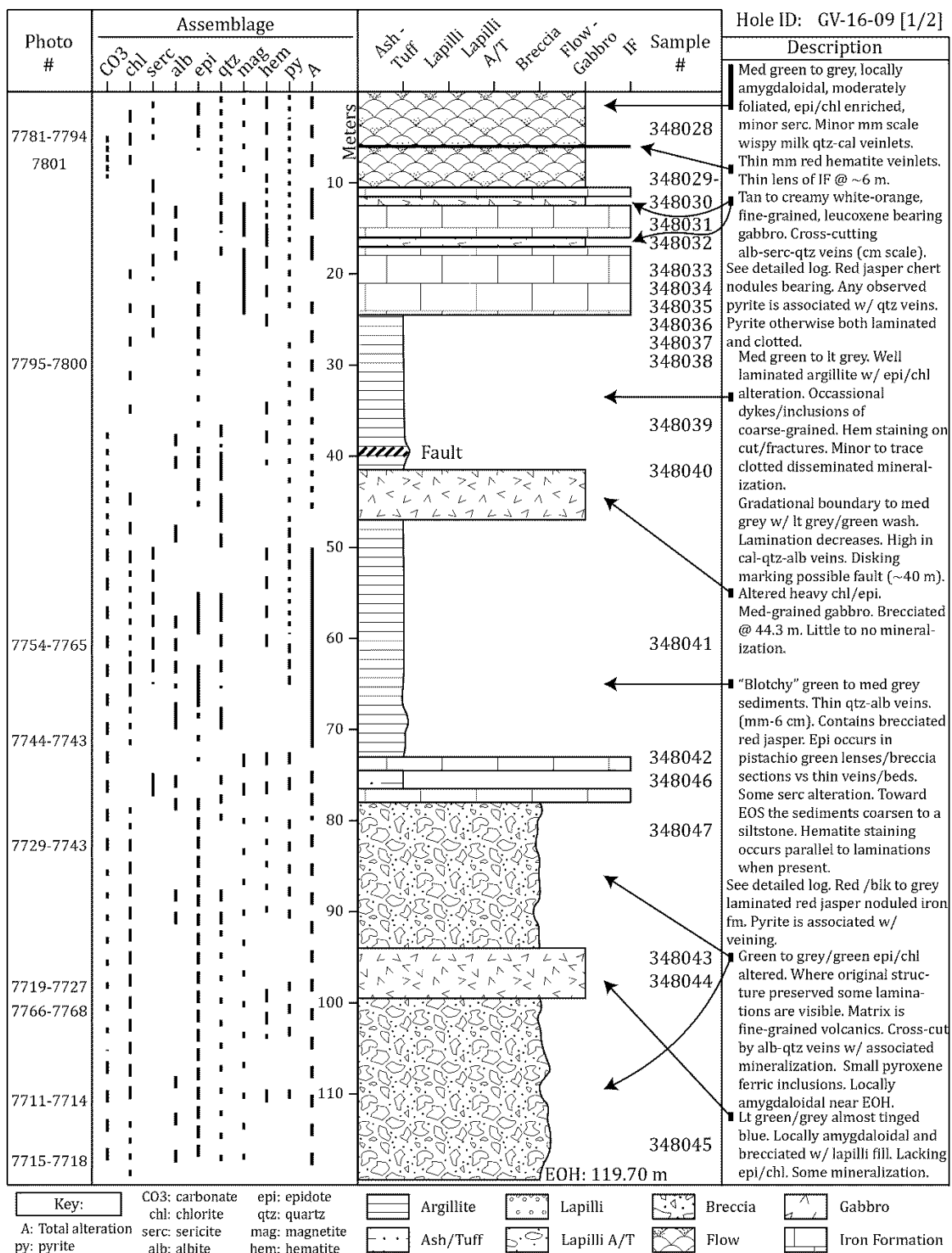
## Appendix A.II (continued) Graphic logs from the 2016 drill program



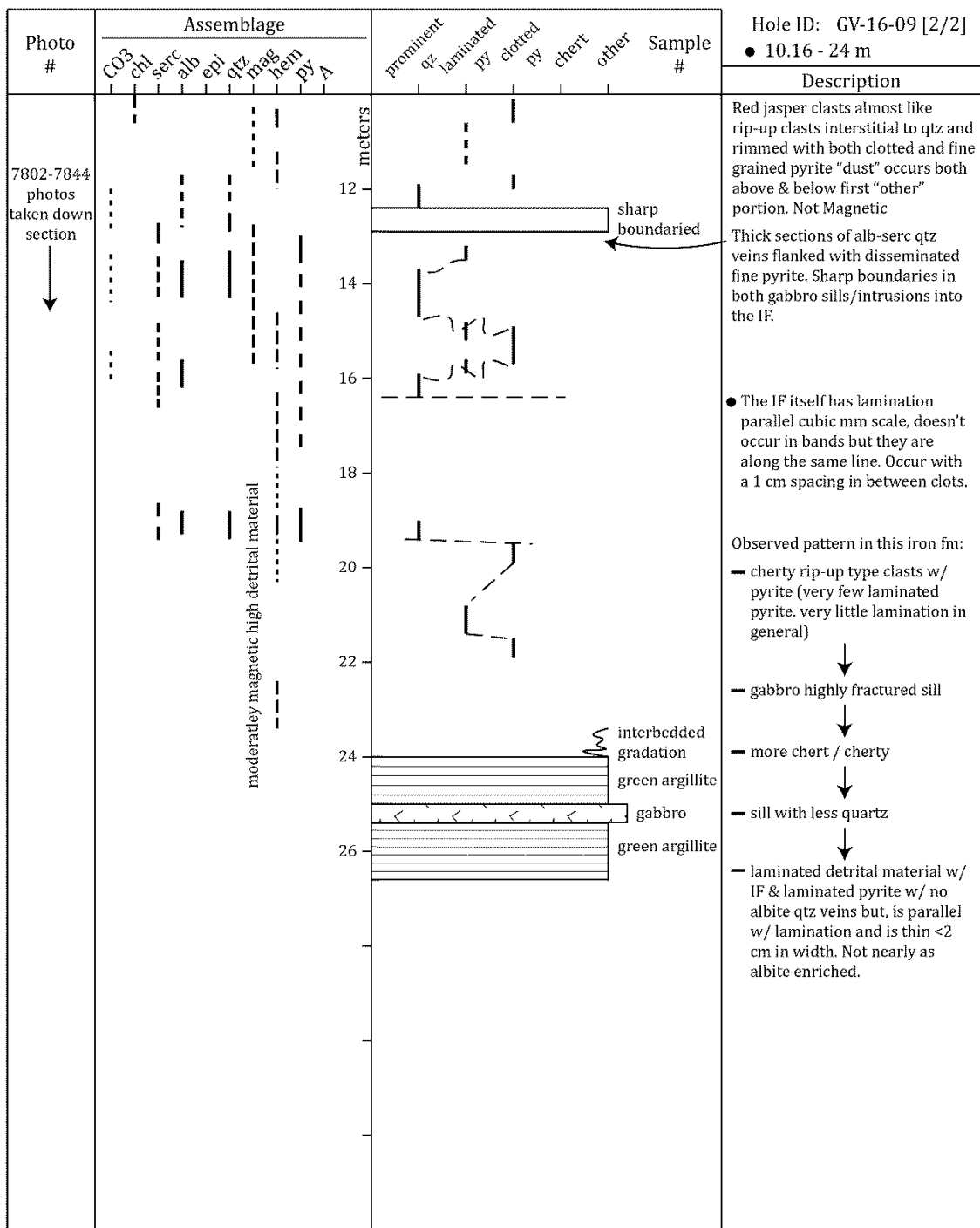
## Appendix A.II (continued) Graphic logs from the 2016 drill program



## Appendix A.II (continued) Graphic logs from the 2016 drill program



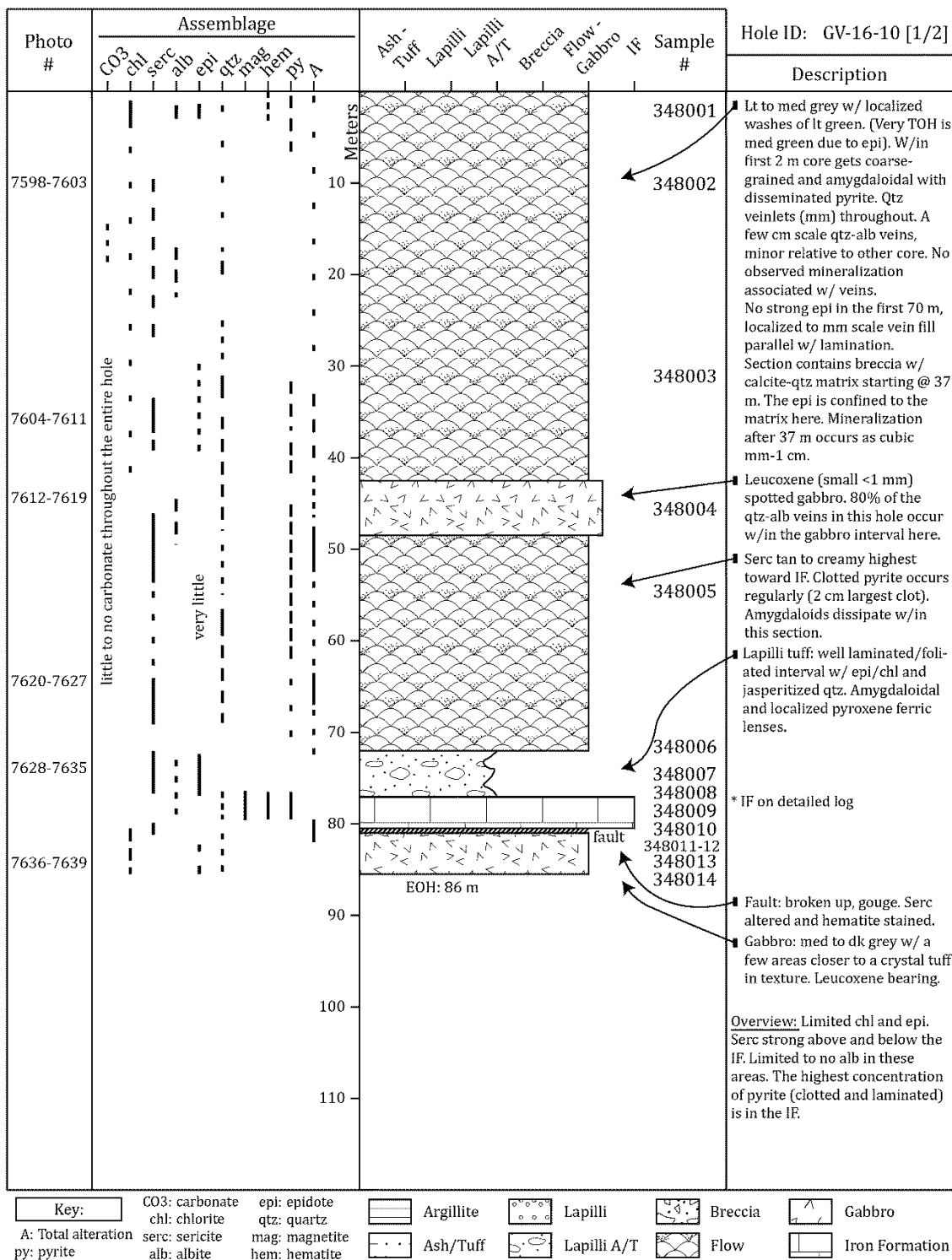
## Appendix A.II (continued) Graphic logs from the 2016 drill program



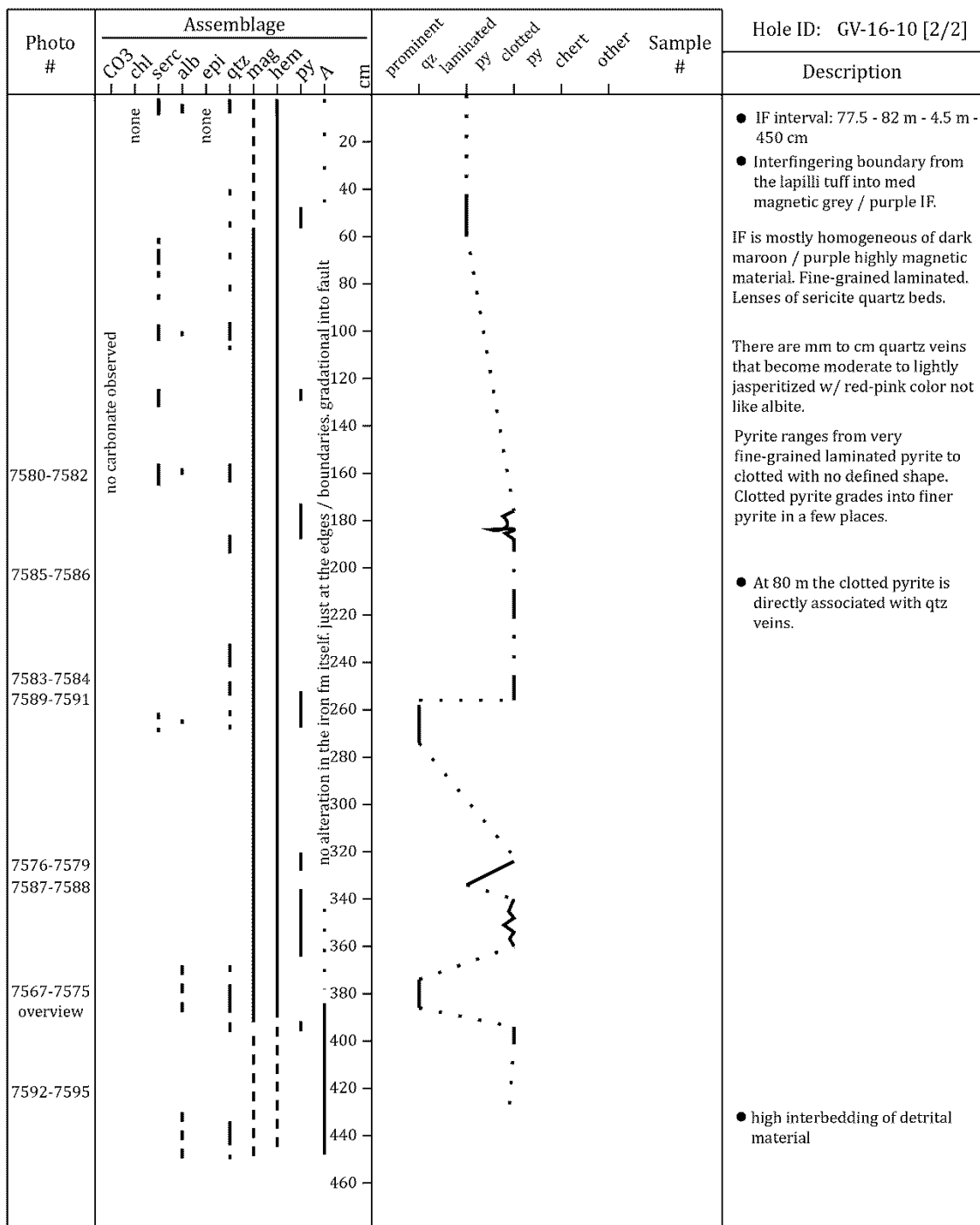
Key:

CO<sub>3</sub>: carbonate      epi: epidote  
chl: chlorite      qtz: quartz  
serc: sericite      mag: magnetite  
alb: albite      hem: hematite  
py: pyrite

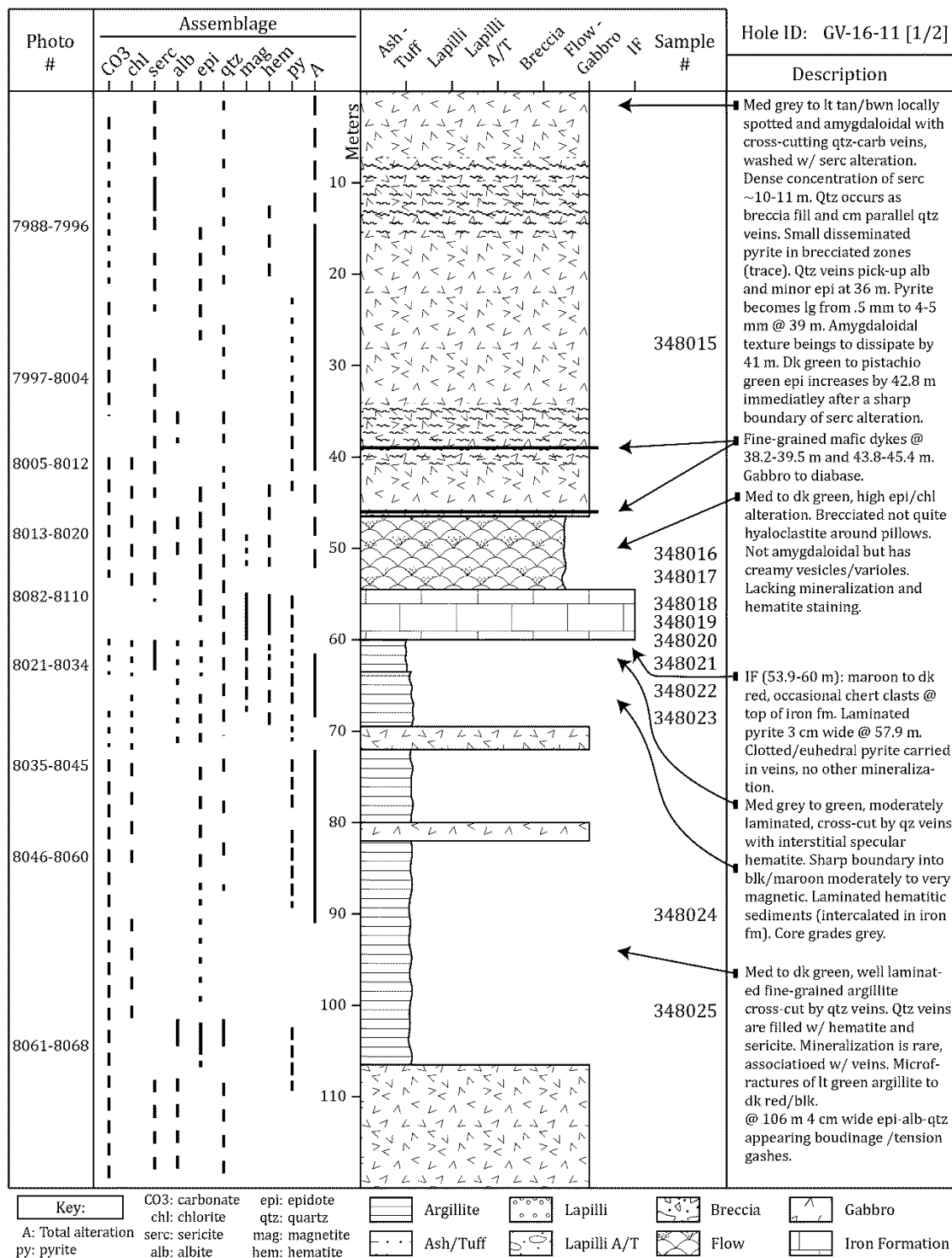
## Appendix A.II (continued) Graphic logs from the 2016 drill program



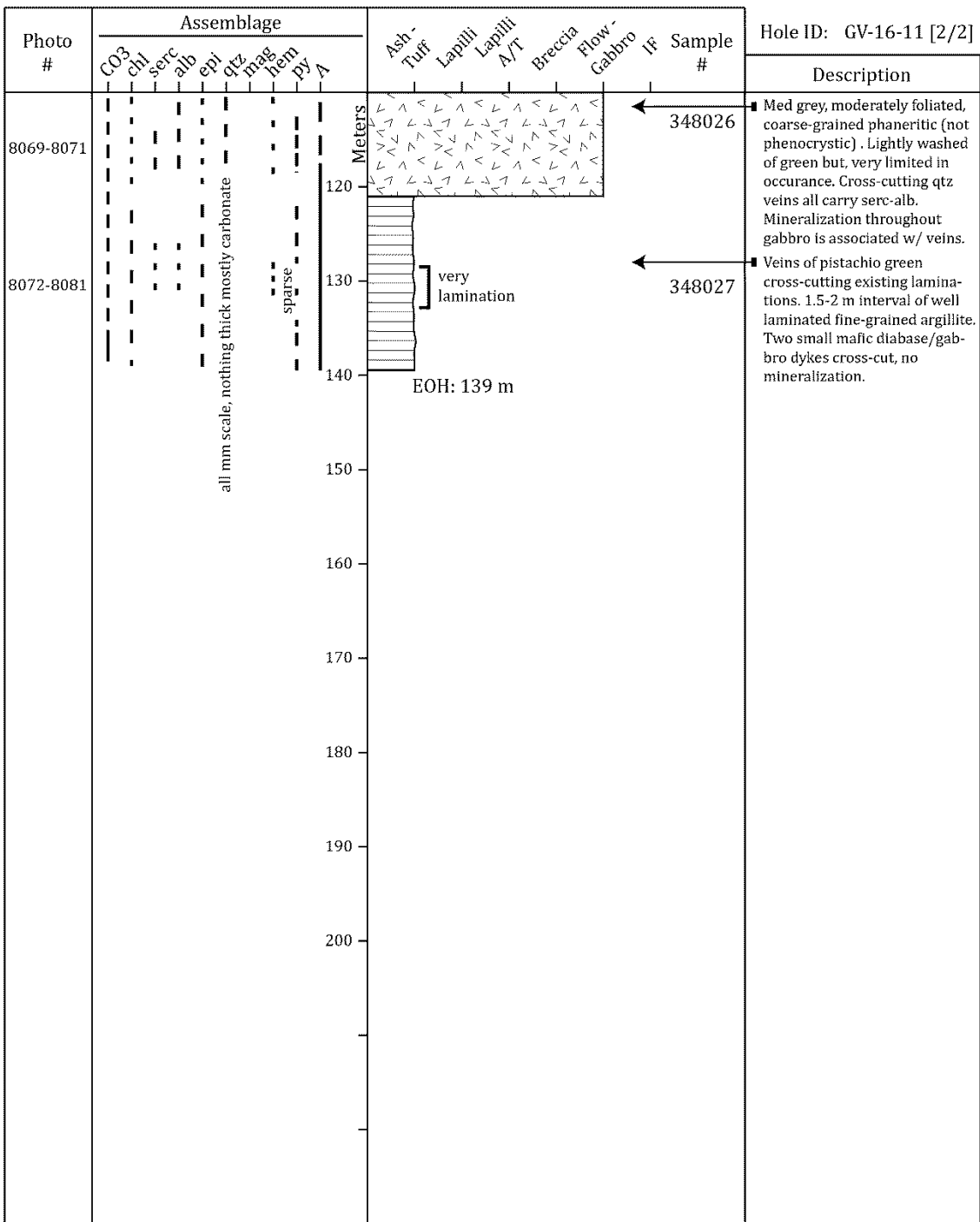
## Appendix A.II (continued) Graphic logs from the 2016 drill program



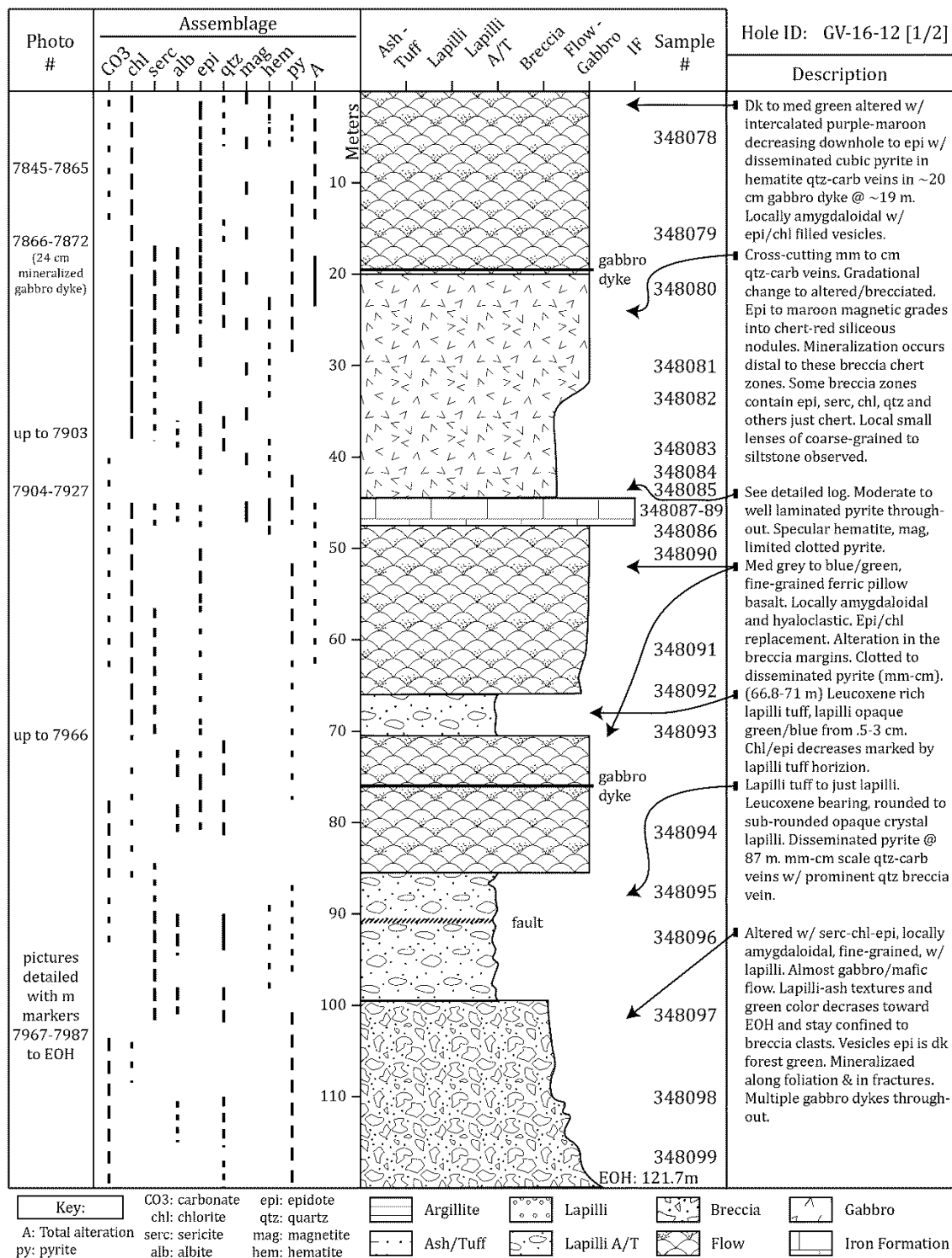
## Appendix A.II (continued) Graphic logs from the 2016 drill program



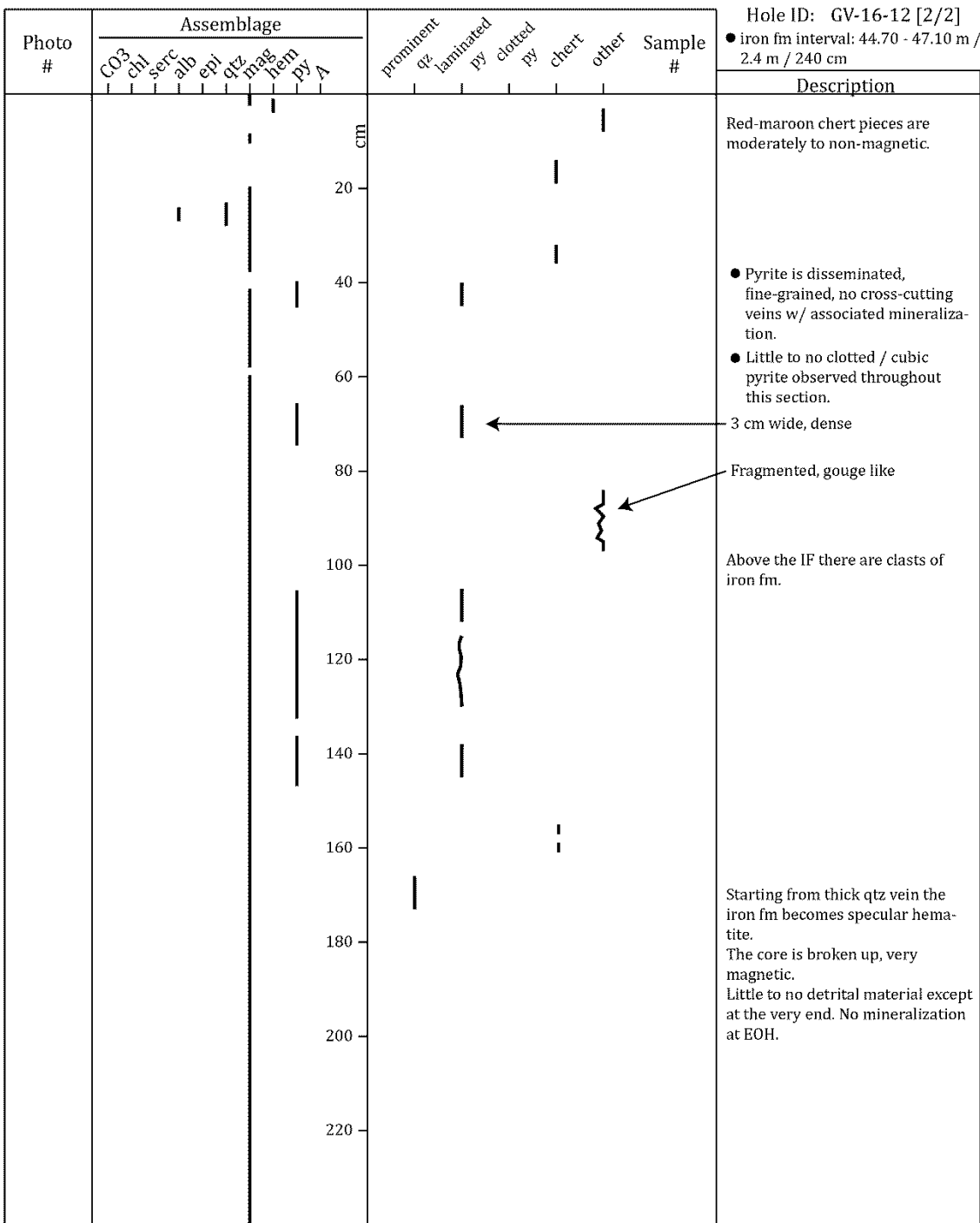
## **Appendix A.II (continued) Graphic logs from the 2016 drill program**



## Appendix A.II (continued) Graphic logs from the 2016 drill program



## **Appendix A.II (continued) Graphic logs from the 2016 drill program**



Key:

### CO<sub>3</sub>: carbonate

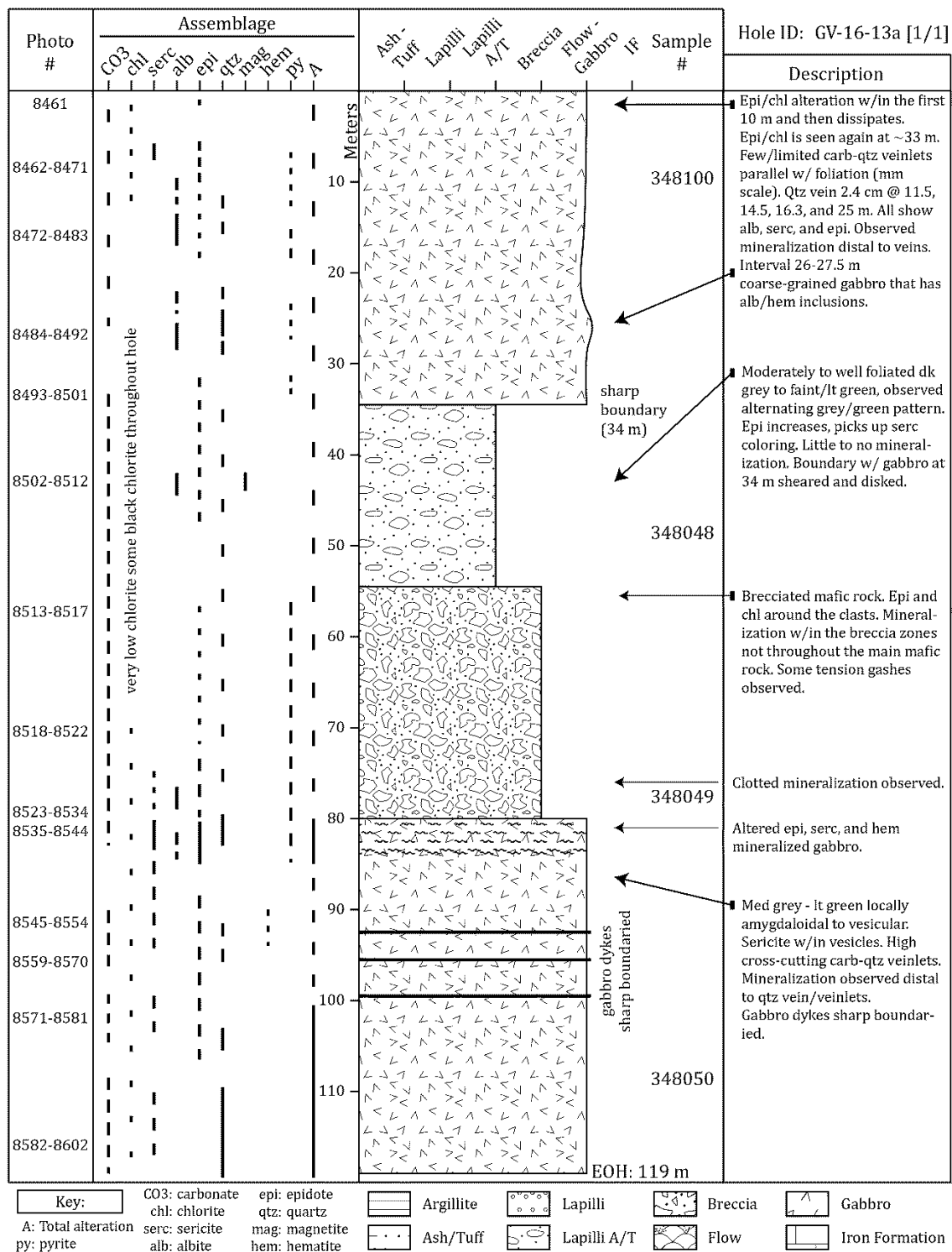
### i: epidote

A: Total alteration  
by: pyrite

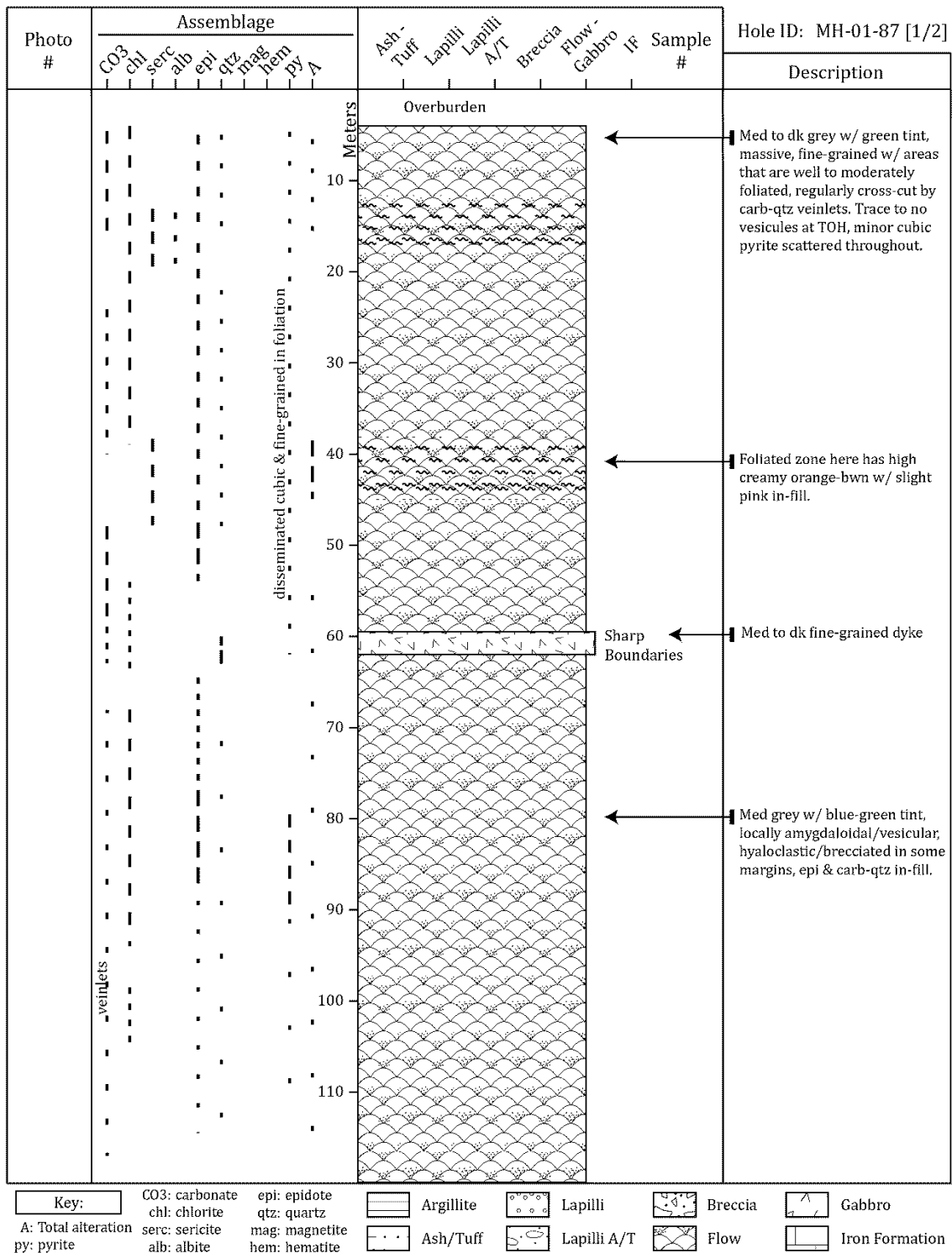
chl: chlorite  
serc: sericite  
alb: albite

qtz: quartz  
mag: magnetite  
hem: hematite

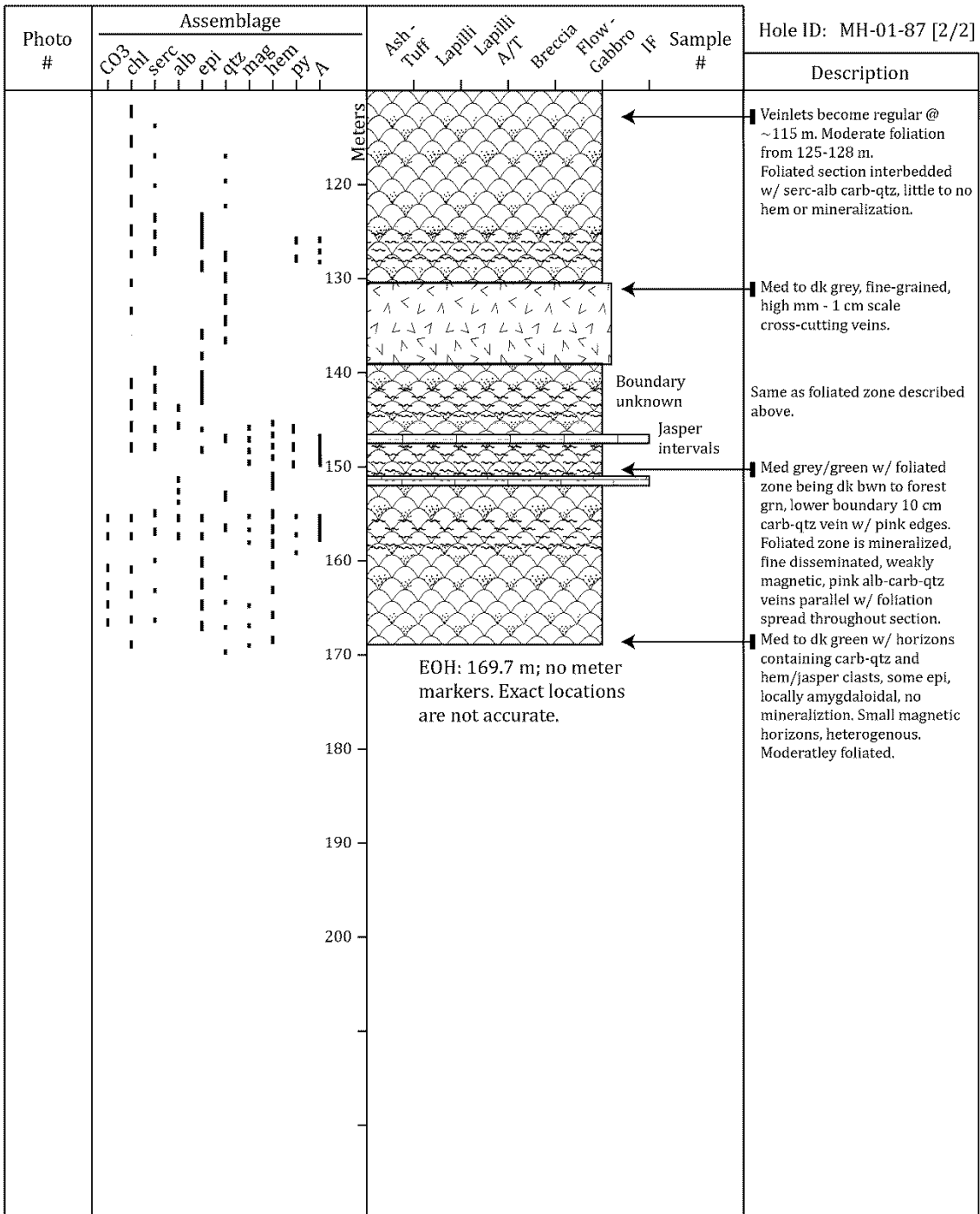
## Appendix A.II (continued) Graphic logs from the 2016 drill program



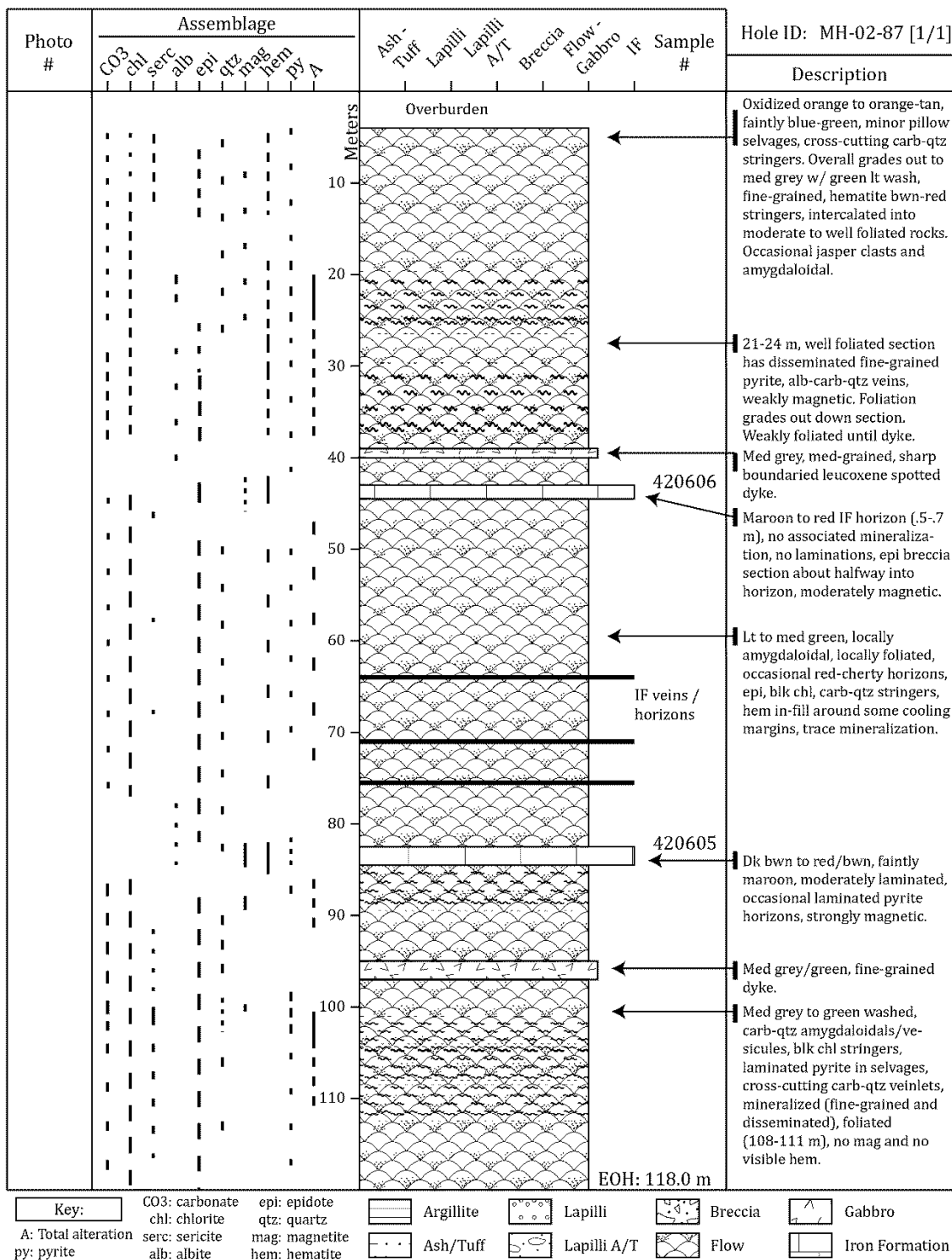
### **Appendix A.III Graphic logs from the 1987/88 drill program**



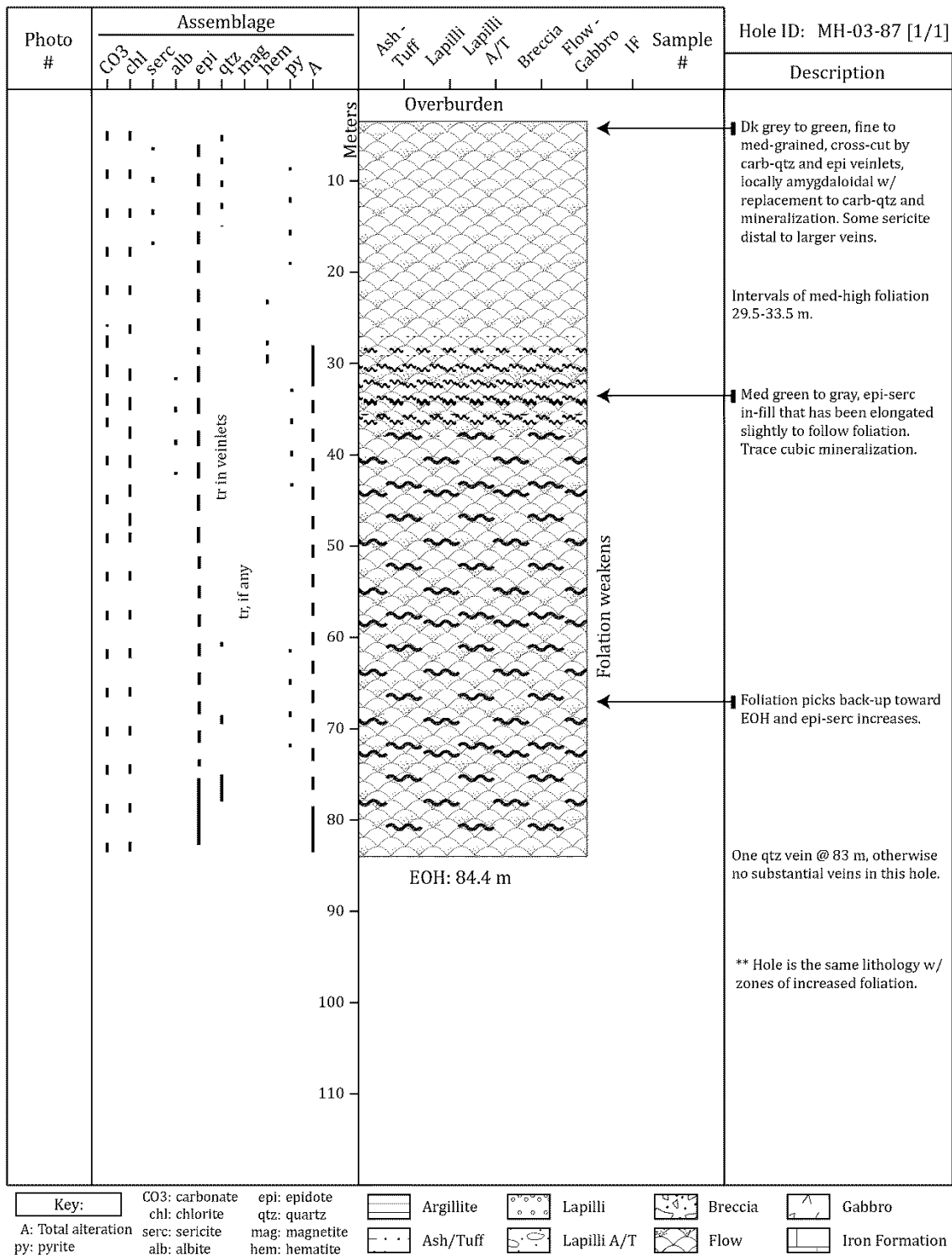
### **Appendix A.III (continued) Graphic logs from the 1987/88 drill program**



### Appendix A.III (continued) Graphic logs from the 1987/88 drill program

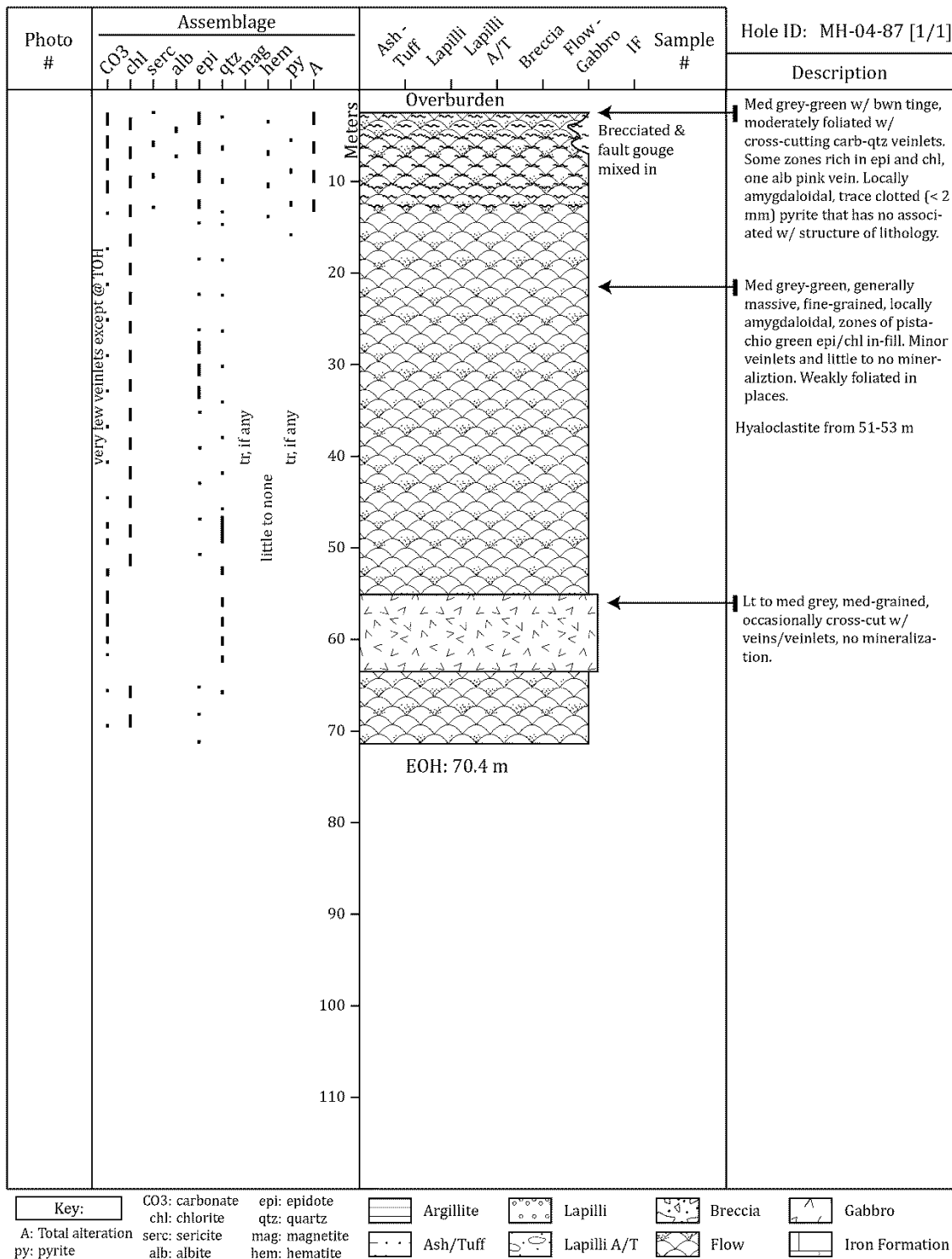


### **Appendix A.III (continued) Graphic logs from the 1987/88 drill program**

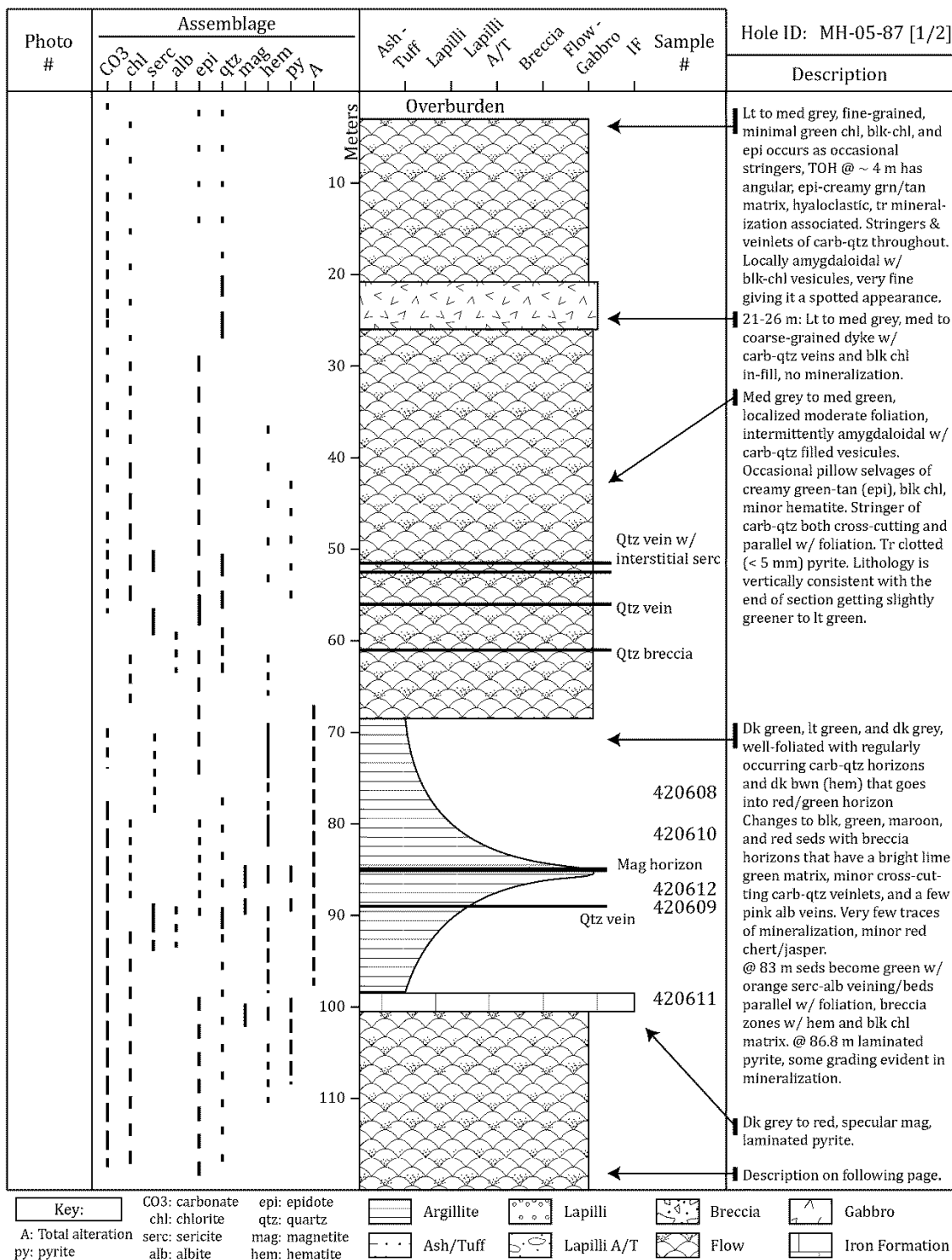


<b>Key:</b>	CO <sub>3</sub> : carbonate	epi: epidote		Argillite		Lapilli		Breccia		Gabbro
A: Total alteration	chl: chlorite	qtz: quartz		Ash/Tuff		Lapilli A/T		Flow		Iron Formation
py: pyrite	serc: sericite	mag: magnetite		hem: hematite						

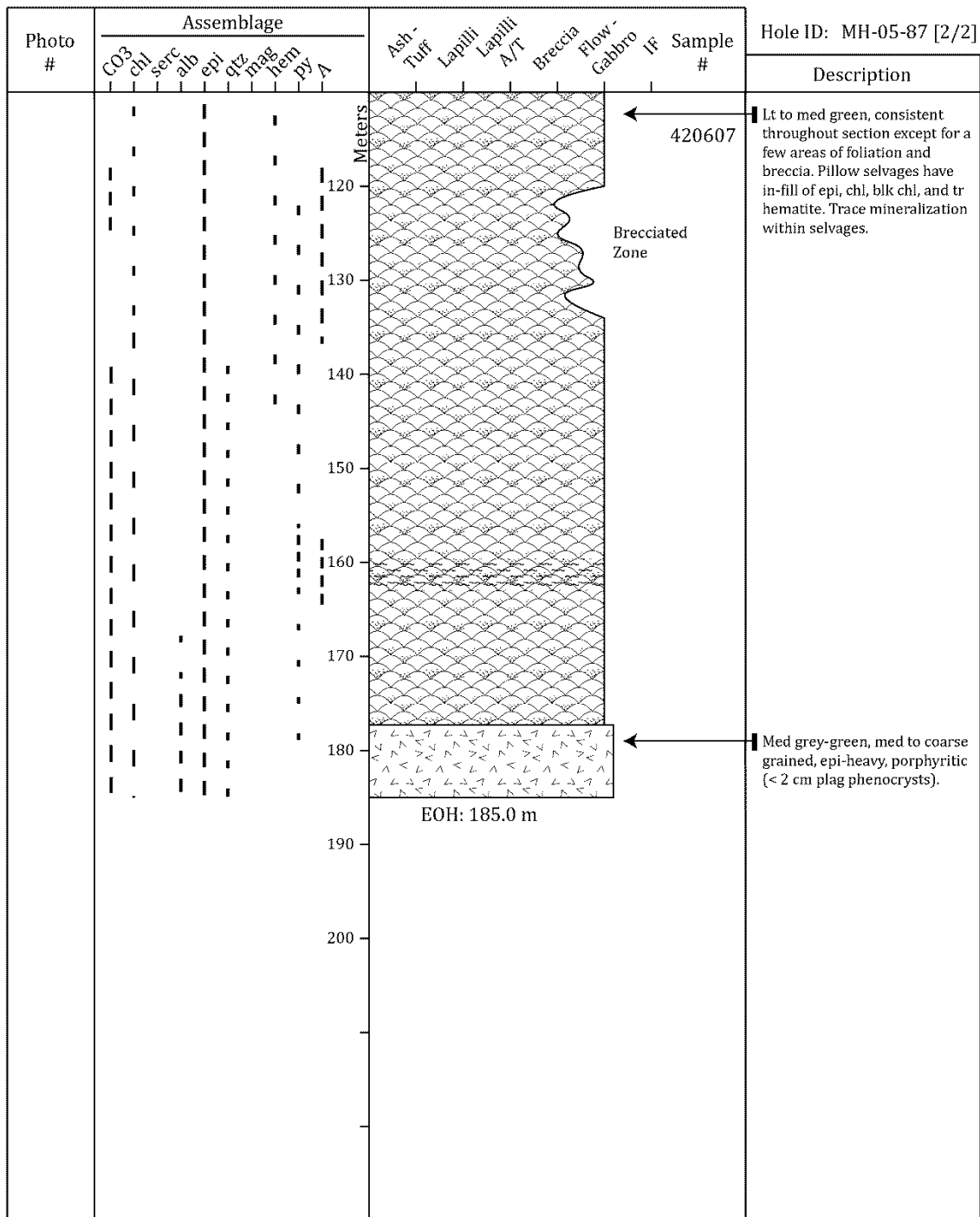
### Appendix A.III (continued) Graphic logs from the 1987/88 drill program



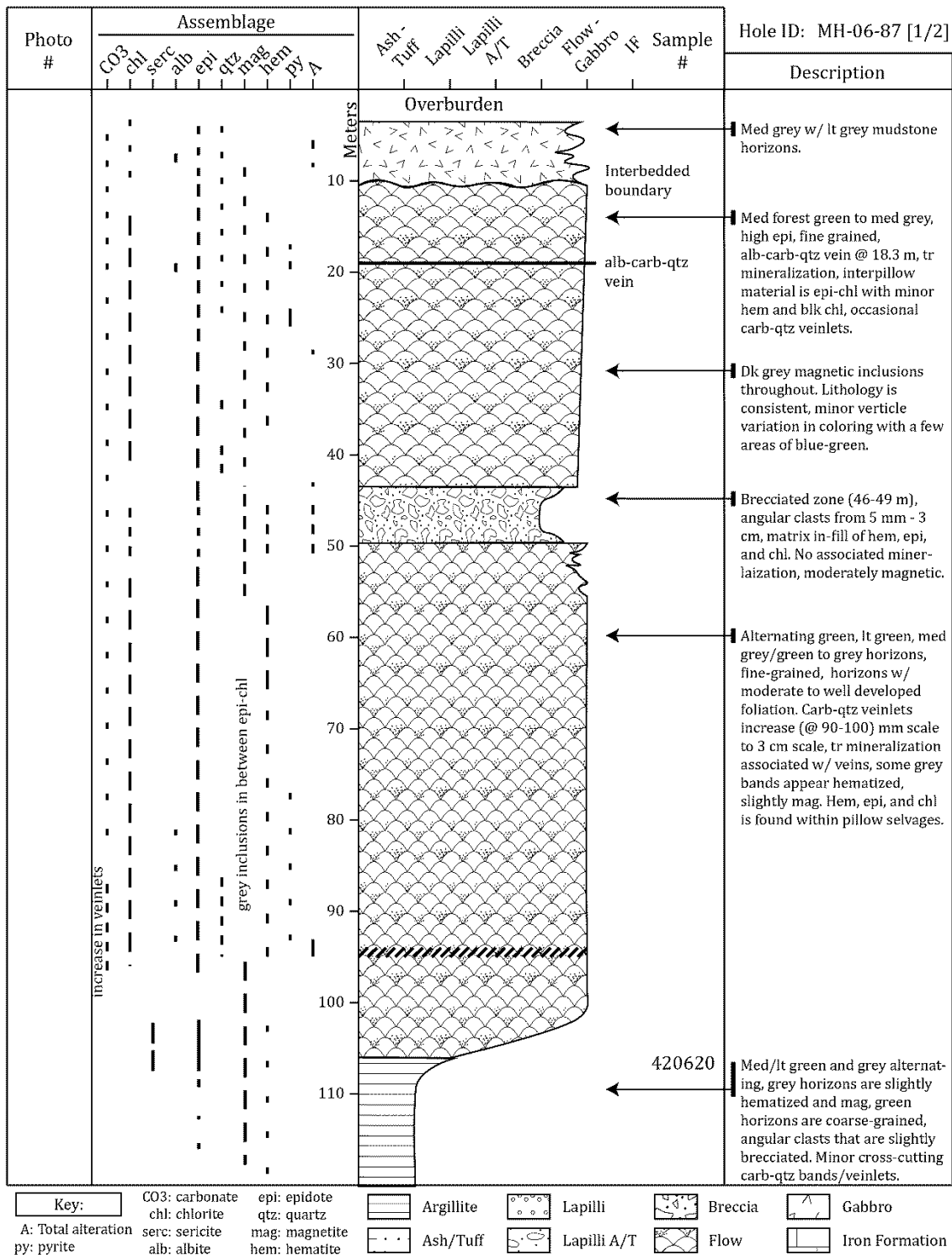
### Appendix A.III (continued) Graphic logs from the 1987/88 drill program



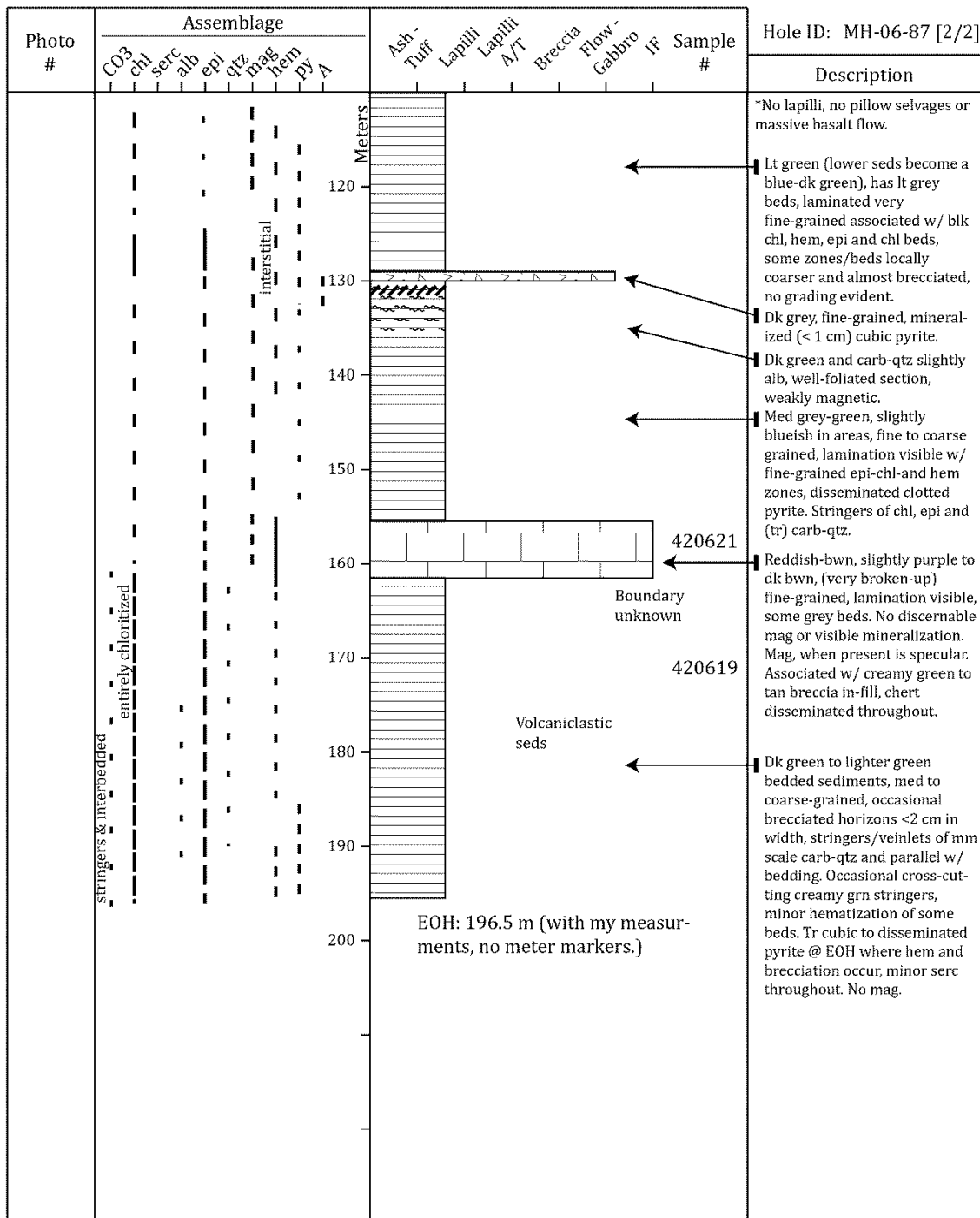
### **Appendix A.III (continued) Graphic logs from the 1987/88 drill program**



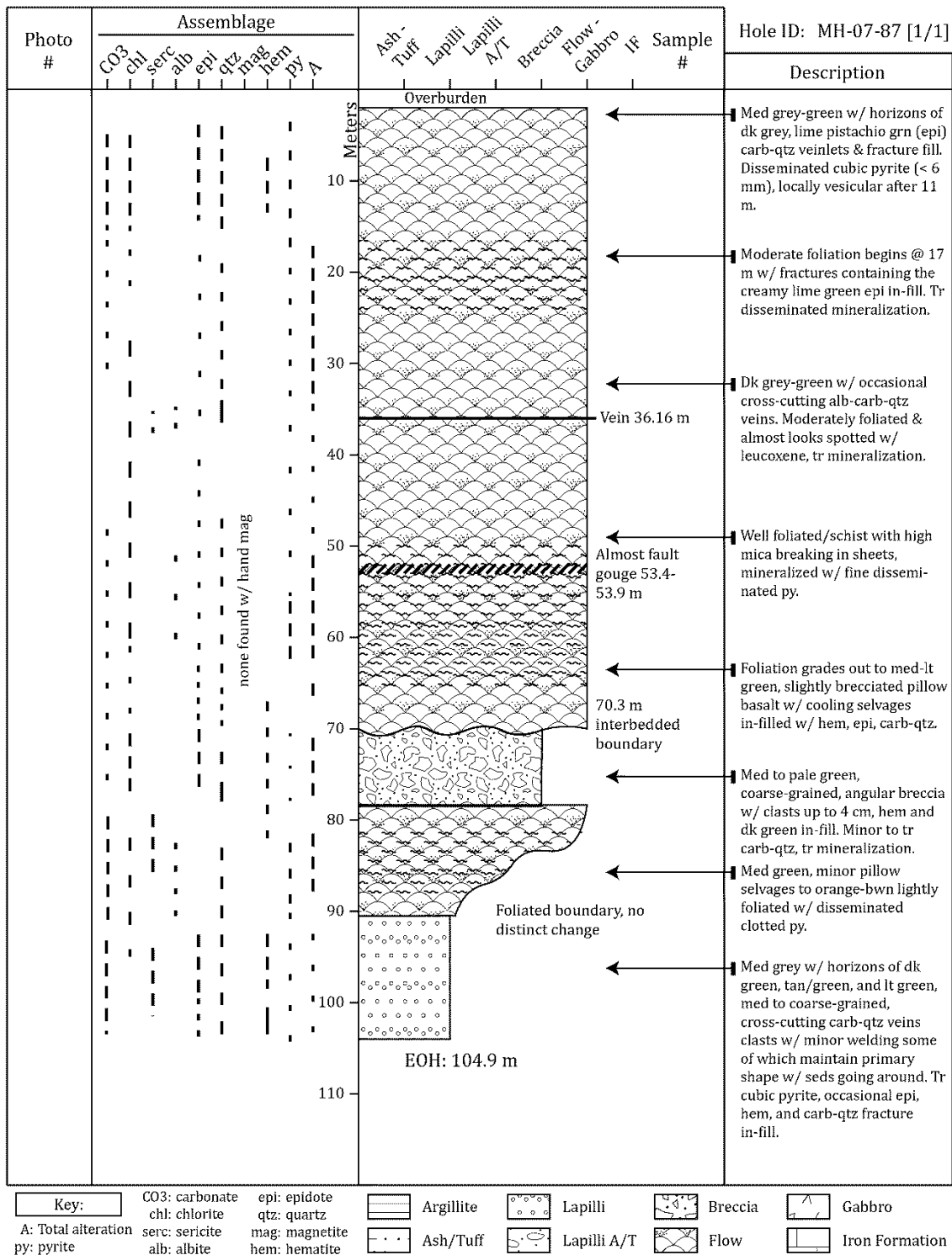
### **Appendix A.III (continued) Graphic logs from the 1987/88 drill program**



**Appendix A.III (continued) Graphic logs from the 1987/88 drill program**



### **Appendix A.III (continued) Graphic logs from the 1987/88 drill program**



Key:

CO<sub>3</sub>: carbonate

### i: epidote

Argilli

Lapilli

Breed

Gahhro

A: Total alteration  
by: pyrite

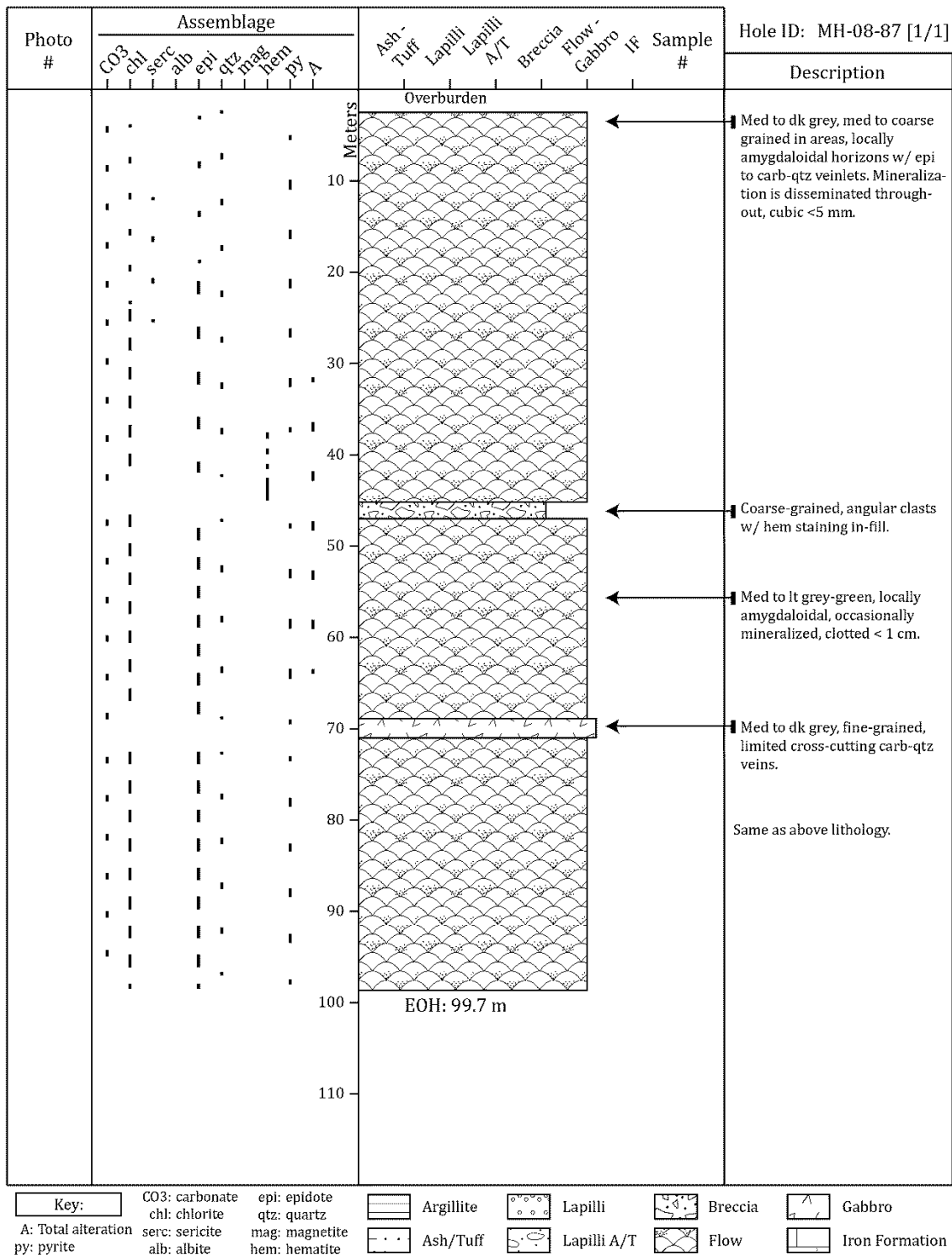
qtz: quartz  
mag: magnetite  
hem: hematite

Ash/Tu

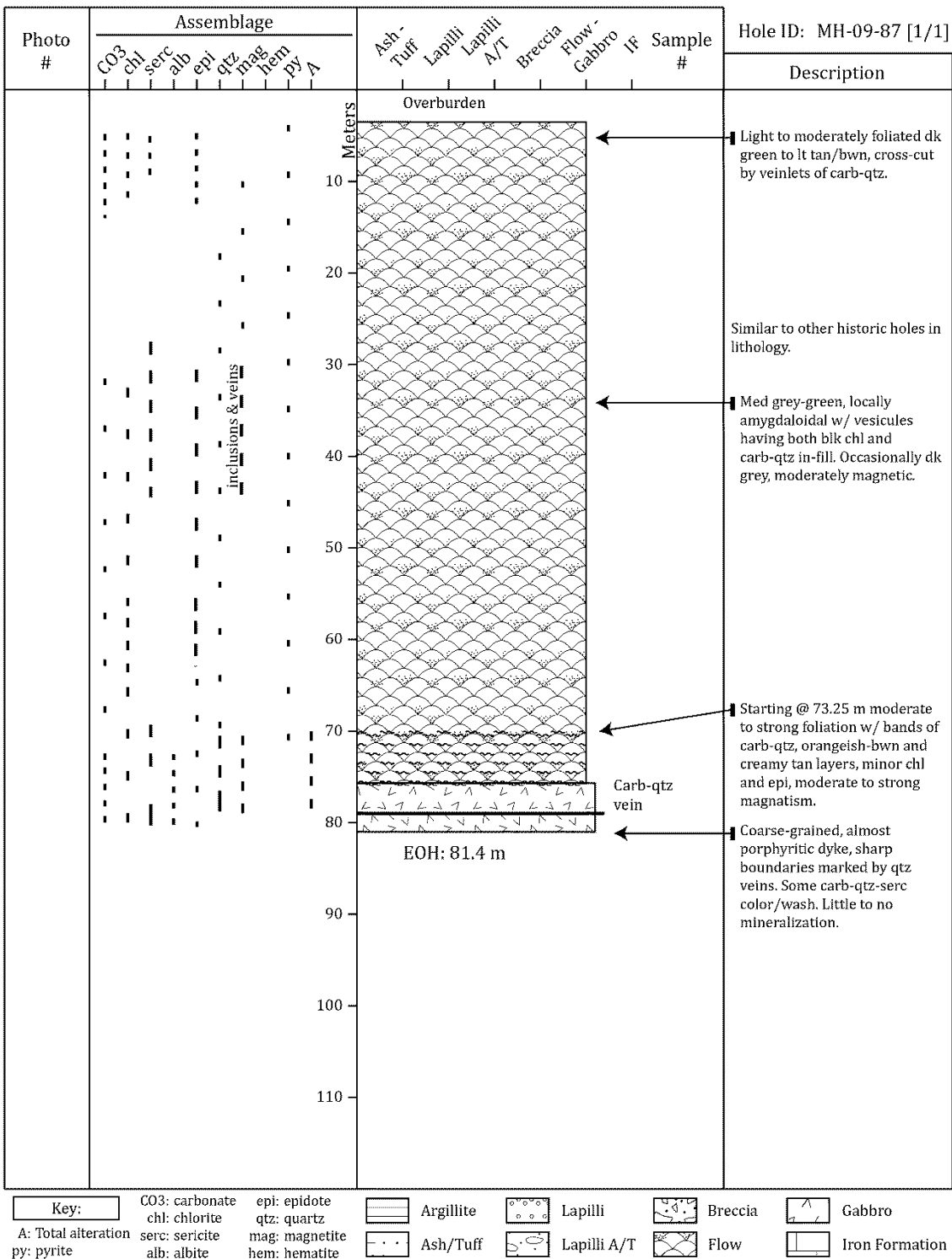
Lapilli

## Iron Formation

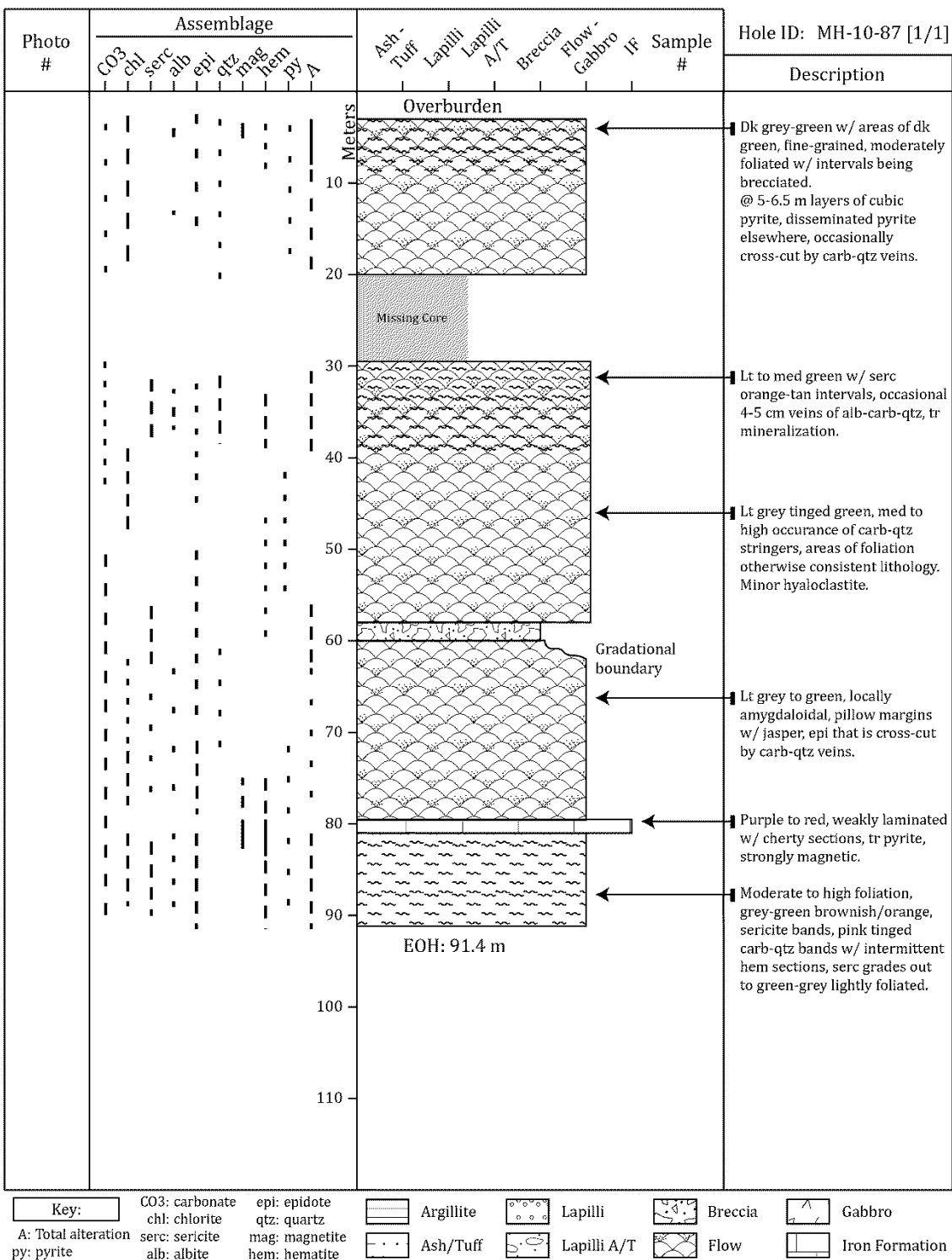
### **Appendix A.III (continued) Graphic logs from the 1987/88 drill program**



### **Appendix A.III (continued) Graphic logs from the 1987/88 drill program**



### **Appendix A.III (continued) Graphic logs from the 1987/88 drill program**



Key:

CO<sub>3</sub>: carbonate

pi: epidote

Argillite

Lapil

B1

1

10

A: Total alteration  
by: pyrite

qtz: quartz  
mag: magnetite  
hem: hematite

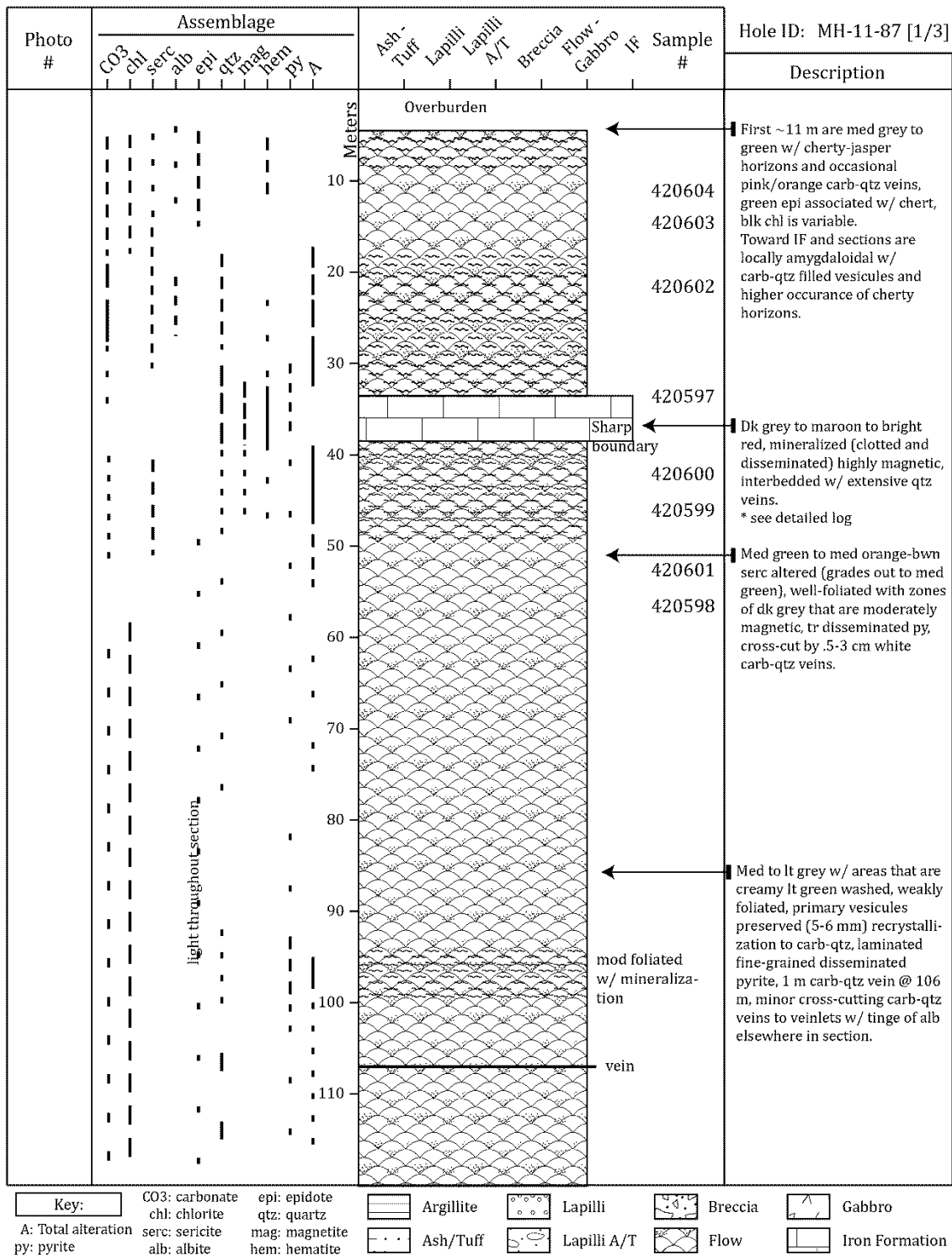
Ash/Tuff

A small icon depicting a simple vessel or pot.

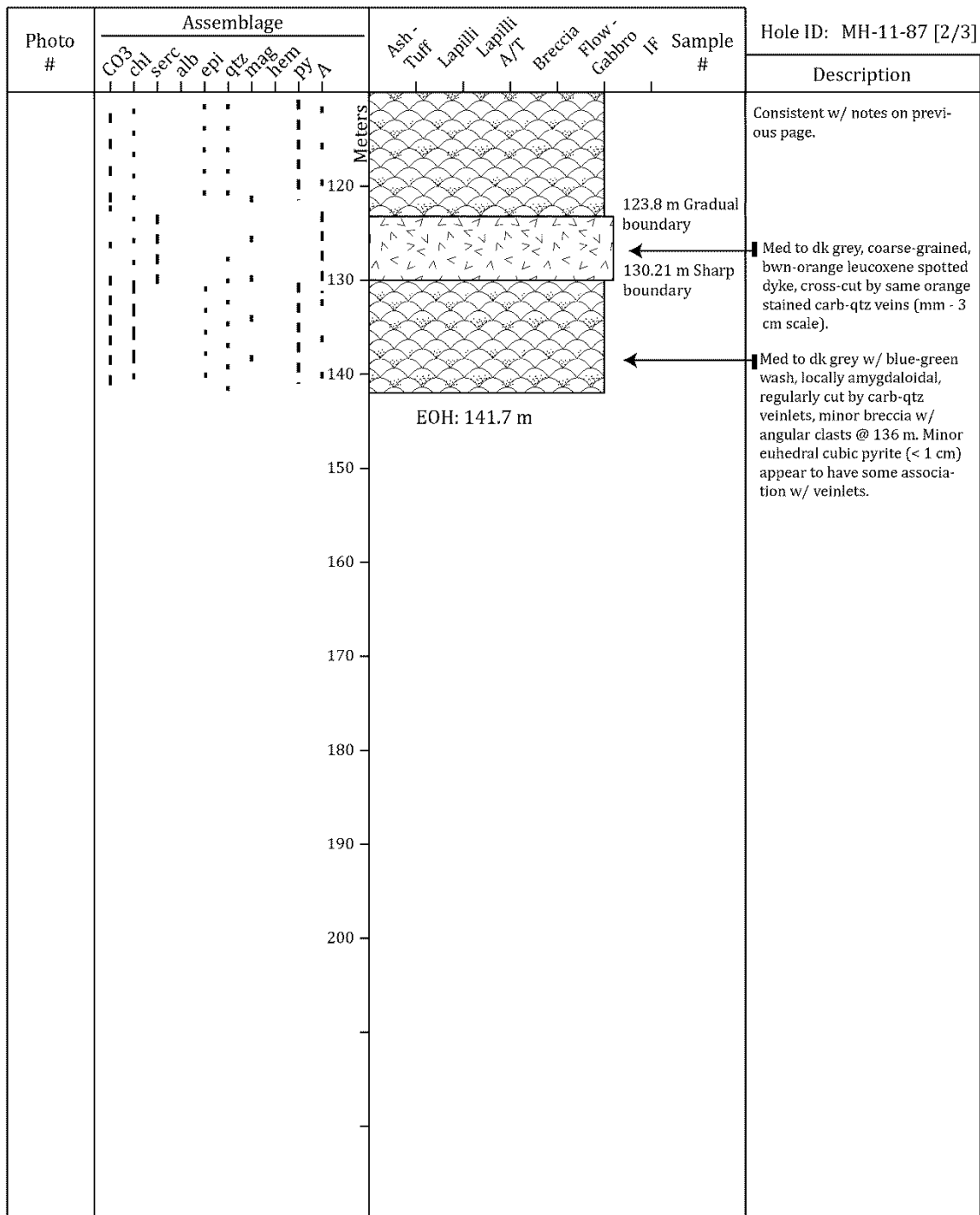
D  
Fl

## Formation

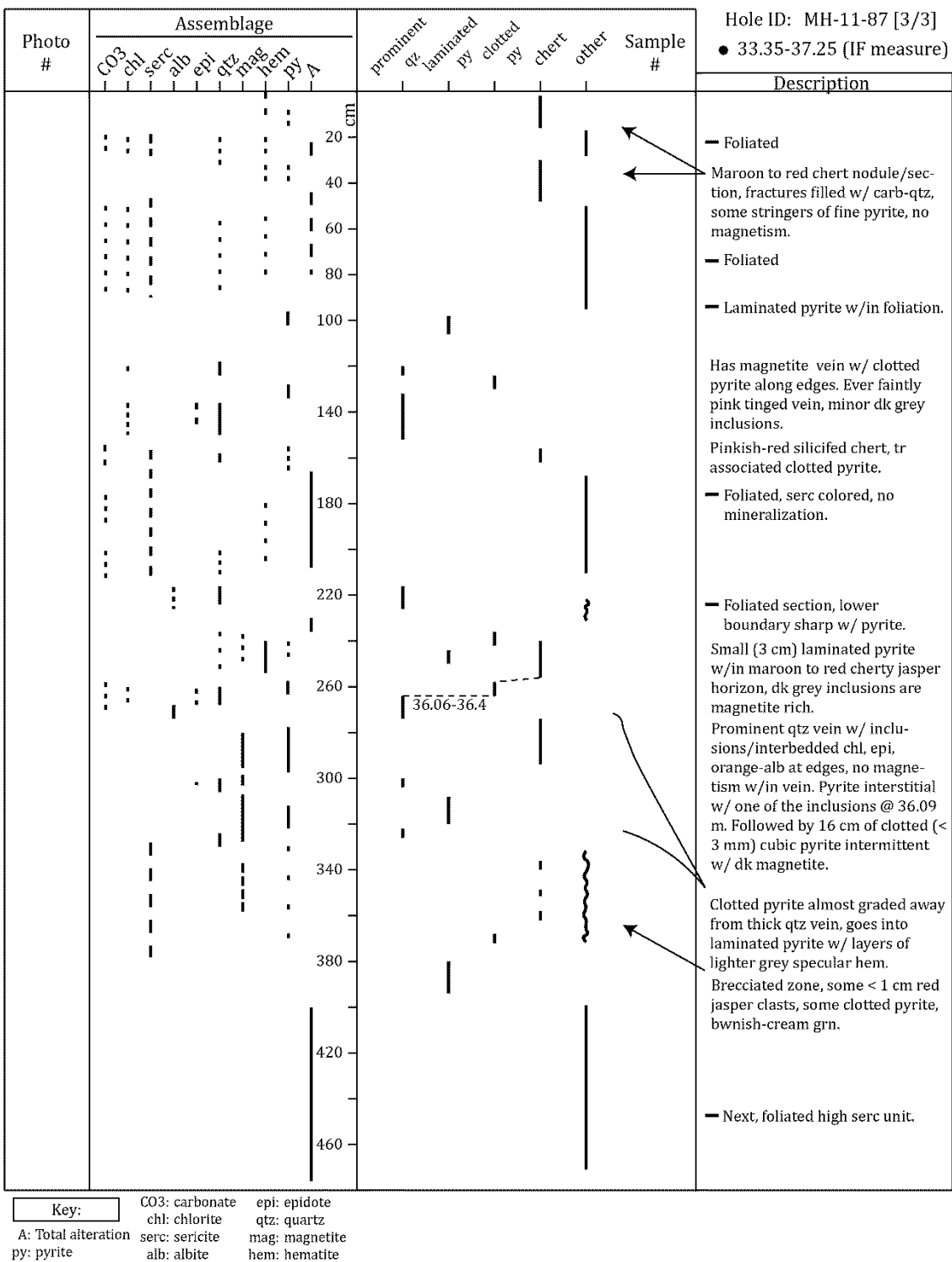
### **Appendix A.III (continued) Graphic logs from the 1987/88 drill program**



### **Appendix A.III (continued) Graphic logs from the 1987/88 drill program**



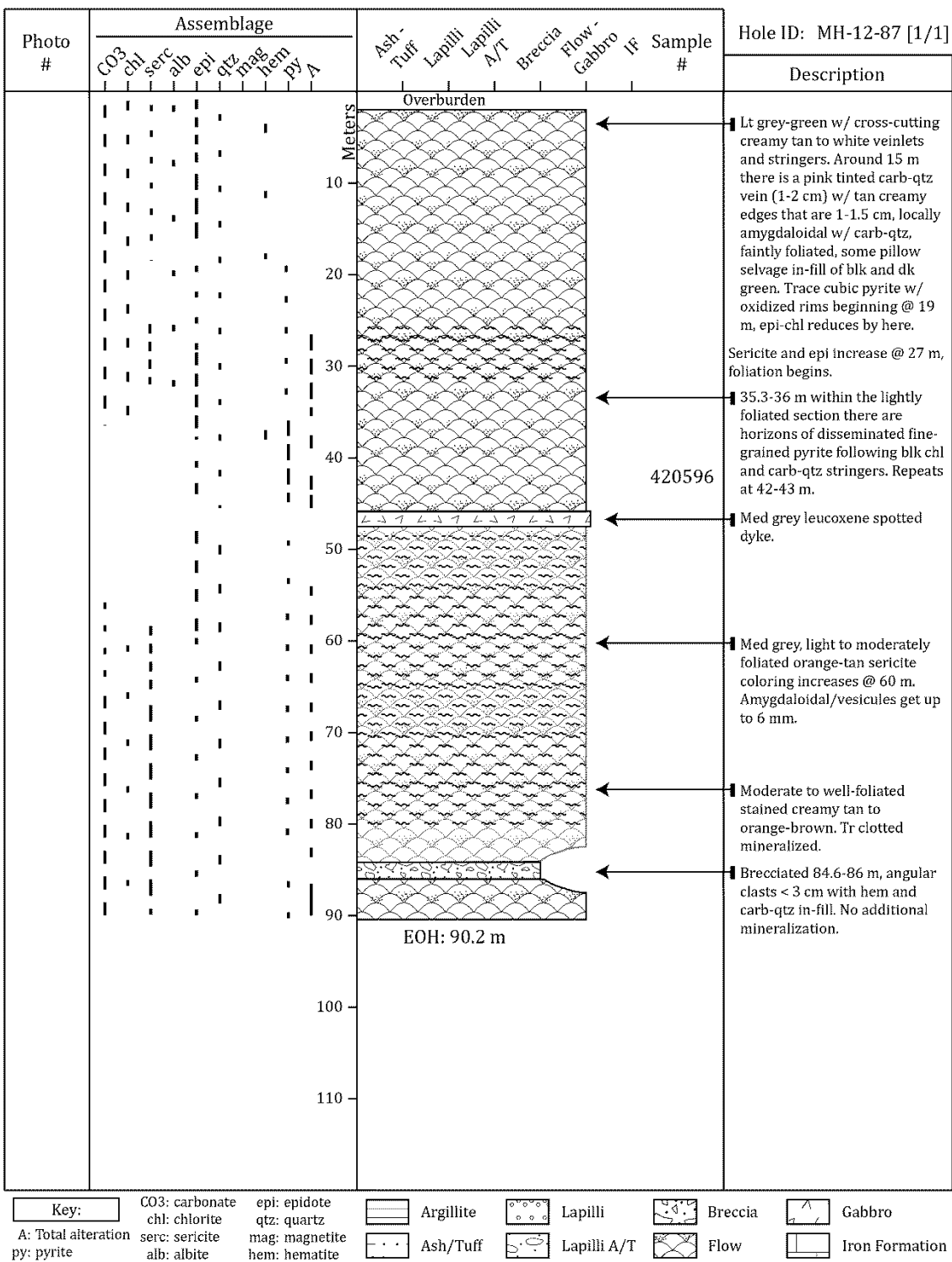
### **Appendix A.III (continued) Graphic logs from the 1987/88 drill program**



Key:

CO3: carbonate	epi: epidote
chl: chlorite	qtz: quartz
serc: sericite	mag: magnetite
alb: albite	hem: hematite

### **Appendix A.III (continued) Graphic logs from the 1987/88 drill program**



Key:

CO<sub>3</sub>: carbonate

pi: epidote

**Argillite**

Lapilli

B

ja  Gahhro

A: Total alteration  
by: pyrite

qtz: quartz  
mag: magnetite  
hem: hematite

Ash/Tu

La

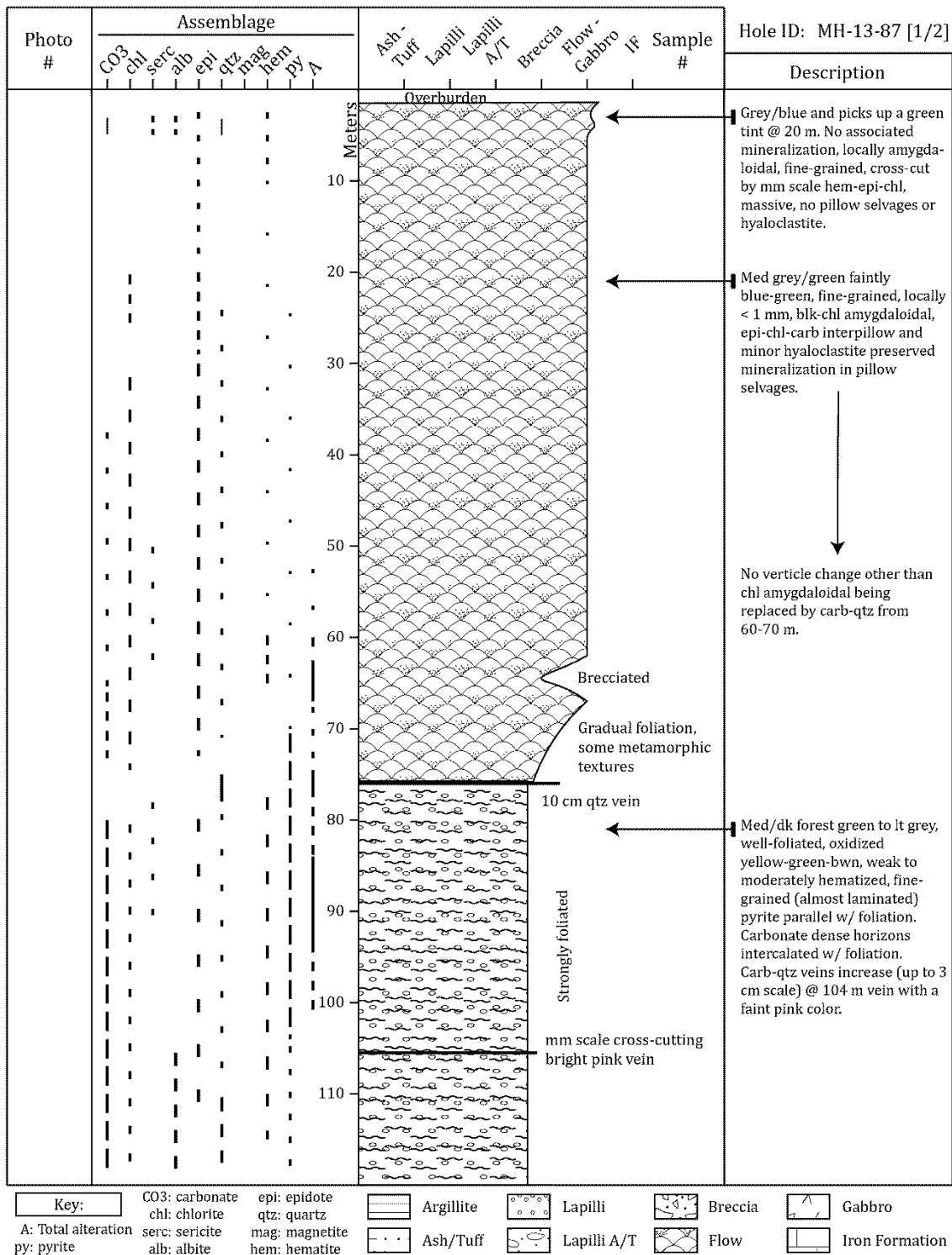
A diagram showing a cross-section of a rock layer. The layer is depicted as a series of horizontal lines, with a prominent, large-scale, upward-sloping fold or arching feature running through it.

2

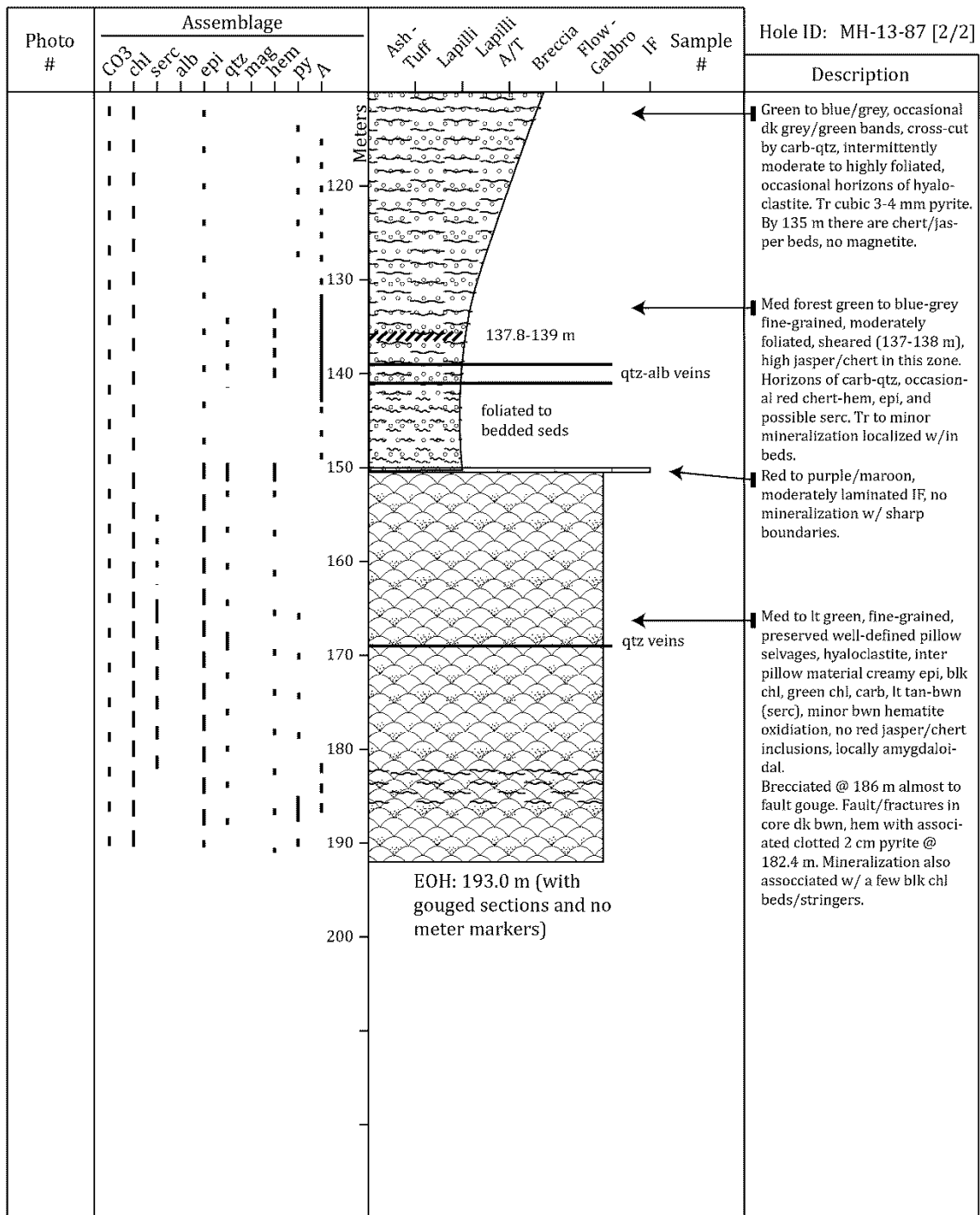
ron Fo

PYTHON

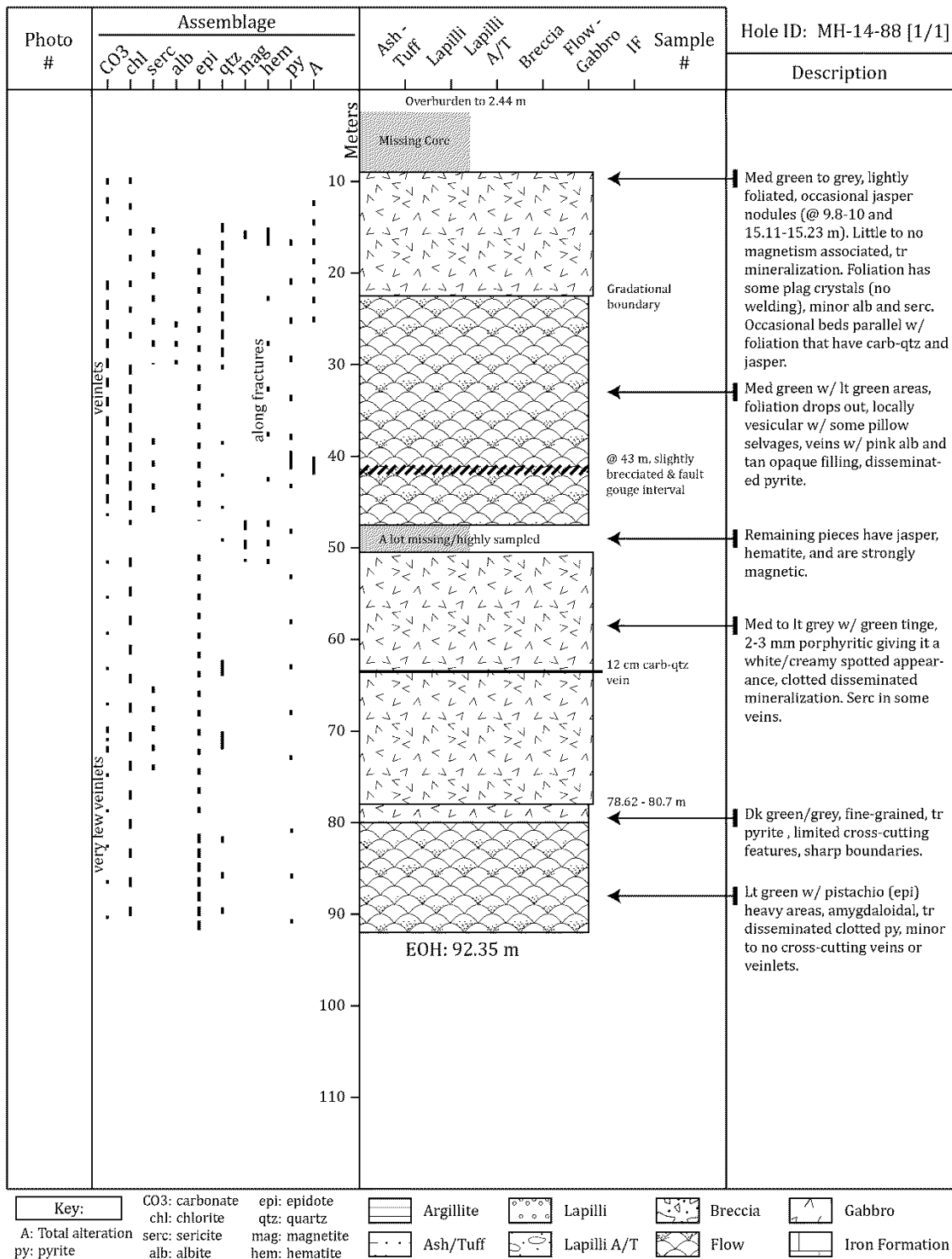
### **Appendix A.III (continued) Graphic logs from the 1987/88 drill program**



**Appendix A.III (continued) Graphic logs from the 1987/88 drill program**



### **Appendix A.III (continued) Graphic logs from the 1987/88 drill program**



**Key:**

$\text{CO}_3$ : carbonate  
chl: chlorite

: epidote  
: quartz

Argi

Lap

2

uccia

## Gabbro

### A: Total alteration py; pyrite

qtz: quartz  
mag: magnetite  
hem: hematite

Ash/T

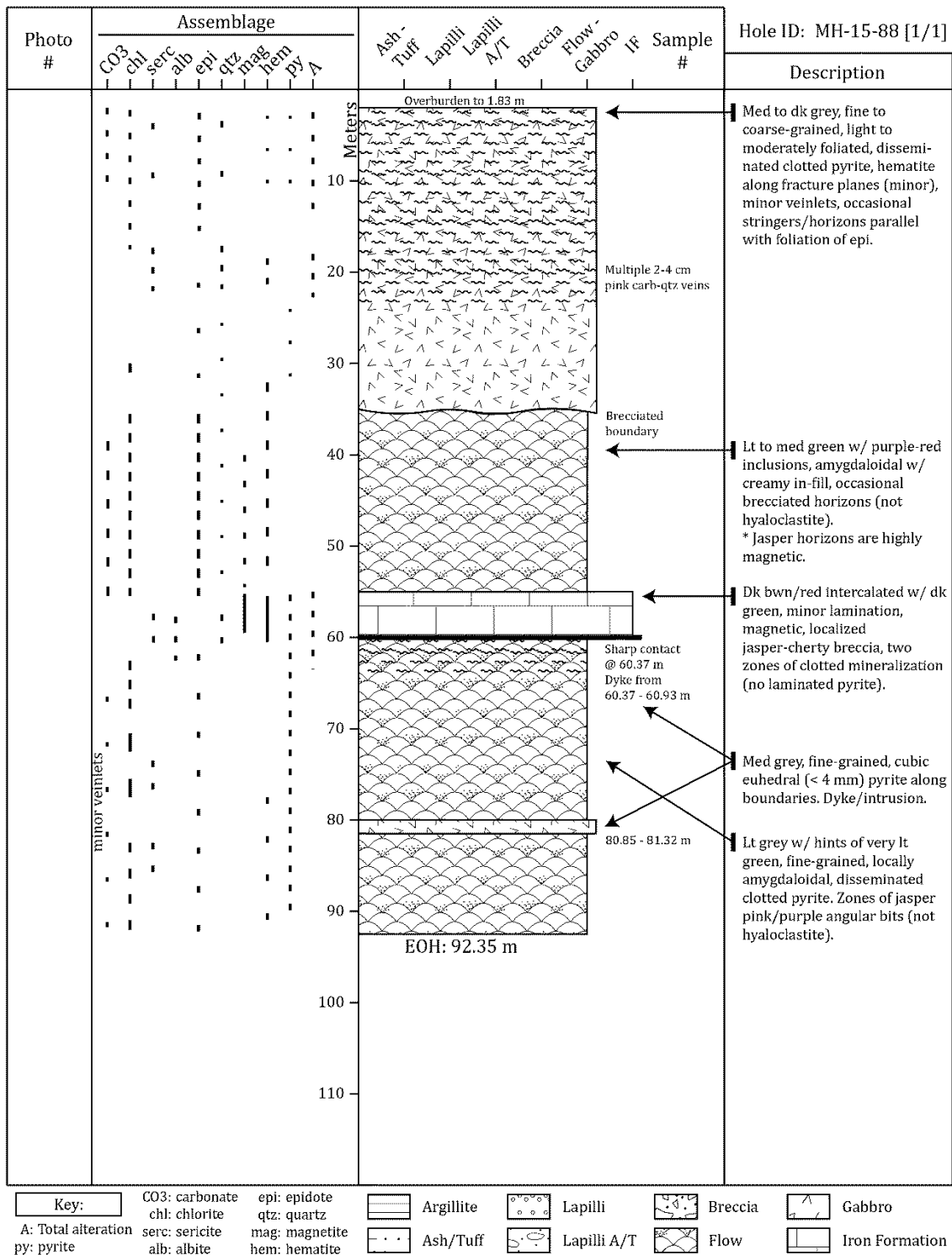
Lap

T  Flo

v

### Iron Formation

### **Appendix A.III (continued) Graphic logs from the 1987/88 drill program**



Key:

CO<sub>3</sub>: carbonate

pi: epidote

## Argillite

Lapilli

1

21

Gahhro

A: Total alteration  
by: pyrite

qtz: quartz  
mag: magnetite  
hem: hematite

Ash/Tuf

La

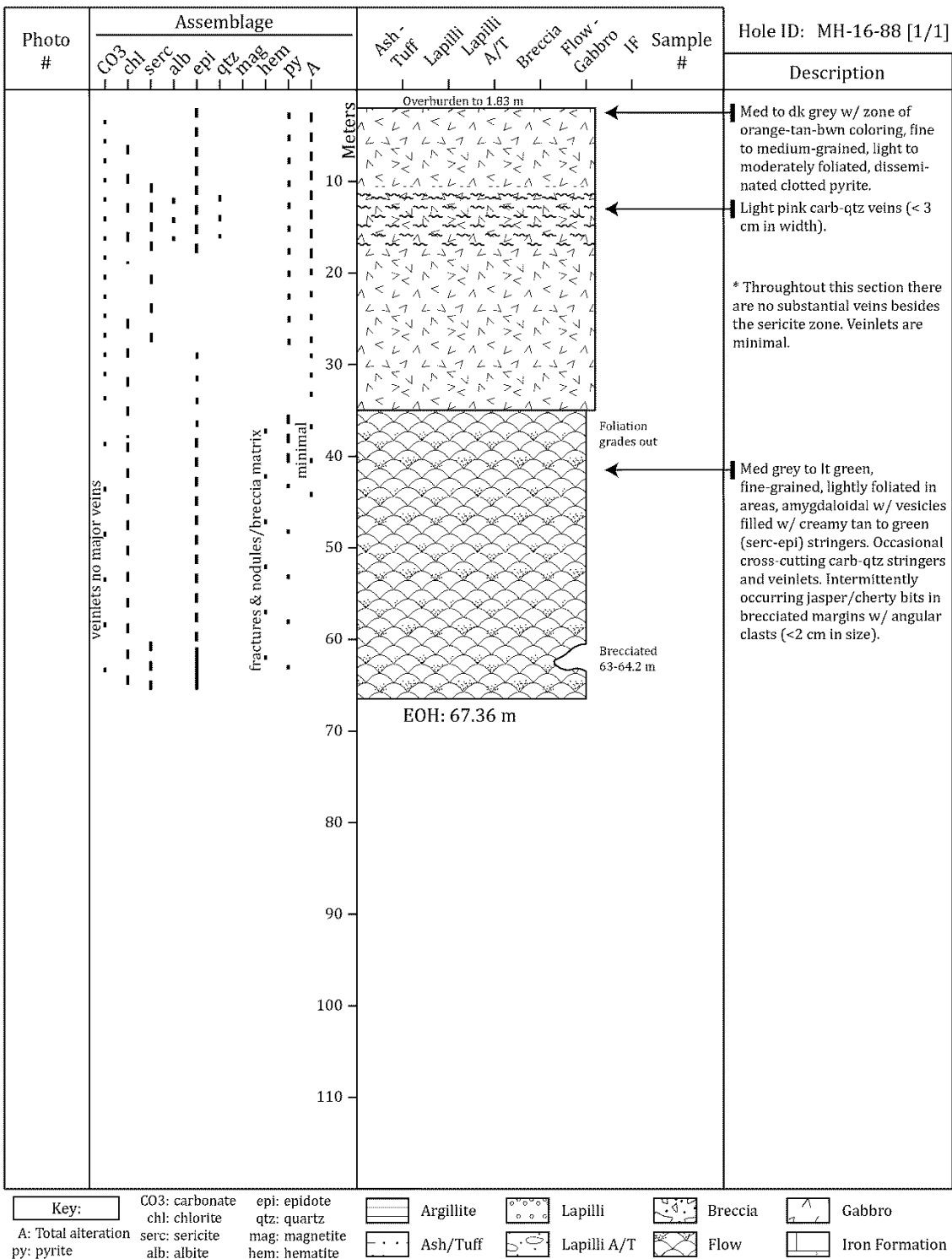
A/T

Flow

1

## Formation

### **Appendix A.III (continued) Graphic logs from the 1987/88 drill program**



Key:

CO<sub>3</sub>: carbonate

### **: epidote**

Argilli

Lapilli

Brec

Gahro

A: Total alteration  
by: pyrite

qtz: quartz  
mag: magnetite  
hem: hematite

Ash/Tuf

A small icon of a rounded, irregular shape, representing a lapilli particle.

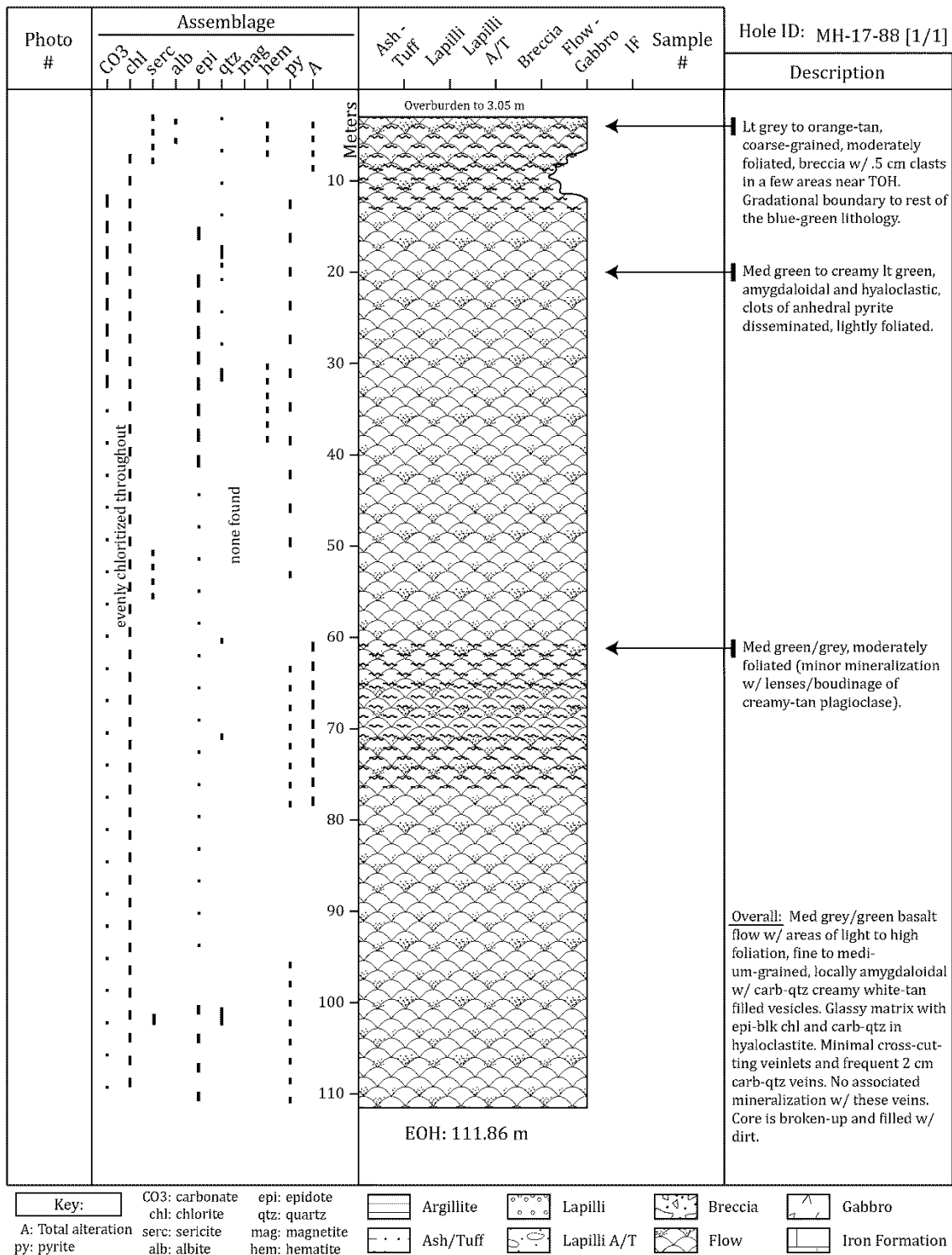
Lapilli

A small square icon containing a flowchart symbol, representing a process or procedure.

Flow

7-1 Cassio  
 Iron Formation

### **Appendix A.III (continued) Graphic logs from the 1987/88 drill program**



Key:

CO<sub>3</sub>: carbonate

## epidote

Auxilli

Lamill

При

© Sabrina

Key:

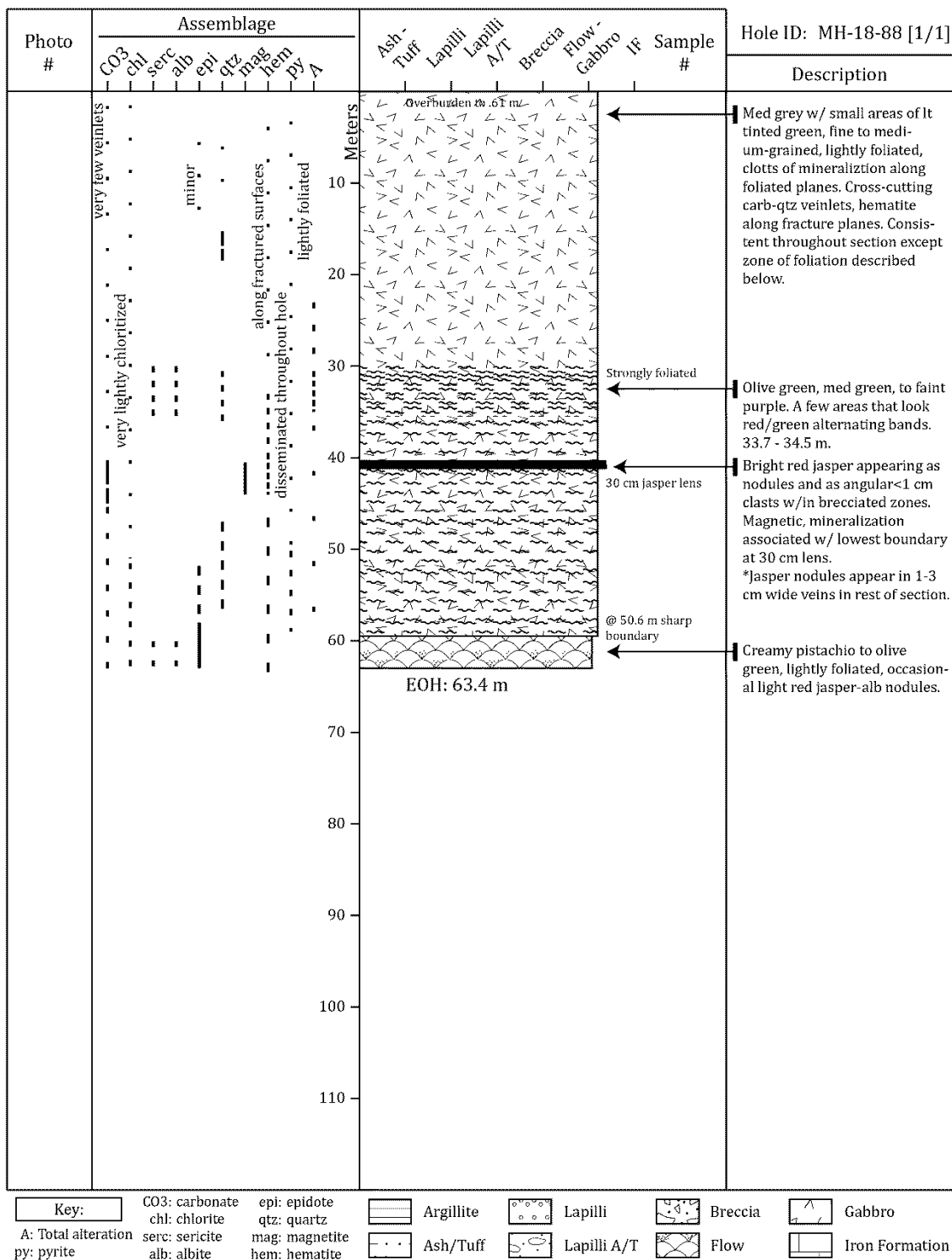
qtz: quartz  
mag: magnetite  
hem: hematite

Argin  
Ash/T

Lapili

 Gabbro  
 Iron Formation

### Appendix A.III (continued) Graphic logs from the 1987/88 drill program



**Appendix B:** List of samples and methods used for rocks from the Goldenville Horizon  
and related stratigraphy

## Appendix B Sample overview

Sample #	Hole ID	Depth From (meter)	Depth To	Whole Rock Geochemistry	Polished Thin Section	SEM analysis
348001	GV-16-10	1.2	1.4	x		
348002	GV-16-10	9	9.2			
348003	GV-16-10	30.72	30.87			
348004	GV-16-10	46.2	46.4			
348005	GV-16-10	53.62	53.8	x		
348006	GV-16-10	71.73	71.87	x		
348007	GV-16-10	76.36	76.76	x		
348008	GV-16-10	77.1	77.26	x		
348009	GV-16-10	79				
348010	GV-16-10	79.5			x	
348011	GV-16-10	80				
348012	GV-16-10	80.2	80.36	x		
348013	GV-16-10	80.58	80.74	x		
348014	GV-16-10	85.5	85.66	x		
348015	GV-16-11	28.22	28.36			
348016	GV-16-11	50.2	50.37			
348017	GV-16-11	53.9	54.1	x		
348018	GV-16-11	55.7				
348019	GV-16-11	56.9			x	
348020	GV-16-11	58.45	58.61	x		
348021	GV-16-11	61.07	61.23	x		
348022	GV-16-11	63.65	63.8	x		
348023	GV-16-11	69.25	69.43			
348024	GV-16-11	90.23	90.44			
348025	GV-16-11	102.44	102.64			
348026	GV-16-11	113	113.22			
348027	GV-16-11	134.17	134.32			
348028	GV-16-09	6.53	6.77	x		
348029	GV-16-09	11.5				
348030	GV-16-09	11.3			x	
348031	GV-16-09	14.7			x	
348032	GV-16-09	15			x	
348033	GV-16-09	15.67	15.82	x		
348034	GV-16-09	15.5				
348035	GV-16-09	19.5	19.68	x		
348036	GV-16-09	22.18	22.32	x		
348037	GV-16-09	24.3	24.44	x		
348038	GV-16-09	25.84	26	x		x
348039	GV-16-09	35.55	35.8		x	

## Appendix B (continued) Sample overview

Sample #	Hole ID	Depth From (meter)	Depth To	Whole Rock Geochemistry	Polished Thin Section	SEM analysis
348040	GV-16-09	43.58	43.74			
348041	GV-16-09	61	61.2	x	x	
348042	GV-16-09	77.3	77.46	x		
348043	GV-16-09	89.5	89.7		x	
348044	GV-16-09	95	95.22			
348045	GV-16-09	116.9	117.07	x		
348046	GV-16-09	73.75	73.92	x		
348047	GV-16-09	83.3	83.47	x	x	
348048	GV-16-13(a)	48.45	48.6	x		
348049	GV-16-13(a)	78.35	78.55			
348050	GV-16-13(a)	108.77	108.9			
348051	GV-16-05	4	4.18	x		
348052	GV-16-05	16.15	16.36			
348053	GV-16-05	28.74	29	x		
348054	GV-16-05	41.2	41.38	x		
348055	GV-16-05	64.06	64.26	x		
348056	GV-16-05	63.6	63.85	x		
348057	GV-16-05	65.8			x	x
348058	GV-16-05	67.1	67.3	x		
348059	GV-16-05	68	68.16	x	x	
348060	GV-16-05	70.58	70.72	x		
348061	GV-16-05	76.2	76.36	x		
348062	GV-16-05	80.77	80.93	x		
348063	GV-16-05	85.8	86	x		
348064	GV-16-05	94.11	94.3	x		
348065	GV-16-05	101.86	102	x		
348066	GV-16-05	111.22	111.4	x		
348067	GV-16-05	118.86	119			
348068	GV-16-05	132.75	132.9	x	x	
348069	GV-16-05	141.1	141.25			
348070	GV-16-05	146.78	146.95	x	x	x
348071	GV-16-05	156.5	156.7	x		
348072	GV-16-05	162.6	162.78	x		x
348073	GV-16-05	167.4	167.53	x		x
348074	GV-16-05	171.7	171.9			
348075	GV-16-05	174.17	174.35	x		
348076	GV-16-05	189.08	189.24			
348077	GV-16-05	200.4	200.53	x		
348078	GV-16-12	5.8	5.95	x		

## Appendix B (continued) Sample overview

Sample #	Hole ID	Depth From (meter)	Depth To	Whole Rock Geochemistry	Polished Thin Section	SEM analysis
348079	GV-16-12	18.38	18.55	x	x	
348080	GV-16-12	22	22.15	x	x	
348081	GV-16-12	29.96	30.13	x		
348082	GV-16-12	35.8	35.93	x		
348083	GV-16-12	39.3	39.44	x		
348084	GV-16-12	40.4				
348085	GV-16-12	44.11	44.28	x		
348086	GV-16-12	46.9	47	x		
348087	GV-16-12	45				
348088	GV-16-12	45.5			x	x
348089	GV-16-12	46				
348090	GV-16-12	49.15	49.3	x		
348091	GV-16-12	63.18	63.33	x	x	
348092	GV-16-12	66.02	66.23	x		
348093	GV-16-12	71.6	71.82	x		
348094	GV-16-12	83.5	83.64	x		
348095	GV-16-12	89	89.15	x		
348096	GV-16-12	93.1	93.28	x	x	
348097	GV-16-12	102.86	103	x		
348098	GV-16-12	110	110.15			
348099	GV-16-12	118.96	119.1	x	x	
348100	GV-16-13(a)	10	10.2	x	x	
348901	GV-16-01	109.5	109.64	x		
348902	GV-16-01	118.7	118.81	x	x	x
348903	GV-16-01	117.08	117.13			
348904	GV-16-01	121.4	121.51	x		
348905	GV-16-01	124.7	124.84	x		
348906	GV-16-01	132.4	132.55	x		
348907	GV-16-01	155.6	155.73	x		
348908	GV-16-01	144.5	144.64	x		
348909	GV-16-01	167.5	167.63	x		
348910	GV-16-01	181.5	181.65	x		
348911	GV-16-04	9.6	9.73	x		
348912	GV-16-04	17.32	17.47	x		
348913	GV-16-04	30	30.15	x		
348914	GV-16-04	46.44	46.64			
348915	GV-16-04	53.36	53.56	x		
348916	GV-16-04	59.9	60.1	x	x	
348917	GV-16-04	65	65.2	x		

## Appendix B (continued) Sample overview

Sample #	Hole ID	Depth From (meter)	Depth To	Whole Rock Geochemistry	Polished Thin Section	SEM analysis
348918	GV-16-04	79.6	79.76	x	x	
348919	GV-16-04	91.26	91.43			
348920	GV-16-04	101.61	101.76	x	x	
348921	GV-16-04	123.76	123.91	x	x	
348922	GV-16-04	130.5	130.65	x		
348923	GV-16-04	107.96	108.1	x		
348924	GV-16-04	110.35	110.47	x		
348925	GV-16-04	110.5			x	x
348926	GV-16-04	111.4				
348927	GV-16-04	115.4				
348928	GV-16-04	114.2	114.32	x		
348929	GV-16-05	116.4	116.53	x	x	
348930	GV-16-06	119.9	120.03	x	x	x
348931	GV-16-04	115.7			x	
348942	Hand sample from historic waste pile				x	x
348951	GV-16-07	21.19	21.34			
348952	GV-16-07	44				
348953	GV-16-07	44	44.12	x		
348954	GV-16-07	52	52.22			
348955	GV-16-08	14.5	14.63	x		
348956	GV-16-08	19			x	
348957	GV-16-08	19.06	19.19	x		
348958	GV-16-08	20.9	21.06	x		
348959	GV-16-08	24.8	24.93	x		
348960	GV-16-08	26.6	26.74	x		
348961	GV-16-08	29.5	29.61	x		
348963	GV-16-03	18.7	18.9			
348964	GV-16-03	29.9	30.15	x		
348965	GV-16-03	62	62.17	x		
348966	GV-16-03	33			x	
348967	GV-16-03	35.2	35.35	x		
348968	GV-16-03	35.5				
348969	GV-16-03	36.3			x	x
348970	GV-16-03	38.54	38.65	x		
348971	GV-16-03	42.81	42.96	x		
348972	GV-16-06	38.84	39	x		
348973	GV-16-06	95	95.22			
348974	GV-16-06	103.34	103.53			
348975	GV-16-06	108.48	108.62			

## Appendix B (continued) Sample overview

Sample #	Hole ID	Depth From (meter)	Depth To	Whole Rock Geochemistry	Polished Thin Section	SEM analysis
348976	GV-16-06	135.07	135.22			
348977	GV-16-06	155.58	155.74	x		
348978	GV-16-06	196.45	196.62			
348979	GV-16-02	18.25	18.43			
348980	GV-16-02	64				
348981	GV-16-02	61.15	61.28	x	x	
348983	GV-16-02	117.5	117.64	x		
348984	GV-16-02	124	124.14	x		
348985	GV-16-02	128.3	128.46	x		
348986	GV-16-02	155	155.18			
348987	GV-16-01	8	8.12	x		
348988	GV-16-01	21.28	21.48	x	x	
348989	GV-16-01	38	38.2	x	x	
348990	GV-16-01	43.43	43.58	x		
348991	GV-16-01	54.55	54.7	x		
348992	GV-16-01	66.44	66.6	x		
348993	GV-16-01	73.14			x	
348994	GV-16-01	71.64	71.75	x		
348995	GV-16-01	69.6			x	
348996	GV-16-01	69.7			x	
348997	GV-16-01	77.5	77.64	x		
348998	GV-16-01					
348999	GV-16-01	88	88.13	x		
349000	GV-16-01	97	97.14	x		
420623	Hand sample: UTM 568627E 5538643N				x	
420622	Hand sample: UTM 568305E 5538557N				x	
420621	MH-06-87	159.8	160			
420620	MH-06-87	108.8	109.1			
420619	MH-06-87	171.3	171.5			
420618	MH-13-87	157.8	158			
420617	MH-13-87	92	92.2			
420616	MH-13-87	87	87.5		x	
420615	MH-13-87	127.6	127.8			
420614	MH-13-87	142.5	142.7			
420613	MH-13-87	152.65	152.95			
420612	MH-05-87	86.8	87		x	
420611	MH-05-87	100	100.3			
420610	MH-05-87	77.5	77.8			
420609	MH-05-87	88.8	89			

**Appendix B (continued) Sample overview**

Sample #	Hole ID	Depth From (meter)	Depth To	Whole Rock Geochemistry	Polished Thin Section	SEM analysis
420608	MH-05-87	73.5	73.9			
420607	MH-05-87	114.1	114.24			
420606	MH-02-87	44.3	44.5			
420605	MH-02-87	84.3	84.5			
420604	MH-11-87	11.18	11.38			
420603	MH-11-87	14.28	14.47			
420602	MH-11-87	22.12	22.27			
420601	MH-11-87	51.71	51.89			
420600	MH-11-87	40.44	40.61		x	
420599	MH-11-87	47.1	47.27			
420598	MH-11-87	55.44	55.6			
420597	MH-11-87	33.67	33.85			
420596	MH-12-87	43.4	43.5			
420595	MH-10-87	79.4	79.67			
420592	GV-16-03	45.95	46.1			
420591	GV-16-08	31.2	31.57		x	

**Appendix C:** Petrography of rocks from the Goldenville Horizon and related stratigraphy

### **Appendix C.I Scans of petrographic thin sections**

**Sample:** 348988  
**DDH:** GV-16-01  
**Depth:** 22 m



**Sample:** 348989  
**DDH:** GV-16-01  
**Depth:** 38.10 m



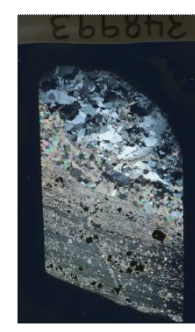
**Sample:** 348995  
**DDH:** GV-16-01  
**Depth:** 69.60 m



**Sample:** 348996  
**DDH:** GV-16-01  
**Depth:** 69.70 m



**Sample:** 348993  
**DDH:** GV-16-01  
**Depth:** 73.14 m



**Sample:** 348902  
**DDH:** GV-16-01  
**Depth:** 118.7 m



**Appendix C.I** (continued) Scans of petrographic thin sections

**Sample:** 348981  
**DDH:** GV-16-02  
**Depth:** 61.5 m



**Sample:** 348966  
**DDH:** GV-16-03  
**Depth:** 33 m



**Sample:** 348969  
**DDH:** GV-16-03  
**Depth:** 36.3 m



**Sample:** 348916  
**DDH:** GV-16-04  
**Depth:** 59.9 m



**Sample:** 348918  
**DDH:** GV-16-04  
**Depth:** 79.7 m



**Sample:** 348920  
**DDH:** GV-16-04  
**Depth:** 101.61 m



**Appendix C.I** (continued) Scans of petrographic thin sections

**Sample:** 348925  
**DDH:** GV-16-04  
**Depth:** 110.5 m



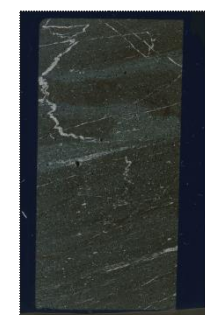
**Sample:** 348931  
**DDH:** GV-16-04  
**Depth:** 115.7 m



**Sample:** 348929  
**DDH:** GV-16-04  
**Depth:** 116.4 m



**Sample:** 348930  
**DDH:** GV-16-04  
**Depth:** 119.9 m



**Sample:** 348921  
**DDH:** GV-16-04  
**Depth:** 123.76 m



**Sample:** 348057  
**DDH:** GV-16-05  
**Depth:** 65.8 m



**Appendix C.I** (continued) Scans of petrographic thin sections

**Sample:** 348059  
**DDH:** GV-16-05  
**Depth:** 68 m



**Sample:** 348068  
**DDH:** GV-16-05  
**Depth:** 132.75 m



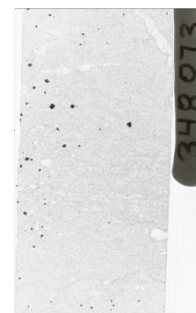
**Sample:** 348070  
**DDH:** GV-16-05  
**Depth:** 146.78 m



**Sample:** 348072  
**DDH:** GV-16-05  
**Depth:** 162.6 m



**Sample:** 348073  
**DDH:** GV-16-05  
**Depth:** 167.4 m



**Sample:** 348956  
**DDH:** GV-16-08  
**Depth:** 19 m



**Appendix C.I** (continued) Scans of petrographic thin sections

**Sample:** 420591

**DDH:** GV-16-08

**Depth:** 31.4 m



**Sample:** 348030

**DDH:** GV-16-09

**Depth:** 11.3 m



**Sample:** 348029

**DDH:** GV-16-09

**Depth:** 11.5 m



**Sample:** 348031

**DDH:** GV-16-09

**Depth:** 14.7 m



**Sample:** 348032

**DDH:** GV-16-09

**Depth:** 15 m



**Sample:** 348038

**DDH:** GV-16-09

**Depth:** 25.84 m



**Appendix C.I** (continued) Scans of petrographic thin sections

**Sample:** 348039  
**DDH:** GV-16-09  
**Depth:** 35.6 m



**Sample:** 348041  
**DDH:** GV-16-09  
**Depth:** 61.1 m



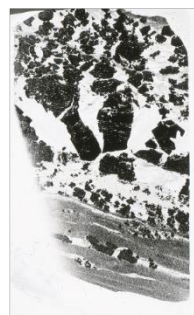
**Sample:** 348047  
**DDH:** GV-16-09  
**Depth:** 83.4 m



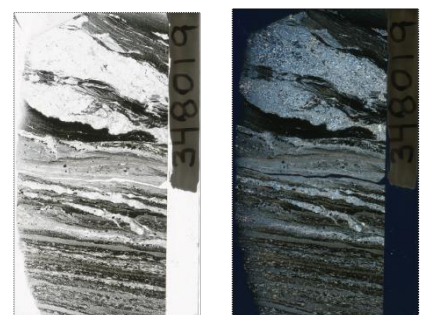
**Sample:** 348043  
**DDH:** GV-16-09  
**Depth:** 89.6 m



**Sample:** 348010  
**DDH:** GV-16-10  
**Depth:** 79.5 m



**Sample:** 348019  
**DDH:** GV-16-11  
**Depth:** 56.9 m



**Appendix C.I** (continued) Scans of petrographic thin sections

**Sample:** 348079  
**DDH:** GV-16-12  
**Depth:** 18.38 m



**Sample:** 348080  
**DDH:** GV-16-12  
**Depth:** 22.1 m



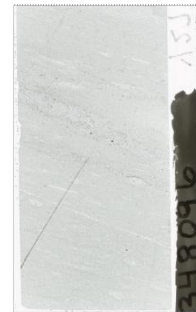
**Sample:** 348088  
**DDH:** GV-16-12  
**Depth:** 45.5 m



**Sample:** 348091  
**DDH:** GV-16-12  
**Depth:** 63.8 m



**Sample:** 348096  
**DDH:** GV-16-12  
**Depth:** 93.1 m



**Sample:** 348099  
**DDH:** GV-16-12  
**Depth:** 118.96 m

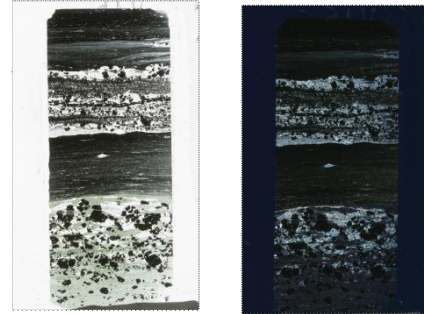


**Appendix C.I** (continued) Scans of petrographic thin sections

**Sample:** 348100  
**DDH:** GV-16-13a  
**Depth:** 10 m



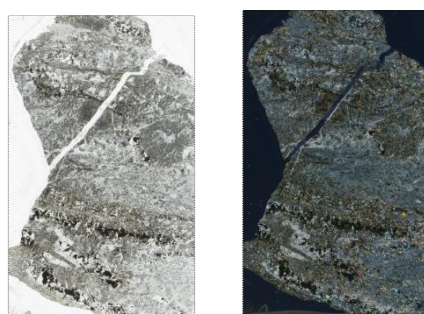
**Sample:** 420612  
**DDH:** MH-05-87  
**Depth:** 86.8 m



**Sample:** 420600  
**DDH:** MH-11-87  
**Depth:** 40.5 m



**Sample:** 420616  
**DDH:** MH-13-88  
**Depth:** 87.3 m



**Appendix C.I** (continued) Scans of petrographic thin sections

**Sample:** 420622

Hand Sample

**UTME:** 568305

**UTMN:** 5538557



**Sample:** 420623

Hand Sample

**UTME:** 568627

**UTMN:** 5538643



**Sample:** 348942

Hand Sample

**UTME:** 40.5 m

**UTMN:** 40.5 m



**Appendix D:** Precision and accuracy data for in house reference materials SLV-MC and

IOC-1

## **Appendix D.I** Precision and accuracy abbreviations

LOD: Limit of detection

BDL: Below limit of detection

NA: Not applicable

### Method Abbreviations:

FUS: Li-B fusion followed by acid digestion

GRAV: Gravimetric, in furnace

AD: Closed-vessel, multi-acid digestion

FA: Fire assay

COM-IR: Combustion infrared absorption

ICP-MS: Inductively coupled plasma-mass spectrometry

ICP-AES: Inductively coupled plasma-atomic emission spectrometry

Note that IOC-1 reference material can be obtained [here](#).

## Appendix D.II Precision and accuracy data for in house reference materials

		Standard	SLV-MC				Mean	$\sigma$	% RSD	
			Given ID	LOD	348938	348939	348943	348944		
SiO <sub>2</sub>	%	FUS-ICP-AES	0.01	49.9	49.9	49.6	49.6	49.75	0.17	0.35
TiO <sub>2</sub>	%	FUS-ICP-AES	0.01	1.47	1.48	1.49	1.49	1.48	0.01	0.65
Al <sub>2</sub> O <sub>3</sub>	%	FUS-ICP-AES	0.01	15.8	15.8	15.35	15.4	15.59	0.25	1.58
Fe <sub>2</sub> O <sub>3T</sub>	%	FUS-ICP-AES	0.01	13.05	13.05	12.72	12.8	12.91	0.17	1.32
MnO	%	FUS-ICP-AES	0.01	0.16	0.16	0.16	0.16	0.16	0.00	0.00
MgO	%	FUS-ICP-AES	0.01	7.71	7.69	7.5	7.52	7.61	0.11	1.45
CaO	%	FUS-ICP-AES	0.01	8.76	8.78	8.5	8.48	8.63	0.16	1.88
Na <sub>2</sub> O	%	FUS-ICP-AES	0.01	3.43	3.44	3.5	3.51	3.47	0.04	1.18
K <sub>2</sub> O	%	FUS-ICP-AES	0.01	0.5	0.5	0.52	0.52	0.51	0.01	2.26
P <sub>2</sub> O <sub>5</sub>	%	FUS-ICP-AES	0.01	0.24	0.24	0.24	0.23	0.24	0.00	2.11
Cr <sub>2</sub> O <sub>3</sub>	%	FUS-ICP-AES	0.002	0.03	0.03	0.031	0.03	0.03	0.00	1.65
BaO	%	FUS-ICP-AES	0.01	0.02	0.02	0.02	0.02	0.02	0.00	0.00
LOI	%	GRAV		-0.81	-0.81	-0.6	-0.6	-0.71	0.12	-17.20
Total	%			100.31	100.33	99.11	99.21	99.74	0.67	0.67
CO <sub>2</sub>	%	COM-IR		0.041	0.054	0.023	0.0115	0.03	0.02	58.22
S	%	COM-IR		0.0015	0.004	0.01	0.008	0.01	0.00	65.33
Li	ppm	AD-ICP-MS	0.4	7	6.9	6.6	6.5	6.75	0.24	3.53
Be	ppm	AD-ICP-MS	0.04	0.88	0.81	0.9	0.9	0.87	0.04	4.90
Sc	ppm	AD-ICP-MS	1.1	20.4	19.9	24	23.9	22.05	2.20	9.99
V	ppm	FUS-ICP-MS	1	193	194	187	185	189.75	4.43	2.33
Co	ppm	AD-ICP-MS	0.13	51	50	54.1	54.3	52.35	2.18	4.16
Ni	ppm	AD-ICP-MS	0.7	162.5	158.5	172	167.5	165.13	5.88	3.56
Cu	ppm	AD-ICP-MS	1.4	59.7	58.8	61.7	60.9	60.28	1.28	2.13
Zn	ppm	AD-ICP-MS	1.8	117	115	128	124	121.00	6.06	5.00
Ga	ppm	FUS-ICP-MS	0.05	21.6	21.8	21.6	20.8	21.45	0.44	2.07
Rb	ppm	FUS-ICP-MS	0.2	5.1	5.4	5.2	5.7	5.35	0.26	4.95
Sr	ppm	FUS-ICP-MS	0.1	454	439	453	451	449.25	6.95	1.55
Y	ppm	FUS-ICP-MS	0.1	16.7	16.5	17.1	16.8	16.78	0.25	1.49
Zr	ppm	FUS-ICP-MS	2	103	100	101	100	101.00	1.41	1.40
Nb	ppm	FUS-ICP-MS	0.2	8.5	8.2	8.6	8.4	8.43	0.17	2.03
Mo	ppm	AD-ICP-MS	0.08	3.82	3.64	3.78	3.69	3.73	0.08	2.20
Ag	ppm	AD-ICP-MS	0.01	0.09	0.12	0.08	0.07	0.09	0.02	24.00
Cd	ppm	AD-ICP-MS	0.013	0.09	0.12	0.11	0.11	0.11	0.01	11.71
In	ppm	AD-ICP-MS	0.002	0.067	0.073	0.074	0.062	0.07	0.01	8.11
Sn	ppm	AD-ICP-MS	0.16	1.7	1.6	1.6	1.6	1.63	0.05	3.08
Sb	ppm	AD-ICP-MS	0.04	0.27	0.28	0.2	0.22	0.24	0.04	15.93

**Appendix D.II** (continued) Precision and accuracy data for in house reference materials

	Standard Given ID	SLV-MC				Mean	$\sigma$	% RSD
		348938	348939	348943	348944			
Cs	ppm AD-ICP-MS	0.01	0.07	0.07	0.08	0.08	0.01	7.70
La	ppm FUS-ICP-MS	0.1	9.4	8.7	9.2	9.1	0.29	3.24
Ce	ppm FUS-ICP-MS	0.1	20.9	20.6	20.3	20	0.39	1.89
Pr	ppm FUS-ICP-MS	0.03	3.01	3.01	2.83	2.9	0.09	3.01
Nd	ppm FUS-ICP-MS	0.1	13.8	13.1	14	14	0.43	3.11
Sm	ppm FUS-ICP-MS	0.03	3.67	3.5	3.56	3.82	0.14	3.86
Eu	ppm FUS-ICP-MS	0.03	1.35	1.3	1.23	1.3	0.05	3.81
Gd	ppm FUS-ICP-MS	0.05	4.04	3.94	4.31	4.53	0.27	6.35
Tb	ppm FUS-ICP-MS	0.01	0.62	0.57	0.64	0.63	0.03	5.06
Dy	ppm FUS-ICP-MS	0.05	3.63	3.95	4.09	3.74	0.21	5.36
Ho	ppm FUS-ICP-MS	0.01	0.68	0.7	0.67	0.71	0.02	2.65
Er	ppm FUS-ICP-MS	0.03	1.67	1.76	1.75	2	0.14	7.94
Tm	ppm FUS-ICP-MS	0.01	0.2	0.23	0.24	0.25	0.02	9.39
Yb	ppm FUS-ICP-MS	0.03	1.37	1.8	1.53	1.59	0.18	11.31
Lu	ppm FUS-ICP-MS	0.01	0.24	0.27	0.23	0.23	0.02	7.81
Hf	ppm FUS-ICP-MS	0.2	2.6	2.4	2.6	2.5	0.10	3.79
Ta	ppm FUS-ICP-MS	0.1	0.6	0.6	0.5	0.5	0.06	10.50
Au	ppm FA-ICP-AES	0.001	0.002	0.001	0.001	BDL	0.00	43.30
Tl	ppm AD-ICP-MS	0.002	BDL	BDL	0.02	0.02	0.00	0.00
Pb	ppm AD-ICP-MS	0.18	5.8	6	5.3	5.4	0.33	5.87
Bi	ppm FUS-ICP-MS	0.01	0.01	0.01	0.01	0.01	0.00	0.00
Th	ppm FUS-ICP-MS	0.05	0.91	0.86	0.89	0.79	0.05	6.09
U	ppm FUS-ICP-MS	0.05	0.31	0.28	0.29	0.29	0.01	4.30

**Appendix D.II** (continued) Precision and accuracy data for in house reference materials

			Measured Value Mean	In-House mean (n=23)	Value Type	%RD
SiO <sub>2</sub>	%	FUS-ICP-AES	49.75	50.03	In-house	-0.56
TiO <sub>2</sub>	%	FUS-ICP-AES	1.48	1.50	In-house	-1.18
Al <sub>2</sub> O <sub>3</sub>	%	FUS-ICP-AES	15.59	15.48	In-house	0.69
Fe <sub>2</sub> O <sub>3T</sub>	%	FUS-ICP-AES	12.91	12.85	In-house	0.43
MnO	%	FUS-ICP-AES	0.16	0.17	In-house	-6.25
MgO	%	FUS-ICP-AES	7.61	7.49	In-house	1.51
CaO	%	FUS-ICP-AES	8.63	8.54	In-house	1.04
Na <sub>2</sub> O	%	FUS-ICP-AES	3.47	3.55	In-house	-2.31
K <sub>2</sub> O	%	FUS-ICP-AES	0.51	0.51	In-house	0.00
P <sub>2</sub> O <sub>5</sub>	%	FUS-ICP-AES	0.24	0.24	In-house	-1.05
Cr <sub>2</sub> O <sub>3</sub>	%	FUS-ICP-AES	0.03	0.03	In-house	0.83
BaO	%	FUS-ICP-AES	0.02	0.02	In-house	0.00
LOI	%	GRAV	-0.71	-0.74	In-house	-4.96
Total	%		99.74	99.70	In-house	0.04
CO <sub>2</sub>	%	COM-IR	0.03	--	--	--
S	%	COM-IR	0.01	--	--	--
Li	ppm	AD-ICP-MS	6.75	--	--	--
Be	ppm	AD-ICP-MS	0.87	--	--	--
Sc	ppm	AD-ICP-MS	22.05	--	--	--
V	ppm	FUS-ICP-MS	189.75	193.64	In-house	-2.05
Co	ppm	AD-ICP-MS	52.35	--	--	--
Ni	ppm	AD-ICP-MS	165.13	--	--	--
Cu	ppm	AD-ICP-MS	60.28	--	--	--
Zn	ppm	AD-ICP-MS	121.00	--	--	--
Ga	ppm	FUS-ICP-MS	21.45	--	--	--
Rb	ppm	FUS-ICP-MS	5.35	5.61	In-house	-4.86
Sr	ppm	FUS-ICP-MS	449.25	469.86	In-house	-4.59
Y	ppm	FUS-ICP-MS	16.78	17.55	In-house	-4.62
Zr	ppm	FUS-ICP-MS	101.00	99.59	In-house	1.40
Nb	ppm	FUS-ICP-MS	8.43	8.51	In-house	-1.01
Mo	ppm	AD-ICP-MS	3.73	--	--	--
Ag	ppm	AD-ICP-MS	0.09	--	--	--
Cd	ppm	AD-ICP-MS	0.11	--	--	--
In	ppm	AD-ICP-MS	0.07	--	--	--
Sn	ppm	AD-ICP-MS	1.63	--	--	--
Sb	ppm	AD-ICP-MS	0.24	--	--	--

**Appendix D.II** (continued) Precision and accuracy data for in house reference materials

			Measured Value Mean	In-House mean (n=23)	Value Type	%RD
Cs	ppm	AD-ICP-MS	0.08	--	--	--
La	ppm	FUS-ICP-MS	9.10	9.45	In-house	-3.85
Ce	ppm	FUS-ICP-MS	20.45	21.24	In-house	-3.86
Pr	ppm	FUS-ICP-MS	2.94	3.01	In-house	-2.47
Nd	ppm	FUS-ICP-MS	13.73	14.20	In-house	-3.46
Sm	ppm	FUS-ICP-MS	3.64	3.89	In-house	-6.94
Eu	ppm	FUS-ICP-MS	1.30	1.36	In-house	-5.02
Gd	ppm	FUS-ICP-MS	4.21	4.04	In-house	3.92
Tb	ppm	FUS-ICP-MS	0.62	0.62	In-house	-0.81
Dy	ppm	FUS-ICP-MS	3.85	3.58	In-house	7.07
Ho	ppm	FUS-ICP-MS	0.69	0.68	In-house	1.45
Er	ppm	FUS-ICP-MS	1.80	1.79	In-house	0.28
Tm	ppm	FUS-ICP-MS	0.23	0.24	In-house	-4.35
Yb	ppm	FUS-ICP-MS	1.57	1.52	In-house	3.34
Lu	ppm	FUS-ICP-MS	0.24	0.22	In-house	9.28
Hf	ppm	FUS-ICP-MS	2.53	2.62	In-house	-3.76
Ta	ppm	FUS-ICP-MS	0.55	0.53	In-house	3.64
Au	ppm	FA-ICP-AES	0.00	--	--	--
Tl	ppm	AD-ICP-MS	0.02	--	--	--
Pb	ppm	AD-ICP-MS	5.63	--	--	--
Bi	ppm	FUS-ICP-MS	0.01	--	--	--
Th	ppm	FUS-ICP-MS	0.86	0.86	In-house	0.29
U	ppm	FUS-ICP-MS	0.29	0.30	In-house	-2.56

**Appendix D.II** (continued) Precision and accuracy data for in house reference materials

		Standard	IOC-1				Mean	$\sigma$	% RSD
			Given ID	LOD	348940	348941	348945	348946	
SiO <sub>2</sub>	%	FUS-ICP-AES	0.01	2.61	2.8	2.7	2.64	2.69	0.08
TiO <sub>2</sub>	%	FUS-ICP-AES	0.01	0.03	0.05	0.05	0.05	0.05	0.01
Al <sub>2</sub> O <sub>3</sub>	%	FUS-ICP-AES	0.01	0.18	0.19	0.17	0.16	0.18	0.01
Fe <sub>2</sub> O <sub>3T</sub>	%	FUS-ICP-AES	0.01	68.4	94.4	93.9	94.6	87.83	12.95
MnO	%	FUS-ICP-AES	0.01	0.42	0.47	0.48	0.48	0.46	0.03
MgO	%	FUS-ICP-AES	0.01	0.92	1.05	1.08	1.08	1.03	0.08
CaO	%	FUS-ICP-AES	0.01	0.97	0.99	1.03	1.01	1.00	0.03
Na <sub>2</sub> O	%	FUS-ICP-AES	0.01	0.01	0.01	BDL	BDL	0.01	0.00
K <sub>2</sub> O	%	FUS-ICP-AES	0.01	BDL	0.04	BDL	0.02	0.03	0.01
P <sub>2</sub> O <sub>5</sub>	%	FUS-ICP-AES	0.01	0.03	0.03	0.03	0.03	0.03	0.00
Cr <sub>2</sub> O <sub>3</sub>	%	FUS-ICP-AES	0.002	0.019	0.023	0.023	0.023	0.02	0.00
BaO	%	FUS-ICP-AES	0.01	BDL	BDL	BDL	0.01	0.01	NA
LOI	%	GRAV		0.83	0.83	0.99	0.91	0.89	0.08
Total	%			74.72	100.88	100.45	100.01	94.02	12.87
CO <sub>2</sub>	%	COM-IR		3.329	3.647	3.35	0.01	2.58	1.72
S	%	COM-IR		0.008	0.005	3.471	0.01	0.87	1.73
Li	ppm	AD-ICP-MS	0.4	1	1	0.8	0.9	0.93	0.10
Be	ppm	AD-ICP-MS	0.04	0.58	0.79	0.72	0.62	0.68	0.10
Sc	ppm	AD-ICP-MS	1.1	0.7	0.7	0.8	0.8	0.75	0.06
V	ppm	FUS-ICP-MS	1	55	42	60	58	53.75	8.10
Co	ppm	AD-ICP-MS	0.13	20	20.4	22.2	21.8	21.10	1.06
Ni	ppm	AD-ICP-MS	0.7	11.6	12.5	12.5	12.1	12.18	0.43
Cu	ppm	AD-ICP-MS	1.4	8.8	8.3	8.7	8.6	8.60	0.22
Zn	ppm	AD-ICP-MS	1.8	5	5	7	7	6.00	1.15
Ga	ppm	FUS-ICP-MS	0.05	2.6	2.1	2.1	2.1	2.23	0.25
Rb	ppm	FUS-ICP-MS	0.2	BDL	BDL	BDL	0.2	0.20	NA
Sr	ppm	FUS-ICP-MS	0.1	4.9	4	4.7	4.9	4.63	0.43
Y	ppm	FUS-ICP-MS	0.1	3.1	5.4	3.4	3.3	3.80	1.07
Zr	ppm	FUS-ICP-MS	2	11	9	10	10	10.00	0.82
Nb	ppm	FUS-ICP-MS	0.2	3.5	3.1	3.1	2.9	3.15	0.25
Mo	ppm	AD-ICP-MS	0.08	20.8	21.8	22.7	23.1	22.10	1.02
Ag	ppm	AD-ICP-MS	0.01	0.01	0.01	0.02	0.03	0.02	0.01
Cd	ppm	AD-ICP-MS	0.013	BDL	BDL	0.02	0.02	0.02	0.00
In	ppm	AD-ICP-MS	0.002	0.006	BDL	BDL	BDL	0.01	NA
Sn	ppm	AD-ICP-MS	0.16	0.6	0.6	0.6	0.6	0.60	0.00
Sb	ppm	AD-ICP-MS	0.04	0.45	0.31	0.29	0.31	0.34	0.07

**Appendix D.II** (continued) Precision and accuracy data for in house reference materials

	Standard	Given ID	IOC-1				Mean	$\sigma$	% RSD
			348940	348941	348945	348946			
Cs	ppm	AD-ICP-MS	0.01	BDL	BDL	BDL	BDL	NA	NA
La	ppm	FUS-ICP-MS	0.1	7.8	5.5	10	11.1	8.60	2.48
Ce	ppm	FUS-ICP-MS	0.1	14.6	11.1	13.8	14	13.38	1.55
Pr	ppm	FUS-ICP-MS	0.03	1.58	1.31	1.54	1.53	1.49	0.12
Nd	ppm	FUS-ICP-MS	0.1	5.1	4.6	5.4	5.3	5.10	0.36
Sm	ppm	FUS-ICP-MS	0.03	0.77	0.77	0.61	0.73	0.72	0.08
Eu	ppm	FUS-ICP-MS	0.03	0.23	0.2	0.23	0.17	0.21	0.03
Gd	ppm	FUS-ICP-MS	0.05	0.67	0.56	0.62	0.64	0.62	0.05
Tb	ppm	FUS-ICP-MS	0.01	0.07	0.07	0.09	0.11	0.09	0.02
Dy	ppm	FUS-ICP-MS	0.05	0.45	0.58	0.6	0.43	0.52	0.09
Ho	ppm	FUS-ICP-MS	0.01	0.08	0.19	0.12	0.1	0.12	0.05
Er	ppm	FUS-ICP-MS	0.03	0.2	0.42	0.27	0.37	0.32	0.10
Tm	ppm	FUS-ICP-MS	0.01	0.02	0.07	0.03	0.04	0.04	0.02
Yb	ppm	FUS-ICP-MS	0.03	0.25	0.44	0.25	0.26	0.30	0.09
Lu	ppm	FUS-ICP-MS	0.01	0.04	0.06	0.03	0.04	0.04	0.01
Hf	ppm	FUS-ICP-MS	0.2	BDL	0.2	0.2	0.2	0.20	0.00
Ta	ppm	FUS-ICP-MS	0.1	0.2	0.1	BDL	BDL	0.15	0.07
Au	ppm	FA-ICP-AES	0.001	BDL	BDL	BDL	BDL	NA	NA
Tl	ppm	AD-ICP-MS	0.002	BDL	BDL	BDL	BDL	NA	NA
Pb	ppm	AD-ICP-MS	0.18	1.5	1.5	1.7	1.6	1.58	0.10
Bi	ppm	FUS-ICP-MS	0.01	0.02	0.02	0.02	0.02	0.02	0.00
Th	ppm	FUS-ICP-MS	0.05	0.84	0.75	0.74	0.78	0.78	0.05
U	ppm	FUS-ICP-MS	0.05	BDL	0.06	0.1	0.12	0.09	0.03

**Appendix D.II** (continued) Precision and accuracy data for in house reference materials

			Measured Value Mean	Value	Value Type	%RD
SiO <sub>2</sub>	%	FUS-ICP-AES	2.69	2.63	Certified	2.03
TiO <sub>2</sub>	%	FUS-ICP-AES	0.05	0.04	Certified	4.67
Al <sub>2</sub> O <sub>3</sub>	%	FUS-ICP-AES	0.18	0.18	Provisional	-5.14
Fe <sub>2</sub> O <sub>3T</sub>	%	FUS-ICP-AES	87.83	93.82	Certified	-6.83
MnO	%	FUS-ICP-AES	0.46	0.47	Certified	-2.05
MgO	%	FUS-ICP-AES	1.03	1.04	Certified	-1.02
CaO	%	FUS-ICP-AES	1.00	0.98	Certified	2.50
Na <sub>2</sub> O	%	FUS-ICP-AES	0.01	--	--	--
K <sub>2</sub> O	%	FUS-ICP-AES	0.03	0.00	Indicative	86.67
P <sub>2</sub> O <sub>5</sub>	%	FUS-ICP-AES	0.03	0.03	Certified	8.33
Cr <sub>2</sub> O <sub>3</sub>	%	FUS-ICP-AES	0.02	0.02	Certified	-1.82
BaO	%	FUS-ICP-AES	0.01	--	--	--
LOI	%	GRAV	0.89	0.86	Certified	3.03
Total	%		94.02	--	--	--
CO <sub>2</sub>	%	COM-IR	2.58	--	--	--
S	%	COM-IR	0.87	--	--	--
Li	ppm	AD-ICP-MS	0.93	--	--	--
Be	ppm	AD-ICP-MS	0.68	--	--	--
Sc	ppm	AD-ICP-MS	0.75	--	--	--
V	ppm	FUS-ICP-MS	53.75	40.80	Provisional	24.09
Co	ppm	AD-ICP-MS	21.10	19.99	Provisional	5.26
Ni	ppm	AD-ICP-MS	12.18	--	--	--
Cu	ppm	AD-ICP-MS	8.60	8.00	Indicative	6.98
Zn	ppm	AD-ICP-MS	6.00	--	--	--
Ga	ppm	FUS-ICP-MS	2.23	2.00	Indicative	10.11
Rb	ppm	FUS-ICP-MS	0.20	--	--	--
Sr	ppm	FUS-ICP-MS	4.63	--	--	--
Y	ppm	FUS-ICP-MS	3.80	--	--	--
Zr	ppm	FUS-ICP-MS	10.00	--	--	--
Nb	ppm	FUS-ICP-MS	3.15	--	--	--
Mo	ppm	AD-ICP-MS	22.10	22.89	Provisional	-3.57
Ag	ppm	AD-ICP-MS	0.02	--	--	--
Cd	ppm	AD-ICP-MS	0.02	--	--	--
In	ppm	AD-ICP-MS	0.01	--	--	--
Sn	ppm	AD-ICP-MS	0.60	--	--	--
Sb	ppm	AD-ICP-MS	0.34	--	--	--

**Appendix D.II** (continued) Precision and accuracy data for in house reference materials

			Measured Value Mean	Value	Value Type	% Bias
Cs	ppm	AD-ICP-MS	NA	--	--	--
La	ppm	FUS-ICP-MS	8.60	--	--	--
Ce	ppm	FUS-ICP-MS	13.38	14.00	Indicative	-4.67
Pr	ppm	FUS-ICP-MS	1.49	--	--	--
Nd	ppm	FUS-ICP-MS	5.10	--	--	--
Sm	ppm	FUS-ICP-MS	0.72	--	--	--
Eu	ppm	FUS-ICP-MS	0.21	--	--	--
Gd	ppm	FUS-ICP-MS	0.62	--	--	--
Tb	ppm	FUS-ICP-MS	0.09	--	--	--
Dy	ppm	FUS-ICP-MS	0.52	--	--	--
Ho	ppm	FUS-ICP-MS	0.12	--	--	--
Er	ppm	FUS-ICP-MS	0.32	--	--	--
Tm	ppm	FUS-ICP-MS	0.04	--	--	--
Yb	ppm	FUS-ICP-MS	0.30	--	--	--
Lu	ppm	FUS-ICP-MS	0.04	--	--	--
Hf	ppm	FUS-ICP-MS	0.20	--	--	--
Ta	ppm	FUS-ICP-MS	0.15	--	--	--
Au	ppm	FA-ICP-AES	NA	--	--	--
Tl	ppm	AD-ICP-MS	NA	--	--	--
Pb	ppm	AD-ICP-MS	1.58	--	--	--
Bi	ppm	FUS-ICP-MS	0.02	--	--	--
Th	ppm	FUS-ICP-MS	0.78	--	--	--
U	ppm	FUS-ICP-MS	0.09	--	--	--

**Appendix E:** Whole-rock geochemistry for rocks from the Goldenville Horizon and  
related stratigraphy

## **Appendix E.I Whole-rock geochemistry abbreviations**

LOD: Limit of detection

Datum for location: N

### **Lithology Abbreviations:**

B-S1: Basaltic volcanic rocks from Suite 1

B-S2: Basaltic volcanic rocks from Suite 2

VC: Volcaniclastic rocks

Arg: Argillite

MR-IF: Magnetite-rich iron formation

ASMM: Argillite with semi-massive magnetite

ADSM: Argillite with disseminated magnetite

Obsolete: Data that was omitted

### **Method Abbreviations:**

FUS: Li-B fusion followed by acid digestion

GRAV: Gravimetric, in furnace

AD: Closed-vessel, multi-acid digestion

FA: Fire assay

COM-IR: Combustion infrared absorption

ICP-MS: Inductively coupled plasma-mass spectrometry

ICP-AES: Inductively coupled plasma-atomic emission spectrometry

## Appendix E.II Whole-rock geochemistry

Sample ID		348001	348005	348006	348012	348013	348014	348020
Drill Hole ID		GV-16-10	GV-16-10	GV-16-10	GV-16-10	GV-16-10	GV-16-10	GV-16-11
Drill Hole Depth (m)		1.2	53.62	71.73	80.2	80.58	85.5	58.45
UTM easting		569008	569008	569008	569008	569008	569008	568323
UTM northing		5538749	5538749	5538749	5538749	5538749	5538749	5538632
Lithology Code	LOD	B-S1	B-S1	B-S1	ASMM	ASMM	ADSM	ASMM
SiO <sub>2</sub> (%)	FUS-ICP-AES	0.01	52.7	51.5	58.5	37	49.7	46.7
TiO <sub>2</sub>	FUS-ICP-AES	0.01	0.61	0.48	0.6	0.39	0.41	1.67
Al <sub>2</sub> O <sub>3</sub>	FUS-ICP-AES	0.01	16.8	15.65	13.95	7.12	8.41	13.85
Fe <sub>2</sub> O <sub>3T</sub>	FUS-ICP-AES	0.01	11.3	9.3	9.34	41.1	22.5	11.4
MnO	FUS-ICP-AES	0.01	0.08	0.13	0.12	2.67	3.41	0.24
MgO	FUS-ICP-AES	0.01	6.4	7.18	5.38	2.59	3.84	6.63
CaO	FUS-ICP-AES	0.01	6.28	7.15	4.11	1.82	2.82	7.91
Na <sub>2</sub> O	FUS-ICP-AES	0.01	2.08	2.42	2.77	0.39	0.18	3.2
K <sub>2</sub> O	FUS-ICP-AES	0.01	0.69	0.04	0.36	0.58	0.25	0.03
P <sub>2</sub> O <sub>5</sub>	FUS-ICP-AES	0.01	0.03	0.04	0.05	1.14	0.33	0.17
Cr <sub>2</sub> O <sub>3</sub>	FUS-ICP-AES	0.002	0.002	0.013	0.001	0.008	0.008	0.03
BaO	FUS-ICP-AES	0.01	0.01	0.005	0.01	0.01	0.005	0.01
LOI	GRAV		4.23	6.37	6.39	4.68	7.98	8.41
Total		101.22	100.28	101.59	99.5	99.84	100.26	100.3
CO <sub>2</sub>	COM-IR		0.185	2.6	2.912	3.714	5.789	4.725
S	COM-IR		0.02	0.571	0.04	0.248	0.142	0.028
Li (ppm)	AD-ICP-MS	0.4	13.4	14.6	23.4	13.1	20.4	16.8
Be	AD-ICP-MS	0.04	0.17	0.19	0.16	1.08	0.62	0.64
Sc	AD-ICP-MS	1.1	35.4	40.1	33	10.8	12.2	41.6
V	FUS-ICP-MS	1	385	309	360	123	127	274
Co	AD-ICP-MS	0.13	38.9	32.3	34.2	30.9	28.4	43.4
Ni	AD-ICP-MS	0.7	31	57.9	14.6	104	66.7	52.9
Cu	AD-ICP-MS	1.4	34.3	83.5	257	53.1	167.5	97.1
Zn	AD-ICP-MS	1.8	106	148	83	223	240	98
Ga	FUS-ICP-MS	0.05	18.1	13.9	15.3	11	13.3	16.6
Rb	FUS-ICP-MS	0.2	14.8	0.4	6.7	8.7	4.4	0.6
Sr	FUS-ICP-MS	0.1	131.5	76.1	60	32.1	36	145
Y	FUS-ICP-MS	0.1	14.2	13.1	16.9	43.8	29.8	29
Zr	FUS-ICP-MS	2	30	22	32	66	73	121
Nb	FUS-ICP-MS	0.2	0.6	0.5	0.7	5.3	6.4	3.3
Mo	AD-ICP-MS	0.08	0.09	0.62	0.96	3.82	1.25	0.54
Ag	AD-ICP-MS	0.01	0.01	0.08	0.06	0.11	0.25	0.05
Cd	AD-ICP-MS	0.013	0.04	0.03	0.03	0.08	0.13	0.1
In	AD-ICP-MS	0.002	0.062	0.056	0.063	0.176	0.143	0.087
Sn	AD-ICP-MS	0.16	0.3	0.3	0.3	1.5	1.6	1.1
Sb	AD-ICP-MS	0.04	0.66	1.06	2.42	0.63	0.39	0.97
Cs	AD-ICP-MS	0.01	0.06	<0.05	0.27	0.06	<0.05	0.13

## Appendix E.II (continued) Whole-rock geochemistry

Sample ID		348001	348005	348006	348012	348013	348014	348020
Drill Hole ID		GV-16-10	GV-16-10	GV-16-10	GV-16-10	GV-16-10	GV-16-10	GV-16-11
Drill Hole Depth (m)		1.2	53.62	71.73	80.2	80.58	85.5	58.45
UTM easting		569008	569008	569008	569008	569008	569008	568323
UTM northing		5538749	5538749	5538749	5538749	5538749	5538749	5538632
Lithology Code	LOD	B-S1	B-S1	B-S1	ASMM	ASMM	ADSM	ASMM
La	FUS-ICP-MS	0.1	1.5	1.3	1.8	41.3	34.6	5.3
Ce	FUS-ICP-MS	0.1	4.5	3	4.2	104	111.5	15.8
Pr	FUS-ICP-MS	0.03	0.7	0.45	0.65	10.05	8.7	2.48
Nd	FUS-ICP-MS	0.1	3.5	2.2	3.2	39.3	36.3	12.6
Sm	FUS-ICP-MS	0.03	1.61	0.97	1.29	8.86	8.6	3.92
Eu	FUS-ICP-MS	0.03	0.61	0.37	0.48	2.36	1.88	1.33
Gd	FUS-ICP-MS	0.05	2.44	1.62	2.08	9.57	8.11	5.37
Tb	FUS-ICP-MS	0.01	0.42	0.28	0.35	1.51	1.18	0.87
Dy	FUS-ICP-MS	0.05	2.8	2.01	2.51	8.87	7.63	5.51
Ho	FUS-ICP-MS	0.01	0.64	0.47	0.69	1.9	1.5	1.14
Er	FUS-ICP-MS	0.03	1.83	1.49	2.04	5.28	4.04	3.33
Tm	FUS-ICP-MS	0.01	0.28	0.26	0.32	0.72	0.56	0.42
Yb	FUS-ICP-MS	0.03	1.91	1.55	1.97	4.36	3.51	2.72
Lu	FUS-ICP-MS	0.01	0.26	0.25	0.32	0.62	0.48	0.41
Hf	FUS-ICP-MS	0.2	1.1	0.7	1	1.7	2	3.4
Ta	FUS-ICP-MS	0.1	0.1	0.1	0.2	0.4	0.3	0.2
Au	FA-ICP-AES	0.001	<0.001	0.001	0.004	0.013	0.011	0.003
Tl	AD-ICP-MS	0.002	0.05	<0.02	0.04	0.06	0.03	<0.02
Pb	AD-ICP-MS	0.18	1.2	5.7	2	43.3	123	5.1
Bi	FUS-ICP-MS	0.01	<0.47	<0.47	<0.47	<0.47	<0.47	<0.47
Th	FUS-ICP-MS	0.05	0.28	0.19	0.32	4.69	5.95	0.31
U	FUS-ICP-MS	0.05	0.24	0.23	0.16	3.06	2.15	0.17
								1.92

## Appendix E.II (continued) Whole-rock geochemistry

Sample ID		348021	348022	348028	348033	348035	348036	348037
Drill Hole ID		GV-16-11	GV-16-11	GV-16-09	GV-16-09	GV-16-09	GV-16-09	GV-16-09
Drill Hole Depth (m)		61.07	63.65	6.53	15.67	19.5	22.18	24.3
UTM easting		568323	568323	568264	568264	568264	568264	568264
UTM northing		5538632	5538632	5538555	5538555	5538555	5538555	5538555
Lithology Code	LOD	Arg	Arg	B-S2	MR-IF	ASMM	ASMM	Arg
SiO <sub>2</sub> (%)	FUS-ICP-AES	0.01	38.9	58.8	43.8	15.85	45.7	43.5
TiO <sub>2</sub>	FUS-ICP-AES	0.01	3.59	0.68	2.93	0.25	0.4	0.34
Al <sub>2</sub> O <sub>3</sub>	FUS-ICP-AES	0.01	13.95	12.6	14.4	4.94	7.6	6.94
Fe <sub>2</sub> O <sub>3T</sub>	FUS-ICP-AES	0.01	13.9	9.93	13	67.4	33.3	35.4
MnO	FUS-ICP-AES	0.01	0.79	1.49	0.2	0.71	4.72	7.44
MgO	FUS-ICP-AES	0.01	4.18	3.11	6.11	1.27	3.04	2.12
CaO	FUS-ICP-AES	0.01	9.32	2.16	11	3.34	1.39	1.79
Na <sub>2</sub> O	FUS-ICP-AES	0.01	0.16	3.77	1.51	1.56	0.05	0.03
K <sub>2</sub> O	FUS-ICP-AES	0.01	3.14	1.79	0.05	0.56	0.22	0.19
P <sub>2</sub> O <sub>5</sub>	FUS-ICP-AES	0.01	0.51	0.15	0.48	0.65	0.43	0.22
Cr <sub>2</sub> O <sub>3</sub>	FUS-ICP-AES	0.002	0.011	0.007	0.008	0.007	0.007	0.006
BaO	FUS-ICP-AES	0.01	0.07	0.04	0.005	0.01	0.005	0.005
LOI	GRAV		11.05	6.48	6.17	2.2	1.71	1.32
Total		99.59	101.02	99.71	98.76	98.57	99.3	100.61
CO <sub>2</sub>	COM-IR		7.514	3.601	2.595	3.912	0.211	0.473
S	COM-IR		0.107	0.013	0.129	0.122	0.021	0.012
Li (ppm)	AD-ICP-MS	0.4	14.3	8.7	14.4	1.8	13	7.2
Be	AD-ICP-MS	0.04	2.12	1.61	1.04	0.89	1.72	2.39
Sc	AD-ICP-MS	1.1	30.8	15	29.6	8.5	13.4	9.5
V	FUS-ICP-MS	1	335	67	342	134	107	95
Co	AD-ICP-MS	0.13	45.8	27.5	52.9	22.3	28.5	35
Ni	AD-ICP-MS	0.7	66.3	47.9	73.4	54.4	134	91.2
Cu	AD-ICP-MS	1.4	25.7	1.3	39.4	86.6	30.8	10.3
Zn	AD-ICP-MS	1.8	133	92	112	84	256	174
Ga	FUS-ICP-MS	0.05	23.3	17.7	22.4	8.6	13.3	13
Rb	FUS-ICP-MS	0.2	68.2	48.6	0.4	14.3	5.9	3.7
Sr	FUS-ICP-MS	0.1	136.5	64.4	461	114.5	8.2	9
Y	FUS-ICP-MS	0.1	32	27.4	31.7	22.8	42.7	34.4
Zr	FUS-ICP-MS	2	247	124	254	45	78	71
Nb	FUS-ICP-MS	0.2	17.1	10.1	17	3.5	6.4	6.3
Mo	AD-ICP-MS	0.08	0.82	0.07	1.19	0.27	0.65	0.19
Ag	AD-ICP-MS	0.01	0.01	0.02	<0.01	0.02	0.03	0.02
Cd	AD-ICP-MS	0.013	0.05	<0.02	0.16	0.12	0.06	0.05
In	AD-ICP-MS	0.002	0.099	0.108	0.081	0.198	0.179	0.18
Sn	AD-ICP-MS	0.16	1.5	2.4	1.7	1.4	2.5	2.8
Sb	AD-ICP-MS	0.04	2.02	1.01	2.14	0.49	0.57	1.24
Cs	AD-ICP-MS	0.01	0.68	0.61	<0.05	0.12	0.05	<0.05

## Appendix E.II (continued) Whole-rock geochemistry

Sample ID		348021	348022	348028	348033	348035	348036	348037	
Drill Hole ID		GV-16-11	GV-16-11	GV-16-09	GV-16-09	GV-16-09	GV-16-09	GV-16-09	
Drill Hole Depth (m)		61.07	63.65	6.53	15.67	19.5	22.18	24.3	
UTM easting		568323	568323	568264	568264	568264	568264	568264	
UTM northing		5538632	5538632	5538555	5538555	5538555	5538555	5538555	
Lithology Code	LOD	Arg	Arg	B-S2	MR-IF	ASMM	ASMM	Arg	
La	FUS-ICP-MS	0.1	18.4	29.1	19.8	19.3	27.3	23	12.8
Ce	FUS-ICP-MS	0.1	44.6	110	49	41.1	82.3	70.6	31
Pr	FUS-ICP-MS	0.03	6.15	7.63	6.79	5.61	7.57	6.41	4.23
Nd	FUS-ICP-MS	0.1	29.5	30	28.6	21.7	28	24.5	18.7
Sm	FUS-ICP-MS	0.03	7.17	6.37	6.45	5.16	6.49	5.77	5.63
Eu	FUS-ICP-MS	0.03	2.43	1.44	2.42	1.17	1.69	1.62	1.85
Gd	FUS-ICP-MS	0.05	7.18	6.18	7.14	5.12	7.4	7.55	6.65
Tb	FUS-ICP-MS	0.01	1.18	0.97	1.02	0.8	1.31	1.3	1.1
Dy	FUS-ICP-MS	0.05	6.98	6	5.92	4.56	8.54	7.84	6.79
Ho	FUS-ICP-MS	0.01	1.29	1.3	1.21	0.96	1.84	1.59	1.53
Er	FUS-ICP-MS	0.03	3.5	3.33	3.38	2.81	5.36	4.36	4.37
Tm	FUS-ICP-MS	0.01	0.51	0.53	0.46	0.44	0.74	0.63	0.62
Yb	FUS-ICP-MS	0.03	3.07	3.52	2.99	2.69	4.64	3.78	4.04
Lu	FUS-ICP-MS	0.01	0.41	0.48	0.44	0.39	0.61	0.53	0.62
Hf	FUS-ICP-MS	0.2	5.5	3.4	5.7	1.1	1.9	1.6	4.5
Ta	FUS-ICP-MS	0.1	1.1	0.6	1.2	0.3	0.5	0.5	0.6
Au	FA-ICP-AES	0.001	<0.001	0.01	0.002	0.003	0.01	0.001	<0.001
Tl	AD-ICP-MS	0.002	0.44	0.35	<0.02	0.07	0.03	0.03	0.09
Pb	AD-ICP-MS	0.18	13.2	46.4	6.5	10.1	4.4	13.9	22
Bi	FUS-ICP-MS	0.01	<0.47	<0.47	<0.47	<0.47	<0.47	<0.47	<0.47
Th	FUS-ICP-MS	0.05	1.02	9.04	0.92	2.65	5.86	5.47	2.27
U	FUS-ICP-MS	0.05	0.62	1.26	0.37	1.24	1.92	1.96	1.35

## Appendix E.II (continued) Whole-rock geochemistry

Sample ID		348038	348041	348042	348045	348046	348048	348051	
Drill Hole ID		GV-16-09	GV-16-09	GV-16-09	GV-16-09	GV-16-09	GV-16-13a	GV-16-05	
Drill Hole Depth (m)		25.84	61	77.3	116.9	73.75	48.45	4	
UTM easting		568264	568264	568264	568264	568264	567404	569136	
UTM northing		5538555	5538555	5538555	5538555	5538555	5537944	5538729	
Lithology Code	LOD	Arg	Arg	ADSM	B-S1	Arg	VC	B-S1	
SiO <sub>2</sub> (%)	FUS-ICP-AES	0.01	51.4	47.1	53.1	54.9	77.8	56.6	53.3
TiO <sub>2</sub>	FUS-ICP-AES	0.01	1.9	0.43	0.58	0.69	0.15	0.55	0.44
Al <sub>2</sub> O <sub>3</sub>	FUS-ICP-AES	0.01	14.7	15.65	16.5	15.15	3.91	14.25	15.1
Fe <sub>2</sub> O <sub>3T</sub>	FUS-ICP-AES	0.01	12.1	9.84	15	10.3	9.64	10.8	8.37
MnO	FUS-ICP-AES	0.01	0.25	0.12	0.08	0.11	0.09	0.13	0.12
MgO	FUS-ICP-AES	0.01	4.53	7.81	0.97	5.6	0.59	6.37	5.32
CaO	FUS-ICP-AES	0.01	8.07	8.93	2.66	4.69	3.99	2.39	10.15
Na <sub>2</sub> O	FUS-ICP-AES	0.01	2.49	1.59	8.13	3.79	0.35	3.38	3.04
K <sub>2</sub> O	FUS-ICP-AES	0.01	0.08	0.79	0.19	0.05	0.67	0.95	0.04
P <sub>2</sub> O <sub>5</sub>	FUS-ICP-AES	0.01	0.24	0.02	0.31	0.07	0.48	0.06	0.04
Cr <sub>2</sub> O <sub>3</sub>	FUS-ICP-AES	0.002	0.012	0.02	0.007	0.002	0.005	0.001	0.003
BaO	FUS-ICP-AES	0.01	0.005	0.01	0.005	0.005	0.01	0.01	0.005
LOI	GRAV		4.53	7.11	2.67	4.89	3.4	4.55	4.5
Total		100.34	99.44	100.21	100.25	101.09	100.05	100.44	
CO <sub>2</sub>	COM-IR		1.427	3.101	1.748	1.575	3.027	1.038	2.691
S	COM-IR		0.057	0.028	0.01	0.072	0.054	0.026	0.046
Li (ppm)	AD-ICP-MS	0.4	15.2	20.1	8.7	22.1	4.7	9.7	6.9
Be	AD-ICP-MS	0.04	1.13	0.19	0.26	0.24	0.21	0.25	0.26
Sc	AD-ICP-MS	1.1	35.9	38.5	36	35.7	8.6	28.1	36.8
V	FUS-ICP-MS	1	279	386	274	383	260	260	285
Co	AD-ICP-MS	0.13	36.4	34	29.5	33.6	14.2	36.7	35.2
Ni	AD-ICP-MS	0.7	45.5	71.3	36.9	26.9	26.2	28.3	35.7
Cu	AD-ICP-MS	1.4	50	25.9	33.7	69	1125	2.2	118
Zn	AD-ICP-MS	1.8	123	70	84	96	42	33	66
Ga	FUS-ICP-MS	0.05	22.4	15.2	10.2	15.2	6.5	14.3	13.9
Rb	FUS-ICP-MS	0.2	1.2	12.4	2.4	0.2	11.1	5.6	0.5
Sr	FUS-ICP-MS	0.1	349	207	79.6	94.9	38.2	83	140.5
Y	FUS-ICP-MS	0.1	41	11.7	21.9	21.3	27.2	14.5	12.7
Zr	FUS-ICP-MS	2	181	24	45	38	12	38	24
Nb	FUS-ICP-MS	0.2	7	0.6	1.3	0.9	0.6	0.9	0.6
Mo	AD-ICP-MS	0.08	0.84	0.09	0.41	0.41	0.78	0.12	0.31
Ag	AD-ICP-MS	0.01	0.01	0.04	0.05	0.02	0.31	<0.01	0.06
Cd	AD-ICP-MS	0.013	0.13	0.19	0.02	0.06	0.03	<0.02	0.14
In	AD-ICP-MS	0.002	0.112	0.052	0.078	0.069	0.056	0.078	0.049
Sn	AD-ICP-MS	0.16	2.2	0.2	0.4	0.4	0.6	0.5	0.4
Sb	AD-ICP-MS	0.04	2.52	0.51	0.52	0.5	0.3	0.3	0.8
Cs	AD-ICP-MS	0.01	<0.05	0.12	0.05	<0.05	0.11	0.06	<0.05

## Appendix E.II (continued) Whole-rock geochemistry

Sample ID		348038	348041	348042	348045	348046	348048	348051
Drill Hole ID		GV-16-09	GV-16-09	GV-16-09	GV-16-09	GV-16-09	GV-16-13a	GV-16-05
Drill Hole Depth (m)		25.84	61	77.3	116.9	73.75	48.45	4
UTM easting		568264	568264	568264	568264	568264	567404	569136
UTM northing		5538555	5538555	5538555	5538555	5538555	5537944	5538729
Lithology Code	LOD	Arg	Arg	ADSM	B-S1	Arg	VC	B-S1
La	FUS-ICP-MS	0.1	12.2	1.4	4.5	2.7	4	2.7
Ce	FUS-ICP-MS	0.1	30.9	3.2	9.6	6.3	7.2	6.5
Pr	FUS-ICP-MS	0.03	4.11	0.45	1.28	0.93	1.24	0.85
Nd	FUS-ICP-MS	0.1	18.8	2.3	5.5	4.2	5.7	4.7
Sm	FUS-ICP-MS	0.03	5.6	0.91	1.7	1.56	1.81	1.69
Eu	FUS-ICP-MS	0.03	1.95	0.35	0.62	0.6	0.56	0.45
Gd	FUS-ICP-MS	0.05	6.92	1.44	2.63	2.58	2.89	2.17
Tb	FUS-ICP-MS	0.01	1.04	0.29	0.45	0.46	0.49	0.41
Dy	FUS-ICP-MS	0.05	6.82	1.88	3.16	3.12	3.54	2.68
Ho	FUS-ICP-MS	0.01	1.56	0.47	0.71	0.79	0.89	0.6
Er	FUS-ICP-MS	0.03	4.44	1.36	2.38	2.41	2.73	1.98
Tm	FUS-ICP-MS	0.01	0.63	0.2	0.42	0.35	0.4	0.26
Yb	FUS-ICP-MS	0.03	4.4	1.56	2.5	2.44	2.62	1.87
Lu	FUS-ICP-MS	0.01	0.64	0.21	0.42	0.39	0.39	0.32
Hf	FUS-ICP-MS	0.2	4.5	0.8	1.3	1.3	0.3	1.3
Ta	FUS-ICP-MS	0.1	0.6	0.1	0.2	0.2	0.2	0.05
Au	FA-ICP-AES	0.001	<0.001	0.001	0.2	<0.001	0.031	0.001
Tl	AD-ICP-MS	0.002	<0.02	0.02	<0.02	<0.02	0.03	0.04
Pb	AD-ICP-MS	0.18	10	1.7	2.8	1	1.7	0.8
Bi	FUS-ICP-MS	0.01	<0.47	<0.47	<0.47	<0.47	0.92	<0.47
Th	FUS-ICP-MS	0.05	2.23	0.27	0.76	0.62	0.5	0.61
U	FUS-ICP-MS	0.05	1.41	0.18	0.44	0.21	0.89	0.18

## Appendix E.II (continued) Whole-rock geochemistry

Sample ID		348053	348054	348055	348056	348058	348059	348060	
Drill Hole ID		GV-16-05							
Drill Hole Depth (m)		28.74	41.2	64.06	63.6	67.1	68	70.58	
UTM easting		569136	569136	569136	569136	569136	569136	569136	
UTM northing		5538729	5538729	5538729	5538729	5538729	5538729	5538729	
Lithology Code	LOD	B-S1	B-S1	B-S1	B-S1	MR-IF	ASMM	VC	
SiO <sub>2</sub> (%)	FUS-ICP-AES	0.01	56.9	49.4	53	45.2	36.2	52.1	61.9
TiO <sub>2</sub>	FUS-ICP-AES	0.01	0.52	0.42	0.5	0.57	0.08	0.47	0.45
Al <sub>2</sub> O <sub>3</sub>	FUS-ICP-AES	0.01	14.85	15.6	15.5	14.6	1.73	9.41	14.85
Fe <sub>2</sub> O <sub>3T</sub>	FUS-ICP-AES	0.01	6.35	8.26	9.11	11.3	53.9	15.15	5.97
MnO	FUS-ICP-AES	0.01	0.03	0.11	0.11	0.2	0.45	4.23	0.25
MgO	FUS-ICP-AES	0.01	1.73	4.93	7.04	6.51	0.62	3.09	2.79
CaO	FUS-ICP-AES	0.01	15.25	11.15	6.23	8.24	3.79	5.21	1.96
Na <sub>2</sub> O	FUS-ICP-AES	0.01	0.49	2.64	3.28	3.24	0.33	1.75	5.83
K <sub>2</sub> O	FUS-ICP-AES	0.01	0.03	0.01	0.13	0.28	0.06	1.23	0.89
P <sub>2</sub> O <sub>5</sub>	FUS-ICP-AES	0.01	0.06	0.04	0.06	0.06	2.19	0.2	0.07
Cr <sub>2</sub> O <sub>3</sub>	FUS-ICP-AES	0.002	0.001	0.003	0.006	0.001	0.002	0.007	0.006
BaO	FUS-ICP-AES	0.01	0.005	0.005	0.005	0.005	0.005	0.02	0.01
LOI	GRAV		3.95	6.09	5.49	8.31	-0.59	8.44	4.03
Total			100.17	98.68	100.47	98.52	98.76	101.31	99.02
CO <sub>2</sub>	COM-IR		3.056	4.298	2.503	6.106	0.956	6.87	2.656
S	COM-IR		0.014	0.043	0.027	0.776	0.034	0.046	0.016
Li (ppm)	AD-ICP-MS	0.4	4.2	13	14.9	20.8	2.5	10.4	13.3
Be	AD-ICP-MS	0.04	0.26	0.17	0.16	0.26	0.25	2.09	0.63
Sc	AD-ICP-MS	1.1	34.1	37.7	34.7	36.6	3.1	11.4	20.5
V	FUS-ICP-MS	1	328	282	361	395	160	82	97
Co	AD-ICP-MS	0.13	16.2	32.9	36.6	47.2	45.2	28.6	15.9
Ni	AD-ICP-MS	0.7	14.9	40.1	38.9	21.3	30.6	58.3	16.4
Cu	AD-ICP-MS	1.4	17.4	131	87.6	88.1	189	317	42
Zn	AD-ICP-MS	1.8	44	70	80	96	73	91	73
Ga	FUS-ICP-MS	0.05	21.2	15.9	14.8	16.4	2.8	13	15.2
Rb	FUS-ICP-MS	0.2	0.6	0.2	0.4	6.6	0.6	29.4	21.8
Sr	FUS-ICP-MS	0.1	88.1	224	108.5	80.2	45.5	54.2	108.5
Y	FUS-ICP-MS	0.1	13.8	14.3	15.7	19.1	29	23.3	25
Zr	FUS-ICP-MS	2	27	22	29	29	16	86	161
Nb	FUS-ICP-MS	0.2	0.6	0.5	0.7	0.7	1.4	7.2	5.2
Mo	AD-ICP-MS	0.08	0.52	0.49	0.2	0.99	0.45	0.11	0.86
Ag	AD-ICP-MS	0.01	0.03	0.05	0.08	0.09	0.08	0.06	0.02
Cd	AD-ICP-MS	0.013	0.4	0.06	0.07	0.05	0.05	0.04	0.04
In	AD-ICP-MS	0.002	0.061	0.047	0.054	0.059	0.18	0.113	0.021
Sn	AD-ICP-MS	0.16	0.3	0.2	0.3	0.3	0.6	2	0.4
Sb	AD-ICP-MS	0.04	1.15	0.72	0.56	1.03	0.22	0.66	0.37
Cs	AD-ICP-MS	0.01	<0.05	<0.05	<0.05	0.15	<0.05	0.22	0.13

## Appendix E.II (continued) Whole-rock geochemistry

Sample ID		348053	348054	348055	348056	348058	348059	348060
Drill Hole ID		GV-16-05						
Drill Hole Depth (m)		28.74	41.2	64.06	63.6	67.1	68	70.58
UTM easting		569136	569136	569136	569136	569136	569136	569136
UTM northing		5538729	5538729	5538729	5538729	5538729	5538729	5538729
Lithology Code	LOD	B-S1	B-S1	B-S1	B-S1	MR-IF	ASMM	VC
La	FUS-ICP-MS	0.1	1.6	1.4	1.6	1.5	17.9	30.3
Ce	FUS-ICP-MS	0.1	3.9	3.1	3.6	3.6	27.7	104.5
Pr	FUS-ICP-MS	0.03	0.57	0.42	0.54	0.54	5.19	7.61
Nd	FUS-ICP-MS	0.1	2.9	2.4	2.8	2.8	20.9	27.8
Sm	FUS-ICP-MS	0.03	1	1.01	1.05	1.05	5.29	5.8
Eu	FUS-ICP-MS	0.03	0.42	0.37	0.39	0.53	1.34	1.37
Gd	FUS-ICP-MS	0.05	1.64	1.45	1.7	2.05	6.19	5.96
Tb	FUS-ICP-MS	0.01	0.35	0.29	0.31	0.38	0.93	0.82
Dy	FUS-ICP-MS	0.05	2.41	2.43	2.4	2.74	5.9	4.75
Ho	FUS-ICP-MS	0.01	0.56	0.51	0.59	0.71	1.2	1.04
Er	FUS-ICP-MS	0.03	1.86	1.75	1.68	2.22	3.33	2.78
Tm	FUS-ICP-MS	0.01	0.24	0.22	0.28	0.34	0.5	0.41
Yb	FUS-ICP-MS	0.03	1.56	1.77	1.81	2.32	2.95	2.53
Lu	FUS-ICP-MS	0.01	0.24	0.26	0.34	0.37	0.37	0.35
Hf	FUS-ICP-MS	0.2	0.8	0.7	1	1.1	0.3	2.3
Ta	FUS-ICP-MS	0.1	0.2	0.2	0.1	0.1	0.2	0.6
Au	FA-ICP-AES	0.001	<0.001	<0.001	<0.001	0.03	0.048	0.196
Tl	AD-ICP-MS	0.002	<0.02	<0.02	<0.02	0.05	<0.02	0.16
Pb	AD-ICP-MS	0.18	1.9	1.7	1.1	2.9	36.7	19.2
Bi	FUS-ICP-MS	0.01	<0.47	<0.47	<0.47	<0.47	<0.47	0.79
Th	FUS-ICP-MS	0.05	0.28	0.21	0.31	0.29	0.92	7.14
U	FUS-ICP-MS	0.05	0.28	0.24	0.21	0.24	1.62	1.12
								1.56

## Appendix E.II (continued) Whole-rock geochemistry

Sample ID		348061	348062	348063	348064	348065	348066	348068
Drill Hole ID		GV-16-05						
Drill Hole Depth (m)		76.2	80.77	85.8	94.11	101.86	111.22	132.75
UTM easting		569136	569136	569136	569136	569136	569136	569136
UTM northing		5538729	5538729	5538729	5538729	5538729	5538729	5538729
Lithology Code	LOD	VC	ASMM	Arg	VC	VC	VC	VC
SiO <sub>2</sub> (%)	FUS-ICP-AES	0.01	51.8	51.4	52.5	51.7	49.8	52.4
TiO <sub>2</sub>	FUS-ICP-AES	0.01	0.82	0.51	1.67	1.36	1.12	0.48
Al <sub>2</sub> O <sub>3</sub>	FUS-ICP-AES	0.01	15.9	10.35	15.55	15.15	16.25	16.7
Fe <sub>2</sub> O <sub>3T</sub>	FUS-ICP-AES	0.01	6.47	19.95	11.6	9.13	6.93	6.29
MnO	FUS-ICP-AES	0.01	0.17	2.85	0.24	0.16	0.13	0.13
MgO	FUS-ICP-AES	0.01	5.36	2.63	3.71	6.93	5.49	6
CaO	FUS-ICP-AES	0.01	4.36	5.06	5.41	6.08	7.99	11
Na <sub>2</sub> O	FUS-ICP-AES	0.01	6.74	1.89	4.79	4.1	5.35	2.23
K <sub>2</sub> O	FUS-ICP-AES	0.01	0.12	0.94	0.27	0.21	0.23	0.24
P <sub>2</sub> O <sub>5</sub>	FUS-ICP-AES	0.01	0.15	0.2	0.29	0.17	0.16	0.07
Cr <sub>2</sub> O <sub>3</sub>	FUS-ICP-AES	0.002	0.044	0.018	0.005	0.011	0.027	0.03
BaO	FUS-ICP-AES	0.01	0.005	0.02	0.01	0.005	0.005	0.01
LOI	GRAV		6.84	3.33	3.59	5.34	6.27	4.45
Total		98.79	99.17	99.66	100.37	99.78	100.05	100.88
CO <sub>2</sub>	COM-IR		4.934	1.382	1.388	2.291	3.916	1.923
S	COM-IR		0.026	0.073	0.069	0.021	0.021	0.02
Li (ppm)	AD-ICP-MS	0.4	14.6	7.1	14.6	22.4	16.6	16.9
Be	AD-ICP-MS	0.04	1.02	2.06	1.09	0.91	0.78	0.69
Sc	AD-ICP-MS	1.1	21	14.3	27.9	33.9	28.9	28.7
V	FUS-ICP-MS	1	130	100	184	209	195	187
Co	AD-ICP-MS	0.13	28.5	32.9	25	31.6	24.2	28.3
Ni	AD-ICP-MS	0.7	141	73.5	19.5	41.6	64.1	63.7
Cu	AD-ICP-MS	1.4	48.6	9.3	22.4	31.7	66.7	27.5
Zn	AD-ICP-MS	1.8	65	162	112	77	61	56
Ga	FUS-ICP-MS	0.05	14.7	14.3	20.5	16.3	17.4	18.2
Rb	FUS-ICP-MS	0.2	2.2	23.6	5.3	2.9	3.5	4.5
Sr	FUS-ICP-MS	0.1	199	169	171.5	276	244	238
Y	FUS-ICP-MS	0.1	27.4	26.2	39.9	25.5	18	9.5
Zr	FUS-ICP-MS	2	161	97	184	133	124	68
Nb	FUS-ICP-MS	0.2	7.4	8.2	6.5	4.6	5.9	3.5
Mo	AD-ICP-MS	0.08	0.23	0.65	0.5	0.12	0.1	0.26
Ag	AD-ICP-MS	0.01	0.08	0.05	<0.01	0.02	0.04	0.02
Cd	AD-ICP-MS	0.013	0.05	0.06	0.11	0.07	0.06	0.05
In	AD-ICP-MS	0.002	0.046	0.159	0.093	0.057	0.051	0.039
Sn	AD-ICP-MS	0.16	1.1	2.5	1.8	1.3	1.2	0.8
Sb	AD-ICP-MS	0.04	0.75	2.5	1.22	1.27	0.94	3
Cs	AD-ICP-MS	0.01	<0.05	0.22	0.07	<0.05	<0.05	0.05

## Appendix E.II (continued) Whole-rock geochemistry

Sample ID		348061	348062	348063	348064	348065	348066	348068	
Drill Hole ID		GV-16-05							
Drill Hole Depth (m)		76.2	80.77	85.8	94.11	101.86	111.22	132.75	
UTM easting		569136	569136	569136	569136	569136	569136	569136	
UTM northing		5538729	5538729	5538729	5538729	5538729	5538729	5538729	
Lithology Code	LOD	VC	ASMM	Arg	VC	VC	VC	VC	
La	FUS-ICP-MS	0.1	14.9	32	10.4	8.8	10.2	7	8.1
Ce	FUS-ICP-MS	0.1	32.8	113.5	28.4	21.9	23.2	15.3	17.1
Pr	FUS-ICP-MS	0.03	4.1	8.8	4.03	2.94	2.91	1.75	2.1
Nd	FUS-ICP-MS	0.1	15.7	32.2	18	13.1	12.5	6.3	8
Sm	FUS-ICP-MS	0.03	3.75	7.09	5.52	3.63	2.98	1.5	2.13
Eu	FUS-ICP-MS	0.03	1.18	1.6	1.85	1.25	1.05	0.6	0.74
Gd	FUS-ICP-MS	0.05	4.39	6.87	6.67	4.39	3.31	1.72	2.4
Tb	FUS-ICP-MS	0.01	0.72	1.01	1.08	0.71	0.5	0.27	0.36
Dy	FUS-ICP-MS	0.05	4.49	5.58	6.76	4.4	3.1	1.67	2.27
Ho	FUS-ICP-MS	0.01	0.96	1.15	1.48	0.95	0.68	0.36	0.52
Er	FUS-ICP-MS	0.03	2.89	3.26	4.22	2.73	2.03	1.12	1.44
Tm	FUS-ICP-MS	0.01	0.44	0.45	0.62	0.4	0.27	0.15	0.22
Yb	FUS-ICP-MS	0.03	2.84	2.86	4.05	2.44	1.84	0.96	1.5
Lu	FUS-ICP-MS	0.01	0.39	0.39	0.56	0.38	0.4	0.13	0.21
Hf	FUS-ICP-MS	0.2	3.8	2.6	4.6	3.3	2.8	1.6	2
Ta	FUS-ICP-MS	0.1	0.6	0.7	0.5	0.5	0.5	0.3	0.3
Au	FA-ICP-AES	0.001	<0.001	0.009	0.001	<0.001	0.003	<0.001	<0.001
Tl	AD-ICP-MS	0.002	0.02	0.16	0.04	<0.02	0.02	0.02	0.05
Pb	AD-ICP-MS	0.18	19.5	66.4	4.8	4	5.2	910	5.1
Bi	FUS-ICP-MS	0.01	<0.47	0.65	<0.47	<0.47	<0.47	<0.47	<0.47
Th	FUS-ICP-MS	0.05	3.73	8.05	1.42	1.91	1.97	2.11	2.29
U	FUS-ICP-MS	0.05	2.72	1.52	0.9	1.2	1.21	1.1	1.34

## Appendix E.II (continued) Whole-rock geochemistry

Sample ID		348070	348071	348072	348073	348075	348077	348078	
Drill Hole ID		GV-16-05	GV-16-05	GV-16-05	GV-16-05	GV-16-05	GV-16-05	GV-16-12	
Drill Hole Depth (m)		146.78	156.5	162.6	167.4	174.17	200.4	5.8	
UTM easting		569136	569136	569136	569136	569136	569136	567665	
UTM northing		5538729	5538729	5538729	5538729	5538729	5538729	5538175	
Lithology Code	LOD	VC	VC	B-S1	B-S1	B-S1	B-S1	B-S1	
SiO <sub>2</sub> (%)	FUS-ICP-AES	0.01	48.7	43.4	45.2	39.6	47.5	51.3	47.7
TiO <sub>2</sub>	FUS-ICP-AES	0.01	0.61	1.32	0.45	0.4	0.51	0.41	0.41
Al <sub>2</sub> O <sub>3</sub>	FUS-ICP-AES	0.01	14.25	16.6	13.75	13.35	15.35	15.35	17.05
Fe <sub>2</sub> O <sub>3T</sub>	FUS-ICP-AES	0.01	7.86	10.05	8.02	5.73	9.52	9.25	9.19
MnO	FUS-ICP-AES	0.01	0.13	0.16	0.1	0.14	0.13	0.12	0.12
MgO	FUS-ICP-AES	0.01	9.55	8.07	7.83	5.98	7.3	8.49	7.76
CaO	FUS-ICP-AES	0.01	9.5	7.39	7.04	11.2	6.37	7.12	7.69
Na <sub>2</sub> O	FUS-ICP-AES	0.01	2.69	3.48	2.04	0.96	3.82	4.01	2.54
K <sub>2</sub> O	FUS-ICP-AES	0.01	0.86	0.25	1.54	3.04	0.13	0.08	1.02
P <sub>2</sub> O <sub>5</sub>	FUS-ICP-AES	0.01	0.09	0.14	0.04	0.02	0.05	0.03	0.02
Cr <sub>2</sub> O <sub>3</sub>	FUS-ICP-AES	0.002	0.161	0.017	0.016	0.015	0.005	0.016	0.02
BaO	FUS-ICP-AES	0.01	0.02	0.005	0.01	0.02	0.005	0.005	0.01
LOI	GRAV		5.34	7.87	12.6	18.45	7.57	3.16	5.34
Total			99.78	98.77	98.65	98.93	98.27	99.35	98.89
CO <sub>2</sub>	COM-IR		3.062	4.082	9.763	16.7	4.421	0.577	1.517
S	COM-IR		0.314	0.153	0.291	0.068	0.031	0.018	0.007
Li (ppm)	AD-ICP-MS	0.4	20.1	28.3	24	4.5	23.5	17.9	19.2
Be	AD-ICP-MS	0.04	0.85	0.45	0.13	0.27	0.15	0.16	0.24
Sc	AD-ICP-MS	1.1	35.7	32	34.2	31	39.2	41.5	33.7
V	FUS-ICP-MS	1	185	224	280	236	312	308	253
Co	AD-ICP-MS	0.13	39.6	45.9	35.2	21.7	36.4	41.7	39.2
Ni	AD-ICP-MS	0.7	304	74.2	67.1	63.6	40.9	68.4	79
Cu	AD-ICP-MS	1.4	58.9	43.5	79.3	4.3	100.5	75.9	26.6
Zn	AD-ICP-MS	1.8	74	89	65	51	89	79	90
Ga	FUS-ICP-MS	0.05	15.4	16.8	12.7	16.1	11.6	13.5	13.3
Rb	FUS-ICP-MS	0.2	14.2	4.4	25.7	48.1	1.4	0.2	16.2
Sr	FUS-ICP-MS	0.1	172	151	99.1	188.5	65.3	88.1	151.5
Y	FUS-ICP-MS	0.1	13.1	24.3	14.4	11.7	14.7	13.1	9.9
Zr	FUS-ICP-MS	2	64	90	21	18	31	21	21
Nb	FUS-ICP-MS	0.2	3	4.2	0.4	0.4	0.9	0.5	0.6
Mo	AD-ICP-MS	0.08	0.4	0.37	0.23	0.55	0.08	0.14	0.42
Ag	AD-ICP-MS	0.01	0.05	0.03	0.03	0.02	0.05	0.03	0.02
Cd	AD-ICP-MS	0.013	0.09	0.06	0.08	0.14	0.07	0.07	0.07
In	AD-ICP-MS	0.002	0.051	0.06	0.044	0.033	0.058	0.055	0.047
Sn	AD-ICP-MS	0.16	0.8	0.8	0.2	0.2	0.3	0.2	0.2
Sb	AD-ICP-MS	0.04	2.2	1.08	0.71	1.28	0.91	0.57	0.75
Cs	AD-ICP-MS	0.01	0.1	0.19	0.37	0.69	0.1	<0.05	0.12

## Appendix E.II (continued) Whole-rock geochemistry

Sample ID		348070	348071	348072	348073	348075	348077	348078
Drill Hole ID		GV-16-05	GV-16-05	GV-16-05	GV-16-05	GV-16-05	GV-16-05	GV-16-12
Drill Hole Depth (m)		146.78	156.5	162.6	167.4	174.17	200.4	5.8
UTM easting		569136	569136	569136	569136	569136	569136	567665
UTM northing		5538729	5538729	5538729	5538729	5538729	5538729	5538175
Lithology Code		LOD	VC	VC	B-S1	B-S1	B-S1	B-S1
La	FUS-ICP-MS	0.1	6.4	4.9	1.3	2.2	1.5	1.2
Ce	FUS-ICP-MS	0.1	15	13.2	2.7	4.8	3.7	2.6
Pr	FUS-ICP-MS	0.03	1.8	2.03	0.41	0.67	0.58	0.4
Nd	FUS-ICP-MS	0.1	7.3	9.8	2.1	3.2	2.7	1.9
Sm	FUS-ICP-MS	0.03	1.93	3.18	0.95	1.05	1.01	0.9
Eu	FUS-ICP-MS	0.03	0.64	1.19	0.37	0.36	0.36	0.33
Gd	FUS-ICP-MS	0.05	2.08	4	1.66	1.51	1.79	1.34
Tb	FUS-ICP-MS	0.01	0.34	0.64	0.31	0.26	0.32	0.25
Dy	FUS-ICP-MS	0.05	2.18	4.08	2.18	1.82	2.32	1.81
Ho	FUS-ICP-MS	0.01	0.48	0.94	0.52	0.42	0.55	0.46
Er	FUS-ICP-MS	0.03	1.36	2.71	1.63	1.33	1.83	1.44
Tm	FUS-ICP-MS	0.01	0.22	0.37	0.26	0.23	0.3	0.24
Yb	FUS-ICP-MS	0.03	1.38	2.41	1.65	1.38	1.77	1.52
Lu	FUS-ICP-MS	0.01	0.22	0.37	0.26	0.2	0.3	0.26
Hf	FUS-ICP-MS	0.2	1.7	2.3	0.7	0.7	1	0.8
Ta	FUS-ICP-MS	0.1	0.3	0.4	0.1	0.1	0.2	0.1
Au	FA-ICP-AES	0.001	<0.001	<0.001	<0.001	0.001	0.001	<0.001
Tl	AD-ICP-MS	0.002	0.1	0.02	0.15	0.31	<0.02	<0.02
Pb	AD-ICP-MS	0.18	3.7	2.5	1.2	3.9	1.1	0.8
Bi	FUS-ICP-MS	0.01	<0.47	<0.47	<0.47	<0.47	<0.47	<0.47
Th	FUS-ICP-MS	0.05	1.82	0.42	0.18	0.19	0.32	0.17
U	FUS-ICP-MS	0.05	1.15	0.18	0.17	0.29	0.16	0.21

## Appendix E.II (continued) Whole-rock geochemistry

Sample ID		348079	348080	348082	348083	348085	348086	348090	
Drill Hole ID		GV-16-12							
Drill Hole Depth (m)		18.38	22	35.8	39.3	44.11	46.9	49.15	
UTM easting		567665	567665	567665	567665	567665	567665	567665	
UTM northing		5538175	5538175	5538175	5538175	5538175	5538175	5538175	
Lithology Code	LOD	B-S1	B-S1	B-S1	B-S1	B-S2	MR-IF	B-S1	
SiO <sub>2</sub> (%)	FUS-ICP-AES	0.01	47.9	46.9	49.2	45.1	41.7	18.5	54.8
TiO <sub>2</sub>	FUS-ICP-AES	0.01	0.64	0.66	0.66	0.41	2.89	0.22	0.44
Al <sub>2</sub> O <sub>3</sub>	FUS-ICP-AES	0.01	15.8	16.15	20.2	12.9	14.65	3.81	15.5
Fe <sub>2</sub> O <sub>3T</sub>	FUS-ICP-AES	0.01	8.36	8.23	10.3	6.35	13.5	68.8	8.37
MnO	FUS-ICP-AES	0.01	0.14	0.11	0.14	0.14	0.24	1.45	0.1
MgO	FUS-ICP-AES	0.01	5.44	4.73	2.06	5.99	6	1.73	5.17
CaO	FUS-ICP-AES	0.01	12.65	12.05	7.51	15.1	7.71	3.43	7.35
Na <sub>2</sub> O	FUS-ICP-AES	0.01	2.67	3.15	4.24	2.39	1.65	0.04	3.39
K <sub>2</sub> O	FUS-ICP-AES	0.01	0.04	0.46	1.72	0.02	1.08	0.03	0.02
P <sub>2</sub> O <sub>5</sub>	FUS-ICP-AES	0.01	0.05	0.06	0.07	0.03	0.49	1.84	0.1
Cr <sub>2</sub> O <sub>3</sub>	FUS-ICP-AES	0.002	0.011	0.015	0.012	0.038	0.007	0.005	0.001
BaO	FUS-ICP-AES	0.01	0.005	0.005	0.03	0.01	0.02	0.005	0.005
LOI	GRAV		6.18	7.66	2.28	11.55	8.92	0.12	4.63
Total		99.89	100.19	98.44	100.04	98.88	99.98	99.9	
CO <sub>2</sub>	COM-IR		3.546	4.917	0.224	7.962	5.361	0.744	1.959
S	COM-IR		0.016	0.011	0.01	0.006	0.009	0.005	0.013
Li (ppm)	AD-ICP-MS	0.4	15.4	16.1	8.4	16	27.3	6.3	13.8
Be	AD-ICP-MS	0.04	0.25	0.28	0.55	0.21	1.26	0.59	0.39
Sc	AD-ICP-MS	1.1	39.2	42.9	37.6	35.2	29.2	6.8	30.3
V	FUS-ICP-MS	1	283	294	222	178	292	238	261
Co	AD-ICP-MS	0.13	36.9	33.3	32.4	33.1	50.1	76.9	30.7
Ni	AD-ICP-MS	0.7	55.2	59.2	54	73.6	64.8	67.5	41.7
Cu	AD-ICP-MS	1.4	97.6	71.5	40.8	44.8	34.9	7.4	110
Zn	AD-ICP-MS	1.8	77	73	91	57	118	265	67
Ga	FUS-ICP-MS	0.05	15.1	14.4	17	10.3	19.6	6.3	16.2
Rb	FUS-ICP-MS	0.2	0.4	9.2	37.8	0.4	19.1	0.7	0.2
Sr	FUS-ICP-MS	0.1	114	132	135	135.5	141	22.7	241
Y	FUS-ICP-MS	0.1	15.9	16.4	14.8	9	26.4	23.3	12.4
Zr	FUS-ICP-MS	2	33	32	46	20	229	23	38
Nb	FUS-ICP-MS	0.2	0.9	0.7	1.2	0.5	15.4	2.7	0.7
Mo	AD-ICP-MS	0.08	0.58	0.2	0.25	0.2	0.4	0.21	0.45
Ag	AD-ICP-MS	0.01	0.04	0.02	0.03	0.02	0.01	0.02	0.03
Cd	AD-ICP-MS	0.013	0.08	0.08	0.04	0.11	0.16	0.04	0.06
In	AD-ICP-MS	0.002	0.054	0.057	0.072	0.042	0.087	0.182	0.049
Sn	AD-ICP-MS	0.16	0.4	0.3	0.3	0.2	1.1	1.1	0.4
Sb	AD-ICP-MS	0.04	0.81	0.92	1.11	0.99	1.58	0.41	0.95
Cs	AD-ICP-MS	0.01	<0.05	0.08	0.28	<0.05	0.16	<0.05	<0.05

## Appendix E.II (continued) Whole-rock geochemistry

Sample ID		348079	348080	348082	348083	348085	348086	348090
Drill Hole ID		GV-16-12						
Drill Hole Depth (m)		18.38	22	35.8	39.3	44.11	46.9	49.15
UTM easting		567665	567665	567665	567665	567665	567665	567665
UTM northing		5538175	5538175	5538175	5538175	5538175	5538175	5538175
Lithology Code		LOD	B-S1	B-S1	B-S1	B-S1	B-S2	MR-IF
La	FUS-ICP-MS	0.1	1.9	1.9	3.1	1.1	18.3	10
Ce	FUS-ICP-MS	0.1	4.5	4.4	7	2.8	43.2	18.9
Pr	FUS-ICP-MS	0.03	0.74	0.74	0.85	0.4	5.6	3.04
Nd	FUS-ICP-MS	0.1	3.9	4.1	4.5	2	26.3	13.7
Sm	FUS-ICP-MS	0.03	1.45	1.87	1.7	1.1	6.25	3.86
Eu	FUS-ICP-MS	0.03	0.61	0.61	0.58	0.31	1.94	0.88
Gd	FUS-ICP-MS	0.05	2.27	2.33	2.12	1.2	6.28	4.29
Tb	FUS-ICP-MS	0.01	0.36	0.35	0.36	0.22	0.9	0.73
Dy	FUS-ICP-MS	0.05	2.49	2.76	2.52	1.62	5.27	4.83
Ho	FUS-ICP-MS	0.01	0.63	0.62	0.58	0.34	0.97	1.03
Er	FUS-ICP-MS	0.03	1.64	1.93	1.78	1.15	2.94	3.48
Tm	FUS-ICP-MS	0.01	0.29	0.29	0.31	0.16	0.42	0.41
Yb	FUS-ICP-MS	0.03	1.61	1.81	2.14	0.97	2.56	2.56
Lu	FUS-ICP-MS	0.01	0.32	0.34	0.26	0.16	0.39	0.4
Hf	FUS-ICP-MS	0.2	1.1	1	1.3	0.5	4.8	0.5
Ta	FUS-ICP-MS	0.1	0.2	0.2	0.2	0.1	1	0.2
Au	FA-ICP-AES	0.001	<0.001	<0.001	0.001	<0.001	0.001	0.001
Tl	AD-ICP-MS	0.002	<0.02	0.03	0.13	<0.02	0.13	<0.02
Pb	AD-ICP-MS	0.18	1	1.1	3.6	2.7	6.9	2.3
Bi	FUS-ICP-MS	0.01	<0.47	<0.47	<0.47	<0.47	<0.47	<0.47
Th	FUS-ICP-MS	0.05	0.25	0.19	0.8	0.18	0.8	1.07
U	FUS-ICP-MS	0.05	0.36	0.81	0.34	0.09	0.37	1.21
								0.4

## Appendix E.II (continued) Whole-rock geochemistry

Sample ID		348091	348092	348093	348094	348095	348096	348097	
Drill Hole ID		GV-16-12							
Drill Hole Depth (m)		63.18	66.02	71.6	83.5	89	93.1	102.86	
UTM easting		567665	567665	567665	567665	567665	567665	567665	
UTM northing		5538175	5538175	5538175	5538175	5538175	5538175	5538175	
Lithology Code	LOD	B-S1	VC	B-S1	B-S1	VC	VC	B-S1	
SiO <sub>2</sub> (%)	FUS-ICP-AES	0.01	50.8	54.1	54.6	59.8	45.5	42.2	40.7
TiO <sub>2</sub>	FUS-ICP-AES	0.01	0.73	0.61	0.73	0.36	0.76	0.89	0.29
Al <sub>2</sub> O <sub>3</sub>	FUS-ICP-AES	0.01	16.5	14.55	15.25	14.8	16.55	16.7	14.2
Fe <sub>2</sub> O <sub>3T</sub>	FUS-ICP-AES	0.01	10.75	9.75	11.75	5.87	11.5	12.45	8.75
MnO	FUS-ICP-AES	0.01	0.07	0.09	0.14	0.04	0.05	0.05	0.09
MgO	FUS-ICP-AES	0.01	7.39	6.75	5.13	4.65	6.83	7.7	8.35
CaO	FUS-ICP-AES	0.01	5.89	5.03	7.77	6.5	6.76	5.42	9.65
Na <sub>2</sub> O	FUS-ICP-AES	0.01	2.98	2.47	1.62	3.94	2.23	1.19	0.87
K <sub>2</sub> O	FUS-ICP-AES	0.01	0.14	0.74	0.15	0.03	0.69	0.77	0.91
P <sub>2</sub> O <sub>5</sub>	FUS-ICP-AES	0.01	0.04	0.05	0.06	0.07	0.07	0.09	0.01
Cr <sub>2</sub> O <sub>3</sub>	FUS-ICP-AES	0.002	0.002	0.001	0.002	0.008	0.002	0.001	0.064
BaO	FUS-ICP-AES	0.01	0.005	0.02	0.005	0.005	0.01	0.01	0.01
LOI	GRAV		4.95	6.62	3.45	4.59	9.25	10.6	15.15
Total		100.25	100.79	100.69	100.69	100.21	98.08	99.06	
CO <sub>2</sub>	COM-IR		1.188	2.802	0.261	2.095	5.27	7.05	10.923
S	COM-IR		0.165	0.075	0.094	0.013	0.246	0.652	0.056
Li (ppm)	AD-ICP-MS	0.4	22.2	22.7	15.4	13.4	31.2	33.4	27.9
Be	AD-ICP-MS	0.04	0.34	0.35	0.25	0.39	0.32	0.41	0.18
Sc	AD-ICP-MS	1.1	34.9	33.1	36	26.3	30.4	32.1	38.2
V	FUS-ICP-MS	1	345	281	400	188	290	366	237
Co	AD-ICP-MS	0.13	34.4	29.4	37.2	26.4	27.6	35.8	40.2
Ni	AD-ICP-MS	0.7	31	25.7	23.5	52.6	21.6	27.6	125
Cu	AD-ICP-MS	1.4	73.8	77.6	69.4	66.9	61.8	98	37.3
Zn	AD-ICP-MS	1.8	92	81	94	52	108	114	62
Ga	FUS-ICP-MS	0.05	15.4	13.9	17.5	13.7	15.6	16.6	12.3
Rb	FUS-ICP-MS	0.2	0.4	10.5	0.4	0.2	7.3	7.1	9.7
Sr	FUS-ICP-MS	0.1	126	74.8	338	227	69.4	109	135
Y	FUS-ICP-MS	0.1	15.9	14.9	16.7	9.6	23.3	23.2	8.4
Zr	FUS-ICP-MS	2	34	28	34	40	45	45	11
Nb	FUS-ICP-MS	0.2	0.6	0.6	0.8	0.5	1.1	1.1	0.3
Mo	AD-ICP-MS	0.08	0.37	0.27	0.37	0.48	0.32	0.73	0.23
Ag	AD-ICP-MS	0.01	0.05	0.02	0.05	0.03	0.05	0.1	0.05
Cd	AD-ICP-MS	0.013	0.11	0.07	0.1	0.06	0.02	0.06	0.14
In	AD-ICP-MS	0.002	0.071	0.053	0.067	0.037	0.08	0.076	0.04
Sn	AD-ICP-MS	0.16	0.3	0.3	0.3	0.4	0.3	0.4	<0.2
Sb	AD-ICP-MS	0.04	0.72	0.54	0.93	0.56	1.11	2.26	0.92
Cs	AD-ICP-MS	0.01	<0.05	0.18	<0.05	<0.05	0.12	0.1	0.23

## Appendix E.II (continued) Whole-rock geochemistry

Sample ID		348091	348092	348093	348094	348095	348096	348097
Drill Hole ID		GV-16-12						
Drill Hole Depth (m)		63.18	66.02	71.6	83.5	89	93.1	102.86
UTM easting		567665	567665	567665	567665	567665	567665	567665
UTM northing		5538175	5538175	5538175	5538175	5538175	5538175	5538175
Lithology Code		LOD	B-S1	VC	B-S1	B-S1	VC	VC
La	FUS-ICP-MS	0.1	1.6	1.6	1.6	4.1	2.3	2.6
Ce	FUS-ICP-MS	0.1	4.4	4.1	4.3	9	5.8	6
Pr	FUS-ICP-MS	0.03	0.6	0.63	0.61	1.08	0.95	0.94
Nd	FUS-ICP-MS	0.1	3.7	3.4	3.9	4.8	4.7	4.3
Sm	FUS-ICP-MS	0.03	1.58	1.43	1.67	1.47	1.68	2.04
Eu	FUS-ICP-MS	0.03	0.53	0.45	0.49	0.45	0.62	0.59
Gd	FUS-ICP-MS	0.05	2.41	2.3	2.27	1.74	2.91	3.01
Tb	FUS-ICP-MS	0.01	0.44	0.38	0.46	0.28	0.53	0.55
Dy	FUS-ICP-MS	0.05	2.66	2.33	2.92	1.73	3.75	3.46
Ho	FUS-ICP-MS	0.01	0.68	0.63	0.67	0.36	0.84	0.89
Er	FUS-ICP-MS	0.03	1.92	1.89	2.39	1.27	2.68	3.05
Tm	FUS-ICP-MS	0.01	0.34	0.29	0.28	0.16	0.49	0.39
Yb	FUS-ICP-MS	0.03	2.06	1.95	2.31	1.06	2.77	2.77
Lu	FUS-ICP-MS	0.01	0.25	0.26	0.32	0.17	0.52	0.43
Hf	FUS-ICP-MS	0.2	1.1	0.9	1.2	1	1.5	1.6
Ta	FUS-ICP-MS	0.1	0.2	0.1	0.1	0.1	0.2	0.1
Au	FA-ICP-AES	0.001	0.001	<0.001	0.001	<0.001	0.002	0.01
Tl	AD-ICP-MS	0.002	<0.02	0.13	<0.02	<0.02	0.12	0.14
Pb	AD-ICP-MS	0.18	1.2	0.8	2.4	1.4	0.9	2.2
Bi	FUS-ICP-MS	0.01	<0.47	<0.47	<0.47	<0.47	<0.47	<0.47
Th	FUS-ICP-MS	0.05	0.26	0.19	0.27	0.81	0.36	0.33
U	FUS-ICP-MS	0.05	0.41	0.29	0.2	0.3	0.62	0.12

## Appendix E.II (continued) Whole-rock geochemistry

Sample ID		348099	348100 GV-16- 13a	348901	348902	348904	348905	348906
Lithology Code	LOD	B-S1	VC	B-S1	MR-IF	ADSM	ADSM	B-S1
SiO <sub>2</sub> (%)	FUS-ICP-AES	0.01	53	49	51.3	28.8	52.5	43.8
TiO <sub>2</sub>	FUS-ICP-AES	0.01	0.78	1.38	0.34	0.15	0.64	3.7
Al <sub>2</sub> O <sub>3</sub>	FUS-ICP-AES	0.01	15.85	14.4	14.9	3.6	19.75	14.55
Fe <sub>2</sub> O <sub>3T</sub>	FUS-ICP-AES	0.01	11.4	11.05	8.32	58.8	11.9	14.7
MnO	FUS-ICP-AES	0.01	0.08	0.18	0.08	1.04	0.11	0.18
MgO	FUS-ICP-AES	0.01	5.59	6.9	5.38	1.44	1.75	5.6
CaO	FUS-ICP-AES	0.01	4.23	9.58	11.25	3.87	4.98	7.51
Na <sub>2</sub> O	FUS-ICP-AES	0.01	3.33	2.96	1.33	0.03	4.16	2.72
K <sub>2</sub> O	FUS-ICP-AES	0.01	0.05	0.34	0.65	0.33	3.02	0.84
P <sub>2</sub> O <sub>5</sub>	FUS-ICP-AES	0.01	0.06	0.16	0.03	2.47	0.1	0.56
Cr <sub>2</sub> O <sub>3</sub>	FUS-ICP-AES	0.002	0.002	0.028	0.031	0.015	0.006	0.008
BaO	FUS-ICP-AES	0.01	0.005	0.01	0.005	0.005	0.06	0.02
LOI	GRAV		4.96	3.12	6.54	-0.8	2.26	5.52
Total		99.34	99.14	100.19	99.75	101.25	99.74	100.51
CO <sub>2</sub>	COM-IR		1.632	0.511	3.804	0.307	0.514	2.622
S	COM-IR		0.242	0.023	0.02	0.034	0.017	0.163
Li (ppm)	AD-ICP-MS	0.4	22.7	7.1	22.9	6.3	5.6	14.6
Be	AD-ICP-MS	0.04	0.28	0.67	0.25	0.88	0.65	1.2
Sc	AD-ICP-MS	1.1	36.7	48.2	33.2	6.7	38.3	31.3
V	FUS-ICP-MS	1	362	280	218	237	272	384
Co	AD-ICP-MS	0.13	36.5	45.1	25.2	69.2	40.4	45.1
Ni	AD-ICP-MS	0.7	16.4	63.5	86.8	46.9	44.3	49.3
Cu	AD-ICP-MS	1.4	81.6	93.6	15.9	204	13.4	44.5
Zn	AD-ICP-MS	1.8	112	94	62	158	74	118
Ga	FUS-ICP-MS	0.05	16.4	17.6	13.7	6.3	20.6	22.9
Rb	FUS-ICP-MS	0.2	0.5	3.4	12.2	7.6	58.1	12.7
Sr	FUS-ICP-MS	0.1	104.5	219	366	27.8	127	234
Y	FUS-ICP-MS	0.1	19.1	25.9	10.7	35.7	17.5	33.6
Zr	FUS-ICP-MS	2	38	104	27	24	47	268
Nb	FUS-ICP-MS	0.2	0.9	5.2	1	2	1.4	18
Mo	AD-ICP-MS	0.08	0.3	0.66	0.1	0.27	0.19	1.72
Ag	AD-ICP-MS	0.01	0.03	0.04	0.01	0.05	0.01	0.04
Cd	AD-ICP-MS	0.013	0.06	0.09	0.06	0.04	0.03	0.1
In	AD-ICP-MS	0.002	0.068	0.074	0.038	0.275	0.072	0.101
Sn	AD-ICP-MS	0.16	0.4	0.9	0.2	1.1	0.4	2
Sb	AD-ICP-MS	0.04	0.64	1.03	0.74	0.41	1.14	0.76
Cs	AD-ICP-MS	0.01	0.05	<0.05	0.14	0.06	0.55	0.16

## Appendix E.II (continued) Whole-rock geochemistry

Sample ID		348099	348100 GV-16- 13a	348901	348902	348904	348905	348906
Lithology Code	LOD	B-S1	VC	B-S1	MR-IF	ADSM	ADSM	B-S1
La	FUS-ICP-MS	0.1	2	6.6	1.9	18.1	3	19.2
Ce	FUS-ICP-MS	0.1	4.8	17.2	4.4	26.1	5.9	48
Pr	FUS-ICP-MS	0.03	0.7	2.49	0.65	5.22	0.92	6.82
Nd	FUS-ICP-MS	0.1	4.1	12.9	3.2	20.6	4	28.3
Sm	FUS-ICP-MS	0.03	1.81	3.9	1.22	5.15	1.34	7.01
Eu	FUS-ICP-MS	0.03	0.62	1.32	0.35	1.48	0.46	2.44
Gd	FUS-ICP-MS	0.05	2.32	4.76	1.4	7.39	2.18	7.39
Tb	FUS-ICP-MS	0.01	0.47	0.8	0.21	1.18	0.43	1.21
Dy	FUS-ICP-MS	0.05	3.35	5.15	1.78	7.6	3.13	6.74
Ho	FUS-ICP-MS	0.01	0.68	1.1	0.34	1.6	0.76	1.35
Er	FUS-ICP-MS	0.03	2.19	3.21	1.42	4.45	1.92	3.49
Tm	FUS-ICP-MS	0.01	0.35	0.42	0.16	0.66	0.37	0.5
Yb	FUS-ICP-MS	0.03	2.47	2.86	1.22	3.95	2.43	2.99
Lu	FUS-ICP-MS	0.01	0.43	0.35	0.2	0.53	0.38	0.51
Hf	FUS-ICP-MS	0.2	1.2	2.7	0.8	0.6	1.4	6
Ta	FUS-ICP-MS	0.1	0.1	0.3	0.2	0.2	0.2	1.4
Au	FA-ICP-AES	0.001	<0.001	<0.001	0.005	0.011	<0.001	<0.001
Tl	AD-ICP-MS	0.002	<0.02	0.02	0.03	0.06	0.52	0.15
Pb	AD-ICP-MS	0.18	1.2	3	1.9	4	4.6	4.1
Bi	FUS-ICP-MS	0.01	<0.47	<0.47	<0.47	<0.47	<0.47	<0.47
Th	FUS-ICP-MS	0.05	0.37	0.69	0.42	1.28	0.69	1.11
U	FUS-ICP-MS	0.05	0.2	0.22	0.12	1.37	0.25	0.43
								0.24

## Appendix E.II (continued) Whole-rock geochemistry

Sample ID		348907	348908	348909	348910	348911	348912	348913	
Drill Hole ID		GV-16-01	GV-16-01	GV-16-01	GV-16-01	GV-16-04	GV-16-04	GV-16-04	
Drill Hole Depth (m)		155.6	144.5	167.5	181.5	9.6	17.32	30	
UTM easting		567749	567749	567749	567749	568631	568631	568631	
UTM northing		5538379	5538379	5538379	5538379	5538742	5538742	5538742	
Lithology Code	LOD	B-S1	B-S1	B-S1	B-S2	B-S1	B-S1	B-S1	
SiO <sub>2</sub> (%)	FUS-ICP-AES	0.01	56.2	55.1	59.3	42.2	42.4	49.8	51.6
TiO <sub>2</sub>	FUS-ICP-AES	0.01	0.64	0.6	0.35	3.55	0.5	0.55	0.5
Al <sub>2</sub> O <sub>3</sub>	FUS-ICP-AES	0.01	15.8	14.65	14.2	13.85	15.1	15.55	17.7
Fe <sub>2</sub> O <sub>3T</sub>	FUS-ICP-AES	0.01	10.8	11.95	6.59	14.3	6.9	10.45	9.62
MnO	FUS-ICP-AES	0.01	0.11	0.16	0.06	0.19	0.11	0.05	0.07
MgO	FUS-ICP-AES	0.01	6.7	5.69	4.28	5.72	5.03	7.65	7.92
CaO	FUS-ICP-AES	0.01	4.79	5.44	9.76	8.73	10.65	7.3	3.6
Na <sub>2</sub> O	FUS-ICP-AES	0.01	3.38	2.81	2.03	3.05	1.61	1.59	5.02
K <sub>2</sub> O	FUS-ICP-AES	0.01	0.12	0.2	0.12	0.05	1.64	0.09	0.02
P <sub>2</sub> O <sub>5</sub>	FUS-ICP-AES	0.01	0.05	0.06	0.06	0.5	0.04	0.02	0.01
Cr <sub>2</sub> O <sub>3</sub>	FUS-ICP-AES	0.002	0.001	0.001	0.008	0.01	0.013	0.002	0.011
BaO	FUS-ICP-AES	0.01	0.005	0.005	0.005	0.01	0.01	0.005	0.005
LOI	GRAV		3.15	3.8	3.72	7.13	16.05	7.58	3.85
Total		101.75	100.48	100.49	99.32	100.06	100.63	99.93	
CO <sub>2</sub>	COM-IR		0.112	0.935	1.973	4.327	13.673	3.567	0.574
S	COM-IR		0.243	0.926	0.164	0.173	0.202	0.147	0.843
Li (ppm)	AD-ICP-MS	0.4	12.2	11.2	8.7	4.2	16	31.9	20.3
Be	AD-ICP-MS	0.04	0.3	0.18	0.28	1.14	0.41	0.2	0.21
Sc	AD-ICP-MS	1.1	34.1	31.9	24.2	30.5	36.4	38.4	35.1
V	FUS-ICP-MS	1	310	351	189	383	285	351	267
Co	AD-ICP-MS	0.13	37	44.7	23	43.8	33.9	38.7	50.2
Ni	AD-ICP-MS	0.7	34	15.1	44.4	56.9	47	31.2	68.5
Cu	AD-ICP-MS	1.4	79.3	52.3	89.4	45	57.4	47.6	112.5
Zn	AD-ICP-MS	1.8	80	152	35	113	65	102	83
Ga	FUS-ICP-MS	0.05	18.4	20.4	19.3	24.2	13.8	15.3	12.7
Rb	FUS-ICP-MS	0.2	1	1.2	1.2	0.6	20	1.4	0.1
Sr	FUS-ICP-MS	0.1	101.5	191.5	86.7	286	123.5	53.7	63
Y	FUS-ICP-MS	0.1	18.1	23.4	9.2	34.3	14.6	14	7.9
Zr	FUS-ICP-MS	2	31	40	37	255	27	26	22
Nb	FUS-ICP-MS	0.2	1.5	0.7	0.5	17.6	0.6	0.7	0.5
Mo	AD-ICP-MS	0.08	0.63	0.47	1.75	1.52	0.19	0.14	0.99
Ag	AD-ICP-MS	0.01	0.03	0.04	0.07	0.04	0.03	0.03	0.04
Cd	AD-ICP-MS	0.013	0.02	0.03	0.05	0.12	0.13	0.13	0.08
In	AD-ICP-MS	0.002	0.07	0.115	0.044	0.101	0.048	0.069	0.058
Sn	AD-ICP-MS	0.16	0.4	0.3	0.3	2.1	0.2	0.3	0.2
Sb	AD-ICP-MS	0.04	0.22	0.24	0.34	0.26	0.75	0.81	0.36
Cs	AD-ICP-MS	0.01	<0.05	<0.05	<0.05	<0.05	0.21	0.14	<0.05

## Appendix E.II (continued) Whole-rock geochemistry

Sample ID		348907	348908	348909	348910	348911	348912	348913	
Drill Hole ID		GV-16-01	GV-16-01	GV-16-01	GV-16-01	GV-16-04	GV-16-04	GV-16-04	
Drill Hole Depth (m)		155.6	144.5	167.5	181.5	9.6	17.32	30	
UTM easting		567749	567749	567749	567749	568631	568631	568631	
UTM northing		5538379	5538379	5538379	5538379	5538742	5538742	5538742	
Lithology Code		LOD	B-S1	B-S1	B-S1	B-S2	B-S1	B-S1	
La	FUS-ICP-MS	0.1	2.1	2.3	3.2	18.6	1.8	1.1	0.8
Ce	FUS-ICP-MS	0.1	5.3	4.9	6.6	46.3	4.2	2.9	1.9
Pr	FUS-ICP-MS	0.03	0.77	0.77	0.9	6.49	0.57	0.48	0.28
Nd	FUS-ICP-MS	0.1	3.7	4	3.9	29.2	3.1	2.8	1.6
Sm	FUS-ICP-MS	0.03	1.44	1.48	1.25	7.2	1.09	1.29	0.67
Eu	FUS-ICP-MS	0.03	0.51	0.45	0.39	2.43	0.51	0.45	0.24
Gd	FUS-ICP-MS	0.05	1.95	2.2	1.43	6.98	1.83	1.72	0.79
Tb	FUS-ICP-MS	0.01	0.42	0.51	0.18	1.08	0.36	0.38	0.2
Dy	FUS-ICP-MS	0.05	2.69	3.79	1.51	6.49	2.31	2.41	1.29
Ho	FUS-ICP-MS	0.01	0.73	0.83	0.3	1.34	0.59	0.57	0.3
Er	FUS-ICP-MS	0.03	2.18	2.85	0.86	3.4	1.7	1.66	0.88
Tm	FUS-ICP-MS	0.01	0.29	0.4	0.13	0.52	0.31	0.28	0.18
Yb	FUS-ICP-MS	0.03	2.31	2.93	0.88	3.19	1.83	1.83	1.12
Lu	FUS-ICP-MS	0.01	0.3	0.42	0.12	0.44	0.29	0.3	0.17
Hf	FUS-ICP-MS	0.2	1	1.4	1.1	5.6	0.9	0.8	0.8
Ta	FUS-ICP-MS	0.1	0.2	0.05	0.05	1	0.1	0.1	0.1
Au	FA-ICP-AES	0.001	0.002	0.003	0.001	<0.001	0.002	<0.001	<0.001
Tl	AD-ICP-MS	0.002	0.02	0.03	0.03	0.02	0.14	<0.02	<0.02
Pb	AD-ICP-MS	0.18	0.8	1.8	2	1.6	2.6	1.5	1
Bi	FUS-ICP-MS	0.01	<0.47	<0.47	<0.47	<0.47	<0.47	<0.47	<0.47
Th	FUS-ICP-MS	0.05	0.33	0.37	0.85	1.01	0.2	0.34	0.17
U	FUS-ICP-MS	0.05	0.33	0.26	0.62	0.47	0.85	0.44	0.78

## Appendix E.II (continued) Whole-rock geochemistry

Sample ID		348915	348916	348917	348918	348920	348921	348922	
Drill Hole ID		GV-16-04							
Drill Hole Depth (m)		53.36	59.9	65	79.6	101.61	123.76	130.5	
UTM easting		568631	568631	568631	568631	568631	568631	568631	
UTM northing		5538742	5538742	5538742	5538742	5538742	5538742	5538742	
Lithology Code	LOD	B-S1	B-S1	B-S1	B-S1	VC	Arg	Arg	
SiO <sub>2</sub> (%)	FUS-ICP-AES	0.01	49.1	45.2	48.6	49.4	41.9	49	51.1
TiO <sub>2</sub>	FUS-ICP-AES	0.01	0.53	0.56	0.57	0.47	0.52	1.69	2.03
Al <sub>2</sub> O <sub>3</sub>	FUS-ICP-AES	0.01	16.5	15.6	16.65	15.35	13.85	13.1	14.15
Fe <sub>2</sub> O <sub>3T</sub>	FUS-ICP-AES	0.01	9.66	9.88	10.15	9.14	11.3	13.05	13.2
MnO	FUS-ICP-AES	0.01	0.05	0.06	0.08	0.12	0.11	0.41	0.24
MgO	FUS-ICP-AES	0.01	5.75	4.99	4.54	6.76	9.48	5.78	4.26
CaO	FUS-ICP-AES	0.01	5.85	7.08	9.85	8.83	9.36	6.63	9.02
Na <sub>2</sub> O	FUS-ICP-AES	0.01	3.33	1.92	2.96	2.68	0.72	2.6	1.77
K <sub>2</sub> O	FUS-ICP-AES	0.01	0.36	0.52	0.02	0.01	0.67	0.02	0.03
P <sub>2</sub> O <sub>5</sub>	FUS-ICP-AES	0.01	0.02	0.03	0.04	0.03	0.02	0.19	0.24
Cr <sub>2</sub> O <sub>3</sub>	FUS-ICP-AES	0.002	0.002	0.001	0.001	0.02	0.061	0.011	0.009
BaO	FUS-ICP-AES	0.01	0.005	0.005	0.005	0.005	0.01	0.005	0.005
LOI	GRAV		7.63	13.05	5.5	6.96	11.9	6.72	4.38
Total			98.79	98.91	98.99	99.78	99.91	99.22	100.46
CO <sub>2</sub>	COM-IR		4.052	9.666	2.588	3.468	6.324	3.246	1.442
S	COM-IR		0.021	0.011	0.009	0.01	0.017	0.015	0.105
Li (ppm)	AD-ICP-MS	0.4	35.8	25.8	18.4	16.9	30.9	14.5	11
Be	AD-ICP-MS	0.04	0.31	0.42	0.44	0.25	0.33	1.05	1.31
Sc	AD-ICP-MS	1.1	38.4	36.5	42	39.7	41	35.9	35.1
V	FUS-ICP-MS	1	325	334	364	275	243	280	281
Co	AD-ICP-MS	0.13	35.2	35.3	29	39.3	53.8	35	33.3
Ni	AD-ICP-MS	0.7	37.9	33.9	29.5	66.5	115	32	39.5
Cu	AD-ICP-MS	1.4	91	70	11.9	63	110	43.9	54.6
Zn	AD-ICP-MS	1.8	85	87	78	79	95	126	119
Ga	FUS-ICP-MS	0.05	18.3	16.7	17.2	13.8	12.6	16.6	27.3
Rb	FUS-ICP-MS	0.2	7.4	8.1	0.4	0.2	15.7	0.3	0.4
Sr	FUS-ICP-MS	0.1	103	185.5	229	96.1	97.1	154.5	285
Y	FUS-ICP-MS	0.1	9	13.4	15.7	12.4	10.2	33.3	46.9
Zr	FUS-ICP-MS	2	36	30	26	21	24	133	207
Nb	FUS-ICP-MS	0.2	0.7	0.8	0.6	0.6	0.4	4.7	8.4
Mo	AD-ICP-MS	0.08	0.11	0.1	0.14	0.25	0.06	0.84	0.61
Ag	AD-ICP-MS	0.01	0.03	0.03	0.02	0.02	0.06	0.05	0.04
Cd	AD-ICP-MS	0.013	0.02	0.03	0.06	0.06	0.16	0.05	0.05
In	AD-ICP-MS	0.002	0.059	0.056	0.072	0.053	0.057	0.096	0.112
Sn	AD-ICP-MS	0.16	0.3	0.2	0.4	0.3	0.3	1.5	2.2
Sb	AD-ICP-MS	0.04	1.35	2.06	0.99	0.51	0.52	0.89	1.78
Cs	AD-ICP-MS	0.01	0.34	0.14	0.07	<0.05	0.18	<0.05	<0.05

## Appendix E.II (continued) Whole-rock geochemistry

Sample ID		348915	348916	348917	348918	348920	348921	348922
Drill Hole ID		GV-16-04						
Drill Hole Depth (m)		53.36	59.9	65	79.6	101.61	123.76	130.5
UTM easting		568631	568631	568631	568631	568631	568631	568631
UTM northing		5538742	5538742	5538742	5538742	5538742	5538742	5538742
Lithology Code	LOD	B-S1	B-S1	B-S1	B-S1	VC	Arg	Arg
La	FUS-ICP-MS	0.1	1.7	1.7	1.9	1.2	1.1	8.2
Ce	FUS-ICP-MS	0.1	4.4	4.1	4.1	2.6	2.6	22.6
Pr	FUS-ICP-MS	0.03	0.6	0.64	0.66	0.41	0.44	3.03
Nd	FUS-ICP-MS	0.1	2.9	2.9	3.5	2.6	1.8	15.1
Sm	FUS-ICP-MS	0.03	1.17	1.35	1.28	1.06	1	4.63
Eu	FUS-ICP-MS	0.03	0.35	0.51	0.52	0.44	0.47	1.44
Gd	FUS-ICP-MS	0.05	1.56	2.02	2.11	1.42	1.18	5.95
Tb	FUS-ICP-MS	0.01	0.28	0.39	0.41	0.25	0.24	0.97
Dy	FUS-ICP-MS	0.05	2.16	2.76	2.84	2.27	1.46	6.11
Ho	FUS-ICP-MS	0.01	0.35	0.58	0.6	0.54	0.4	1.37
Er	FUS-ICP-MS	0.03	1.16	1.78	2.1	1.65	1.47	3.82
Tm	FUS-ICP-MS	0.01	0.17	0.27	0.36	0.21	0.21	0.56
Yb	FUS-ICP-MS	0.03	0.95	1.64	2.08	1.44	1.27	3.58
Lu	FUS-ICP-MS	0.01	0.21	0.24	0.32	0.19	0.21	0.52
Hf	FUS-ICP-MS	0.2	1.1	1	0.9	0.7	0.8	3.4
Ta	FUS-ICP-MS	0.1	0.2	0.1	0.2	0.1	0.1	0.4
Au	FA-ICP-AES	0.001	0.001	0.019	0.001	0.001	0.004	<0.001
Tl	AD-ICP-MS	0.002	0.05	0.06	<0.02	<0.02	0.07	<0.02
Pb	AD-ICP-MS	0.18	1.6	2.5	3.4	1.3	1.2	6.3
Bi	FUS-ICP-MS	0.01	<0.47	<0.47	<0.47	<0.47	<0.47	<0.47
Th	FUS-ICP-MS	0.05	0.49	0.26	0.21	0.23	0.2	1.19
U	FUS-ICP-MS	0.05	0.14	0.13	0.28	0.08	0.23	0.54
								1.35

## Appendix E.II (continued) Whole-rock geochemistry

Sample ID		348923	348924	348928	348929	348930	348953	348957
Drill Hole ID		GV-16-04	GV-16-04	GV-16-04	GV-16-04	GV-16-04	GV-16-07	GV-16-08
Drill Hole Depth (m)		107.96	110.35	114.2	116.4	119.9	44	19.06
UTM easting		568631	568631	568631	568631	568631	569075	569155
UTM northing		5538742	5538742	5538742	5538742	5538742	5538640	5538679
Lithology Code	LOD	ADSM	ASMM	ADSM	ASMM	ASMM	VC	MR-IF
SiO <sub>2</sub> (%)	FUS-ICP-AES	0.01	53.3	43.5	56.3	46.4	58.6	52.3
TiO <sub>2</sub>	FUS-ICP-AES	0.01	0.46	0.34	0.43	0.37	0.42	0.51
Al <sub>2</sub> O <sub>3</sub>	FUS-ICP-AES	0.01	17.1	8.25	15.55	8.81	10.15	17.05
Fe <sub>2</sub> O <sub>3T</sub>	FUS-ICP-AES	0.01	6.22	38.6	9.64	34.7	15.45	7.66
MnO	FUS-ICP-AES	0.01	0.19	2.52	0.37	1.99	2.52	0.09
MgO	FUS-ICP-AES	0.01	4.43	3.25	6.56	3.51	3.56	6.53
CaO	FUS-ICP-AES	0.01	5.89	0.79	2.33	0.71	4.37	4.34
Na <sub>2</sub> O	FUS-ICP-AES	0.01	5.9	0.06	1.76	0.04	1.7	4.53
K <sub>2</sub> O	FUS-ICP-AES	0.01	0.54	0.05	2.03	0.71	0.17	0.98
P <sub>2</sub> O <sub>5</sub>	FUS-ICP-AES	0.01	0.04	0.32	0.06	0.27	0.16	0.1
Cr <sub>2</sub> O <sub>3</sub>	FUS-ICP-AES	0.002	0.056	0.006	0.059	0.007	0.007	0.024
BaO	FUS-ICP-AES	0.01	0.005	0.005	0.03	0.01	0.005	0.01
LOI	GRAV		6.21	1.89	5.33	2.06	3.3	5.69
Total			100.35	99.58	100.45	99.59	100.43	99.83
CO <sub>2</sub>	COM-IR		4.153	0.117	1.435	0.023	1.568	2.942
S	COM-IR		0.175	0.033	0.025	0.022	0.012	0.612
Li (ppm)	AD-ICP-MS	0.4	14.1	13.1	18.8	11.4	9	22.1
Be	AD-ICP-MS	0.04	0.37	1.22	1.07	1.34	1.67	0.89
Sc	AD-ICP-MS	1.1	43.9	11	41	12.5	11.6	25.9
V	FUS-ICP-MS	1	262	185	244	142	81	146
Co	AD-ICP-MS	0.13	38.2	14.1	47.3	21	28.7	23.6
Ni	AD-ICP-MS	0.7	90.9	129	127	136	60.5	67.2
Cu	AD-ICP-MS	1.4	188	207	135.5	106.5	55.2	35.9
Zn	AD-ICP-MS	1.8	59	326	92	259	98	71
Ga	FUS-ICP-MS	0.05	14.6	14.8	12.7	12.8	13.8	16.7
Rb	FUS-ICP-MS	0.2	13.2	1.3	47.2	15.3	3.9	20.3
Sr	FUS-ICP-MS	0.1	81.6	8.5	41.1	14.4	214	153.5
Y	FUS-ICP-MS	0.1	15.9	32.7	13.3	34.3	23.5	10.5
Zr	FUS-ICP-MS	2	27	67	25	70	84	80
Nb	FUS-ICP-MS	0.2	0.7	5.6	0.8	6.5	7.8	3.7
Mo	AD-ICP-MS	0.08	0.66	0.74	1.77	2.36	0.55	0.44
Ag	AD-ICP-MS	0.01	0.1	0.05	0.03	0.03	0.06	0.02
Cd	AD-ICP-MS	0.013	0.24	0.04	0.15	0.03	0.04	0.05
In	AD-ICP-MS	0.002	0.049	0.155	0.059	0.176	0.119	0.037
Sn	AD-ICP-MS	0.16	0.4	1.9	0.4	2.1	2.2	1.1
Sb	AD-ICP-MS	0.04	0.56	0.28	0.43	0.28	1.48	0.23
Cs	AD-ICP-MS	0.01	0.14	<0.05	0.43	0.12	0.07	0.11

## Appendix E.II (continued) Whole-rock geochemistry

Sample ID		348923	348924	348928	348929	348930	348953	348957	
Drill Hole ID		GV-16-04	GV-16-04	GV-16-04	GV-16-04	GV-16-04	GV-16-07	GV-16-08	
Drill Hole Depth (m)		107.96	110.35	114.2	116.4	119.9	44	19.06	
UTM easting		568631	568631	568631	568631	568631	569075	569155	
UTM northing		5538742	5538742	5538742	5538742	5538742	5538640	5538679	
Lithology Code		LOD	ADSM	ASMM	ADSM	ASMM	ASMM	VC	
								MR-IF	
La	FUS-ICP-MS	0.1	2.1	33.6	2.7	35.3	37.5	7.9	26.7
Ce	FUS-ICP-MS	0.1	5.3	104.5	6.9	118.5	109.5	17.8	36.4
Pr	FUS-ICP-MS	0.03	0.81	9.46	0.93	9.32	8.84	1.98	7.85
Nd	FUS-ICP-MS	0.1	4	38.6	4.6	38.1	33	8.1	32
Sm	FUS-ICP-MS	0.03	1.61	8.22	1.39	8.76	6.6	2.05	7.92
Eu	FUS-ICP-MS	0.03	0.49	1.93	0.48	2.5	1.63	0.53	1.87
Gd	FUS-ICP-MS	0.05	2.19	8.32	2.09	8.15	6.37	1.89	9.23
Tb	FUS-ICP-MS	0.01	0.4	1.31	0.32	1.35	1.01	0.32	1.46
Dy	FUS-ICP-MS	0.05	2.48	7.77	2.22	9.12	5.76	1.98	8.98
Ho	FUS-ICP-MS	0.01	0.62	1.47	0.52	1.8	1.16	0.35	1.82
Er	FUS-ICP-MS	0.03	1.65	4.37	1.54	4.8	3.18	1.04	4.73
Tm	FUS-ICP-MS	0.01	0.27	0.66	0.26	0.62	0.4	0.16	0.67
Yb	FUS-ICP-MS	0.03	1.65	3.86	1.89	4.14	2.72	1.27	4.35
Lu	FUS-ICP-MS	0.01	0.27	0.56	0.29	0.59	0.37	0.19	0.6
Hf	FUS-ICP-MS	0.2	0.6	1.6	1	1.7	2.2	2	0.5
Ta	FUS-ICP-MS	0.1	0.1	0.6	0.2	0.5	0.6	0.3	0.3
Au	FA-ICP-AES	0.001	0.015	<0.001	0.001	<0.001	0.061	0.001	0.039
Tl	AD-ICP-MS	0.002	0.06	<0.02	0.25	0.09	<0.02	0.12	0.06
Pb	AD-ICP-MS	0.18	7.4	42	3.7	11.3	45	6.3	3.5
Bi	FUS-ICP-MS	0.01	0.67	<0.47	<0.47	<0.47	<0.47	<0.47	<0.47
Th	FUS-ICP-MS	0.05	0.34	4.96	0.49	5.36	7.13	2.93	1.04
U	FUS-ICP-MS	0.05	0.64	2.17	0.71	1.64	1.2	1.77	2.05

## Appendix E.II (continued) Whole-rock geochemistry

Sample ID		348958	348959	348960	348964	348965	348967	348970	
Drill Hole ID		GV-16-08	GV-16-08	GV-16-08	GV-16-03	GV-16-03	GV-16-03	GV-16-03	
Drill Hole Depth (m)		20.9	24.8	26.6	29.9	62	35.2	38.54	
UTM easting		569155	569155	569155	568689	568689	568689	568689	
UTM northing		5538679	5538679	5538679	5538731	5538731	5538731	5538731	
Lithology Code	LOD	ADSM	ADSM	ADSM	B-S1	Arg	MR-IF	ADSM	
SiO <sub>2</sub> (%)	FUS-ICP-AES	0.01	53.9	60.2	47.6	47.3	48.2	11.6	55.3
TiO <sub>2</sub>	FUS-ICP-AES	0.01	0.61	0.39	1.62	0.31	1.58	0.21	0.31
Al <sub>2</sub> O <sub>3</sub>	FUS-ICP-AES	0.01	13.45	15.05	14.75	16.6	16.7	4.54	19.65
Fe <sub>2</sub> O <sub>3T</sub>	FUS-ICP-AES	0.01	10.55	7.07	11.6	8.45	10.8	66.1	6.18
MnO	FUS-ICP-AES	0.01	1.32	0.64	0.22	0.18	0.2	0.82	0.18
MgO	FUS-ICP-AES	0.01	2.96	3	6.79	6.33	7.03	1.83	1.78
CaO	FUS-ICP-AES	0.01	3.77	1.73	7.53	6.76	5.75	7.52	2.99
Na <sub>2</sub> O	FUS-ICP-AES	0.01	4.22	1.14	3.07	5.37	5.27	0.19	7.45
K <sub>2</sub> O	FUS-ICP-AES	0.01	1.5	4.44	0.14	0.03	0.03	0.08	1.79
P <sub>2</sub> O <sub>5</sub>	FUS-ICP-AES	0.01	0.13	0.06	0.16	0.03	0.18	3.37	0.14
Cr <sub>2</sub> O <sub>3</sub>	FUS-ICP-AES	0.002	0.005	0.002	0.03	0.027	0.01	0.021	0.004
BaO	FUS-ICP-AES	0.01	0.06	0.07	0.01	0.005	0.005	0.005	0.02
LOI	GRAV		6.59	4.73	6.77	7.13	4.42	3.79	4.95
Total		99.09	98.52	100.31	98.53	100.18	100.09	100.75	
CO <sub>2</sub>	COM-IR		6.09	2.433	3.482	5.268	1.801	4.891	4.165
S	COM-IR		0.059	0.027	0.022	0.025	0.03	0.132	0.028
Li (ppm)	AD-ICP-MS	0.4	6.9	10	15	22	13.3	3.9	4.7
Be	AD-ICP-MS	0.04	1.5	1.33	0.98	0.5	0.91	1.69	1.08
Sc	AD-ICP-MS	1.1	12.5	16.9	41.1	39.5	35.8	10.9	13
V	FUS-ICP-MS	1	92	51	310	204	232	270	62
Co	AD-ICP-MS	0.13	25.6	12.6	44.5	48.3	39.3	68.6	10.2
Ni	AD-ICP-MS	0.7	40.6	23.3	54.3	112.5	40.2	51.7	17.8
Cu	AD-ICP-MS	1.4	593	8.6	92.3	71.4	37.5	1185	56.3
Zn	AD-ICP-MS	1.8	103	97	90	72	86	72	46
Ga	FUS-ICP-MS	0.05	18.8	20.2	19	12.1	18.2	7.2	15.1
Rb	FUS-ICP-MS	0.2	49.1	140	2.8	0.5	0.2	1.5	33.3
Sr	FUS-ICP-MS	0.1	207	56.5	217	120.5	98.2	157.5	103.5
Y	FUS-ICP-MS	0.1	26.4	47.6	29	9.2	26.3	46.8	33.6
Zr	FUS-ICP-MS	2	130	197	128	12	115	26	184
Nb	FUS-ICP-MS	0.2		5	3.5	0.3	4.4	2	4
Mo	AD-ICP-MS	0.08	0.08	0.06	0.49	0.13	0.39	0.68	0.95
Ag	AD-ICP-MS	0.01	0.12	<0.01	0.01	0.02	0.01	0.58	0.05
Cd	AD-ICP-MS	0.013	0.07	0.02	0.09	0.07	0.07	0.07	0.06
In	AD-ICP-MS	0.002	0.101	0.122	0.081	0.036	0.076	0.37	0.068
Sn	AD-ICP-MS	0.16	2.2	2.1	1.2	0.2	1.2	1.3	1.7
Sb	AD-ICP-MS	0.04	0.38	0.26	0.89	0.5	0.72	1.73	1.04
Cs	AD-ICP-MS	0.01	0.21	1.03	0.06	<0.05	<0.05	<0.05	0.38

## Appendix E.II (continued) Whole-rock geochemistry

Sample ID		348958	348959	348960	348964	348965	348967	348970
Drill Hole ID		GV-16-08	GV-16-08	GV-16-08	GV-16-03	GV-16-03	GV-16-03	GV-16-03
Drill Hole Depth (m)		20.9	24.8	26.6	29.9	62	35.2	38.54
UTM easting		569155	569155	569155	568689	568689	568689	568689
UTM northing		5538679	5538679	5538679	5538731	5538731	5538731	5538731
Lithology Code		LOD	ADSM	ADSM	ADSM	B-S1	Arg	MR-IF
La	FUS-ICP-MS	0.1	27.1	19.1	5.4	0.9	6.9	26.8
Ce	FUS-ICP-MS	0.1	86.8	51.8	16	2.2	18.4	42.3
Pr	FUS-ICP-MS	0.03	7.24	6.17	2.5	0.3	2.69	8.03
Nd	FUS-ICP-MS	0.1	28.6	25.7	12.4	1.5	13.7	33.6
Sm	FUS-ICP-MS	0.03	6.64	7.1	4.1	0.65	4.23	8.83
Eu	FUS-ICP-MS	0.03	1.34	1.38	1.34	0.22	1.31	2.3
Gd	FUS-ICP-MS	0.05	6.11	7.33	5.31	0.85	4.81	9.62
Tb	FUS-ICP-MS	0.01	0.96	1.3	0.83	0.23	0.8	1.6
Dy	FUS-ICP-MS	0.05	5.85	8.52	5.57	1.54	5.61	9.79
Ho	FUS-ICP-MS	0.01	1.12	1.96	1.16	0.39	1.09	2
Er	FUS-ICP-MS	0.03	2.79	5.41	3.35	1.35	3.16	6.18
Tm	FUS-ICP-MS	0.01	0.42	0.84	0.42	0.18	0.42	0.75
Yb	FUS-ICP-MS	0.03	2.86	5.83	3.01	1.28	3.16	5.09
Lu	FUS-ICP-MS	0.01	0.44	0.97	0.45	0.18	0.45	0.63
Hf	FUS-ICP-MS	0.2	3.4	5.7	3.3	0.3	3	0.5
Ta	FUS-ICP-MS	0.1	0.8	0.4	0.5	0.1	0.4	0.2
Au	FA-ICP-AES	0.001	0.515	0.004	<0.001	0.001	<0.001	0.148
Tl	AD-ICP-MS	0.002	0.27	0.56	0.02	<0.02	<0.02	0.02
Pb	AD-ICP-MS	0.18	73.4	4.4	2.8	3.6	3.8	7.7
Bi	FUS-ICP-MS	0.01	1.15	<0.47	<0.47	<0.47	<0.47	<0.47
Th	FUS-ICP-MS	0.05	7.25	5.44	0.37	0.19	0.87	1.11
U	FUS-ICP-MS	0.05	1.11	0.64	0.13	0.12	0.5	3.09
								5.55

## Appendix E.II (continued) Whole-rock geochemistry

Sample ID		348971	348972	348977	348981	348983	348984	348985	
Drill Hole ID		GV-16-03	GV-16-06	GV-16-06	GV-16-02	GV-16-02	GV-16-02	GV-16-02	
Drill Hole Depth (m)		42.81	38.84	155.58	61.15	117.5	124	128.3	
UTM easting		568689	569304	569304	568132	568132	568132	568132	
UTM northing		5538731	5538764	5538764	5538611	5538611	5538611	5538611	
Lithology Code	LOD	ADSM	B-S1	VC	B-S1	ADSM	ADSM	B-S1	
SiO <sub>2</sub> (%)	FUS-ICP-AES	0.01	50.2	55.1	44.7	49.6	58.1	49.7	46.2
TiO <sub>2</sub>	FUS-ICP-AES	0.01	2.11	0.53	0.54	0.51	0.53	0.74	0.64
Al <sub>2</sub> O <sub>3</sub>	FUS-ICP-AES	0.01	13.65	16.25	14	15.3	12.5	20.4	15.25
Fe <sub>2</sub> O <sub>3T</sub>	FUS-ICP-AES	0.01	14.15	11.05	8.4	10.45	10.25	13.25	11.15
MnO	FUS-ICP-AES	0.01	0.21	0.05	0.16	0.2	0.74	0.16	0.12
MgO	FUS-ICP-AES	0.01	4.45	7.13	8.41	7.81	3.29	1.25	6.17
CaO	FUS-ICP-AES	0.01	4.63	3.2	7.57	7.77	3.36	4.22	10.55
Na <sub>2</sub> O	FUS-ICP-AES	0.01	2.25	3.79	0.99	3.1	1.9	4.62	2.8
K <sub>2</sub> O	FUS-ICP-AES	0.01	0.73	0.23	2.44	0.4	2.11	2.92	0.4
P <sub>2</sub> O <sub>5</sub>	FUS-ICP-AES	0.01	0.35	0.03	0.04	0.04	0.12	0.11	0.05
Cr <sub>2</sub> O <sub>3</sub>	FUS-ICP-AES	0.002	0.002	0.001	0.041	0.014	0.007	0.009	0.003
BaO	FUS-ICP-AES	0.01	0.01	0.005	0.02	0.005	0.06	0.06	0.01
LOI	GRAV		6.49	3.74	13.65	4.31	6.12	2.27	6.11
Total		99.24	101.1	100.98	99.51	99.1	99.73	99.47	
CO <sub>2</sub>	COM-IR		3.516	0.096	10.134	1.686	4.898	1.3	4.697
S	COM-IR		0.036	0.018	0.028	0.063	0.054	0.016	0.028
Li (ppm)	AD-ICP-MS	0.4	19.4	22.9	13	11.6	10.1	6.3	16.4
Be	AD-ICP-MS	0.04	1.01	0.21	0.15	0.34	1.2	0.65	0.18
Sc	AD-ICP-MS	1.1	31.4	30.7	31.4	36.6	16.8	42.9	35.5
V	FUS-ICP-MS	1	194	286	236	253	72	279	288
Co	AD-ICP-MS	0.13	28.1	44.8	36.9	36.1	25.9	39.7	35.8
Ni	AD-ICP-MS	0.7	13.1	27.8	99.9	61.8	41.4	38.1	39.2
Cu	AD-ICP-MS	1.4	45.6	55.5	70	80.8	421	10.8	17.8
Zn	AD-ICP-MS	1.8	135	101	73	159	99	107	83
Ga	FUS-ICP-MS	0.05	21.4	15.4	13.8	15.8	15.4	22.2	16.1
Rb	FUS-ICP-MS	0.2	13.5	5.9	35.2	4.5	46.3	58.4	8.5
Sr	FUS-ICP-MS	0.1	94	55	195.5	113.5	95	141	189.5
Y	FUS-ICP-MS	0.1	54	10.8	13	14.1	22.3	19.5	19
Zr	FUS-ICP-MS	2	216	28	24	21	100	44	33
Nb	FUS-ICP-MS	0.2	9.3	0.5	0.4	0.4	7.4	1.6	0.6
Mo	AD-ICP-MS	0.08	0.59	0.09	0.09	0.59	0.13	0.23	0.12
Ag	AD-ICP-MS	0.01	0.03	0.01	0.03	0.09	0.05	0.02	0.02
Cd	AD-ICP-MS	0.013	0.04	0.03	0.07	0.04	0.03	<0.02	0.05
In	AD-ICP-MS	0.002	0.121	0.065	0.039	0.052	0.102	0.066	0.054
Sn	AD-ICP-MS	0.16	1.6	0.4	0.4	0.5	2	0.5	0.3
Sb	AD-ICP-MS	0.04	1.24	0.55	1.21	0.48	0.63	0.76	0.73
Cs	AD-ICP-MS	0.01	0.24	0.08	0.47	0.07	0.35	0.42	0.07

## Appendix E.II (continued) Whole-rock geochemistry

Sample ID		348971	348972	348977	348981	348983	348984	348985
Drill Hole ID		GV-16-03	GV-16-06	GV-16-06	GV-16-02	GV-16-02	GV-16-02	GV-16-02
Drill Hole Depth (m)		42.81	38.84	155.58	61.15	117.5	124	128.3
UTM easting		568689	569304	569304	568132	568132	568132	568132
UTM northing		5538731	5538764	5538764	5538611	5538611	5538611	5538611
Lithology Code		LOD	ADSM	B-S1	VC	B-S1	ADSM	ADSM
La	FUS-ICP-MS	0.1	14.6	1.6	0.9	1.1	27.9	3.6
Ce	FUS-ICP-MS	0.1	37.7	4	2.7	3	87.6	9
Pr	FUS-ICP-MS	0.03	5.45	0.52	0.49	0.52	6.86	1.24
Nd	FUS-ICP-MS	0.1	26.1	2.5	2.9	2.8	26.6	6.2
Sm	FUS-ICP-MS	0.03	7.82	1.02	1.2	1.03	6.46	2.17
Eu	FUS-ICP-MS	0.03	2.18	0.3	0.48	0.39	1.35	0.7
Gd	FUS-ICP-MS	0.05	8.98	1.84	1.8	1.74	5.55	2.8
Tb	FUS-ICP-MS	0.01	1.54	0.3	0.34	0.36	0.86	0.5
Dy	FUS-ICP-MS	0.05	10.8	1.9	2.27	2.72	5.19	3.72
Ho	FUS-ICP-MS	0.01	2.14	0.45	0.52	0.58	0.98	0.88
Er	FUS-ICP-MS	0.03	6.41	0.97	1.4	1.85	2.83	2.55
Tm	FUS-ICP-MS	0.01	0.9	0.18	0.26	0.24	0.35	0.31
Yb	FUS-ICP-MS	0.03	5.46	1.12	1.56	1.93	2.76	2.22
Lu	FUS-ICP-MS	0.01	0.93	0.18	0.24	0.24	0.4	0.37
Hf	FUS-ICP-MS	0.2	5.3	1	0.8	0.7	2.8	1.4
Ta	FUS-ICP-MS	0.1	0.7	0.3	0.2	0.1	0.6	0.2
Au	FA-ICP-AES	0.001	0.001	0.001	<0.001	<0.001	0.005	<0.001
Tl	AD-ICP-MS	0.002	0.09	0.02	0.19	0.15	0.23	0.22
Pb	AD-ICP-MS	0.18	5	0.7	5.3	5.2	8.4	7.3
Bi	FUS-ICP-MS	0.01	<0.47	<0.47	<0.47	<0.47	0.57	<0.47
Th	FUS-ICP-MS	0.05	2.21	0.35	0.06	0.19	7.23	0.67
U	FUS-ICP-MS	0.05	1.27	0.09	0.025	0.1	0.89	0.51
								0.18

## Appendix E.II (continued) Whole-rock geochemistry

Sample ID		348987	348988	348989	348990	348991	348992	348994	
Drill Hole ID		GV-16-01							
Drill Hole Depth (m)		8	21.28	38	43.43	54.55	66.44	71.64	
UTM easting		567749	567749	567749	567749	567749	567749	567749	
UTM northing		5538379	5538379	5538379	5538379	5538379	5538379	5538379	
Lithology Code	LOD	VC	B-S1	B-S1	B-S2	B-S1	VC	ADSM	
SiO <sub>2</sub> (%)	FUS-ICP-AES	0.01	44	48.5	47.3	41.4	51.2	60.2	44.9
TiO <sub>2</sub>	FUS-ICP-AES	0.01	2.23	0.32	0.45	4.1	0.62	0.28	0.93
Al <sub>2</sub> O <sub>3</sub>	FUS-ICP-AES	0.01	14.8	16.9	15.4	15.2	20.6	11.95	15.7
Fe <sub>2</sub> O <sub>3T</sub>	FUS-ICP-AES	0.01	17.15	10.05	8.84	15.45	7.28	6.64	12.35
MnO	FUS-ICP-AES	0.01	0.13	0.05	0.13	0.16	0.08	0.03	0.46
MgO	FUS-ICP-AES	0.01	6.26	9.02	7.76	6.1	5.08	2.18	6.31
CaO	FUS-ICP-AES	0.01	5.57	9.75	11.7	7.74	6.66	8.52	5.14
Na <sub>2</sub> O	FUS-ICP-AES	0.01	1.33	1.62	2.45	2.54	4.79	0.23	0.15
K <sub>2</sub> O	FUS-ICP-AES	0.01	1.11	0.22	0.09	0.02	0.17	2.2	2.86
P <sub>2</sub> O <sub>5</sub>	FUS-ICP-AES	0.01	0.34	0.02	0.02	0.98	0.06	0.01	0.12
Cr <sub>2</sub> O <sub>3</sub>	FUS-ICP-AES	0.002	0.007	0.008	0.023	0.007	0.025	0.005	0.026
BaO	FUS-ICP-AES	0.01	0.01	0.005	0.005	0.005	0.005	0.01	0.03
LOI	GRAV		5.28	4.17	5.93	5.32	4.62	8.48	10.3
Total		98.22	100.64	100.1	99.03	101.2	100.75	99.28	
CO <sub>2</sub>	COM-IR		2.517	0.936	3.241	2	1.638	5.754	7.037
S	COM-IR		2.228	0.29	0.06	0.857	0.167	0.016	0.469
Li (ppm)	AD-ICP-MS	0.4	13.1	14.8	12.9	22	18.7	13.5	23.3
Be	AD-ICP-MS	0.04	0.48	0.15	0.14	1.14	0.18	0.32	0.76
Sc	AD-ICP-MS	1.1	26.9	37.4	38.7	31.7	45.3	19.2	32.8
V	FUS-ICP-MS	1	281	272	269	375	349	147	205
Co	AD-ICP-MS	0.13	51.3	34.8	52.9	48.2	40.2	21	50.4
Ni	AD-ICP-MS	0.7	60.3	63.8	92.9	60.1	54.3	56	112
Cu	AD-ICP-MS	1.4	45.9	108.5	84.2	76	80	2.9	672
Zn	AD-ICP-MS	1.8	240	73	69	122	83	52	211
Ga	FUS-ICP-MS	0.05	19.8	15.7	14.6	25.2	18.9	12	17.4
Rb	FUS-ICP-MS	0.2	12.9	2.7	1.2	0.2	2.1	51.5	47.6
Sr	FUS-ICP-MS	0.1	61.2	93	115.5	126.5	103.5	144.5	60.6
Y	FUS-ICP-MS	0.1	26.8	12.3	12	43.9	17.9	2.1	25.1
Zr	FUS-ICP-MS	2	176	53	19	365	30	41	81
Nb	FUS-ICP-MS	0.2	11.4	0.9	0.3	26.6	0.8	0.5	4.6
Mo	AD-ICP-MS	0.08	4.81	0.35	0.18	1.97	0.16	0.08	1.3
Ag	AD-ICP-MS	0.01	0.08	0.04	0.03	0.04	0.05	0.01	0.18
Cd	AD-ICP-MS	0.013	0.07	0.1	0.23	0.15	0.09	0.04	0.17
In	AD-ICP-MS	0.002	0.061	0.05	0.048	0.121	0.064	0.027	0.072
Sn	AD-ICP-MS	0.16	1.2	0.2	0.3	2.4	0.3	0.3	0.7
Sb	AD-ICP-MS	0.04	0.37	0.46	0.7	0.81	0.59	0.38	0.39
Cs	AD-ICP-MS	0.01	0.17	<0.05	<0.05	<0.05	0.1	0.35	0.32

## Appendix E.II (continued) Whole-rock geochemistry

Sample ID		348987	348988	348989	348990	348991	348992	348994	
Drill Hole ID		GV-16-01							
Drill Hole Depth (m)		8	21.28	38	43.43	54.55	66.44	71.64	
UTM easting		567749	567749	567749	567749	567749	567749	567749	
UTM northing		5538379	5538379	5538379	5538379	5538379	5538379	5538379	
Lithology Code		LOD	VC	B-S1	B-S1	B-S2	B-S1	VC	
								ADSM	
La	FUS-ICP-MS	0.1	13.5	2	0.8	29.8	1.8	1.2	9.9
Ce	FUS-ICP-MS	0.1	33	4.5	2.2	73.4	4.3	3.1	26.9
Pr	FUS-ICP-MS	0.03	4.63	0.52	0.4	9.96	0.66	0.38	2.92
Nd	FUS-ICP-MS	0.1	19.6	2.4	2.1	45.4	3.6	1.6	13.7
Sm	FUS-ICP-MS	0.03	4.86	1.19	0.99	10.85	1.62	0.54	3.36
Eu	FUS-ICP-MS	0.03	1.42	0.32	0.37	3.5	0.56	0.2	0.98
Gd	FUS-ICP-MS	0.05	5.3	1.67	1.42	9.86	2.11	0.52	4.11
Tb	FUS-ICP-MS	0.01	0.85	0.26	0.3	1.57	0.41	0.06	0.64
Dy	FUS-ICP-MS	0.05	5.12	2.05	2.11	8.86	2.89	0.42	4.01
Ho	FUS-ICP-MS	0.01	1.07	0.47	0.5	1.79	0.7	0.08	0.89
Er	FUS-ICP-MS	0.03	3.08	1.72	1.6	5.02	2.36	0.24	2.82
Tm	FUS-ICP-MS	0.01	0.43	0.23	0.2	0.61	0.33	0.02	0.39
Yb	FUS-ICP-MS	0.03	2.89	1.39	1.26	4.1	1.69	0.35	2.64
Lu	FUS-ICP-MS	0.01	0.38	0.27	0.18	0.57	0.28	0.04	0.38
Hf	FUS-ICP-MS	0.2	3.8	1.4	0.5	7.7	1.1	1.3	2.3
Ta	FUS-ICP-MS	0.1	0.8	0.3	0.2	1.7	0.2	0.2	0.4
Au	FA-ICP-AES	0.001	0.009	<0.001	<0.001	0.003	<0.001	<0.001	0.109
Tl	AD-ICP-MS	0.002	0.25	0.05	<0.02	<0.02	<0.02	0.18	0.17
Pb	AD-ICP-MS	0.18	3.4	1.9	0.6	1.4	1.6	1.6	6.1
Bi	FUS-ICP-MS	0.01	1.09	<0.47	<0.47	<0.47	<0.47	<0.47	<0.47
Th	FUS-ICP-MS	0.05	3.64	2.66	0.27	1.68	0.45	1	1.51
U	FUS-ICP-MS	0.05	0.46	0.46	0.44	0.62	0.75	0.09	2.1

## Appendix E.II (continued) Whole-rock geochemistry

Sample ID		348997	348999	349000
Drill Hole ID		GV-16-01	GV-16-01	GV-16-01
Drill Hole Depth (m)		77.5	88	97
UTM easting		567749	567749	567749
UTM northing		5538379	5538379	5538379
Lithology Code	LOD	VC	VC	B-S2
SiO <sub>2</sub> (%)	FUS-ICP-AES	0.01	56.6	48.8
TiO <sub>2</sub>	FUS-ICP-AES	0.01	0.38	0.61
Al <sub>2</sub> O <sub>3</sub>	FUS-ICP-AES	0.01	13.3	17.35
Fe <sub>2</sub> O <sub>3T</sub>	FUS-ICP-AES	0.01	11.75	10.75
MnO	FUS-ICP-AES	0.01	0.15	0.09
MgO	FUS-ICP-AES	0.01	7.99	5.84
CaO	FUS-ICP-AES	0.01	2.28	10.85
Na <sub>2</sub> O	FUS-ICP-AES	0.01	0.93	1.46
K <sub>2</sub> O	FUS-ICP-AES	0.01	0.69	0.23
P <sub>2</sub> O <sub>5</sub>	FUS-ICP-AES	0.01	0.03	0.02
Cr <sub>2</sub> O <sub>3</sub>	FUS-ICP-AES	0.002	0.015	0.006
BaO	FUS-ICP-AES	0.01	0.01	0.005
LOI	GRAV		5.81	4.67
Total			99.94	100.7
CO <sub>2</sub>	COM-IR		1.943	1.388
S	COM-IR		0.671	0.041
Li (ppm)	AD-ICP-MS	0.4	36.6	20.9
Be	AD-ICP-MS	0.04	0.16	0.28
Sc	AD-ICP-MS	1.1	30.5	35.9
V	FUS-ICP-MS	1	271	388
Co	AD-ICP-MS	0.13	47.6	35.8
Ni	AD-ICP-MS	0.7	61.8	43.4
Cu	AD-ICP-MS	1.4	973	39.8
Zn	AD-ICP-MS	1.8	96	87
Ga	FUS-ICP-MS	0.05	15.7	18.6
Rb	FUS-ICP-MS	0.2	11.5	4.2
Sr	FUS-ICP-MS	0.1	30.1	206
Y	FUS-ICP-MS	0.1	11.6	14.4
Zr	FUS-ICP-MS	2	21	34
Nb	FUS-ICP-MS	0.2	0.6	0.7
Mo	AD-ICP-MS	0.08	0.15	0.08
Ag	AD-ICP-MS	0.01	0.11	0.01
Cd	AD-ICP-MS	0.013	0.02	0.15
In	AD-ICP-MS	0.002	0.086	0.058
Sn	AD-ICP-MS	0.16	<0.2	0.3
Sb	AD-ICP-MS	0.04	0.18	0.91
Cs	AD-ICP-MS	0.01	0.1	<0.05

## Appendix E.II (continued) Whole-rock geochemistry

Sample ID		348997	348999	349000
Drill Hole ID		GV-16-01	GV-16-01	GV-16-01
Drill Hole Depth (m)		77.5	88	97
UTM easting		567749	567749	567749
UTM northing		5538379	5538379	5538379
Lithology Code	LOD	VC	VC	B-S2
La	FUS-ICP-MS	0.1	1.6	1.5
Ce	FUS-ICP-MS	0.1	3.6	3.9
Pr	FUS-ICP-MS	0.03	0.61	0.56
Nd	FUS-ICP-MS	0.1	2.5	3.2
Sm	FUS-ICP-MS	0.03	1.08	1.4
Eu	FUS-ICP-MS	0.03	0.38	0.53
Gd	FUS-ICP-MS	0.05	1.42	1.97
Tb	FUS-ICP-MS	0.01	0.32	0.35
Dy	FUS-ICP-MS	0.05	2.06	2.64
Ho	FUS-ICP-MS	0.01	0.5	0.61
Er	FUS-ICP-MS	0.03	1.36	1.63
Tm	FUS-ICP-MS	0.01	0.24	0.31
Yb	FUS-ICP-MS	0.03	1.49	2.01
Lu	FUS-ICP-MS	0.01	0.22	0.28
Hf	FUS-ICP-MS	0.2	0.8	1
Ta	FUS-ICP-MS	0.1	0.2	0.2
Au	FA-ICP-AES	0.001	0.02	<0.001
Tl	AD-ICP-MS	0.002	0.04	<0.02
Pb	AD-ICP-MS	0.18	1.5	1.4
Bi	FUS-ICP-MS	0.01	<0.47	<0.47
Th	FUS-ICP-MS	0.05	0.27	0.32
U	FUS-ICP-MS	0.05	0.18	0.34
				0.64

## Appendix E.II (continued) Whole-rock geochemistry

Sample ID		348007	348008	348017	348047	348081	348955	348961
Drill Hole ID		GV-16-10	GV-16-10	GV-16-11	GV-16-09	GV-16-12	GV-16-08	GV-16-08
Drill Hole Depth (m)		76.36	77.1	53.9	83.3	29.96	14.5	29.5
UTM easting		569008	569008	568323	568264	567665	569155	569155
UTM northing		5538749	5538749	5538632	5538555	5538175	5538679	5538679
Lithology Code	LOD	Obsolete						
SiO <sub>2</sub> (%)	FUS-ICP-AES	0.01	51.6	78.6	52.6	46.5	49.8	56.6
TiO <sub>2</sub>	FUS-ICP-AES	0.01	0.51	0.05	0.09	1.51	0.57	1.3
Al <sub>2</sub> O <sub>3</sub>	FUS-ICP-AES	0.01	15.8	1.64	1.89	17.4	16.6	15
Fe <sub>2</sub> O <sub>3T</sub>	FUS-ICP-AES	0.01	9.9	12	42.1	11	9.54	6.37
MnO	FUS-ICP-AES	0.01	0.24	0.24	0.75	0.16	0.1	0.07
MgO	FUS-ICP-AES	0.01	4.49	1.06	1	4.34	4.09	4.07
CaO	FUS-ICP-AES	0.01	5.58	3.72	1.91	9.34	11	4.58
Na <sub>2</sub> O	FUS-ICP-AES	0.01	3.72	0.05	0.04	4.23	2.91	3.36
K <sub>2</sub> O	FUS-ICP-AES	0.01	1.21	0.15	0.2	0.18	0.05	2.04
P <sub>2</sub> O <sub>5</sub>	FUS-ICP-AES	0.01	0.04	0.4	0.7	0.19	0.05	0.48
Cr <sub>2</sub> O <sub>3</sub>	FUS-ICP-AES	0.002	0.05	0.004	0.012	0.016	0.01	0.016
BaO	FUS-ICP-AES	0.01	0.02	0.005	0.005	0.005	0.005	0.07
LOI	GRAV		7.66	3.86	0.57	4.73	5.04	4.45
Total		100.83	101.77	101.86	99.63	99.77	98.43	100.15
CO <sub>2</sub>	COM-IR		4.6	3.543	0.848	1.893	2.552	2.298
S	COM-IR		0.025	0.016	0.012	0.022	0.006	0.725
Li (ppm)	AD-ICP-MS	0.4	21.1	3.6	2.5	15.3	12.1	9.5
Be	AD-ICP-MS	0.04	0.56	0.21	1.18	0.61	0.24	2.39
Sc	AD-ICP-MS	1.1	39.6	3.1	3.9	36.2	40	14.7
V	FUS-ICP-MS	1	208	72	100	245	306	193
Co	AD-ICP-MS	0.13	30.4	6.8	39.8	52.5	37.3	20.6
Ni	AD-ICP-MS	0.7	95.4	12.8	31.4	89.7	48.5	59.2
Cu	AD-ICP-MS	1.4	91.9	65.2	32	61.7	15.4	92.3
Zn	AD-ICP-MS	1.8	78	38	50	104	82	65
Ga	FUS-ICP-MS	0.05	13.1	2.5	2.2	18.8	15.4	21
Rb	FUS-ICP-MS	0.2	26.3	3.1	3.3	3.2	1	51
Sr	FUS-ICP-MS	0.1	122	47.8	12.4	243	123.5	175
Y	FUS-ICP-MS	0.1	9.7	7.8	9.2	32.8	14.8	17.6
Zr	FUS-ICP-MS	2	28	5	9	115	36	515
Nb	FUS-ICP-MS	0.2	0.7	0.3	0.6	5.3	1.1	9.3
Mo	AD-ICP-MS	0.08	0.07	0.46	0.55	0.28	0.26	0.2
Ag	AD-ICP-MS	0.01	0.01	0.08	0.01	0.01	0.02	0.12
Cd	AD-ICP-MS	0.013	0.06	0.07	0.02	0.09	0.08	0.06
In	AD-ICP-MS	0.002	0.049	0.049	0.075	0.085	0.06	0.056
Sn	AD-ICP-MS	0.16	0.2	0.2	0.5	1.1	0.3	2.3
Sb	AD-ICP-MS	0.04	0.61	0.19	0.84	1.09	0.9	0.65
Cs	AD-ICP-MS	0.01	0.18	0.025	0.025	0.07	0.025	0.33

## Appendix E.II (continued) Whole-rock geochemistry

Sample ID		348007	348008	348017	348047	348081	348955	348961
Drill Hole ID		GV-16-10	GV-16-10	GV-16-11	GV-16-09	GV-16-12	GV-16-08	GV-16-08
Drill Hole Depth (m)		76.36	77.1	53.9	83.3	29.96	14.5	29.5
UTM easting		569008	569008	568323	568264	567665	569155	569155
UTM northing		5538749	5538749	5538632	5538555	5538175	5538679	5538679
Lithology Code	LOD	Obsolete						
La	FUS-ICP-MS	0.1	1.6	3.8	5	6.6	2.4	48.9
Ce	FUS-ICP-MS	0.1	3.7	6.2	9.4	17.4	5.3	107.5
Pr	FUS-ICP-MS	0.03	0.54	1.3	1.6	2.72	0.66	12.75
Nd	FUS-ICP-MS	0.1	2.7	5.5	6.7	12.7	3.8	46.3
Sm	FUS-ICP-MS	0.03	1.06	1.37	1.65	4.09	1.62	8.17
Eu	FUS-ICP-MS	0.03	0.35	0.37	0.41	1.44	0.51	1.87
Gd	FUS-ICP-MS	0.05	1.45	1.59	1.49	5.34	1.93	6.01
Tb	FUS-ICP-MS	0.01	0.22	0.25	0.31	0.87	0.39	0.76
Dy	FUS-ICP-MS	0.05	1.58	1.49	1.87	5.53	2.83	4.1
Ho	FUS-ICP-MS	0.01	0.36	0.32	0.42	1.18	0.58	0.72
Er	FUS-ICP-MS	0.03	1.02	0.91	1.21	3.55	1.8	1.78
Tm	FUS-ICP-MS	0.01	0.18	0.12	0.2	0.48	0.26	0.23
Yb	FUS-ICP-MS	0.03	1.27	0.81	1.11	3.22	1.67	1.6
Lu	FUS-ICP-MS	0.01	0.19	0.12	0.17	0.46	0.27	0.19
Hf	FUS-ICP-MS	0.2	0.9	0.1	0.2	3	1.3	12.5
Ta	FUS-ICP-MS	0.1	0.1	0.1	0.05	0.4	0.2	0.6
Au	FA-ICP-AES	0.001	0.014	0.022	0.014	<0.001	0.001	0.06
Tl	AD-ICP-MS	0.002	0.16	0.03	0.04	0.01	0.01	0.19
Pb	AD-ICP-MS	0.18	4.7	2.3	4.4	1.4	2	4.8
Bi	FUS-ICP-MS	0.01	<0.47	<0.47	<0.47	<0.47	<0.47	<0.47
Th	FUS-ICP-MS	0.05	683	0.28	0.45	0.5	0.41	13.5
U	FUS-ICP-MS	0.05	0.72	0.4	0.37	0.24	0.55	3.09
								0.92

**Appendix F:** Additional whole-rock geochemistry collected for rocks from the  
Goldenville Horizon and related stratigraphy

## **Appendix F.I Whole-rock geochemistry abbreviations, additional data**

### Lithology Abbreviations:

B-S1: Basaltic volcanic rocks from Suite 1  
B-S2: Basaltic volcanic rocks from Suite 2  
VC: Volcaniclastic rocks  
Arg: Argillite  
MR-IF: Magnetite-rich iron formation  
ASMM: Argillite with semi-massive magnetite  
ADSM: Argillite with disseminated magnetite

### Method Abbreviations:

FUS: Li-B fusion followed by acid digestion  
GRAV: Gravimetric, in furnace  
AD: Closed-vessel, multi-acid digestion  
FA: Fire assay  
COM-IR: Combustion infrared absorption  
ICP-MS: Inductively coupled plasma-mass spectrometry  
ICP-AES: Inductively coupled plasma-atomic emission spectrometry

## Appendix F.II Whole-rock geochemistry, additional data

Sample ID		348001	348005	348006	348012	348013	348014	348020	
Drill Hole ID		GV-16-10	GV-16-10	GV-16-10	GV-16-10	GV-16-10	GV-16-10	GV-16-11	
Drill Hole Depth (m)		1.2	53.62	71.73	80.2	80.58	85.5	58.45	
UTM easting		569008	569008	569008	569008	569008	569008	568323	
UTM northing		5538749	5538749	5538749	5538749	5538749	5538749	5538632	
Lithology Code	LOD	B-S1	B-S1	B-S1	ASMM	ASMM	ADSM	ASMM	
SiO <sub>2</sub> (%)		--	--	--	--	--	--	--	
TiO <sub>2</sub>		--	--	--	--	--	--	--	
Al <sub>2</sub> O <sub>3</sub>		--	--	--	--	--	--	--	
Fe <sub>2</sub> O <sub>3T</sub>		--	--	--	--	--	--	--	
MnO		--	--	--	--	--	--	--	
MgO		--	--	--	--	--	--	--	
CaO		--	--	--	--	--	--	--	
Na <sub>2</sub> O		--	--	--	--	--	--	--	
K <sub>2</sub> O		--	--	--	--	--	--	--	
P <sub>2</sub> O <sub>5</sub>		--	--	--	--	--	--	--	
Cr <sub>2</sub> O <sub>3</sub>		--	--	--	--	--	--	--	
BaO		--	--	--	--	--	--	--	
LOI		--	--	--	--	--	--	--	
Total		--	--	--	--	--	--	--	
CO <sub>2</sub>		--	--	--	--	--	--	--	
S (ppm)	AD-ICP-AES	39	<39	5167	216	<39	1308	59	45
Li	AD-ICP-AES	2	11	11	20	16	18	15	10
Be	AD-ICP-AES	0.1	0.1	0.1	0.2	0.1	0.5	0.5	1.4
Na	AD-ICP-AES	530	13984	16002	19115	18514	1418	21812	6718
Mg	AD-ICP-AES	140	36334	40286	32067	34050	23170	38887	25009
Al	AD-ICP-AES	260	86513	80101	75667	76185	45694	72753	46424
P	AD-ICP-AES	4	139	159	221	179	1405	736	2349
K	AD-ICP-AES	98	5102	190	2990	2957	2126	293	5225
Ca	AD-ICP-AES	46	43152	49529	29741	70611	20960	56086	9687
Sc	AD-ICP-AES	0.3	33.3	32.7	27.2	31	9.7	36.4	9.4
Ti	AD-ICP-MS	7	3511	2792	3497	3707	2456	10489	2242
Ti	AD-ICP-AES	6	3579	2708	3657	3523	2464	10133	2372
V	AD-ICP-MS	0.8	333.6	299.9	304.4	284.6	124.8	291.5	79.1
V	AD-ICP-AES	3	320.8	276	301.2	265.3	125.1	271.5	87.8
Cr	AD-ICP-MS	3	12	96	5	18	49	240	53
Cr	AD-ICP-AES	17	<17	87	<17	17	49	211	55
Mn	AD-ICP-AES	1	560	919	874	844	>13000	2174	>13000
Fe	AD-ICP-AES	110	76800	63211	66892	68579	157878	80408	192351
Co	AD-ICP-AES	1	32	25	27	29	23	32	27
Ni	AD-ICP-AES	4	28	49	12	36	58	47	78
Cu	AD-ICP-AES	3	38	74	237	25	158	100	51
Zn	AD-ICP-AES	3	103	134	81	83	242	94	275
Ga	AD-ICP-MS	0.04	18.2	15.59	15.49	15.7	12.26	16.11	11.59
Rb	AD-ICP-MS	0.11	14.38	0.41	6.86	8.42	4.64	0.72	19.27

**Appendix F.II (continued) Whole-rock geochemistry, additional data**

Sample ID		348001	348005	348006	348012	348013	348014	348020
Drill Hole ID		GV-16-10	GV-16-10	GV-16-10	GV-16-10	GV-16-10	GV-16-10	GV-16-11
Drill Hole Depth (m)		1.2	53.62	71.73	80.2	80.58	85.5	58.45
UTM easting		569008	569008	569008	569008	569008	569008	568323
UTM northing		5538749	5538749	5538749	5538749	5538749	5538749	5538632
Lithology Code	LOD	B-S1	B-S1	B-S1	ASMM	ASMM	ADSM	ASMM
Sr	AD-ICP-MS	0.6	117.6	80	55.3	191.3	37.5	144
Sr	AD-ICP-AES	3	126	78	57	193	39	151
Y	AD-ICP-MS	0.05	14.32	13.9	16.22	20.34	33.06	31.24
Y	AD-ICP-AES	0.6	13	12.6	15.2	17.6	29.7	28.5
Zr	AD-ICP-MS	6	29	23	29	28	76	122
Zr	AD-ICP-AES	7	29	22	29	26	73	114
Nb	AD-ICP-MS	0.028	0.627	0.531	0.635	0.55	5.975	3.291
Mo	AD-ICP-AES	2	<2	<2	<2	<2	<2	<2
Ag		--	--	--	--	--	--	--
Cd	AD-ICP-AES	0.8	0.8	0.9	<0.8	<0.8	0.9	<0.8
In		--	--	--	--	--	--	--
Sn		--	--	--	--	--	--	--
Sb		--	--	--	--	--	--	--
Cs	AD-ICP-MS	0.013	0.087	0.034	0.261	0.069	0.033	0.026
Ba	AD-ICP-MS	0.8	60.4	4.7	58	111.1	43.3	39.6
Ba	AD-ICP-AES	2	54	5	57	102	40	38
La	AD-ICP-MS	0.1	1.5	1.3	1.4	1.5	35.6	5.7
Ce	AD-ICP-MS	0.12	4.23	2.98	3.71	3.57	115.61	16.94
Pr	AD-ICP-MS	0.014	0.718	0.481	0.582	0.614	9.4	2.667
Nd	AD-ICP-MS	0.06	3.86	2.4	2.96	3.19	35.88	13.02
Sm	AD-ICP-MS	0.026	1.554	0.984	1.299	1.415	8.115	3.955
Eu	AD-ICP-MS	0.0031	0.6342	0.4111	0.4589	0.5023	2.1675	1.5994
Gd	AD-ICP-MS	0.009	2.359	1.657	2.119	2.243	8.215	5.435
Tb	AD-ICP-MS	0.0023	0.4308	0.3142	0.3881	0.4215	1.3172	0.9261
Dy	AD-ICP-MS	0.009	3.054	2.345	2.814	2.946	7.678	5.653
Ho	AD-ICP-MS	0.0025	0.6737	0.5534	0.6309	0.7085	1.6205	1.2112
Er	AD-ICP-MS	0.007	1.965	1.748	1.982	2.216	4.389	3.414
Tm	AD-ICP-MS	0.0019	0.2762	0.2556	0.3045	0.3484	0.6185	0.4791
Yb	AD-ICP-MS	0.009	1.904	1.797	2.06	2.343	3.836	3.081
Lu	AD-ICP-MS	0.002	0.302	0.273	0.326	0.37	0.517	0.456
Hf	AD-ICP-MS	0.14	1.02	0.79	0.98	0.95	1.91	3.04
Ta	AD-ICP-MS	0.007	0.051	0.04	0.047	0.04	0.403	0.221
Au	AD-ICP-MS	0.05	0.47	0.39	1.85	0.25	1.9	0.59
Tl		--	--	--	--	--	--	--
Pb	AD-ICP-AES	8	<8	<8	<8	<8	113	<8
Bi	AD-ICP-MS	0.47	<0.47	<0.47	<0.47	<0.47	<0.47	<0.47
Th	AD-ICP-MS	0.018	0.27	0.205	0.256	0.245	6.148	0.427
U	AD-ICP-MS	0.011	0.238	0.233	0.157	0.195	2.312	0.187
								2.116

## Appendix F.II (continued) Whole-rock geochemistry, additional data

Sample		348021	348022	348028	348033	348035	348036	348037
Drill Hole ID		GV-16-11	GV-16-11	GV-16-09	GV-16-09	GV-16-09	GV-16-09	GV-16-09
Drill Hole Depth (m)		61.07	63.65	6.53	15.67	19.5	22.18	24.3
UTM easting		568323	568323	568264	568264	568264	568264	568264
UTM northing		5538632	5538632	5538555	5538555	5538555	5538555	5538555
Lithology Code	LOD	Arg	Arg	B-S2	MR-IF	ASMM	ASMM	Arg
SiO <sub>2</sub> (%)		--	--	--	--	--	--	--
TiO <sub>2</sub>		--	--	--	--	--	--	--
Al <sub>2</sub> O <sub>3</sub>		--	--	--	--	--	--	--
Fe <sub>2</sub> O <sub>3T</sub>		--	--	--	--	--	--	--
MnO		--	--	--	--	--	--	--
MgO		--	--	--	--	--	--	--
CaO		--	--	--	--	--	--	--
Na <sub>2</sub> O		--	--	--	--	--	--	--
K <sub>2</sub> O		--	--	--	--	--	--	--
P <sub>2</sub> O <sub>5</sub>		--	--	--	--	--	--	--
Cr <sub>2</sub> O <sub>3</sub>		--	--	--	--	--	--	--
BaO		--	--	--	--	--	--	--
LOI		--	--	--	--	--	--	--
Total		--	--	--	--	--	--	--
CO <sub>2</sub>		--	--	--	--	--	--	--
S (ppm)	AD-ICP-AES	39	995	57	1235	1209	<39	<39
Li	AD-ICP-AES	2	12	6	12	<2	9	5
Be	AD-ICP-AES	0.1	1.9	1.5	0.9	0.8	1.5	2.1
Na	AD-ICP-AES	530	1131	25748	10870	11270	<530	<530
Mg	AD-ICP-AES	140	24200	17879	36248	7947	18925	13319
Al	AD-ICP-AES	260	72550	65056	78357	26542	42534	39233
P	AD-ICP-AES	4	2221	635	2140	2734	1912	930
K	AD-ICP-AES	98	25672	14594	193	4645	1689	1005
Ca	AD-ICP-AES	46	66814	15018	80866	24263	10293	14109
Sc	AD-ICP-AES	0.3	25.7	12.3	23.9	5.1	9.2	6.6
Ti	AD-ICP-MS	7	21160	4097	17736	1504	2226	2161
Ti	AD-ICP-AES	6	21138	4046	17807	1555	2361	2041
V	AD-ICP-MS	0.8	342.2	65.6	301.5	122.4	94.9	89.5
V	AD-ICP-AES	3	322.3	65.4	290	130.3	105	95.1
Cr	AD-ICP-MS	3	85	56	62	43	41	37
Cr	AD-ICP-AES	17	79	51	60	41	46	40
Mn	AD-ICP-AES	1	6236	11106	1533	5624	>13000	>13000
Fe	AD-ICP-AES	110	94644	68651	91555	>320000	243405	260414
Co	AD-ICP-AES	1	28	21	35	17	22	31
Ni	AD-ICP-AES	4	56	40	61	49	115	78
Cu	AD-ICP-AES	3	59	9	65	79	33	16
Zn	AD-ICP-AES	3	131	89	107	111	262	188
Ga	AD-ICP-MS	0.04	22.3	16.59	21.37	8.08	10.96	9.92
Rb	AD-ICP-MS	0.11	69.71	51.1	0.37	13.16	5.83	3.74

**Appendix F.II (continued) Whole-rock geochemistry, additional data**

Sample		348021	348022	348028	348033	348035	348036	348037
Drill Hole ID		GV-16-11	GV-16-11	GV-16-09	GV-16-09	GV-16-09	GV-16-09	GV-16-09
Drill Hole Depth (m)		61.07	63.65	6.53	15.67	19.5	22.18	24.3
UTM easting		568323	568323	568264	568264	568264	568264	568264
UTM northing		5538632	5538632	5538555	5538555	5538555	5538555	5538555
Lithology Code	LOD	Arg	Arg	B-S2	MR-IF	ASMM	ASMM	Arg
Sr	AD-ICP-MS	0.6	137.9	63.7	433.9	106.4	9	12.8
Sr	AD-ICP-AES	3	143	64	450	97	9	11
Y	AD-ICP-MS	0.05	33.19	30.15	30.96	22.71	41.3	34.45
Y	AD-ICP-AES	0.6	31.1	27	28.8	21.5	39.3	33.1
Zr	AD-ICP-MS	6	245	125	233	41	74	68
Zr	AD-ICP-AES	7	228	115	221	55	78	74
Nb	AD-ICP-MS	0.028	15.994	9.749	15.559	3.434	6.18	6.326
Mo	AD-ICP-AES	2	<2	<2	<2	<2	<2	<2
Ag		--	--	--	--	--	--	--
Cd	AD-ICP-AES	0.8	0.9	<0.8	0.8	0.9	1.1	1
In		--	--	--	--	--	--	--
Sn		--	--	--	--	--	--	--
Sb		--	--	--	--	--	--	--
Cs	AD-ICP-MS	0.013	0.617	0.58	0.021	0.114	0.044	0.031
Ba	AD-ICP-MS	0.8	571.9	371.1	17.3	55.3	32.7	34.6
Ba	AD-ICP-AES	2	538	355	17	57	33	36
La	AD-ICP-MS	0.1	18.7	30	18.3	18.8	26.1	25
Ce	AD-ICP-MS	0.12	46.74	111.66	44.92	40.46	78.08	74.29
Pr	AD-ICP-MS	0.014	6.595	7.932	6.387	5.712	7.517	7.194
Nd	AD-ICP-MS	0.06	28.76	29.54	26.84	22.11	29.05	28.31
Sm	AD-ICP-MS	0.026	6.981	6.294	6.752	5.107	7.002	7.178
Eu	AD-ICP-MS	0.0031	2.7803	1.5443	2.4556	1.0899	1.8822	1.9428
Gd	AD-ICP-MS	0.009	7.825	6.39	6.917	5.423	7.947	8.227
Tb	AD-ICP-MS	0.0023	1.1394	0.9867	1.0441	0.8544	1.4694	1.47
Dy	AD-ICP-MS	0.009	6.752	5.959	5.979	5.075	9.425	8.992
Ho	AD-ICP-MS	0.0025	1.3733	1.2595	1.216	1.0891	2.0035	1.7996
Er	AD-ICP-MS	0.007	3.667	3.528	3.343	3.077	5.548	5.063
Tm	AD-ICP-MS	0.0019	0.512	0.5311	0.455	0.4554	0.8071	0.7008
Yb	AD-ICP-MS	0.009	3.056	3.493	2.763	2.761	4.77	4.187
Lu	AD-ICP-MS	0.002	0.452	0.511	0.41	0.415	0.686	0.604
Hf	AD-ICP-MS	0.14	5.41	3.21	4.97	1.02	1.85	1.68
Ta	AD-ICP-MS	0.007	1.079	0.656	0.993	0.176	0.393	0.363
Au	AD-ICP-MS	0.05	7.43	3.3	0.52	2.56	1.4	4.97
Tl		--	--	--	--	--	--	--
Pb	AD-ICP-AES	8	14	42	8	20	11	23
Bi	AD-ICP-MS	0.47	<0.47	<0.47	<0.47	<0.47	<0.47	<0.47
Th	AD-ICP-MS	0.018	1.105	10.656	0.919	2.525	5.931	5.383
U	AD-ICP-MS	0.011	0.695	1.448	0.368	1.192	1.924	2.014
								1.316

## Appendix F.II (continued) Whole-rock geochemistry, additional data

Sample ID		348038	348041	348042	348045	348046	348048	348051
Drill Hole ID		GV-16-09	GV-16-09	GV-16-09	GV-16-09	GV-16-09	GV-16-13a	GV-16-05
Drill Hole Depth (m)		25.84	61	77.3	116.9	73.75	48.45	4
UTM easting		568264	568264	568264	568264	568264	567404	569136
UTM northing		5538555	5538555	5538555	5538555	5538555	5537944	5538729
Lithology Code	LOD	Arg	Arg	ADSM	B-S1	Arg	VC	B-S1
SiO <sub>2</sub>		--	--	--	--	--	--	--
TiO <sub>2</sub>		--	--	--	--	--	--	--
Al <sub>2</sub> O <sub>3</sub>		--	--	--	--	--	--	--
Fe <sub>2</sub> O <sub>3T</sub>		--	--	--	--	--	--	--
MnO		--	--	--	--	--	--	--
MgO		--	--	--	--	--	--	--
CaO		--	--	--	--	--	--	--
Na <sub>2</sub> O		--	--	--	--	--	--	--
K <sub>2</sub> O		--	--	--	--	--	--	--
P <sub>2</sub> O <sub>5</sub>		--	--	--	--	--	--	--
Cr <sub>2</sub> O <sub>3</sub>		--	--	--	--	--	--	--
BaO		--	--	--	--	--	--	--
LOI		--	--	--	--	--	--	--
Total		--	--	--	--	--	--	--
CO <sub>2</sub>		--	--	--	--	--	--	--
S (ppm)	AD-ICP-AES	39	368	<39	41	499	403	<39
Li	AD-ICP-AES	2	12	17	6	17	3	7
Be	AD-ICP-AES	0.1	1.1	0.1	0.2	0.1	0.2	0.2
Na	AD-ICP-AES	530	16846	10834	53043	24190	2417	23111
Mg	AD-ICP-AES	140	27434	43877	6313	30625	3535	36848
Al	AD-ICP-AES	260	79775	80854	84710	75645	20011	74340
P	AD-ICP-AES	4	1051	100	1288	282	1952	240
K	AD-ICP-AES	98	679	6079	1341	221	5037	7771
Ca	AD-ICP-AES	46	60057	63307	19293	31574	28124	17369
Sc	AD-ICP-AES	0.3	28	33	29.7	28.7	7.1	23.8
Ti	AD-ICP-MS	7	11301	2716	3557	4396	775	3066
Ti	AD-ICP-AES	6	11729	2510	3400	3863	822	3374
V	AD-ICP-MS	0.8	238.9	363.4	258.2	359	235.8	250.1
V	AD-ICP-AES	3	240.7	326.4	240	309.7	220.6	249.6
Cr	AD-ICP-MS	3	88	148	50	19	33	15
Cr	AD-ICP-AES	17	85	127	44	<17	30	<17
Mn	AD-ICP-AES	1	1999	857	613	757	693	1050
Fe	AD-ICP-AES	110	87697	66575	105695	67871	66814	75460
Co	AD-ICP-AES	1	23	28	23	26	13	29
Ni	AD-ICP-AES	4	38	63	33	22	24	24
Cu	AD-ICP-AES	3	67	33	34	65	992	9
Zn	AD-ICP-AES	3	115	67	83	89	44	34
Ga	AD-ICP-MS	0.04	22.01	15.18	10.48	15.73	6.87	14.2
Rb	AD-ICP-MS	0.11	1.19	12.06	2.91	0.28	11.42	5.97

**Appendix F.II (continued) Whole-rock geochemistry, additional data**

Sample ID		348038	348041	348042	348045	348046	348048 GV-16- 13a	348051 GV-16-05
Lithology Code	LOD	Arg	Arg	ADSM	B-S1	Arg	VC	B-S1
Sr	AD-ICP-MS	0.6	322.6	190.6	75.8	88.5	40.1	82.3
Sr	AD-ICP-AES	3	347	198	78	89	39	84
Y	AD-ICP-MS	0.05	41.16	11.54	23.59	20.52	25.99	14.85
Y	AD-ICP-AES	0.6	38.9	10.6	21.2	18.3	23.4	13.6
Zr	AD-ICP-MS	6	172	23	44	36	8	36
Zr	AD-ICP-AES	7	163	23	43	34	11	37
Nb	AD-ICP-MS	0.028	6.796	0.615	1.377	0.873	0.527	0.737
M								
o	AD-ICP-AES	2	<2	<2	<2	<2	<2	<2
Ag		--	--	--	--	--	--	--
Cd	AD-ICP-AES	0.8	<0.8	0.8	0.9	<0.8	<0.8	1
In		--	--	--	--	--	--	--
Sn		--	--	--	--	--	--	--
Sb		--	--	--	--	--	--	--
Cs	AD-ICP-MS	0.013	0.034	0.125	0.045	0.019	0.13	0.064
Ba	AD-ICP-MS	0.8	44.6	54.2	23.4	10.9	84.5	75.5
Ba	AD-ICP-AES	2	43	51	23	10	81	72
La	AD-ICP-MS	0.1	11.4	1.3	4.3	1.9	3.4	2.2
Ce	AD-ICP-MS	0.12	28.56	3.14	9.31	4.75	6.29	5.75
Pr	AD-ICP-MS	0.014	4.305	0.484	1.375	0.795	1.16	0.824
Nd	AD-ICP-MS	0.06	19.14	2.44	6.44	4	5.35	3.94
Sm	AD-ICP-MS	0.026	5.771	0.795	1.867	1.552	1.69	1.329
Eu	AD-ICP-MS	0.0031	1.9609	0.4061	0.7164	0.5814	0.5861	0.4456
Gd	AD-ICP-MS	0.009	7.126	1.404	2.814	2.589	2.702	2.022
Tb	AD-ICP-MS	0.0023	1.2106	0.2855	0.5445	0.508	0.4988	0.3691
Dy	AD-ICP-MS	0.009	7.525	1.98	3.868	3.556	3.498	2.548
Ho	AD-ICP-MS	0.0025	1.6006	0.4853	0.8913	0.8515	0.889	0.5916
Er	AD-ICP-MS	0.007	4.793	1.493	2.894	2.6	2.851	1.89
Tm	AD-ICP-MS	0.0019	0.7143	0.2281	0.4525	0.395	0.4313	0.2856
Yb	AD-ICP-MS	0.009	4.431	1.598	3.014	2.63	2.691	1.906
Lu	AD-ICP-MS	0.002	0.692	0.265	0.479	0.431	0.422	0.306
Hf	AD-ICP-MS	0.14	4.3	0.76	1.32	1.29	0.24	1.21
Ta	AD-ICP-MS	0.007	0.48	0.044	0.105	0.064	0.03	0.048
Au	AD-ICP-MS	0.05	1.22	0.33	4.85	0.32	1.35	0.21
Tl		--	--	--	--	--	--	--
Pb	AD-ICP-AES	8	<8	<8	<8	<8	<8	<8
Bi	AD-ICP-MS	0.47	<0.47	<0.47	<0.47	<0.47	0.92	<0.47
Th	AD-ICP-MS	0.018	2.163	0.274	0.844	0.357	0.44	0.6
U	AD-ICP-MS	0.011	1.422	0.198	0.465	0.223	0.845	0.202

**Appendix F.II (continued) Whole-rock geochemistry, additional data**

Sample ID		348053	348054	348055	348056	348058	348059	348060
Drill Hole ID		GV-16-05						
Drill Hole Depth (m)		28.74	41.2	64.06	63.6	67.1	68	70.58
UTM easting		569136	569136	569136	569136	569136	569136	569136
UTM northing		5538729	5538729	5538729	5538729	5538729	5538729	5538729
Lithology Code	LOD	B-S1	B-S1	B-S1	B-S1	MR-IF	ASMM	VC
SiO <sub>2</sub>		--	--	--	--	--	--	--
TiO <sub>2</sub>		--	--	--	--	--	--	--
Al <sub>2</sub> O <sub>3</sub>		--	--	--	--	--	--	--
Fe <sub>2</sub> O <sub>3T</sub>		--	--	--	--	--	--	--
MnO		--	--	--	--	--	--	--
MgO		--	--	--	--	--	--	--
CaO		--	--	--	--	--	--	--
Na <sub>2</sub> O		--	--	--	--	--	--	--
K <sub>2</sub> O		--	--	--	--	--	--	--
P <sub>2</sub> O <sub>5</sub>		--	--	--	--	--	--	--
Cr <sub>2</sub> O <sub>3</sub>		--	--	--	--	--	--	--
BaO		--	--	--	--	--	--	--
LOI		--	--	--	--	--	--	--
Total		--	--	--	--	--	--	--
CO <sub>2</sub>		--	--	--	--	--	--	--
S (ppm)	AD-ICP-AES	39	59	132	58	7910	306	337
Li	AD-ICP-AES	2	5	12	13	20	2	9
Be	AD-ICP-AES	0.1	0.2	<0.1	0.1	0.2	0.3	1.9
Na	AD-ICP-AES	530	3554	18188	21218	22317	2497	12001
Mg	AD-ICP-AES	140	9972	28131	38962	37718	4283	17993
Al	AD-ICP-AES	260	74782	79562	77852	76866	9406	49760
P	AD-ICP-AES	4	218	154	167	183	>7000	810
K	AD-ICP-AES	98	236	146	181	2133	130	9739
Ca	AD-ICP-AES	46	104739	77625	41429	58025	27684	37223
Sc	AD-ICP-AES	0.3	28.2	32.1	31.4	31	1.1	9.1
Ti	AD-ICP-MS	7	2968	2341	2894	3210	418	2506
Ti	AD-ICP-AES	6	3146	2535	2841	3405	457	2704
V	AD-ICP-MS	0.8	323.1	269.1	309.3	338.5	145.2	79.8
V	AD-ICP-AES	3	307.5	267.3	284	327.1	155.3	84.9
Cr	AD-ICP-MS	3	14	27	40	9	16	31
Cr	AD-ICP-AES	17	<17	26	37	<17	<17	34
Mn	AD-ICP-AES	1	278	849	752	1464	3546	>13000
Fe	AD-ICP-AES	110	42421	55082	60408	77778	>320000	103924
Co	AD-ICP-AES	1	13	27	29	40	39	24
Ni	AD-ICP-AES	4	13	34	34	19	31	52
Cu	AD-ICP-AES	3	22	116	81	89	183	318
Zn	AD-ICP-AES	3	45	71	79	102	103	104
Ga	AD-ICP-MS	0.04	21.23	15.46	15.12	15.74	2.65	12.31
Rb	AD-ICP-MS	0.11	0.58	0.25	0.36	6.11	0.6	31.82
								21.29

**Appendix F.II (continued) Whole-rock geochemistry, additional data**

Sample ID		348053	348054	348055	348056	348058	348059	348060
Drill Hole ID		GV-16-05						
Drill Hole Depth (m)		28.74	41.2	64.06	63.6	67.1	68	70.58
UTM easting		569136	569136	569136	569136	569136	569136	569136
UTM northing		5538729	5538729	5538729	5538729	5538729	5538729	5538729
Lithology Code	LOD	B-S1	B-S1	B-S1	B-S1	MR-IF	ASMM	VC
Sr	AD-ICP-MS	0.6	87.5	219.8	101.6	73.7	45.9	57.7
Sr	AD-ICP-AES	3	90	229	98	75	38	57
Y	AD-ICP-MS	0.05	14.38	14.97	15.35	18.51	29.81	25.25
Y	AD-ICP-AES	0.6	13.1	13.6	13.2	17.5	27.8	22.6
Zr	AD-ICP-MS	6	27	23	27	26	<6	85
Zr	AD-ICP-AES	7	27	23	26	27	12	85
Nb	AD-ICP-MS	0.028	0.66	0.557	0.623	0.61	1.156	6.457
M								4.199
o	AD-ICP-AES	2	<2	2	<2	<2	<2	<2
Ag		--	--	--	--	--	--	--
Cd	AD-ICP-AES	0.8	1.1	0.8	<0.8	0.9	<0.8	1
In		--	--	--	--	--	--	--
Sn		--	--	--	--	--	--	--
Sb		--	--	--	--	--	--	--
Cs	AD-ICP-MS	0.013	0.033	0.032	0.039	0.135	<0.013	0.214
Ba	AD-ICP-MS	0.8	5.2	5.7	13.4	32.9	3.6	212.3
Ba	AD-ICP-AES	2	5	6	12	32	8	199
La	AD-ICP-MS	0.1	1.7	1.5	1.4	1.4	15.7	31.8
Ce	AD-ICP-MS	0.12	3.93	3.31	3.31	3.41	24.28	107.78
Pr	AD-ICP-MS	0.014	0.61	0.524	0.547	0.552	5.075	8.522
Nd	AD-ICP-MS	0.06	3.15	2.51	2.68	2.84	20.53	31
Sm	AD-ICP-MS	0.026	1.12	1.03	1.016	1.133	5.534	6.895
Eu	AD-ICP-MS	0.0031	0.4819	0.4482	0.4293	0.5289	1.5746	1.6881
Gd	AD-ICP-MS	0.009	1.882	1.744	1.832	2.19	6.541	6.558
Tb	AD-ICP-MS	0.0023	0.3499	0.3477	0.3493	0.4507	1.1107	1.0453
Dy	AD-ICP-MS	0.009	2.446	2.455	2.684	3.283	6.8	6.04
Ho	AD-ICP-MS	0.0025	0.5699	0.6017	0.6151	0.7845	1.3884	1.2131
Er	AD-ICP-MS	0.007	1.868	1.961	1.984	2.524	3.923	3.421
Tm	AD-ICP-MS	0.0019	0.2748	0.2972	0.3067	0.383	0.5454	0.4833
Yb	AD-ICP-MS	0.009	1.758	1.976	2.047	2.622	3.206	2.941
Lu	AD-ICP-MS	0.002	0.293	0.324	0.356	0.422	0.462	0.424
Hf	AD-ICP-MS	0.14	0.95	0.82	0.91	0.96	<0.14	2.3
Ta	AD-ICP-MS	0.007	0.038	0.048	0.047	0.05	0.056	0.206
Au	AD-ICP-MS	0.05	0.33	0.23	0.34	1.21	2.52	5.2
Tl		--	--	--	--	--	--	--
Pb	AD-ICP-AES	8	<8	<8	<8	<8	40	26
Bi	AD-ICP-MS	0.47	<0.47	<0.47	<0.47	<0.47	<0.47	0.79
Th	AD-ICP-MS	0.018	0.3	0.305	0.291	0.293	0.84	7.41
U	AD-ICP-MS	0.011	0.283	0.253	0.222	0.277	1.73	1.285
								1.616

## Appendix F.II Whole-rock geochemistry, additional data

Sample ID		348061	348062	348063	348064	348065	348066	348068
Drill Hole ID		GV-16-05						
Drill Hole Depth (m)		76.2	80.77	85.8	94.11	101.86	111.22	132.75
UTM easting		569136	569136	569136	569136	569136	569136	569136
UTM northing		5538729	5538729	5538729	5538729	5538729	5538729	5538729
Lithology Code	LOD	VC	ASMM	Arg	VC	VC	VC	VC
SiO <sub>2</sub>		--	--	--	--	--	--	--
TiO <sub>2</sub>		--	--	--	--	--	--	--
Al <sub>2</sub> O <sub>3</sub>		--	--	--	--	--	--	--
Fe <sub>2</sub> O <sub>3T</sub>		--	--	--	--	--	--	--
MnO		--	--	--	--	--	--	--
MgO		--	--	--	--	--	--	--
CaO		--	--	--	--	--	--	--
Na <sub>2</sub> O		--	--	--	--	--	--	--
K <sub>2</sub> O		--	--	--	--	--	--	--
P <sub>2</sub> O <sub>5</sub>		--	--	--	--	--	--	--
Cr <sub>2</sub> O <sub>3</sub>		--	--	--	--	--	--	--
BaO		--	--	--	--	--	--	--
LOI		--	--	--	--	--	--	--
Total		--	--	--	--	--	--	--
CO <sub>2</sub>		--	--	--	--	--	--	--
S (ppm)	AD-ICP-AES	39	172	<39	638	<39	157	<39
Li	AD-ICP-AES	2	12	5	12	18	13	15
Be	AD-ICP-AES	0.1	0.8	1.9	1.1	0.8	1.2	0.6
Na	AD-ICP-AES	530	44202	13806	33268	27834	9844	15033
Mg	AD-ICP-AES	140	30497	16189	22274	39560	27984	34599
Al	AD-ICP-AES	260	82617	57958	85383	80266	74222	87534
P	AD-ICP-AES	4	613	899	1254	684	978	245
K	AD-ICP-AES	98	885	8067	1909	1478	4636	1459
Ca	AD-ICP-AES	46	30368	37971	39777	42907	50159	76628
Sc	AD-ICP-AES	0.3	17.7	11.6	23.7	28.2	28.3	25.7
Ti	AD-ICP-MS	7	4826	3018	9147	7523	13030	2639
Ti	AD-ICP-AES	6	4812	3172	10226	8073	12116	2795
V	AD-ICP-MS	0.8	126.4	98.8	175.3	186.1	288.9	163.9
V	AD-ICP-AES	3	117	102.9	184.6	185.2	259.1	161.5
Cr	AD-ICP-MS	3	321	100	31	73	108	207
Cr	AD-ICP-AES	17	290	97	31	70	99	196
Mn	AD-ICP-AES	1	1236	>13000	1856	1148	4077	918
Fe	AD-ICP-AES	110	44915	147111	83265	63207	82787	43349
Co	AD-ICP-AES	1	22	29	18	23	22	23
Ni	AD-ICP-AES	4	129	67	18	36	37	55
Cu	AD-ICP-AES	3	55	14	37	47	67	29
Zn	AD-ICP-AES	3	68	168	115	75	102	52
Ga	AD-ICP-MS	0.04	14.81	13.84	22.12	16.13	21.93	17.35
Rb	AD-ICP-MS	0.11	2.35	24.27	5.66	2.9	14.55	3.77

**Appendix F.II (continued) Whole-rock geochemistry, additional data**

Sample ID		348061	348062	348063	348064	348065	348066	348068
Drill Hole ID		GV-16-05						
Drill Hole Depth (m)		76.2	80.77	85.8	94.11	101.86	111.22	132.75
UTM easting		569136	569136	569136	569136	569136	569136	569136
UTM northing		5538729	5538729	5538729	5538729	5538729	5538729	5538729
Lithology Code	LOD	VC	ASMM	Arg	VC	VC	VC	VC
Sr	AD-ICP-MS	0.6	196.8	168.1	174.8	253.6	455.9	217.9
Sr	AD-ICP-AES	3	190	183	188	262	419	222
Y	AD-ICP-MS	0.05	27.26	27.76	42.97	25.53	39.03	9.65
Y	AD-ICP-AES	0.6	23.7	27.2	40.7	23.6	35.1	8.4
Zr	AD-ICP-MS	6	153	97	187	122	162	63
Zr	AD-ICP-AES	7	140	102	182	117	147	60
Nb	AD-ICP-MS	0.028	6.801	7.599	6.285	3.996	6.141	3.27
M								
o	AD-ICP-AES	2	<2	<2	<2	<2	<2	<2
Ag		--	--	--	--	--	--	--
Cd	AD-ICP-AES	0.8	0.9	<0.8	0.9	0.9	0.9	0.9
In		--	--	--	--	--	--	--
Sn		--	--	--	--	--	--	--
Sb		--	--	--	--	--	--	--
Cs	AD-ICP-MS	0.013	0.03	0.23	0.066	0.037	0.157	0.026
Ba	AD-ICP-MS	0.8	21.5	166.2	57.4	30.3	365.1	20.6
Ba	AD-ICP-AES	2	21	162	56	29	336	19
La	AD-ICP-MS	0.1	13.2	32.6	10.7	8.1	11.4	6.5
Ce	AD-ICP-MS	0.12	29.39	115.93	28.96	20.24	29.19	13.66
Pr	AD-ICP-MS	0.014	3.796	9.655	4.436	2.976	4.173	1.653
Nd	AD-ICP-MS	0.06	15.74	36.37	21.08	13.12	19.06	6.51
Sm	AD-ICP-MS	0.026	3.815	8.023	6.281	3.72	5.669	1.61
Eu	AD-ICP-MS	0.0031	1.2068	1.863	2.118	1.2226	1.9613	0.5906
Gd	AD-ICP-MS	0.009	4.321	7.871	7.998	4.586	6.94	1.725
Tb	AD-ICP-MS	0.0023	0.7082	1.2176	1.3441	0.772	1.1773	0.2806
Dy	AD-ICP-MS	0.009	4.515	6.857	8.174	4.857	7.105	1.759
Ho	AD-ICP-MS	0.0025	0.9966	1.322	1.7724	1.0401	1.5484	0.3647
Er	AD-ICP-MS	0.007	2.982	3.789	5.284	3.119	4.514	1.155
Tm	AD-ICP-MS	0.0019	0.4264	0.5381	0.7474	0.4368	0.672	0.1592
Yb	AD-ICP-MS	0.009	2.775	3.334	4.852	2.817	4.189	1.071
Lu	AD-ICP-MS	0.002	0.427	0.504	0.748	0.414	0.645	0.17
Hf	AD-ICP-MS	0.14	3.61	2.67	4.87	3.15	4.04	1.66
Ta	AD-ICP-MS	0.007	0.307	0.293	0.402	0.246	0.425	0.216
Au	AD-ICP-MS	0.05	0.7	3.51	1.88	0.67	1.56	0.81
Tl		--	--	--	--	--	--	--
Pb	AD-ICP-AES	8	16	67	<8	<8	22	<8
Bi	AD-ICP-MS	0.47	<0.47	0.65	<0.47	<0.47	<0.47	<0.47
Th	AD-ICP-MS	0.018	3.506	8.585	1.671	1.867	2.163	2.064
U	AD-ICP-MS	0.011	2.633	1.698	1.075	1.19	1.388	1.192
								1.335

## Appendix F.II (continued) Whole-rock geochemistry, additional data

Sample ID		348070	348071	348072	348073	348075	348077	348078	
Drill Hole ID		GV-16-05	GV-16-05	GV-16-05	GV-16-05	GV-16-05	GV-16-05	GV-16-12	
Drill Hole Depth (m)		146.78	156.5	162.6	167.4	174.17	200.4	5.8	
UTM easting		569136	569136	569136	569136	569136	569136	567665	
UTM northing		5538729	5538729	5538729	5538729	5538729	5538729	5538175	
Lithology Code	LOD	VC	VC	B-S1	B-S1	B-S1	B-S1	B-S1	
SiO <sub>2</sub>		--	--	--	--	--	--	--	
TiO <sub>2</sub>		--	--	--	--	--	--	--	
Al <sub>2</sub> O <sub>3</sub>		--	--	--	--	--	--	--	
Fe <sub>2</sub> O <sub>3T</sub>		--	--	--	--	--	--	--	
MnO		--	--	--	--	--	--	--	
MgO		--	--	--	--	--	--	--	
CaO		--	--	--	--	--	--	--	
Na <sub>2</sub> O		--	--	--	--	--	--	--	
K <sub>2</sub> O		--	--	--	--	--	--	--	
P <sub>2</sub> O <sub>5</sub>		--	--	--	--	--	--	--	
Cr <sub>2</sub> O <sub>3</sub>		--	--	--	--	--	--	--	
BaO		--	--	--	--	--	--	--	
LOI		--	--	--	--	--	--	--	
Total		--	--	--	--	--	--	--	
CO <sub>2</sub>		--	--	--	--	--	--	--	
S (ppm)	AD-ICP-AES	39	2882	1289	2945	639	64	89	92
Li	AD-ICP-AES	2	17	24	20	4	20	14	7
Be	AD-ICP-AES	0.1	0.6	0.4	0.1	0.2	0.1	0.1	0.4
Na	AD-ICP-AES	530	17980	24097	13617	6433	25882	26530	31149
Mg	AD-ICP-AES	140	53604	47767	44368	33250	41956	47852	12951
Al	AD-ICP-AES	260	74106	90310	72299	68651	81510	79700	109050
P	AD-ICP-AES	4	396	574	141	60	193	104	290
K	AD-ICP-AES	98	6878	1957	11694	23870	878	314	15446
Ca	AD-ICP-AES	46	65930	54057	49299	76344	47035	49172	55759
Sc	AD-ICP-AES	0.3	28.8	27.3	28.9	23.8	32	32.2	36.1
Ti	AD-ICP-MS	7	3551	7412	2541	2276	2939	2353	2521
Ti	AD-ICP-AES	6	3583	8222	2616	2315	3066	2351	4231
V	AD-ICP-MS	0.8	186.8	192.4	239.1	211.7	263.5	279.7	247.4
V	AD-ICP-AES	3	175.6	197.9	228.6	200	255.8	250.6	228.5
Cr	AD-ICP-MS	3	1147	116	107	105	37	117	156
Cr	AD-ICP-AES	17	1043	113	101	93	34	104	96
Mn	AD-ICP-AES	1	946	1208	708	1018	998	911	1177
Fe	AD-ICP-AES	110	53482	71597	55264	38537	66106	62695	74928
Co	AD-ICP-AES	1	32	35	28	15	29	30	27
Ni	AD-ICP-AES	4	260	62	57	50	35	54	50
Cu	AD-ICP-AES	3	59	53	74	7	95	70	48
Zn	AD-ICP-AES	3	71	87	60	45	81	71	95
Ga	AD-ICP-MS	0.04	14.77	16.26	12.57	16.76	11.23	13.49	14.66
Rb	AD-ICP-MS	0.11	13.62	4.04	24.63	46.86	1.65	0.32	17.37

**Appendix F.II (continued) Whole-rock geochemistry, additional data**

Sample ID		348070	348071	348072	348073	348075	348077	348078
Drill Hole ID		GV-16-05	GV-16-05	GV-16-05	GV-16-05	GV-16-05	GV-16-05	GV-16-12
Drill Hole Depth (m)		146.78	156.5	162.6	167.4	174.17	200.4	5.8
UTM easting		569136	569136	569136	569136	569136	569136	567665
UTM northing		5538729	5538729	5538729	5538729	5538729	5538729	5538175
Lithology Code	LOD	VC	VC	B-S1	B-S1	B-S1	B-S1	B-S1
Sr	AD-ICP-MS	0.6	155.6	134.5	89.5	171.5	61.9	85.8
Sr	AD-ICP-AES	3	160	143	92	168	66	81
Y	AD-ICP-MS	0.05	13.15	23.76	13.89	12.92	14.89	12.9
Y	AD-ICP-AES	0.6	11.8	22.2	12.7	10.7	13.1	11.1
Zr	AD-ICP-MS	6	58	80	19	17	30	20
Zr	AD-ICP-AES	7	56	79	19	16	30	20
Nb	AD-ICP-MS	0.028	2.74	3.882	0.38	0.359	0.816	0.449
M								
o	AD-ICP-AES	2	<2	<2	<2	<2	<2	<2
Ag		--	--	--	--	--	--	--
Cd	AD-ICP-AES	0.8	1.3	0.9	1.2	0.9	1.1	<0.8
In		--	--	--	--	--	--	--
Sn		--	--	--	--	--	--	--
Sb		--	--	--	--	--	--	--
Cs	AD-ICP-MS	0.013	0.09	0.19	0.379	0.629	0.094	<0.013
Ba	AD-ICP-MS	0.8	149.7	26.3	97	137.8	9.4	4.6
Ba	AD-ICP-AES	2	142	26	89	123	9	5
La	AD-ICP-MS	0.1	6.5	4.6	1	1.1	1.3	1
Ce	AD-ICP-MS	0.12	14.5	11.9	2.41	2.7	3.4	2.38
Pr	AD-ICP-MS	0.014	1.874	1.892	0.399	0.427	0.57	0.383
Nd	AD-ICP-MS	0.06	7.64	9.63	2.33	2.29	2.73	1.89
Sm	AD-ICP-MS	0.026	1.893	3.108	0.939	0.886	1.088	0.781
Eu	AD-ICP-MS	0.0031	0.6801	1.1653	0.3887	0.4052	0.4031	0.3533
Gd	AD-ICP-MS	0.009	2.231	4.01	1.594	1.556	1.694	1.328
Tb	AD-ICP-MS	0.0023	0.3484	0.6896	0.336	0.296	0.347	0.2772
Dy	AD-ICP-MS	0.009	2.39	4.454	2.325	2.155	2.433	2.039
Ho	AD-ICP-MS	0.0025	0.5013	0.9624	0.5605	0.4902	0.5885	0.4684
Er	AD-ICP-MS	0.007	1.556	2.817	1.727	1.514	1.872	1.429
Tm	AD-ICP-MS	0.0019	0.2382	0.3966	0.2538	0.2362	0.2878	0.2287
Yb	AD-ICP-MS	0.009	1.488	2.535	1.692	1.453	1.934	1.523
Lu	AD-ICP-MS	0.002	0.235	0.397	0.272	0.237	0.308	0.253
Hf	AD-ICP-MS	0.14	1.66	2.17	0.69	0.64	0.92	0.67
Ta	AD-ICP-MS	0.007	0.182	0.217	0.025	0.019	0.059	0.03
Au	AD-ICP-MS	0.05	0.8	1.65	3.66	8.44	0.68	0.18
Tl		--	--	--	--	--	--	--
Pb	AD-ICP-AES	8	<8	<8	<8	<8	<8	<8
Bi	AD-ICP-MS	0.47	<0.47	<0.47	<0.47	<0.47	<0.47	<0.47
Th	AD-ICP-MS	0.018	1.762	0.411	0.147	0.156	0.288	0.182
U	AD-ICP-MS	0.011	1.211	0.189	0.184	0.264	0.157	0.089
								0.207

**Appendix F.II (continued) Whole-rock geochemistry, additional data**

Sample ID		348079	348080	348082	348083	348085	348086	348090
Drill Hole ID		GV-16-12						
Drill Hole Depth (m)		18.38	22	35.8	39.3	44.11	46.9	49.15
UTM easting		567665	567665	567665	567665	567665	567665	567665
UTM northing		5538175	5538175	5538175	5538175	5538175	5538175	5538175
Lithology Code	LOD	B-S1	B-S1	B-S1	B-S1	B-S2	MR-IF	B-S1
SiO <sub>2</sub>		--	--	--	--	--	--	--
TiO <sub>2</sub>		--	--	--	--	--	--	--
Al <sub>2</sub> O <sub>3</sub>		--	--	--	--	--	--	--
Fe <sub>2</sub> O <sub>3T</sub>		--	--	--	--	--	--	--
MnO		--	--	--	--	--	--	--
MgO		--	--	--	--	--	--	--
CaO		--	--	--	--	--	--	--
Na <sub>2</sub> O		--	--	--	--	--	--	--
K <sub>2</sub> O		--	--	--	--	--	--	--
P <sub>2</sub> O <sub>5</sub>		--	--	--	--	--	--	--
Cr <sub>2</sub> O <sub>3</sub>		--	--	--	--	--	--	--
BaO		--	--	--	--	--	--	--
LOI		--	--	--	--	--	--	--
Total		--	--	--	--	--	--	--
CO <sub>2</sub>		--	--	--	--	--	--	--
S (ppm)	AD-ICP-AES	39	73	<39	96	1733	852	1147
Li	AD-ICP-AES	2	14	24	10	18	16	14
Be	AD-ICP-AES	0.1	0.1	1.1	0.2	0.3	0.2	0.3
Na	AD-ICP-AES	530	16579	12234	22635	19680	16310	10699
Mg	AD-ICP-AES	140	34050	36709	28746	43230	37059	30524
Al	AD-ICP-AES	260	64690	78403	74948	86268	70166	79395
P	AD-ICP-AES	4	132	2241	380	197	216	229
K	AD-ICP-AES	98	227	9506	242	323	5860	247
Ca	AD-ICP-AES	46	101687	56138	49276	42948	32664	55480
Sc	AD-ICP-AES	0.3	27.2	24.1	23.2	32.6	25.6	30.8
Ti	AD-ICP-MS	7	3976	3941	4365	2657	18376	1187
Ti	AD-ICP-AES	6	2418	18202	2475	4339	3401	4322
V	AD-ICP-MS	0.8	276.1	275.2	248.4	195.2	302.9	260.2
V	AD-ICP-AES	3	172.9	288.1	222.4	334.8	260.5	381.2
Cr	AD-ICP-MS	3	86	111	114	306	64	38
Cr	AD-ICP-AES	17	250	57	<17	<17	<17	<17
Mn	AD-ICP-AES	1	1095	1934	755	514	667	1049
Fe	AD-ICP-AES	110	42379	95591	53654	74978	62368	81715
Co	AD-ICP-AES	1	25	33	23	24	21	32
Ni	AD-ICP-AES	4	60	57	33	24	20	21
Cu	AD-ICP-AES	3	46	65	88	82	72	69
Zn	AD-ICP-AES	3	65	119	59	92	75	93
Ga	AD-ICP-MS	0.04	15.75	14.95	21.21	10.79	21.9	6.85
Rb	AD-ICP-MS	0.11	0.46	9.38	46.13	0.5	21.57	0.55

**Appendix F.II (continued) Whole-rock geochemistry, additional data**

Sample ID		348079	348080	348082	348083	348085	348086	348090
Drill Hole ID		GV-16-12	GV-16-12	GV-16-12	GV-16-12	GV-16-12	GV-16-12	GV-16-12
Drill Hole Depth (m)		18.38	22	35.8	39.3	44.11	46.9	49.15
UTM easting		567665	567665	567665	567665	567665	567665	567665
UTM northing		5538175	5538175	5538175	5538175	5538175	5538175	5538175
Lithology Code	LOD	B-S1	B-S1	B-S1	B-S1	B-S2	MR-IF	B-S1
Sr	AD-ICP-MS	0.6	108.1	130.8	157.8	154.9	153.4	26.4
Sr	AD-ICP-AES	3	141	152	216	136	75	328
Y	AD-ICP-MS	0.05	18.31	18.51	19.43	11.28	32.56	32.83
Y	AD-ICP-AES	0.6	9.6	30.1	12.2	17.9	15.4	17.6
Zr	AD-ICP-MS	6	35	34	54	23	249	29
Zr	AD-ICP-AES	7	21	234	38	37	29	36
Nb	AD-ICP-MS	0.028	0.853	0.749	1.414	0.445	17.463	3.353
M	o	AD-ICP-AES	2	<2	<2	<2	<2	<2
Ag		--	--	--	--	--	--	--
Cd	AD-ICP-AES	0.8	1	<0.8	<0.8	<0.8	1.1	<0.8
In		--	--	--	--	--	--	--
Sn		--	--	--	--	--	--	--
Sb		--	--	--	--	--	--	--
Cs	AD-ICP-MS	0.013	<0.013	0.075	0.309	<0.013	0.149	<0.013
Ba	AD-ICP-MS	0.8	14.3	36	291.2	100	207	7.8
Ba	AD-ICP-AES	2	93	195	13	19	126	11
La	AD-ICP-MS	0.1	1.8	1.7	3.3	1.2	19.4	13.1
Ce	AD-ICP-MS	0.12	4.54	4.36	7.74	2.83	47	23.36
Pr	AD-ICP-MS	0.014	0.74	0.712	1.082	0.437	6.529	4.104
Nd	AD-ICP-MS	0.06	3.84	3.92	5.36	2.26	28.65	17.52
Sm	AD-ICP-MS	0.026	1.4	1.581	1.837	0.832	6.362	4.642
Eu	AD-ICP-MS	0.0031	0.5535	0.619	0.7111	0.3585	2.3464	0.9473
Gd	AD-ICP-MS	0.009	2.149	2.382	2.499	1.404	6.608	5.499
Tb	AD-ICP-MS	0.0023	0.412	0.4223	0.4558	0.2336	1.0092	0.9836
Dy	AD-ICP-MS	0.009	2.666	3.046	3.269	1.606	6.06	6.344
Ho	AD-ICP-MS	0.0025	0.6438	0.6861	0.6928	0.3771	1.1986	1.335
Er	AD-ICP-MS	0.007	1.903	2.046	2.084	1.167	3.248	3.85
Tm	AD-ICP-MS	0.0019	0.288	0.2967	0.3244	0.1871	0.4347	0.5741
Yb	AD-ICP-MS	0.009	1.875	1.917	2.073	1.108	2.83	3.388
Lu	AD-ICP-MS	0.002	0.295	0.297	0.299	0.172	0.39	0.463
Hf	AD-ICP-MS	0.14	1.03	1.08	1.51	0.67	4.98	0.61
Ta	AD-ICP-MS	0.007	0.054	0.052	0.091	0.028	1.023	0.129
Au	AD-ICP-MS	0.05	0.23	0.32	0.68	0.28	1.66	4.49
Tl		--	--	--	--	--	--	--
Pb	AD-ICP-AES	8	<8	8	<8	<8	<8	<8
Bi	AD-ICP-MS	0.47	<0.47	<0.47	<0.47	<0.47	<0.47	<0.47
Th	AD-ICP-MS	0.018	0.396	0.32	0.866	0.244	0.942	1.279
U	AD-ICP-MS	0.011	0.34	0.811	0.353	0.099	0.417	1.578
								0.374

**Appendix F.II (continued) Whole-rock geochemistry, additional data**

Sample ID		348091	348092	348093	348094	348095	348096	348097	
Drill Hole ID		GV-16-12							
Drill Hole Depth (m)		63.18	66.02	71.6	83.5	89	93.1	102.86	
UTM easting		567665	567665	567665	567665	567665	567665	567665	
UTM northing		5538175	5538175	5538175	5538175	5538175	5538175	5538175	
Lithology Code	LOD	B-S1	VC	B-S1	B-S1	VC	VC	B-S1	
SiO <sub>2</sub>		--	--	--	--	--	--	--	
TiO <sub>2</sub>		--	--	--	--	--	--	--	
Al <sub>2</sub> O <sub>3</sub>		--	--	--	--	--	--	--	
Fe <sub>2</sub> O <sub>3T</sub>		--	--	--	--	--	--	--	
MnO		--	--	--	--	--	--	--	
MgO		--	--	--	--	--	--	--	
CaO		--	--	--	--	--	--	--	
Na <sub>2</sub> O		--	--	--	--	--	--	--	
K <sub>2</sub> O		--	--	--	--	--	--	--	
P <sub>2</sub> O <sub>5</sub>		--	--	--	--	--	--	--	
Cr <sub>2</sub> O <sub>3</sub>		--	--	--	--	--	--	--	
BaO		--	--	--	--	--	--	--	
LOI		--	--	--	--	--	--	--	
Total		--	--	--	--	--	--	--	
CO <sub>2</sub>		--	--	--	--	--	--	--	
S (ppm)	AD-ICP-AES	39	2526	6384	581	1823	1340	1198	8348
Li	AD-ICP-AES	2	28	29	25	19	14	27	17
Be	AD-ICP-AES	0.1	0.2	0.3	0.1	0.2	0.3	0.1	0.2
Na	AD-ICP-AES	530	15749	8655	6327	22980	11233	11250	34777
Mg	AD-ICP-AES	140	40695	45505	49217	32278	28714	44280	46367
Al	AD-ICP-AES	260	85782	86247	73876	79815	75826	78597	89798
P	AD-ICP-AES	4	329	404	89	280	178	98	85
K	AD-ICP-AES	98	5877	6519	7799	453	13572	753	128
Ca	AD-ICP-AES	46	47758	38179	68240	29357	72877	49494	24883
Sc	AD-ICP-AES	0.3	29.7	28.7	31.9	29.6	29.3	30.9	33.5
Ti	AD-ICP-MS	7	4629	3561	3601	2388	4687	5776	1860
Ti	AD-ICP-AES	6	4621	5384	1769	4581	2909	3229	2995
V	AD-ICP-MS	0.8	>370	293.2	356	203	286.9	>370	249.1
V	AD-ICP-AES	3	273.2	358.4	231.7	340.1	251.1	319.6	263
Cr	AD-ICP-MS	3	11	9	15	74	19	3	484
Cr	AD-ICP-AES	17	18	<17	435	19	92	22	81
Mn	AD-ICP-AES	1	402	387	721	617	854	394	534
Fe	AD-ICP-AES	110	79139	85374	60103	75764	45104	69532	66453
Co	AD-ICP-AES	1	19	25	33	27	23	30	43
Ni	AD-ICP-AES	4	17	18	106	14	38	24	59
Cu	AD-ICP-AES	3	66	99	42	84	57	46	109
Zn	AD-ICP-AES	3	106	110	62	109	60	95	82
Ga	AD-ICP-MS	0.04	17.85	14.68	17.94	14.58	16.72	18.4	12.73
Rb	AD-ICP-MS	0.11	0.45	11.91	0.3	0.36	7.89	8.36	10.87

**Appendix F.II (continued) Whole-rock geochemistry, additional data**

Sample ID		348091	348092	348093	348094	348095	348096	348097
Drill Hole ID		GV-16-12						
Drill Hole Depth (m)		63.18	66.02	71.6	83.5	89	93.1	102.86
UTM easting		567665	567665	567665	567665	567665	567665	567665
UTM northing		5538175	5538175	5538175	5538175	5538175	5538175	5538175
Lithology Code	LOD	B-S1	VC	B-S1	B-S1	VC	VC	B-S1
Sr	AD-ICP-MS	0.6	140.8	80.1	320.1	248	69.5	123.7
Sr	AD-ICP-AES	3	69	111	127	103	109	51
Y	AD-ICP-MS	0.05	20.48	17.95	18.61	11.87	25.48	28.72
Y	AD-ICP-AES	0.6	24.2	26.6	8.3	19.8	15.1	14.7
Zr	AD-ICP-MS	6	39	31	33	45	49	49
Zr	AD-ICP-AES	7	45	48	14	40	25	26
Nb	AD-ICP-MS	0.028	0.887	0.69	0.728	0.663	1.059	1.191
M								
o	AD-ICP-AES	2	<2	<2	<2	<2	<2	<2
Ag		--	--	--	--	--	--	--
Cd	AD-ICP-AES	0.8	0.8	0.8	0.9	<0.8	0.8	0.8
In		--	--	--	--	--	--	--
Sn		--	--	--	--	--	--	--
Sb		--	--	--	--	--	--	--
Cs	AD-ICP-MS	0.013	<0.013	0.155	<0.013	0.015	0.162	0.141
Ba	AD-ICP-MS	0.8	20.6	140.3	10.3	15.7	65.8	84.9
Ba	AD-ICP-AES	2	67	80	73	12	75	36
La	AD-ICP-MS	0.1	1.9	1.6	1.8	4.3	2.3	2.7
Ce	AD-ICP-MS	0.12	5.1	4.19	4.76	9.18	5.63	6.79
Pr	AD-ICP-MS	0.014	0.816	0.649	0.734	1.162	0.905	1.037
Nd	AD-ICP-MS	0.06	4.43	3.46	4.18	5.63	4.72	5.33
Sm	AD-ICP-MS	0.026	1.734	1.187	1.611	1.58	1.877	1.796
Eu	AD-ICP-MS	0.0031	0.69	0.4864	0.6307	0.4845	0.7165	0.7457
Gd	AD-ICP-MS	0.009	2.642	2.186	2.555	1.636	2.965	3.096
Tb	AD-ICP-MS	0.0023	0.5001	0.4002	0.4952	0.262	0.5815	0.5988
Dy	AD-ICP-MS	0.009	3.346	2.931	3.553	1.841	4.184	4.144
Ho	AD-ICP-MS	0.0025	0.737	0.6203	0.8092	0.3857	0.932	0.9543
Er	AD-ICP-MS	0.007	2.313	2.006	2.613	1.159	2.826	3.093
Tm	AD-ICP-MS	0.0019	0.3537	0.2951	0.3831	0.1734	0.462	0.4834
Yb	AD-ICP-MS	0.009	2.262	2	2.588	1.183	3.043	3.062
Lu	AD-ICP-MS	0.002	0.355	0.305	0.41	0.171	0.481	0.488
Hf	AD-ICP-MS	0.14	1.21	0.93	1.24	1.15	1.52	1.53
Ta	AD-ICP-MS	0.007	0.055	0.045	0.058	0.038	0.072	0.072
Au	AD-ICP-MS	0.05	0.47	0.89	0.28	0.13	17.75	13.26
Tl		--	--	--	--	--	--	--
Pb	AD-ICP-AES	8	<8	<8	<8	<8	<8	<8
Bi	AD-ICP-MS	0.47	<0.47	<0.47	<0.47	<0.47	<0.47	<0.47
Th	AD-ICP-MS	0.018	0.325	0.26	0.389	0.928	0.377	0.415
U	AD-ICP-MS	0.011	0.428	0.337	0.206	0.354	0.339	0.758

## Appendix F.II Whole-rock geochemistry, additional data

Sample ID		348099	348100	348901	348902	348904	348905	348906	
Drill Hole ID		GV-16-12	GV-16-13a	GV-16-01	GV-16-01	GV-16-01	GV-16-01	GV-16-01	
Drill Hole Depth (m)		118.96	10	109.5	118.7	121.4	124.7	132.4	
UTM easting		567665	567404	567749	567749	567749	567749	567749	
UTM northing		5538175	5537944	5538379	5538379	5538379	5538379	5538379	
Lithology Code	LOD	B-S1	VC	B-S1	MR-IF	ADSM	ADSM	B-S1	
SiO <sub>2</sub>		--	--	--	--	--	--	--	
TiO <sub>2</sub>		--	--	--	--	--	--	--	
Al <sub>2</sub> O <sub>3</sub>		--	--	--	--	--	--	--	
Fe <sub>2</sub> O <sub>3T</sub>		--	--	--	--	--	--	--	
MnO		--	--	--	--	--	--	--	
MgO		--	--	--	--	--	--	--	
CaO		--	--	--	--	--	--	--	
Na <sub>2</sub> O		--	--	--	--	--	--	--	
K <sub>2</sub> O		--	--	--	--	--	--	--	
P <sub>2</sub> O <sub>5</sub>		--	--	--	--	--	--	--	
Cr <sub>2</sub> O <sub>3</sub>		--	--	--	--	--	--	--	
BaO		--	--	--	--	--	--	--	
LOI		--	--	--	--	--	--	--	
Total		--	--	--	--	--	--	--	
CO <sub>2</sub>		--	--	--	--	--	--	--	
S (ppm)	AD-ICP-AES	39	144	117	43	307	86	1438	10940
Li	AD-ICP-AES	2	30	6	19	6	3	11	13
Be	AD-ICP-AES	0.1	0.3	0.5	0.1	0.9	0.5	1.1	0.1
Na	AD-ICP-AES	530	24008	21194	9720	<530	27803	19251	23605
Mg	AD-ICP-AES	140	34755	41125	30881	11269	9741	32126	32500
Al	AD-ICP-AES	260	86942	77894	76254	23647	96189	74442	70884
P	AD-ICP-AES	4	106	682	142	>7000	377	2435	249
K	AD-ICP-AES	98	3117	2902	5677	3631	24668	7043	5826
Ca	AD-ICP-AES	46	41878	70346	78384	35064	33561	52650	35744
Sc	AD-ICP-AES	0.3	32.1	39.6	29.5	4.4	34.5	27.4	26.4
Ti	AD-ICP-MS	7	4960	8012	2287	889	3944	21653	3300
Ti	AD-ICP-AES	6	3297	8498	2090	1124	3738	22488	3278
V	AD-ICP-MS	0.8	>370	284.3	215.4	218	264.5	>370	218.6
V	AD-ICP-AES	3	301.8	280	198.5	287.2	234.8	359.4	203.8
Cr	AD-ICP-MS	3	21	207	248	107	54	67	20
Cr	AD-ICP-AES	17	22	197	217	136	46	63	19
Mn	AD-ICP-AES	1	398	1438	640	10754	880	1461	2139
Fe	AD-ICP-AES	110	67897	77984	55635	>320000	76742	99566	60622
Co	AD-ICP-AES	1	26	35	21	74	31	26	24
Ni	AD-ICP-AES	4	32	55	76	53	38	43	21
Cu	AD-ICP-AES	3	105	98	18	235	20	83	69
Zn	AD-ICP-AES	3	83	92	62	233	74	121	182
Ga	AD-ICP-MS	0.04	17.85	17.4	12.84	5.74	20.07	22.8	14.66
Rb	AD-ICP-MS	0.11	0.59	3.41	13.84	8.08	61.92	14.66	5.67

**Appendix F.II (continued) Whole-rock geochemistry, additional data**

Sample ID		348099	348100 GV-16-	348901	348902	348904	348905	348906
Lithology Code	LOD	B-S1	VC	B-S1	MR-IF	ADSM	ADSM	B-S1
Sr	AD-ICP-MS	0.6	116	216.9	390.4	27.6	131.4	247
Sr	AD-ICP-AES	3	97	227	375	35	126	239
Y	AD-ICP-MS	0.05	22.18	27.77	11.71	38.84	18.78	36.31
Y	AD-ICP-AES	0.6	9.5	25.8	9.8	45.3	16.1	33.4
Zr	AD-ICP-MS	6	41	103	30	25	47	274
Zr	AD-ICP-AES	7	36	100	26	45	42	251
Nb	AD-ICP-MS	0.028	0.956	4.487	1.011	1.967	1.341	18.472
M								
o	AD-ICP-AES	2	<2	<2	<2	<2	<2	<2
Ag		--	--	--	--	--	--	--
Cd	AD-ICP-AES	0.8	<0.8	1.1	0.9	1.2	<0.8	0.8
In		--	--	--	--	--	--	--
Sn		--	--	--	--	--	--	--
Sb		--	--	--	--	--	--	--
Cs	AD-ICP-MS	0.013	0.043	0.041	0.142	0.057	0.562	0.153
Ba	AD-ICP-MS	0.8	12.3	51	46.1	35.2	525.5	180.2
Ba	AD-ICP-AES	2	27	52	41	46	469	173
La	AD-ICP-MS	0.1	1.9	6.8	2.1	19	2.7	20.1
Ce	AD-ICP-MS	0.12	4.87	17.96	4.51	27.89	5.89	48.71
Pr	AD-ICP-MS	0.014	0.773	2.795	0.705	5.63	0.868	6.976
Nd	AD-ICP-MS	0.06	3.93	13.14	2.94	24.41	4.38	31.05
Sm	AD-ICP-MS	0.026	1.493	3.965	0.982	6.114	1.594	7.513
Eu	AD-ICP-MS	0.0031	0.5881	1.4539	0.3619	1.7286	0.4852	2.7325
Gd	AD-ICP-MS	0.009	2.445	5.054	1.401	7.469	2.129	7.823
Tb	AD-ICP-MS	0.0023	0.4878	0.832	0.2312	1.233	0.4079	1.2433
Dy	AD-ICP-MS	0.009	3.575	5.153	1.797	8.587	3.08	7.179
Ho	AD-ICP-MS	0.0025	0.8138	1.1214	0.4115	1.6698	0.6775	1.4291
Er	AD-ICP-MS	0.007	2.561	3.234	1.263	4.736	2.069	3.931
Tm	AD-ICP-MS	0.0019	0.3554	0.4612	0.1777	0.6582	0.3309	0.5323
Yb	AD-ICP-MS	0.009	2.504	2.898	1.299	4.098	2.36	3.488
Lu	AD-ICP-MS	0.002	0.387	0.462	0.2	0.544	0.352	0.492
Hf	AD-ICP-MS	0.14	1.3	2.73	0.76	0.54	1.31	5.95
Ta	AD-ICP-MS	0.007	0.06	0.228	0.076	0.096	0.1	1.136
Au	AD-ICP-MS	0.05	0.42	0.63	0.19	0.76	0.79	0.67
Tl		--	--	--	--	--	--	--
Pb	AD-ICP-AES	8	<8	<8	<8	18	<8	8
Bi	AD-ICP-MS	0.47	<0.47	<0.47	<0.47	<0.47	<0.47	<0.47
Th	AD-ICP-MS	0.018	0.393	0.767	0.401	1.281	0.653	1.064
U	AD-ICP-MS	0.011	0.229	0.29	0.118	1.487	0.232	0.447
								0.184

**Appendix F.II (continued) Whole-rock geochemistry, additional data**

Sample ID		348907	348908	348909	348910	348911	348912	348913
Drill Hole ID		GV-16-01	GV-16-01	GV-16-01	GV-16-01	GV-16-04	GV-16-04	GV-16-04
Drill Hole Depth (m)		155.6	144.5	167.5	181.5	9.6	17.32	30
UTM easting		567749	567749	567749	567749	568631	568631	568631
UTM northing		5538379	5538379	5538379	5538379	5538742	5538742	5538742
Lithology Code	LOD	B-S1	B-S1	B-S1	B-S2	B-S1	B-S1	B-S1
SiO <sub>2</sub>		--	--	--	--	--	--	--
TiO <sub>2</sub>		--	--	--	--	--	--	--
Al <sub>2</sub> O <sub>3</sub>		--	--	--	--	--	--	--
Fe <sub>2</sub> O <sub>3T</sub>		--	--	--	--	--	--	--
MnO		--	--	--	--	--	--	--
MgO		--	--	--	--	--	--	--
CaO		--	--	--	--	--	--	--
Na <sub>2</sub> O		--	--	--	--	--	--	--
K <sub>2</sub> O		--	--	--	--	--	--	--
P <sub>2</sub> O <sub>5</sub>		--	--	--	--	--	--	--
Cr <sub>2</sub> O <sub>3</sub>		--	--	--	--	--	--	--
BaO		--	--	--	--	--	--	--
LOI		--	--	--	--	--	--	--
Total		--	--	--	--	--	--	--
CO <sub>2</sub>		--	--	--	--	--	--	--
S (ppm)	AD-ICP-AES	39	2132	9351	1479	1673	86	<39
Li	AD-ICP-AES	2	9	8	7	3	22	15
Be	AD-ICP-AES	0.1	0.2	0.1	0.2	1	0.3	0.2
Na	AD-ICP-AES	530	22917	19372	15343	21928	13865	21315
Mg	AD-ICP-AES	140	36814	32450	26447	33202	29802	27523
Al	AD-ICP-AES	260	77495	74661	77944	72281	81209	86817
P	AD-ICP-AES	4	216	259	234	2235	159	187
K	AD-ICP-AES	98	991	1663	1189	465	4473	213
Ca	AD-ICP-AES	46	32529	38054	74003	62643	50141	69539
Sc	AD-ICP-AES	0.3	29.8	28	22.9	27.6	31.4	34.4
Ti	AD-ICP-MS	7	3616	3544	2338	21766	3118	3236
Ti	AD-ICP-AES	6	3708	3557	2289	21757	3381	3479
V	AD-ICP-MS	0.8	313.2	327.5	206.2	>370	283.5	349.5
V	AD-ICP-AES	3	295.8	303.4	186.4	359.4	309	358.8
Cr	AD-ICP-MS	3	20	5	72	87	105	24
Cr	AD-ICP-AES	17	18	<17	65	75	<17	<17
Mn	AD-ICP-AES	1	860	1266	570	1517	467	630
Fe	AD-ICP-AES	110	70259	80319	47932	97325	68142	70616
Co	AD-ICP-AES	1	26	38	18	27	28	22
Ni	AD-ICP-AES	4	28	13	41	51	29	26
Cu	AD-ICP-AES	3	69	52	86	70	70	18
Zn	AD-ICP-AES	3	79	150	38	118	84	76
Ga	AD-ICP-MS	0.04	17.94	17.31	20.43	23.38	14.79	15.86
Rb	AD-ICP-MS	0.11	1.06	1.22	1.36	0.57	20.09	1.41
								<0.11

**Appendix F.II (continued) Whole-rock geochemistry, additional data**

Sample ID		348907	348908	348909	348910	348911	348912	348913
Drill Hole ID		GV-16-01	GV-16-01	GV-16-01	GV-16-01	GV-16-04	GV-16-04	GV-16-04
Drill Hole Depth (m)		155.6	144.5	167.5	181.5	9.6	17.32	30
UTM easting		567749	567749	567749	567749	568631	568631	568631
UTM northing		5538379	5538379	5538379	5538379	5538742	5538742	5538742
Lithology Code	LOD	B-S1	B-S1	B-S1	B-S2	B-S1	B-S1	B-S1
Sr	AD-ICP-MS	0.6	99.6	182.5	104	293.8	127.6	57.6
Sr	AD-ICP-AES	3	99	189	98	300	176	233
Y	AD-ICP-MS	0.05	17.93	22.31	11.09	36.78	17.27	16.62
Y	AD-ICP-AES	0.6	16.3	20.7	9.2	31.8	13.4	18
Zr	AD-ICP-MS	6	32	35	43	266	26	27
Zr	AD-ICP-AES	7	31	36	38	235	31	30
Nb	AD-ICP-MS	0.028	0.788	0.811	0.591	17.384	0.543	0.589
M								
o	AD-ICP-AES	2	<2	<2	2	<2	<2	<2
Ag		--	--	--	--	--	--	--
Cd	AD-ICP-AES	0.8	0.8	<0.8	0.9	0.8	<0.8	<0.8
In		--	--	--	--	--	--	--
Sn		--	--	--	--	--	--	--
Sb		--	--	--	--	--	--	--
Cs	AD-ICP-MS	0.013	0.023	0.025	0.024	0.029	0.202	0.144
Ba	AD-ICP-MS	0.8	14.1	11.4	16.3	43.8	84.3	35.3
Ba	AD-ICP-AES	2	13	12	14	43	40	6
La	AD-ICP-MS	0.1	1.7	1.9	3.4	18.4	1.6	1.1
Ce	AD-ICP-MS	0.12	4.18	4.64	7.57	46.22	3.87	3.08
Pr	AD-ICP-MS	0.014	0.654	0.711	1.071	6.57	0.627	0.515
Nd	AD-ICP-MS	0.06	3.62	3.85	4.81	30.19	3.19	2.5
Sm	AD-ICP-MS	0.026	1.518	1.4	1.156	7.445	1.295	1.267
Eu	AD-ICP-MS	0.0031	0.5576	0.5224	0.5262	2.7345	0.5377	0.4474
Gd	AD-ICP-MS	0.009	2.25	2.423	1.849	7.558	1.969	2.015
Tb	AD-ICP-MS	0.0023	0.4584	0.4726	0.2682	1.1954	0.3448	0.4182
Dy	AD-ICP-MS	0.009	3.054	3.707	1.826	6.772	2.406	2.708
Ho	AD-ICP-MS	0.0025	0.6894	0.8449	0.399	1.3333	0.5905	0.6337
Er	AD-ICP-MS	0.007	2.169	2.512	1.274	3.575	1.898	2.012
Tm	AD-ICP-MS	0.0019	0.3318	0.4003	0.1683	0.5157	0.2847	0.3131
Yb	AD-ICP-MS	0.009	2.252	2.632	1.146	3.185	1.913	2.071
Lu	AD-ICP-MS	0.002	0.351	0.404	0.159	0.478	0.297	0.33
Hf	AD-ICP-MS	0.14	1.09	1.14	1.31	5.47	0.81	0.91
Ta	AD-ICP-MS	0.007	0.051	0.06	0.041	1.043	0.036	0.044
Au	AD-ICP-MS	0.05	0.14	0.11	0.17	0.4	9.54	0.54
Tl		--	--	--	--	--	--	--
Pb	AD-ICP-AES	8	<8	<8	<8	<8	<8	<8
Bi	AD-ICP-MS	0.47	<0.47	<0.47	<0.47	<0.47	<0.47	<0.47
Th	AD-ICP-MS	0.018	0.267	0.372	0.845	1.052	0.241	0.339
U	AD-ICP-MS	0.011	0.38	0.211	0.635	0.437	0.859	0.485

**Appendix F.II (continued) Whole-rock geochemistry, additional data**

Sample ID		348915	348916	348917	348918	348920	348921	348922	
Drill Hole ID		GV-16-04							
Drill Hole Depth (m)		53.36	59.9	65	79.6	101.61	123.76	130.5	
UTM easting		568631	568631	568631	568631	568631	568631	568631	
UTM northing		5538742	5538742	5538742	5538742	5538742	5538742	5538742	
Lithology Code	LOD	B-S1	B-S1	B-S1	B-S1	VC	Arg	Arg	
SiO <sub>2</sub>		--	--	--	--	--	--	--	
TiO <sub>2</sub>		--	--	--	--	--	--	--	
Al <sub>2</sub> O <sub>3</sub>		--	--	--	--	--	--	--	
Fe <sub>2</sub> O <sub>3T</sub>		--	--	--	--	--	--	--	
MnO		--	--	--	--	--	--	--	
MgO		--	--	--	--	--	--	--	
CaO		--	--	--	--	--	--	--	
Na <sub>2</sub> O		--	--	--	--	--	--	--	
K <sub>2</sub> O		--	--	--	--	--	--	--	
P <sub>2</sub> O <sub>5</sub>		--	--	--	--	--	--	--	
Cr <sub>2</sub> O <sub>3</sub>		--	--	--	--	--	--	--	
BaO		--	--	--	--	--	--	--	
LOI		--	--	--	--	--	--	--	
Total		--	--	--	--	--	--	--	
CO <sub>2</sub>		--	--	--	--	--	--	--	
S (ppm)	AD-ICP-AES	39	39	42	1335	1731	226	150	107
Li	AD-ICP-AES	2	29	12	9	11	11	14	10
Be	AD-ICP-AES	0.1	0.2	0.8	1.1	0.3	1.2	0.8	1.2
Na	AD-ICP-AES	530	5344	18168	13037	40828	<530	12257	<530
Mg	AD-ICP-AES	140	57441	33547	24328	24552	21530	31264	23060
Al	AD-ICP-AES	260	73996	66540	72900	85139	48632	65987	51535
P	AD-ICP-AES	4	77	824	1109	173	1614	228	1291
K	AD-ICP-AES	98	5851	222	194	4353	471	16795	6680
Ca	AD-ICP-AES	46	66912	45762	62452	39722	6452	15492	5630
Sc	AD-ICP-AES	0.3	40.1	29.4	28.5	35.6	8.2	22.3	10.1
Ti	AD-ICP-MS	7	3375	3433	3670	2927	3371	10043	11929
Ti	AD-ICP-AES	6	3212	9972	12506	2730	2265	2550	2496
V	AD-ICP-MS	0.8	323	336.9	>370	301.9	278.5	270.9	268.2
V	AD-ICP-AES	3	254.7	255.9	257.6	233.8	198.8	222.5	148.9
Cr	AD-ICP-MS	3	24	14	16	161	471	85	67
Cr	AD-ICP-AES	17	421	77	62	369	46	391	57
Mn	AD-ICP-AES	1	904	3186	1834	1467	>13000	2770	>13000
Fe	AD-ICP-AES	110	79575	87697	90841	41250	297302	62452	259728
Co	AD-ICP-AES	1	45	24	20	31	12	38	19
Ni	AD-ICP-AES	4	100	26	34	79	123	106	134
Cu	AD-ICP-AES	3	120	55	71	164	212	127	109
Zn	AD-ICP-AES	3	94	119	119	57	369	86	295
Ga	AD-ICP-MS	0.04	17.18	16.4	19.31	15.63	13.96	17.01	24.19
Rb	AD-ICP-MS	0.11	7.95	8.73	0.37	0.16	17.86	0.35	0.32

**Appendix F.II (continued) Whole-rock geochemistry, additional data**

Sample ID		348915	348916	348917	348918	348920	348921	348922
Drill Hole ID		GV-16-04						
Drill Hole Depth (m)		53.36	59.9	65	79.6	101.61	123.76	130.5
UTM easting		568631	568631	568631	568631	568631	568631	568631
UTM northing		5538742	5538742	5538742	5538742	5538742	5538742	5538742
Lithology Code	LOD	B-S1	B-S1	B-S1	B-S1	VC	Arg	Arg
Sr	AD-ICP-MS	0.6	104.8	187.3	253.1	103	109.8	156.9
Sr	AD-ICP-AES	3	105	159	286	83	10	41
Y	AD-ICP-MS	0.05	10.63	14.65	20.41	15.33	12.88	37.39
Y	AD-ICP-AES	0.6	11.7	34.2	46.7	14.6	37.4	9.1
Zr	AD-ICP-MS	6	35	32	29	24	28	137
Zr	AD-ICP-AES	7	28	129	191	25	78	25
Nb	AD-ICP-MS	0.028	0.803	0.769	0.694	0.523	0.558	4.744
M								7.851
o	AD-ICP-AES	2	<2	<2	<2	<2	<2	<2
Ag		--	--	--	--	--	--	--
Cd	AD-ICP-AES	0.8	1.1	<0.8	<0.8	0.8	1.2	0.8
In		--	--	--	--	--	--	--
Sn		--	--	--	--	--	--	--
Sb		--	--	--	--	--	--	--
Cs	AD-ICP-MS	0.013	0.329	0.146	0.063	0.028	0.2	0.014
Ba	AD-ICP-MS	0.8	26.9	41.9	6	2.5	50.3	6.2
Ba	AD-ICP-AES	2	49	7	13	42	8	151
La	AD-ICP-MS	0.1	1.7	1.7	2	1.2	1.2	8.5
Ce	AD-ICP-MS	0.12	4.14	4.29	4.45	3.25	2.87	22.29
Pr	AD-ICP-MS	0.014	0.623	0.63	0.713	0.509	0.457	3.304
Nd	AD-ICP-MS	0.06	2.86	3.18	3.99	2.65	2.49	15.78
Sm	AD-ICP-MS	0.026	1.132	1.271	1.459	1.169	0.885	4.606
Eu	AD-ICP-MS	0.0031	0.3916	0.491	0.6634	0.5177	0.4525	1.5278
Gd	AD-ICP-MS	0.009	1.646	2.2	2.347	1.899	1.419	6.048
Tb	AD-ICP-MS	0.0023	0.2762	0.4243	0.4849	0.3483	0.2593	1.083
Dy	AD-ICP-MS	0.009	2.102	2.923	3.18	2.43	1.922	6.587
Ho	AD-ICP-MS	0.0025	0.439	0.65	0.7579	0.5404	0.4508	1.4495
Er	AD-ICP-MS	0.007	1.332	1.957	2.333	1.81	1.409	4.17
Tm	AD-ICP-MS	0.0019	0.1854	0.2809	0.3597	0.2706	0.2139	0.6123
Yb	AD-ICP-MS	0.009	1.256	1.798	2.382	1.765	1.549	4.014
Lu	AD-ICP-MS	0.002	0.217	0.261	0.346	0.289	0.254	0.588
Hf	AD-ICP-MS	0.14	1.18	1.01	0.98	0.8	0.85	3.49
Ta	AD-ICP-MS	0.007	0.057	0.057	0.049	0.033	0.033	0.318
Au	AD-ICP-MS	0.05	0.29	1.99	0.42	0.35	0.45	0.85
Tl		--	--	--	--	--	--	--
Pb	AD-ICP-AES	8	<8	<8	8	<8	49	<8
Bi	AD-ICP-MS	0.47	<0.47	<0.47	<0.47	<0.47	<0.47	<0.47
Th	AD-ICP-MS	0.018	0.5	0.31	0.27	0.293	0.268	1.408
U	AD-ICP-MS	0.011	0.185	0.146	0.276	0.107	0.285	0.651
								1.445

**Appendix F.II (continued) Whole-rock geochemistry, additional data**

Sample ID		348923	348924	348928	348929	348930	348953	348957	
Drill Hole ID		GV-16-04	GV-16-04	GV-16-04	GV-16-04	GV-16-04	GV-16-07	GV-16-08	
Drill Hole Depth (m)		107.96	110.35	114.2	116.4	119.9	44	19.06	
UTM easting		568631	568631	568631	568631	568631	569075	569155	
UTM northing		5538742	5538742	5538742	5538742	5538742	5538640	5538679	
Lithology Code	LOD	ADSM	ASMM	ADSM	ASMM	ASMM	VC	MR-IF	
SiO <sub>2</sub>		--	--	--	--	--	--	--	
TiO <sub>2</sub>		--	--	--	--	--	--	--	
Al <sub>2</sub> O <sub>3</sub>		--	--	--	--	--	--	--	
Fe <sub>2</sub> O <sub>3T</sub>		--	--	--	--	--	--	--	
MnO		--	--	--	--	--	--	--	
MgO		--	--	--	--	--	--	--	
CaO		--	--	--	--	--	--	--	
Na <sub>2</sub> O		--	--	--	--	--	--	--	
K <sub>2</sub> O		--	--	--	--	--	--	--	
P <sub>2</sub> O <sub>5</sub>		--	--	--	--	--	--	--	
Cr <sub>2</sub> O <sub>3</sub>		--	--	--	--	--	--	--	
BaO		--	--	--	--	--	--	--	
LOI		--	--	--	--	--	--	--	
Total		--	--	--	--	--	--	--	
CO <sub>2</sub>		--	--	--	--	--	--	--	
S (ppm)	AD-ICP-AES	39	<39	<39	<39	96	87	5830	313
Li	AD-ICP-AES	2	7	5	5	<2	<2	18	7
Be	AD-ICP-AES	0.1	1.5	0.7	0.7	0.9	0.9	0.8	1.1
Na	AD-ICP-AES	530	12067	23204	24576	<530	<530	30348	<530
Mg	AD-ICP-AES	140	20366	41087	43577	11863	11065	35949	16635
Al	AD-ICP-AES	260	51357	77124	81386	1772	1586	83982	27300
P	AD-ICP-AES	4	700	1011	1073	192	178	400	>7000
K	AD-ICP-AES	98	1421	4113	4333	<98	<98	8127	3911
Ca	AD-ICP-AES	46	30168	58153	61570	12515	11458	29347	38175
Sc	AD-ICP-AES	0.3	10.5	16.7	17.8	<0.3	<0.3	23.6	7
Ti	AD-ICP-MS	7	2909	2083	2555	1912	2644	3002	1039
Ti	AD-ICP-AES	6	2530	8528	9091	435	417	2961	1190
V	AD-ICP-MS	0.8	260.2	185.3	232.7	120.6	81.3	137.5	285
V	AD-ICP-AES	3	78.5	174	182	106.4	98.9	129.8	332.2
Cr	AD-ICP-MS	3	423	43	435	51	46	189	164
Cr	AD-ICP-AES	17	42	197	209	282	258	168	177
Mn	AD-ICP-AES	1	>13000	1189	1254	6489	6002	741	3749
Fe	AD-ICP-AES	110	103882	82773	87755	>320000	>320000	48874	>320000
Co	AD-ICP-AES	1	25	36	38	30	28	18	76
Ni	AD-ICP-AES	4	53	131	141	30	26	58	73
Cu	AD-ICP-AES	3	62	66	71	30	25	37	245
Zn	AD-ICP-AES	3	105	111	118	93	86	68	236
Ga	AD-ICP-MS	0.04	14.09	12.5	12.11	11.45	12.88	15.27	6.61
Rb	AD-ICP-MS	0.11	13.75	1.16	47.1	12.51	4.39	19.6	11.21

**Appendix F.II (continued) Whole-rock geochemistry, additional data**

Sample ID		348923	348924	348928	348929	348930	348953	348957	
Drill Hole ID		GV-16-04	GV-16-04	GV-16-04	GV-16-04	GV-16-04	GV-16-07	GV-16-08	
Drill Hole Depth (m)		107.96	110.35	114.2	116.4	119.9	44	19.06	
UTM easting		568631	568631	568631	568631	568631	569075	569155	
UTM northing		5538742	5538742	5538742	5538742	5538742	5538640	5538679	
Lithology Code	LOD	ADSM	ASMM	ADSM	ASMM	ASMM	VC	MR-IF	
Sr	AD-ICP-MS	0.6	86.4	9.4	41.5	14.4	234.5	157	90.2
Sr	AD-ICP-AES	3	232	443	458	7	9	151	109
Y	AD-ICP-MS	0.05	16.44	36.49	13.67	38.43	26.44	11.42	45.3
Y	AD-ICP-AES	0.6	23.6	15.7	16.7	5.8	4.9	9.6	48.9
Zr	AD-ICP-MS	6	28	67	26	69	89	79	24
Zr	AD-ICP-AES	7	84	90	95	52	48	71	40
Nb	AD-ICP-MS	0.028	0.642	5.776	0.694	5.84	7.489	3.631	1.611
M									
o	AD-ICP-AES	2	<2	3	3	32	29	<2	<2
Ag		--	--	--	--	--	--	--	--
Cd	AD-ICP-AES	0.8	0.9	<0.8	0.8	1.1	1.6	1.1	1.2
In		--	--	--	--	--	--	--	--
Sn		--	--	--	--	--	--	--	--
Sb		--	--	--	--	--	--	--	--
Cs	AD-ICP-MS	0.013	0.133	<0.013	0.429	0.097	0.065	0.112	0.048
Ba	AD-ICP-MS	0.8	44.1	5.7	203.8	81.7	39.2	112.5	63.5
Ba	AD-ICP-AES	2	38	138	151	59	52	104	75
La	AD-ICP-MS	0.1	2.2	37.6	2.4	38.8	40.2	7.8	25.5
Ce	AD-ICP-MS	0.12	5.08	111.47	6.11	129.89	119.22	17.87	35.04
Pr	AD-ICP-MS	0.014	0.747	10.151	0.872	10.746	9.413	2.15	7.532
Nd	AD-ICP-MS	0.06	4.02	39.72	3.81	42.21	35.96	8.23	31.88
Sm	AD-ICP-MS	0.026	1.335	9.241	1.35	9.562	7.5	1.947	7.585
Eu	AD-ICP-MS	0.0031	0.5827	2.2572	0.4595	2.8697	1.578	0.5542	1.949
Gd	AD-ICP-MS	0.009	2.137	9.164	1.811	10.211	6.981	1.924	8.679
Tb	AD-ICP-MS	0.0023	0.4086	1.4532	0.3222	1.6408	1.0857	0.2957	1.3409
Dy	AD-ICP-MS	0.009	2.764	8.424	2.388	10.197	6.233	2.027	8.328
Ho	AD-ICP-MS	0.0025	0.6158	1.6637	0.5124	2.0067	1.2015	0.4286	1.6762
Er	AD-ICP-MS	0.007	1.957	4.807	1.704	5.626	3.317	1.125	4.911
Tm	AD-ICP-MS	0.0019	0.2752	0.6722	0.2484	0.8215	0.4722	0.1876	0.6582
Yb	AD-ICP-MS	0.009	1.653	4.254	1.771	4.993	2.952	1.136	3.983
Lu	AD-ICP-MS	0.002	0.231	0.577	0.292	0.705	0.408	0.153	0.507
Hf	AD-ICP-MS	0.14	0.81	1.55	0.81	1.95	2.19	2.02	0.51
Ta	AD-ICP-MS	0.007	0.044	0.303	0.048	0.414	0.485	0.22	0.066
Au	AD-ICP-MS	0.05	0.45	0.99	1.11	1.53	0.84	0.82	7.5
Tl		--	--	--	--	--	--	--	--
Pb	AD-ICP-AES	8	45	<8	<8	28	25	<8	17
Bi	AD-ICP-MS	0.47	<0.47	<0.47	<0.47	<0.47	0.67	<0.47	<0.47
Th	AD-ICP-MS	0.018	0.33	5.177	0.446	6.705	8.175	3.281	0.963
U	AD-ICP-MS	0.011	0.64	2.227	0.749	1.967	1.429	1.845	1.951

## Appendix F.II Whole-rock geochemistry, additional data

Sample ID		348958	348959	348960	348964	348965	348967	348970
Drill Hole ID		GV-16-08	GV-16-08	GV-16-08	GV-16-03	GV-16-03	GV-16-03	GV-16-03
Drill Hole Depth (m)		20.9	24.8	26.6	29.9	62	35.2	38.54
UTM easting		569155	569155	569155	568689	568689	568689	568689
UTM northing		5538679	5538679	5538679	5538731	5538731	5538731	5538731
Lithology Code	LOD	ADSM	ADSM	ADSM	B-S1	Arg	MR-IF	ADSM
SiO <sub>2</sub>		--	--	--	--	--	--	--
TiO <sub>2</sub>		--	--	--	--	--	--	--
Al <sub>2</sub> O <sub>3</sub>		--	--	--	--	--	--	--
Fe <sub>2</sub> O <sub>3T</sub>		--	--	--	--	--	--	--
MnO		--	--	--	--	--	--	--
MgO		--	--	--	--	--	--	--
CaO		--	--	--	--	--	--	--
Na <sub>2</sub> O		--	--	--	--	--	--	--
K <sub>2</sub> O		--	--	--	--	--	--	--
P <sub>2</sub> O <sub>5</sub>		--	--	--	--	--	--	--
Cr <sub>2</sub> O <sub>3</sub>		--	--	--	--	--	--	--
BaO		--	--	--	--	--	--	--
LOI		--	--	--	--	--	--	--
Total		--	--	--	--	--	--	--
CO <sub>2</sub>		--	--	--	--	--	--	--
S (ppm)	AD-ICP-AES	39	589	209	68	482	569	1431
Li	AD-ICP-AES	2	4	7	12	18	11	5
Be	AD-ICP-AES	0.1	1.3	1.1	0.7	0.4	0.8	1.8
Na	AD-ICP-AES	530	28019	8126	21748	35755	34488	1478
Mg	AD-ICP-AES	140	16201	17123	38936	34603	38681	11853
Al	AD-ICP-AES	260	65487	77117	75382	81108	81917	24800
P	AD-ICP-AES	4	573	241	713	96	700	>7000
K	AD-ICP-AES	98	12235	37240	1065	223	242	616
Ca	AD-ICP-AES	46	25471	12597	53459	44910	39275	57890
Sc	AD-ICP-AES	0.3	10.6	15.6	36.6	32.1	29	8.5
Ti	AD-ICP-MS	7	3518	2415	10548	1815	9303	1196
Ti	AD-ICP-AES	6	3544	2356	10059	1813	9122	1318
V	AD-ICP-MS	0.8	78.4	46.5	300.8	197.8	230.4	265.6
V	AD-ICP-AES	3	76.3	44.9	280.2	191.6	222.2	286.6
Cr	AD-ICP-MS	3	33	19	240	190	74	147
Cr	AD-ICP-AES	17	30	<17	219	176	67	151
Mn	AD-ICP-AES	1	9655	5237	1785	1270	1456	6801
Fe	AD-ICP-AES	110	66658	48469	79048	54387	69692	>320000
Co	AD-ICP-AES	1	20	10	32	38	27	63
Ni	AD-ICP-AES	4	33	19	47	93	34	54
Cu	AD-ICP-AES	3	517	13	99	62	49	1189
Zn	AD-ICP-AES	3	101	97	93	68	84	112
Ga	AD-ICP-MS	0.04	16.12	18.38	16.89	11.66	17.8	6.37
Rb	AD-ICP-MS	0.11	48.8	133.88	3.38	0.46	0.23	1.62
								34.18

**Appendix F.II (continued) Whole-rock geochemistry, additional data**

Sample ID		348958	348959	348960	348964	348965	348967	348970
Drill Hole ID		GV-16-08	GV-16-08	GV-16-08	GV-16-03	GV-16-03	GV-16-03	GV-16-03
Drill Hole Depth (m)		20.9	24.8	26.6	29.9	62	35.2	38.54
UTM easting		569155	569155	569155	568689	568689	568689	568689
UTM northing		5538679	5538679	5538679	5538731	5538731	5538731	5538731
Lithology Code	LOD	ADSM	ADSM	ADSM	B-S1	Arg	MR-IF	ADSM
Sr	AD-ICP-MS	0.6	198.7	55.4	216.2	120.4	98.1	159.2
Sr	AD-ICP-AES	3	194	55	213	120	102	164
Y	AD-ICP-MS	0.05	25.28	48.5	30.3	9.87	28.17	51.89
Y	AD-ICP-AES	0.6	22.3	42.6	28.1	8.2	25.1	49.9
Zr	AD-ICP-MS	6	119	181	125	14	120	28
Zr	AD-ICP-AES	7	105	165	116	13	109	42
Nb	AD-ICP-MS	0.028	7.78	4.903	3.579	0.362	4.367	1.944
M								3.987
o	AD-ICP-AES	2	<2	<2	<2	<2	<2	<2
Ag		--	--	--	--	--	--	--
Cd	AD-ICP-AES	0.8	0.8	<0.8	1.3	1	<0.8	1
In		--	--	--	--	--	--	--
Sn		--	--	--	--	--	--	--
Sb		--	--	--	--	--	--	--
Cs	AD-ICP-MS	0.013	0.215	1.054	0.063	0.025	<0.013	0.027
Ba	AD-ICP-MS	0.8	532.6	628.8	46.4	14.2	10.7	14.5
Ba	AD-ICP-AES	2	498	574	45	13	10	18
La	AD-ICP-MS	0.1	24.8	17.3	5.1	0.8	6.8	28.7
Ce	AD-ICP-MS	0.12	78.39	46.41	14.97	1.81	18.13	45.85
Pr	AD-ICP-MS	0.014	6.773	5.518	2.525	0.256	2.877	8.996
Nd	AD-ICP-MS	0.06	27.23	24.37	12.64	1.3	13.36	36.67
Sm	AD-ICP-MS	0.026	5.406	6.307	3.688	0.537	4.092	9.373
Eu	AD-ICP-MS	0.0031	1.3836	1.3292	1.442	0.2444	1.4841	2.773
Gd	AD-ICP-MS	0.009	5.381	7.002	4.995	1.014	5.134	11.256
Tb	AD-ICP-MS	0.0023	0.8383	1.2129	0.8777	0.2211	0.8581	1.816
Dy	AD-ICP-MS	0.009	5.054	8.156	5.5	1.575	5.394	11.185
Ho	AD-ICP-MS	0.0025	0.9724	1.7357	1.1002	0.3708	1.1162	2.2847
Er	AD-ICP-MS	0.007	2.683	5.307	3.051	1.204	3.377	6.422
Tm	AD-ICP-MS	0.0019	0.3975	0.809	0.4496	0.1954	0.4901	0.9297
Yb	AD-ICP-MS	0.009	2.629	5.655	2.759	1.287	3.047	5.409
Lu	AD-ICP-MS	0.002	0.395	0.846	0.39	0.207	0.47	0.79
Hf	AD-ICP-MS	0.14	2.92	5.22	2.94	0.49	3.01	0.71
Ta	AD-ICP-MS	0.007	0.524	0.273	0.208	0.026	0.299	0.107
Au	AD-ICP-MS	0.05	2.11	2.42	1.07	0.29	0.52	75.23
Tl		--	--	--	--	--	--	--
Pb	AD-ICP-AES	8	63	<8	<8	<8	<8	20
Bi	AD-ICP-MS	0.47	1.15	<0.47	<0.47	<0.47	<0.47	<0.47
Th	AD-ICP-MS	0.018	6.265	4.965	0.33	0.14	0.955	1.385
U	AD-ICP-MS	0.011	1.008	0.557	0.114	0.124	0.578	3.625
								6.083

## Appendix F.II (continued) Whole-rock geochemistry, additional data

Sample ID		348971	348972	348977	348981	348983	348984	348985
Drill Hole ID		GV-16-03	GV-16-06	GV-16-06	GV-16-02	GV-16-02	GV-16-02	GV-16-02
Drill Hole Depth (m)		42.81	38.84	155.58	61.15	117.5	124	128.3
UTM easting		568689	569304	569304	568132	568132	568132	568132
UTM northing		5538731	5538764	5538764	5538611	5538611	5538611	5538611
Lithology Code	LOD	ADSM	B-S1	VC	B-S1	ADSM	ADSM	B-S1
SiO <sub>2</sub>		--	--	--	--	--	--	--
TiO <sub>2</sub>		--	--	--	--	--	--	--
Al <sub>2</sub> O <sub>3</sub>		--	--	--	--	--	--	--
Fe <sub>2</sub> O <sub>3T</sub>		--	--	--	--	--	--	--
MnO		--	--	--	--	--	--	--
MgO		--	--	--	--	--	--	--
CaO		--	--	--	--	--	--	--
Na <sub>2</sub> O		--	--	--	--	--	--	--
K <sub>2</sub> O		--	--	--	--	--	--	--
P <sub>2</sub> O <sub>5</sub>		--	--	--	--	--	--	--
Cr <sub>2</sub> O <sub>3</sub>		--	--	--	--	--	--	--
BaO		--	--	--	--	--	--	--
LOI		--	--	--	--	--	--	--
Total		--	--	--	--	--	--	--
CO <sub>2</sub>		--	--	--	--	--	--	--
S (ppm)	AD-ICP-AES	39	496	<39	222	515	375	<39
Li	AD-ICP-AES	2	17	16	11	11	8	5
Be	AD-ICP-AES	0.1	0.9	0.1	0.1	0.2	1	0.5
Na	AD-ICP-AES	530	15070	24958	6873	21541	12678	31050
Mg	AD-ICP-AES	140	24790	38250	46193	45351	18471	7195
Al	AD-ICP-AES	260	67622	78877	69287	78673	62596	101953
P	AD-ICP-AES	4	1412	87	143	179	472	426
K	AD-ICP-AES	98	5729	1723	19969	3363	16784	23133
Ca	AD-ICP-AES	46	31649	21296	50982	54201	23094	28547
Sc	AD-ICP-AES	0.3	25	26.5	29.4	31.8	14	39.3
Ti	AD-ICP-MS	7	12805	2959	3411	3100	3200	4591
Ti	AD-ICP-AES	6	12188	3020	3173	3108	3142	4472
V	AD-ICP-MS	0.8	191.7	258.9	226.2	250.9	72.1	266.9
V	AD-ICP-AES	3	181.7	248.5	209.7	246	71.4	256.1
Cr	AD-ICP-MS	3	21	7	302	106	53	71
Cr	AD-ICP-AES	17	21	<17	271	99	50	65
Mn	AD-ICP-AES	1	1538	379	1219	1501	5455	1174
Fe	AD-ICP-AES	110	91275	70348	54277	70659	67636	86035
Co	AD-ICP-AES	1	16	33	30	30	20	33
Ni	AD-ICP-AES	4	12	38	87	55	36	36
Cu	AD-ICP-AES	3	62	48	70	82	387	20
Zn	AD-ICP-AES	3	131	96	73	156	98	108
Ga	AD-ICP-MS	0.04	20.96	13.5	12.74	14.61	15.21	22.18
Rb	AD-ICP-MS	0.11	14.34	5.26	36.47	4.84	46.4	60.17

**Appendix F.II (continued) Whole-rock geochemistry, additional data**

Sample ID		348971	348972	348977	348981	348983	348984	348985
Drill Hole ID		GV-16-03	GV-16-06	GV-16-06	GV-16-02	GV-16-02	GV-16-02	GV-16-02
Drill Hole Depth (m)		42.81	38.84	155.58	61.15	117.5	124	128.3
UTM easting		568689	569304	569304	568132	568132	568132	568132
UTM northing		5538731	5538764	5538764	5538611	5538611	5538611	5538611
Lithology Code	LOD	ADSM	B-S1	VC	B-S1	ADSM	ADSM	B-S1
Sr	AD-ICP-MS	0.6	93.1	55.4	191.9	109.1	93.4	136.6
Sr	AD-ICP-AES	3	92	52	191	114	98	140
Y	AD-ICP-MS	0.05	57.25	11.04	13.4	15	24.95	20.87
Y	AD-ICP-AES	0.6	50	9.7	11.9	13.6	22.1	18.9
Zr	AD-ICP-MS	6	231	24	24	23	108	48
Zr	AD-ICP-AES	7	204	24	22	23	98	46
Nb	AD-ICP-MS	0.028	8.724	0.54	0.429	0.467	7.184	1.673
M								
o	AD-ICP-AES	2	<2	<2	<2	<2	<2	<2
Ag		--	--	--	--	--	--	--
Cd	AD-ICP-AES	0.8	0.9	<0.8	1	0.9	<0.8	0.8
In		--	--	--	--	--	--	--
Sn		--	--	--	--	--	--	--
Sb		--	--	--	--	--	--	--
Cs	AD-ICP-MS	0.013	0.219	0.096	0.511	0.064	0.34	0.417
Ba	AD-ICP-MS	0.8	121.5	7.2	160.7	37.3	530.4	493.7
Ba	AD-ICP-AES	2	106	8	150	36	473	445
La	AD-ICP-MS	0.1	14.9	1.6	0.9	1.2	29.2	3.9
Ce	AD-ICP-MS	0.12	37.64	3.62	2.84	3.02	88.9	8.97
Pr	AD-ICP-MS	0.014	5.813	0.58	0.516	0.521	7.517	1.326
Nd	AD-ICP-MS	0.06	26.96	2.78	2.96	2.91	28.49	6.26
Sm	AD-ICP-MS	0.026	8.011	1.117	1.176	1.156	6.208	2.115
Eu	AD-ICP-MS	0.0031	2.5937	0.3578	0.513	0.516	1.5384	0.8094
Gd	AD-ICP-MS	0.009	9.741	1.73	1.738	1.976	5.808	3.213
Tb	AD-ICP-MS	0.0023	1.6857	0.3125	0.3217	0.3763	0.924	0.5956
Dy	AD-ICP-MS	0.009	10.527	2.247	2.301	2.56	5.354	3.813
Ho	AD-ICP-MS	0.0025	2.2909	0.4693	0.5135	0.5817	1.0462	0.854
Er	AD-ICP-MS	0.007	6.78	1.342	1.523	1.86	3.013	2.578
Tm	AD-ICP-MS	0.0019	0.9447	0.2007	0.2251	0.2872	0.438	0.3892
Yb	AD-ICP-MS	0.009	6.14	1.376	1.473	1.849	2.652	2.571
Lu	AD-ICP-MS	0.002	0.936	0.192	0.226	0.287	0.399	0.384
Hf	AD-ICP-MS	0.14	6	0.89	0.76	0.84	3.14	1.55
Ta	AD-ICP-MS	0.007	0.623	0.036	0.027	0.035	0.525	0.116
Au	AD-ICP-MS	0.05	8.92	0.23	1.81	0.32	2.32	1.25
Tl		--	--	--	--	--	--	--
Pb	AD-ICP-AES	8	<8	<8	<8	<8	8	8
Bi	AD-ICP-MS	0.47	<0.47	<0.47	<0.47	<0.47	0.57	<0.47
Th	AD-ICP-MS	0.018	2.603	0.331	0.101	0.226	8.007	0.735
U	AD-ICP-MS	0.011	1.465	0.072	0.04	0.114	1.126	0.58
								0.21

**Appendix F.II (continued) Whole-rock geochemistry, additional data**

Sample ID		348987	348988	348989	348990	348991	348992	348994	
Drill Hole ID		GV-16-01							
Drill Hole Depth (m)		8	21.28	38	43.43	54.55	66.44	71.64	
UTM easting		567749	567749	567749	567749	567749	567749	567749	
UTM northing		5538379	5538379	5538379	5538379	5538379	5538379	5538379	
Lithology Code	LOD	VC	B-S1	B-S1	B-S2	B-S1	VC	ADSM	
SiO <sub>2</sub>		--	--	--	--	--	--	--	
TiO <sub>2</sub>		--	--	--	--	--	--	--	
Al <sub>2</sub> O <sub>3</sub>		--	--	--	--	--	--	--	
Fe <sub>2</sub> O <sub>3T</sub>		--	--	--	--	--	--	--	
MnO		--	--	--	--	--	--	--	
MgO		--	--	--	--	--	--	--	
CaO		--	--	--	--	--	--	--	
Na <sub>2</sub> O		--	--	--	--	--	--	--	
K <sub>2</sub> O		--	--	--	--	--	--	--	
P <sub>2</sub> O <sub>5</sub>		--	--	--	--	--	--	--	
Cr <sub>2</sub> O <sub>3</sub>		--	--	--	--	--	--	--	
BaO		--	--	--	--	--	--	--	
LOI		--	--	--	--	--	--	--	
Total		--	--	--	--	--	--	--	
CO <sub>2</sub>		--	--	--	--	--	--	--	
S (ppm)	AD-ICP-AES	39	22768	2991	760	9065	1639	39	4609
Li	AD-ICP-AES	2	10	13	11	21	14	11	19
Be	AD-ICP-AES	0.1	0.3	0.1	0.1	1	0.2	0.2	0.6
Na	AD-ICP-AES	530	10168	12198	17290	19958	32440	1518	1035
Mg	AD-ICP-AES	140	38043	53899	43552	38096	28080	11735	35596
Al	AD-ICP-AES	260	79888	90245	77863	85001	100413	58236	79916
P	AD-ICP-AES	4	1629	85	90	4724	260	19	544
K	AD-ICP-AES	98	9997	2060	745	264	1416	17982	24266
Ca	AD-ICP-AES	46	41588	70699	80436	59067	44072	56587	35694
Sc	AD-ICP-AES	0.3	24.3	35.8	33.8	29.6	41.7	17.1	28.4
Ti	AD-ICP-MS	7	12522	1992	2625	>25000	3681	1649	5386
Ti	AD-ICP-AES	6	14441	2043	2714	>25000	3659	1588	5626
V	AD-ICP-MS	0.8	250.2	273.9	255.6	>370	341	135	184.3
V	AD-ICP-AES	3	272.7	259.7	243.5	372.9	318.1	121.3	184.7
Cr	AD-ICP-MS	3	62	71	181	66	197	49	197
Cr	AD-ICP-AES	17	61	63	158	61	171	40	184
Mn	AD-ICP-AES	1	1104	476	1074	1408	621	227	3609
Fe	AD-ICP-AES	110	123081	70424	58900	113670	47537	42870	82681
Co	AD-ICP-AES	1	37	32	43	29	32	18	41
Ni	AD-ICP-AES	4	56	59	79	56	46	47	100
Cu	AD-ICP-AES	3	67	102	83	117	80	5	600
Zn	AD-ICP-AES	3	253	77	68	138	84	50	209
Ga	AD-ICP-MS	0.04	17.17	15.41	13.1	25.84	17.47	11.21	17.02
Rb	AD-ICP-MS	0.11	12.27	2.88	1.04	0.4	2.32	50.77	45.38

**Appendix F.II (continued) Whole-rock geochemistry, additional data**

Sample ID		348987	348988	348989	348990	348991	348992	348994
Drill Hole ID		GV-16-01						
Drill Hole Depth (m)		8	21.28	38	43.43	54.55	66.44	71.64
UTM easting		567749	567749	567749	567749	567749	567749	567749
UTM northing		5538379	5538379	5538379	5538379	5538379	5538379	5538379
Lithology Code	LOD	VC	B-S1	B-S1	B-S2	B-S1	VC	ADSM
Sr	AD-ICP-MS	0.6	61.9	98.3	117.2	147	107.1	141.9
Sr	AD-ICP-AES	3	67	98	115	141	102	137
Y	AD-ICP-MS	0.05	29.26	14.05	12.5	53.36	18.73	2.27
Y	AD-ICP-AES	0.6	29.2	12.3	10.9	47.7	16.1	1.7
Zr	AD-ICP-MS	6	175	25	19	411	31	40
Zr	AD-ICP-AES	7	178	24	18	372	27	35
Nb	AD-ICP-MS	0.028	11.545	0.822	0.288	28.917	0.796	0.478
M								
o	AD-ICP-AES	2	3	<2	<2	<2	<2	<2
Ag		--	--	--	--	--	--	--
Cd	AD-ICP-AES	0.8	1	0.8	1.1	1.2	<0.8	<0.8
In		--	--	--	--	--	--	--
Sn		--	--	--	--	--	--	--
Sb		--	--	--	--	--	--	--
Cs	AD-ICP-MS	0.013	0.151	0.03	0.015	<0.013	0.133	0.341
Ba	AD-ICP-MS	0.8	62.3	17.6	10.3	31.1	18.5	97.4
Ba	AD-ICP-AES	2	60	17	10	28	17	88
La	AD-ICP-MS	0.1	14.3	2	0.7	35	1.7	1.1
Ce	AD-ICP-MS	0.12	33.58	4.22	2.17	85.89	4.2	2.87
Pr	AD-ICP-MS	0.014	4.929	0.601	0.361	12.047	0.675	0.356
Nd	AD-ICP-MS	0.06	22.3	2.64	2.22	55.53	3.67	1.37
Sm	AD-ICP-MS	0.026	5.423	1.287	1.023	12.552	1.453	0.493
Eu	AD-ICP-MS	0.0031	1.7118	0.3779	0.3937	4.3786	0.549	0.1827
Gd	AD-ICP-MS	0.009	5.925	1.784	1.578	12.129	2.239	0.471
Tb	AD-ICP-MS	0.0023	0.9222	0.3527	0.2982	1.7495	0.4263	0.0785
Dy	AD-ICP-MS	0.009	5.964	2.272	2.177	10.567	3.208	0.466
Ho	AD-ICP-MS	0.0025	1.145	0.5182	0.4986	2.0997	0.7034	0.0806
Er	AD-ICP-MS	0.007	3.204	1.618	1.484	5.552	2.11	0.212
Tm	AD-ICP-MS	0.0019	0.4463	0.2467	0.2255	0.7652	0.3177	0.0314
Yb	AD-ICP-MS	0.009	2.847	1.647	1.4	4.908	1.974	0.279
Lu	AD-ICP-MS	0.002	0.413	0.249	0.212	0.687	0.263	0.045
Hf	AD-ICP-MS	0.14	3.99	0.75	0.64	8.65	0.94	1.13
Ta	AD-ICP-MS	0.007	0.758	0.053	0.022	1.856	0.055	0.038
Au	AD-ICP-MS	0.05	0.95	0.33	0.36	11.83	2.32	0.59
Tl		--	--	--	--	--	--	--
Pb	AD-ICP-AES	8	<8	<8	<8	<8	<8	<8
Bi	AD-ICP-MS	0.47	1.09	<0.47	<0.47	<0.47	<0.47	<0.47
Th	AD-ICP-MS	0.018	3.849	3.078	0.251	1.951	0.867	1.009
U	AD-ICP-MS	0.011	0.517	0.423	0.407	0.702	0.775	0.104
								2.193

## Appendix F.II (continued) Whole-rock geochemistry, additional data

Sample ID		348997	348999	349000
Drill Hole ID		GV-16-01	GV-16-01	GV-16-01
Drill Hole Depth (m)		77.5	88	97
UTM easting		567749	567749	567749
UTM northing		5538379	5538379	5538379
Lithology Code	LOD	VC	VC	B-S2
SiO <sub>2</sub>		--	--	--
TiO <sub>2</sub>		--	--	--
Al <sub>2</sub> O <sub>3</sub>		--	--	--
Fe <sub>2</sub> O <sub>3T</sub>		--	--	--
MnO		--	--	--
MgO		--	--	--
CaO		--	--	--
Na <sub>2</sub> O		--	--	--
K <sub>2</sub> O		--	--	--
P <sub>2</sub> O <sub>5</sub>		--	--	--
Cr <sub>2</sub> O <sub>3</sub>		--	--	--
BaO		--	--	--
LOI		--	--	--
Total		--	--	--
CO <sub>2</sub>		--	--	--
S (ppm)	AD-ICP-AES	39	6801	211
Li	AD-ICP-AES	2	29	17
Be	AD-ICP-AES	0.1	0.1	0.1
Na	AD-ICP-AES	530	6595	10327
Mg	AD-ICP-AES	140	44145	32252
Al	AD-ICP-AES	260	66479	85688
P	AD-ICP-AES	4	131	134
K	AD-ICP-AES	98	5758	1988
Ca	AD-ICP-AES	46	15723	73175
Sc	AD-ICP-AES	0.3	25.8	32.7
Ti	AD-ICP-MS	7	2349	3581
Ti	AD-ICP-AES	6	2293	3625
V	AD-ICP-MS	0.8	236.5	362
V	AD-ICP-AES	3	223.8	350.4
Cr	AD-ICP-MS	3	119	47
Cr	AD-ICP-AES	17	106	45
Mn	AD-ICP-AES	1	1209	683
Fe	AD-ICP-AES	110	78791	69667
Co	AD-ICP-AES	1	38	27
Ni	AD-ICP-AES	4	53	37
Cu	AD-ICP-AES	3	897	47
Zn	AD-ICP-AES	3	95	87
Ga	AD-ICP-MS	0.04	13.11	18.16
Rb	AD-ICP-MS	0.11	10.72	4.49
				21.66

**Appendix F.II (continued) Whole-rock geochemistry, additional data**

Sample ID		348997	348999	349000
Drill Hole ID		GV-16-01	GV-16-01	GV-16-01
Drill Hole Depth (m)		77.5	88	97
UTM easting		567749	567749	567749
UTM northing		5538379	5538379	5538379
Lithology Code	LOD	VC	VC	B-S2
Sr	AD-ICP-MS	0.6	29.3	203.7
Sr	AD-ICP-AES	3	30	206
Y	AD-ICP-MS	0.05	11.51	15.12
Y	AD-ICP-AES	0.6	10.3	13.6
Zr	AD-ICP-MS	6	20	32
Zr	AD-ICP-AES	7	21	31
Nb	AD-ICP-MS	0.028	0.568	0.779
Mo	AD-ICP-AES	2	<2	<2
Ag		--	--	--
Cd	AD-ICP-AES	0.8	0.8	<0.8
In		--	--	--
Sn		--	--	--
Sb		--	--	--
Cs	AD-ICP-MS	0.013	0.09	0.056
Ba	AD-ICP-MS	0.8	66	18.1
Ba	AD-ICP-AES	2	59	16
La	AD-ICP-MS	0.1	1.5	1.6
Ce	AD-ICP-MS	0.12	3.64	3.75
Pr	AD-ICP-MS	0.014	0.544	0.593
Nd	AD-ICP-MS	0.06	2.69	3.27
Sm	AD-ICP-MS	0.026	1.081	1.304
Eu	AD-ICP-MS	0.0031	0.4014	0.4974
Gd	AD-ICP-MS	0.009	1.437	2.136
Tb	AD-ICP-MS	0.0023	0.2782	0.3864
Dy	AD-ICP-MS	0.009	1.871	2.729
Ho	AD-ICP-MS	0.0025	0.44	0.6022
Er	AD-ICP-MS	0.007	1.367	1.854
Tm	AD-ICP-MS	0.0019	0.2291	0.2926
Yb	AD-ICP-MS	0.009	1.436	1.99
Lu	AD-ICP-MS	0.002	0.222	0.295
Hf	AD-ICP-MS	0.14	0.66	1.1
Ta	AD-ICP-MS	0.007	0.037	0.052
Au	AD-ICP-MS	0.05	0.76	0.27
Tl		--	--	--
Pb	AD-ICP-AES	8	<8	<8
Bi	AD-ICP-MS	0.47	<0.47	<0.47
Th	AD-ICP-MS	0.018	0.264	0.309
U	AD-ICP-MS	0.011	0.182	0.339
				0.673

**Appendix F.II (continued) Whole-rock geochemistry, additional data**

Sample ID		348007	348008	348017	348047	348081	348955	348961
Drill Hole ID		GV-16-10	GV-16-10	GV-16-11	GV-16-09	GV-16-12	GV-16-08	GV-16-08
Drill Hole Depth (m)		76.36	77.1	53.9	83.3	29.96	14.5	29.5
UTM easting		569008	569008	568323	568264	567665	569155	569155
UTM northing		5538749	5538749	5538632	5538555	5538175	5538679	5538679
Lithology Code	LOD	Obsolete						
SiO <sub>2</sub>		--	--	--	--	--	--	--
TiO <sub>2</sub>		--	--	--	--	--	--	--
Al <sub>2</sub> O <sub>3</sub>		--	--	--	--	--	--	--
Fe <sub>2</sub> O <sub>3T</sub>		--	--	--	--	--	--	--
MnO		--	--	--	--	--	--	--
MgO		--	--	--	--	--	--	--
CaO		--	--	--	--	--	--	--
Na <sub>2</sub> O		--	--	--	--	--	--	--
K <sub>2</sub> O		--	--	--	--	--	--	--
P <sub>2</sub> O <sub>5</sub>		--	--	--	--	--	--	--
Cr <sub>2</sub> O <sub>3</sub>		--	--	--	--	--	--	--
BaO		--	--	--	--	--	--	--
LOI		--	--	--	--	--	--	--
Total		--	--	--	--	--	--	--
CO <sub>2</sub>		--	--	--	--	--	--	--
S (ppm)	AD-ICP-AES	39	90	121	81	67	<39	7154
Li	AD-ICP-AES	2	16	2	<2	12	7	6
Be	AD-ICP-AES	0.1	0.4	0.1	1.2	0.5	0.7	2
Na	AD-ICP-AES	530	23288	<530	<530	28356	<530	23396
Mg	AD-ICP-AES	140	23456	6340	7055	24820	15489	23610
Al	AD-ICP-AES	260	76176	8623	11394	91133	28281	76977
P	AD-ICP-AES	4	185	1819	3543	770	>7000	2167
K	AD-ICP-AES	98	8993	1096	1714	1198	334	17533
Ca	AD-ICP-AES	46	37424	26619	16197	65427	35098	33263
Sc	AD-ICP-AES	0.3	30.9	1.6	1.6	29.8	5.1	13.4
Ti	AD-ICP-MS	7	2797	273	572	8502	3538	8294
Ti	AD-ICP-AES	6	2748	257	606	9051	1840	8028
V	AD-ICP-MS	0.8	205.4	66.3	167	207.6	280.1	196.1
V	AD-ICP-AES	3	189.6	63.4	183.4	207.1	387.8	183.4
Cr	AD-ICP-MS	3	354	25	79	109	78	133
Cr	AD-ICP-AES	17	313	23	83	107	53	117
Mn	AD-ICP-AES	1	1664	1811	6319	1143	>13000	615
Fe	AD-ICP-AES	110	64061	83923	309931	75194	>320000	42981
Co	AD-ICP-AES	1	22	5	38	42	101	14
Ni	AD-ICP-AES	4	78	11	34	80	93	52
Cu	AD-ICP-AES	3	80	60	36	70	19	102
Zn	AD-ICP-AES	3	70	39	73	103	432	66
Ga	AD-ICP-MS	0.04	14.15	2.47	3.39	18.07	15.84	20.49
Rb	AD-ICP-MS	0.11	25.89	3.27	5.77	3.12	0.97	56.1

## Appendix F.II (continued) Whole-rock geochemistry, additional data

Sample ID		348007	348008	348017	348047	348081	348955	348961
Drill Hole ID		GV-16-10	GV-16-10	GV-16-11	GV-16-09	GV-16-12	GV-16-08	GV-16-08
Drill Hole Depth (m)		76.36	77.1	53.9	83.3	29.96	14.5	29.5
UTM easting		569008	569008	568323	568264	567665	569155	569155
UTM northing		5538749	5538749	5538632	5538555	5538175	5538679	5538679
Lithology Code	LOD	Obsolete						
Sr	AD-ICP-MS	0.6	120.8	45.1	23.7	219.3	114.9	194.8
Sr	AD-ICP-AES	3	120	47	25	242	38	180
Y	AD-ICP-MS	0.05	10.3	8.08	16.48	32.74	15.77	20.61
Y	AD-ICP-AES	0.6	8.9	7.2	16.6	29.7	42.9	17.5
Zr	AD-ICP-MS	6	29	6	17	106	35	562
Zr	AD-ICP-AES	7	26	8	26	101	60	486
Nb	AD-ICP-MS	0.028	0.655	0.331	1.075	4.609	1.118	9.537
Mo	AD-ICP-AES	2	<2	<2	<2	<2	<2	<2
Ag		--	--	--	--	--	--	--
Cd	AD-ICP-AES	0.8	0.8	<0.8	0.8	0.9	1.4	<0.8
In		--	--	--	--	--	--	--
Sn		--	--	--	--	--	--	--
Sb		--	--	--	--	--	--	--
Cs	AD-ICP-MS	0.013	0.167	0.018	0.037	0.063	0.013	0.336
Ba	AD-ICP-MS	0.8	176	18.1	21.6	33.2	21.1	645.9
Ba	AD-ICP-AES	2	150	17	25	30	17	619
La	AD-ICP-MS	0.1	1.6	3.9	9.1	6.1	2.1	49.6
Ce	AD-ICP-MS	0.12	3.6	6.17	16.56	15.85	5.06	105.94
Pr	AD-ICP-MS	0.014	0.61	1.345	2.922	2.695	0.722	12.907
Nd	AD-ICP-MS	0.06	2.76	5.56	11.29	12.83	3.53	48.23
Sm	AD-ICP-MS	0.026	1.092	1.377	2.76	4.223	1.373	8.168
Eu	AD-ICP-MS	0.0031	0.4227	0.4089	0.6947	1.6412	0.5221	2.1153
Gd	AD-ICP-MS	0.009	1.52	1.569	2.698	5.64	1.978	5.835
Tb	AD-ICP-MS	0.0023	0.2719	0.2534	0.4836	0.9745	0.3656	0.7368
Dy	AD-ICP-MS	0.009	1.92	1.65	3.133	6.328	2.464	3.686
Ho	AD-ICP-MS	0.0025	0.434	0.3305	0.7422	1.3322	0.5743	0.7005
Er	AD-ICP-MS	0.007	1.316	0.893	2.135	3.871	1.789	1.865
Tm	AD-ICP-MS	0.0019	0.1975	0.1314	0.3193	0.5718	0.2815	0.2396
Yb	AD-ICP-MS	0.009	1.378	0.823	1.953	3.618	1.799	1.688
Lu	AD-ICP-MS	0.002	0.216	0.123	0.279	0.552	0.283	0.229
Hf	AD-ICP-MS	0.14	0.95	0.16	0.37	2.87	1.06	12.81
Ta	AD-ICP-MS	0.007	0.049	0.017	0.06	0.249	0.077	0.522
Au	AD-ICP-MS	0.05	1.88	0.87	2.85	0.5	0.3	2.84
Tl		--	--	--	--	--	--	--
Pb	AD-ICP-AES	8	<8	<8	11	<8	18	<8
Bi	AD-ICP-MS	0.47	<0.47	<0.47	<0.47	<0.47	<0.47	<0.47
Th	AD-ICP-MS	0.018	0.384	0.301	0.825	0.532	0.52	13.673
U	AD-ICP-MS	0.011	0.521	0.329	0.686	0.275	0.312	3.094